UNIVERSITY OF ICELAND

**Ph.D. Thesis**

**in Geophysics**

# Regional thermal anomalies in Tanzania and improved geothermal conceptual models of the Ngozi and Rungwe prospects in SW Tanzania based on results from resistivity and potential field studies

**Makoye Mabula Didas**

October 2024

**FACULTY OF EARTH SCIENCES**

# Regional thermal anomalies in Tanzania and improved geothermal conceptual models of the Ngozi and Rungwe prospects in SW Tanzania based on results from resistivity and potential field studies

Makoye Mabula Didas

Dissertation submitted in partial fulfillment of a
*Philosophiae Doctor* degree in Geophysics

**Advisor**

Gylfi Páll Hersir

**Ph.D. Committee**

Gylfi Páll Hersir, Independent Researcher, Reykjavík, Iceland
Egidio Armadillo, University of Genoa, Italy
William Cumming, Cumming Geoscience, USA
Daniele Rizzello, Tellus S.A.S, Italy
Ásdís Benediktsdóttir, Reykjavík Energy, Iceland
Halldór Geirsson, University of Iceland

Opponents
Prof. Adam Schultz, Oregon State University, USA
Prof. Juanjo Ledo, University of Madrid, Spain

Faculty of Earth Sciences
School of Engineering and Natural Sciences
University of Iceland
Reykjavik, October 2024

Regional thermal anomalies in Tanzania and improved geothermal conceptual models of the Ngozi and Rungwe prospects in SW Tanzania based on results from resistivity and potential field studies
Dissertation submitted in partial fulfillment of a *Ph.D.* degree in Geophysics



Faculty of Earth Sciences
School of Engineering and Natural Sciences
University of Iceland
Sturlugata 7
101 Reykjavik
Iceland

Telephone: +354 525 4000

Bibliographic information:
Makoye M. Didas, 2024, *Regional thermal anomalies in Tanzania and improved geothermal conceptual models of the Ngozi and Rungwe prospects in SW Tanzania based on results from resistivity and potential field studies*, PhD dissertation, Faculty of Earth Sciences, University of Iceland, 177 pp.

Author ORCID: 0000-0002-8012-1958

ISBN: 978-9935-9772-2-9

Printing: Háskólaprent
Reykjavik, Iceland, October 2024

# Abstract

This study investigates for the first time the heat flux distribution in Tanzania, the only East African country intersected by the eastern and western branches of the East African Rift System (EARS). The main goal of the project is to evaluate the geothermal potential of the region by integrating magnetotelluric, magnetic, and gravimetric data and models with existing petrophysical, seismological, volcanological, geochemical and structural information.

At the regional scale, heat flux in Tanzania has been determined from the radially averaged power spectra of the total magnetic field, interpreted as a proxy for the Curie Point Depth. These findings have been correlated to the Moho depth estimates from seismic receiver functions and 3D inversion of gravity data. The results indicate that high heat flow anomalies (exceeding 100 $mW/m^2$) in Tanzania are situated along the EARS at the Proterozoic collision boundaries. Generally, these high heat flow anomalies align with known surface geothermal manifestations and shallow Moho depth (ranging from approximately 30 to 35 km). A high heat flow anomaly has also been detected in the central region of the Tanzanian craton, likely associated with the mantle plume imaged by seismic tomography. According to our findings, the most compelling areas for geothermal exploration in Tanzania are the EARS triple junction in the Rungwe Volcanic Province (RVP), the north Tanzania divergent zone in the eastern branch of the EARS, and the areas of the Proterozoic collision boundaries reactivated by the EARS.

At a more detailed level, the project focuses on the RVP, one of the most promising areas in Tanzania for prospective geothermal resources. High-resolution aeromagnetic data combined with known faults, seismic epicentres, and known surface geothermal manifestations, including thermal springs, hot ground areas, and 3D MT resistivity anomalies are employed to identify concealed structures likely to enhance the permeability of geothermal systems and to delineate structures and formations likely to demarcate the boundaries of geothermal systems within the RVP, particularly in the three most promising prospects: Ngozi (with geothermometry >230°C), Songwe (112°C), and Kiejo-Mbaka (140°C). The 3D resistivity model derived from the inversion of newly acquired and existing magnetotelluric data has been instrumental in updating the geothermal conceptual model of the Ngozi system and defining a new prospective high-temperature geothermal system beneath Rungwe volcano in the RVP.

The 3D MT resistivity inversion results indicate the presence of magmatically heated high-temperature geothermal systems with two discrete reservoirs, a small reservoir below Ngozi caldera and a larger reservoir beneath the Rungwe volcano. A magma chamber is imaged as a deep conductor situated approximately 6 km below the newly identified Ndaga ring structure located between the Ngozi and Rungwe volcanoes and is supported by several young monogenetic eruption centres, the Ngozi volcano to the north that developed into a caldera less than 1,000 years ago and the Rungwe volcano to the south that was formed about 10,000 years ago. The margin of the Ndaga ring structure is defined by the resistive phonolite domes formed approximately 9 million years ago, predominantly overlain by young volcanic

lavas and/or pyroclastic materials. Modelling results that have identified the Rungwe geothermal prospect in addition to the previously interpreted Ngozi prospect have significantly expanded opportunities for discovering geothermal resources in the planned drilling campaign.

Structural investigations in the RVP utilizing magnetic data have revealed that the potential areas for geothermal resources in the RVP are located at the intersections between the NW-SE trending intra-rift faults with NE-SW, N-S, and E-W trending faults. These zones of likely enhanced permeability are bounded by generally low permeable Precambrian rocks to the west and east, respectively, which has significant implications for geothermal resource targeting and development in the RVP. As part of the efforts to bolster geothermal resource targeting in the RVP, an updated structural map has been developed based on aeromagnetic data interpretation constrained by 2D-forward modelling of magnetic anomalies, integrated with previously reported faults, seismic epicentres, 3D magnetotelluric resistivity models, and surface geothermal features.

# Útdráttur

Hér er í fyrsta sinn lagt mat á varmaflæðið í Tansaníu, eina landinu í Austur-Afríku sem er skorið í sundur af bæði eystra og vestra rekbelti Austur-Afríku sigdalsins (EARS). Megin markmið þessa verkefnis er að meta umfang jarðhitans á svæðinu með því að samtúlka MT viðnámsmælingar, og segul- og þyngarmælingar ásamt tiltækum upplýsingum á sviði efna- og eðlisfræði bergsins, jarðskjálfta- og eldfjallarannsókna, jarðefnafræði og höggunar.

Svæðisbundið varmaflæði í Tansaníu hefur verið metið út frá meðal aflrófi heildarsegulsviðsins, miðað við dýpi á Curie flötinn. Niðurstöður eru bornar saman við dýpi á Moho samkvæmt viðtökufalli jarðskjálfta og þrívíðri túlkun þyngdarmælinga. Niðurstöður benda til þess að í Tansaníu sé varmaflæði umtalsvert (meira en 100 $mW/m^2$) í Austur-Afríku sigdalnum við plötuskilin frá frumlífsöld. Almennt falla þessi háu frávik saman við þekkt jarðhitaummerki á yfirborði og lítið dýpi á Moho (um 30-35 km). Há frávik í varmaflæði sjást einnig miðsvæðis í meginlandskjarna Tansaníu og tengjast líklega möttulstróki sem kemur fram í túlkun skjálftamælinga. Samkvæmt okkar niðurstöðum eru áhugaverðustu svæðin til frekari jarðhitarannsókna í Tansaníu við þrípunktinn í Austur-Afríku sigdalnum nærri Rungwe eldfjallasvæðinu (RVP), auk fráreksskila sigdalsins í norðurhluta landsins og svæðinu við plötuskilin frá frumlífsöld sem EARS hefur hreyft við á nýjan leik

Hér er sjónum einkum beint að Rungwe eldfjallasvæðinu, einu álitlegasta jarðhitasvæði landsins. Niðurstöður flugsegulmælinga með hárri upplausn ásamt staðsetningu þekktra misgengja og jarðskjálfta, jarðhitaummerkja á yfirborði þar með talin goshverir og svæði með háum yfirborðshita auk viðnámsfrávika samkvæmt þrívíðri túlkun MT viðnámsmælinga voru nýtt til þess að kortleggja sprungur sem ekki sjást á yfirborði. Þær geta gefið vísbendingar um góða lekt í jarðhitakerfinu og afmarkað jarðhitakerfin á Rungwe svæðinu, einkum þau þrjú vænlegustu: Ngozi (hiti samkvæmt efnahitamælum >230°C), Songwe (112°C) og Kiejo-Mbaka (140°C). Viðnámslíkan samkvæmt þrívíðri túlkun nýrri og eldri MT mælinga gegndi lykilhlutverki við endurgerð hugmyndalíkans af Ngozi jarðhitakerfinu. Líkanið benti jafnframt til nýs háhitakerfis undir Rungwe eldstöðinni.

Þrívíð túlkun MT mælinga bendir til þess að þar sé að finna háhita jarðhitakerfi, varmagjafinn sé kólnandi kvika. Þar séu tveir aðskildir jarðhitageymar, sá minni undir Ngozi öskjunni og sá stærri undir Rungwe eldstöðinni. Kvikuhólf kemur fram sem velleiðandi skrokkur á u.þ.b. 6 km dýpi neðan hinnar nýkortlögðu Ndaga hringlaga myndunar milli Ngozi og Rungwe eldstöðvanna. Tilgátan um kvikuhólf styðst jafnframt við það að þarna eru nokkur stök ung eldvörp, Ngozi eldstöðin fyrir norðan þróaðist í öskju fyrir minna en 1.000 árum síðan og fyrir sunnan er Rungwe eldstöðin sem myndaðist fyrir um 10.000 árum. Barmar Ndaga hringgangakerfisins takmarkast af háviðnáms fónólít-gúlum sem urðu til fyrir um 9 milljón árum. Eftir það hafa ung hraun og/eða gjóska lagst þar ofan á. Niðurstöður reiknilíkana hafa leitt líkur að tilvist Rungwe jarðhitakerfisins til viðbótar við Ngozi kerfið sem var þekkt fyrir. Þar með hafa aukist umtalsvert möguleikar á að finna jarðhita í fyrirhuguðu borverkefni.

Sprungukortlagning RVP-svæðisins með segulmælingum bendir til þess að vænlegar jarðhita auðlindir á RVP-svæðinu séu að finna þar sem misgengi í sigdalnum með NV-SA stefnu skera misgengi með NA-SV, N-S og A-V stefnu. Þessi belti þar sem vænta má góðrar lektar afmarkast til vestur og til austurs af bergi frá forkambrium sem er almennt með lélega

lekt og gefa þar af leiðandi góðar vísbendingar um jarðhita auðlindina á RVP-svæðinu og nýtingu hennar. Til þess að átta sig frekar á eiginleikum RVP-svæðisins var höggunarkortið betrumbætt með túlkun flugsegulmælinga og tvívíðri túlkun segulfrávika ásamt áður kortlögðum misgengjum, staðsetningum jarðskjálfta, þrívíðum viðnámslíkönum og jarðhita ummerkjum á yfirborði.

*Dedication*

*I dedicate this work to my beloved wife Jane Gerald Kilongo, my son Ebenezer Makoye and my daughter Eliana Makoye.*

# Preface

This PhD research project was carried out at the University of Iceland with three main goals: (i) to investigate the regional heat flux distribution throughout the country of Tanzania, (ii) to update the high-temperature magmatically heated geothermal resource conceptual models of the Ngozi and Rungwe prospects in southwest Tanzania and (iii) to investigate surface and subsurface structures in the Rungwe volcanic province using aeromagnetic data integrated with known faults, seismic epicentre locations, existing resource conceptual models and surface geothermal manifestations in order to identify zones with likely high permeability for geothermal resource targeting. At the regional scale, the magnetic method was applied to investigate the regional thermal anomalies in Tanzania aimed at defining heat flux distribution. The interpretation of the regional heat flux distribution was supported by the thickness of the crust estimated from 3D inversion of gravity data. At a more local scale, the magnetotelluric method has been used to investigate the geothermal systems in the Ngozi and Rungwe prospects located in Rungwe Volcanic Province in southwest Tanzania and update the existing geothermal conceptual model of the Ngozi prospect. In addition, magnetic data have been used to investigate the subsurface structures in the RVP including faults and magmatic intrusive bodies. The results were interpreted with known faults, seismic epicentres, petrophysical information and developed geothermal conceptual models based on MT data to define potential areas for targeting geothermal wells.

The results of this study have already been published in two scientific papers in the Journal of Geothermics while the third paper has been submitted to the Journal of African Earth Sciences, reviewed and resubmitted.

# Table of Contents

# List of Figures

# List of Publications

Didas, M. M., Armadillo, E., Hersir, G. P., Cumming, W., Rizzello, D., 2022. Regional thermal anomalies derived from magnetic spectral analysis and 3D gravity inversion: Implications for potential geothermal sites in Tanzania. *Geothermics*, 103, 10243. https://doi.org/10.1016/j.geothermics.2022.102431.

Didas, M. M., Armadillo, E., Hersir, G. P., Cumming, W., Rizzello, D., Benediktsdóttir, Á., Geirsson, H., 2023. New MT surveys and 3D resistivity imaging beneath the Ngozi-Rungwe volcanoes at the triple rift junction of the East African Rift System in SW Tanzania: Support for integrated interpretations of geothermal conceptual models. *Geothermics*, 118, 102893 https://doi.org/10.1016/j.geothermics.2023.102893.

Didas, M. M., Armadillo, E., Hersir, G. P., Cumming, W., Rizzello, D., Geirsson, H., 2024. Imaging and modelling the subsurface structure of the Rungwe Volcanic Province in SW Tanzania with aeromagnetic data: An improved structural map to support geothermal exploration targeting. Manuscript submitted to *Journal of African Earth Sciences.*

Contribution of the author.

Article 1: Conceptualization, Methodology, Software, Formal analysis, Writing – original draft, Writing – reviewing & editing.

Article 2: Conceptualization, Methodology, Software, Formal analysis, Writing – original draft, Writing – reviewing & editing.

Article 3: Conceptualization, Methodology, Software, Formal analysis, Writing – original draft, Writing – reviewing & editing.

# Abbreviations

| | |
|---|---|
| 1D | One-Dimensional |
| 2D | Two-Dimensional |
| 3D | Three-Dimensional |
| CPD | Curie Point Depth |
| E | Electric field |
| EARS | East African Rift System |
| EDI | Electrical Data Interchange |
| EM | Electromagnetic |
| GRÓ-GTP | GRÓ Geothermal Training Programme |
| H | Magnetic field |
| HF | Heat flux |
| ÍSOR | Iceland GeoSurvey |
| ka | Thousand years in geological annotation |
| km | Kilometre |
| NRFZ | Ngozi Rungwe Fracture Zone |
| Ma | Million years in geological annotation |
| m a.s.l | Metres above sea level |
| m b.s.l | Metres below sea level |
| mGal | MilliGal |
| MT | Magnetotelluric |
| MTU-5A | Magnetotelluric data acquisition unit with 5-channels |
| MWe | Megawatt electric |
| ModEM | Modular system for EM inversion (a 3D inversion code) |
| TE | Transverse Electric |
| TEM | Transient Electromagnetic |

| | |
|---|---|
| TGDC | Tanzania Geothermal Development Company |
| TEMTD | A software for 1D inversion of MT and TEM data |
| TM | Transverse Magnetic |
| Ωm | Ohm-metre |

# Acknowledgements

This journey started in 2018 during the UNU Six Month Geothermal Training Programme in Iceland when I re-processed the MT and TEM data from the Ngozi geothermal prospect located in SW Tanzania, followed by 1D joint inversion under the supervision of Gylfi Páll Hersir and Ásdís Benediktsdóttir. The results indicated a possible extension of the Ngozi system southeast towards the Rungwe volcano. This was followed by a discussion with Gylfi Páll Hersir, William Cumming (Bill Cumming) and Daniele Rizzello in 2018 during the seventh African Rift Geothermal Congress (ARGeo-C7) in Kigali-Rwanda about the challenges of the MT data and resistivity anomalies of the Ngozi high-temperature magmatically heated prospective geothermal system and the possibility of extending the research through the Rungwe volcano. Later on, Egidio Armadillo became part of the discussion. This discussion subsequently led to an application for a scholarship to study the Ngozi geothermal system in detail. Ultimately, the United Nations University Geothermal Training Programme (UNU-GTP), currently known as GRÓ-GTP granted me a scholarship to pursue my PhD studies at the University of Iceland. Later during the early stage of this study Egidio Armadillo (University of Genoa, Italy) introduced to me the idea of investigating the regional heat flux distribution in Tanzania using the magnetic method and the thicknesses of the crust using 3D inversion of gravity data.

Firstly, I thank the Almighty God for innumerable mercies and blessings that have enabled me to achieve this big milestone.

Thank you to my beloved wife Jane, my son Ebenezer and my daughter Eliana, for the WhatsApp calls and for forgiving my temporary absence as a father of the family. Time to come home.

I am greatly indebted to my academic supervisors, Gylfi Páll Hersir (Independent Researcher, Reykjavik-Iceland, formerly at Iceland GeoSurvey (ÍSOR)), Egidio Armadillo (University of Genoa), William Cumming (Cumming Geoscience), Ásdís Benediktsdóttir (Reykjavík Energy, formerly at Iceland GeoSurvey (ÍSOR)), Halldór Geirsson (University of Iceland) and Daniele Rizzello (Tellus S.A.S.) for many ideas, suggestions, and comments that greatly shaped and enhanced my understanding. The search for heat flux distribution in Tanzania, the geothermal systems of the Ngozi and Rungwe volcanoes, and the surface and subsurface deformation structures of the Rungwe Volcanic Province was not easy! Their close supervision, endless discussions, advice, guidance and constructive criticism are the lifeblood of my achievement. Our relationship was not strictly academic, they always treated me as a friend, and I enjoyed working with them! You created a positive atmosphere around me and made my life in Iceland enjoyable.

Many thanks go to my employer the Tanzania Geothermal Development Company Limited (TGDC) for the technical and financial support, granting me a leave of absence to pursue my studies in Iceland and allowing the use of data, Geotools®CGG software for the 3D MT inversion and financing additional fieldwork during my PhD project, and for granting me the opportunity of being the first Tanzanian candidate to pursue a PhD in geothermal. Special thanks go to Eng. Kato Kabaka (retired General Manager), Eng. Boniface Njombe (retired

General Manager), Eng. Mathew Mwangomba (current General Manager), TGDC management and my fellow employees, in particular, Eng. Job Mwantinda, Lucas Tumbu, Sadock Josephat, Philibert Phillimon, Adonia Mkangala, Ariph Kimani, and Annastacia Ndimbo among others. You opened doors whenever I needed your assistance during my studies, thank you very much!

It is difficult to find words to thank the Government of Iceland through GRÓ-GTP for the financial support that enabled me to reach my goals. Thank you for the financial support for my school fees, field trips, publications, conferences and living costs in Iceland.

I recognize the invaluable support from the staff of the GRÓ-GTP for their immeasurable support during this academic journey. Special thanks go to Lúðvík Georgsson (retired Director), Guðni Axelsson (Director), Ingimar Haraldsson (Deputy Director), Málfríður Ómarsdóttir, Thórhildur Ísberg (Tori), Markús Wilde etc.

I can not finish this piece without thanking Knútur Árnason for providing his TEMTD program, for the 1D joint inversion of MT and TEM data, support from CGG including Alice Pavesi and Wolfgang Soyer on the use of GeoTools software. Furthermore, I thank ModEM Geophysics for providing an academic license to the ModEM software for the 3D MT inversion. I am thankful to Naser Meqbel for useful discussions, and insights on the use of the ModEM software. Iceland GeoSurvey (ÍSOR) is thanked for helping with running the 3D MT inversion. Thanks to Juan Luis Carrillo-de la Cruz at UNAM in Mexico for providing MAGCPD software used for CPD estimations. Seequent is thanked for providing an academic license to the Geosoft Oasis Montaj software for gravity and magnetic modelling.

Last but not least, I thank my fellow PhD colleagues in the Faculty of Earth Sciences at the University of Iceland, especially the Geophysics PhD students for sharing experiences. Thank you for helping me in facing difficulties, and frustrations but also enjoying good satisfaction during the period of my study. My sincere thanks to the opponents, Professor Adam Schultz at Oregon State University, USA, and Professor Juanjo Ledo from the Department of Geodynamics and Geophysics, University of Madrid, Spain for their constructive comments that greatly improved the thesis.

# 1 Introduction

The distribution of regional thermal anomalies of the Earth's crust can be used to delineate potential areas with geothermal resources and improve the understanding of crustal thickness and magma movement in the subsurface. Geothermal systems are found in regions with high thermal flux, particularly along active tectonic settings such as the convergent or divergent plate boundaries. The East African Rift System (EARS) is a good example of an active divergent tectonic plate continental rift zone which is rich in geothermal resources associated with shallow magmatic movement and deep circulation of meteoric water through faults in a thinning crust. In the EARS, thinning of the crust and rifting has been ascribed to stress linked to plate tectonics and asthenospheric magma upwelling and convection processes (Ebinger, 2005). The EARS is focused and extends through weak zones of continental-continental convergent margins of Proterozoic orogenic belts. Tanzania is one of the several countries in East Africa which is intersected by the EARS.

An overall pattern of extensional stress within the EARS has facilitated the development of fault zones that localize magmatic intrusions and fracture zones that host geothermal upflows. High-temperature geothermal systems draw their energy from shallow magmatic intrusions which serve as heat sources. This intrusive activity also interacts with faults to augment the fracture permeability that hosts hydrothermal flow. A detailed investigation of these geological processes at both regional and volcanic scales is essential for updating resource conceptual models for geothermal exploration and exploitation within a specific area. Furthermore, such research aids in the assessment of geohazard risks and contributes to a deeper understanding of the underlying crustal structure.

This is the first study to investigate the crustal heat flux distribution in Tanzania in order to define potential geothermal areas, with a focus on the Rungwe Volcanic Province (RVP) in SW Tanzania. The project aims to assess the geothermal potential of the region by integrating magnetotelluric, magnetic and gravimetric data and models with existing petrophysical, seismological, volcanological, structural and geochemical information of the hot springs. The study uses the magnetic method to investigate the regional crustal heat flux distribution in Tanzania which is interpreted from Curie Point Depths determined from magnetic data with the thicknesses of the crust estimated from the constrained 3D inversion of gravity data. At a more local scale, the thesis focuses on the RVP to update the geothermal conceptual model of the Ngozi prospect, develop a new resource conceptual model of the Rungwe geothermal system and support geothermal resource targeting in the RVP. Moreover, the study investigates likely permeable zones for geothermal well targeting through the integrated interpretations of surface and subsurface structures from magnetic data which are complemented by previously reported faults, seismic epicentres, and existing and new resource geothermal conceptual models in the four most promising prospects in the RVP, namely Ngozi, Rungwe, Songwe and Kiejo-Mbaka.

## 1.1 Research background

Geothermal systems worldwide are known to exist mainly in areas associated with high heat flows usually along major tectonic plate boundaries associated with young volcanic activities, shallow magmatic plumbing systems, and occurrency of earthquakes. In areas with active geothermal systems underneath, the systems normally manifest on the surface as geysers, fumaroles, mud pools, hot grounds, hydrothermally altered grounds, hot springs, geothermal grasses and other hydrothermal phenomena. However, not all geothermal systems do manifest themselves on the surface. Sometimes they do not or show very limited surface manifestations. Such systems are commonly known as blind or semi-blind geothermal systems. Most hidden and blind systems are <180℃, such as McGinness Hills (140 MWe) and Blue Mountain (>30 MWe) in Nevada. Potential example of a semi-blind system currently producing power includes Svartsengi in SW Iceland (66 MWe and 190 MWt).

In developing geothermal resources, the area of interest is typically first investigated by surface geoscientific studies which include geological mapping, geochemistry and geophysics. This is followed by the development of geothermal conceptual models that are used for targeting and assessing the potential generation capacity of geothermal reservoirs and planning the next well-drilling exploration phase.

Geophysical exploration provides the subsurface information used to characterize the geological elements and structures that may influence the flow of geothermal fluids. In order to characterize the geothermal systems, geophysical methods investigate subsurface physical parameters like electrical resistivity, density, fault motion and magnetization in order to infer the reservoir boundaries and depth, fluid saturation, water table, fracture distribution and low permeability clay cap geometry/distribution, boiling versus liquid state etc. The MT method is the main electrical resistivity method that is used to investigate the 3D geometry of the clay cap and magmatic heat source of the geothermal systems associated with volcanoes. The magnetic and gravity methods, on the other hand, are used to map regional crustal heat flux distribution and, at a local scale, to define the subsurface structures related to the geothermal systems. The micro-seismic studies are used to infer active fault zones; possible presence of magma, and the geometry and stress fields associated with active faults before the geothermal resource is developed.

Detailed geophysical exploration studies have been conducted in some individual geothermal prospects in the RVP. However, the heat flux distribution in the prospects and regional and local structures linking the prospects have not been established in the RVP in Tanzania. In addition, the RVP has not been fully investigated with geophysics including Kiejo, Tukuyu, Mwakaleli, Ngozi, and Rungwe volcanoes. Therefore, there are still some possibilities of finding geothermal systems below or close to the volcanoes. A good example of a recently identified system is the Rungwe geothermal system that has been imaged in the present study.

## 1.2 Research Aims and Objectives

This study aims at:

1. Investigating the distribution of heat flux anomalies over the entire country of Tanzania that could be used to identify potential geothermal areas within and outside the EARS, using spectral analysis of magnetic data to estimate the depths to the Curie Point temperature and 3D inversion of gravity data to estimate crustal thicknesses.

2. Detailed investigation and consequent update of the geothermal conceptual model of the Ngozi prospect and developing the first geothermal conceptual model of the Rungwe prospect using 3D electrical resistivity inversion models of MT data. The main features to be investigated include the geometry of the clay cap and the existence or absence of a shallow magma chamber below the Ngozi caldera or near the Ngozi and Rungwe volcanoes.

3. Using magnetic data to map subsurface structures possibly related to the geothermal systems in the Rungwe volcanic province. Our primary goal is to map the extent of faults where they are concealed below recent sediments and volcanics and to investigate their relationships with the hot springs, hot ground areas, and the interpreted geothermal systems in the Ngozi, Rungwe, Songwe, and Kiejo-Mbaka in the RVP. Our secondary goal is to identify more permeable zones suitable for geothermal wells targeting in the RVP through identification of unmapped faults or part of them below the thick pyroclastic materials using magnetic data, supported by earthquake locations and previously reported faults distributions.

The first goal was accomplished in the first paper published in Geothermics. The second objective was archived and published in the second paper again published in Geothermics. The last objective was fulfilled in the third paper submitted to the African Journal of Earth Sciences presently being reviewed.

## 1.3 The East African Rift System

The African continental plate is in the process of splitting into two tectonic plates, the Nubian plate and the Somali plate that diverge at a rate of 6 to 7 mm per year forming the EARS (Stamps et al., 2008). The EARS stretches over a total distance of 4000 km from North Africa in the Afar region in Ethiopia in the north extending across Tanzania to Beira, Mozambique in the south(Figure 1.1).

The development of the EARS is structurally controlled whereby the magmatic activity and rifting from the Miocene to Quaternary is focused on the weak zones in Proterozoic orogenic belts (Ebinger, 2012). The rifting tensional forces which cause the development of EARS have been modelled and discussed by Ebinger (2012), attributed to three main sources: (i) Tensional forces generated by far-field plate motion, (ii) pressure and stress gradients induced by asthenospheric upwelling (iii) traction forces at the base of lithosphere generated by convecting mantle sufficient to thin the 100-250 km lithospheric plates. However, it is not clear which forces are pre-dominant over the others. Stamp et al. (2014) used geodynamic modelling to quantify the forces driving present-day continental rifting in East Africa and found that the development of the EARS is driven mostly by tensional forces associated with lithospheric gravitational potential energy gradients in the EARS and, the minimum tensional forces resulting from basal shear along the EARS.

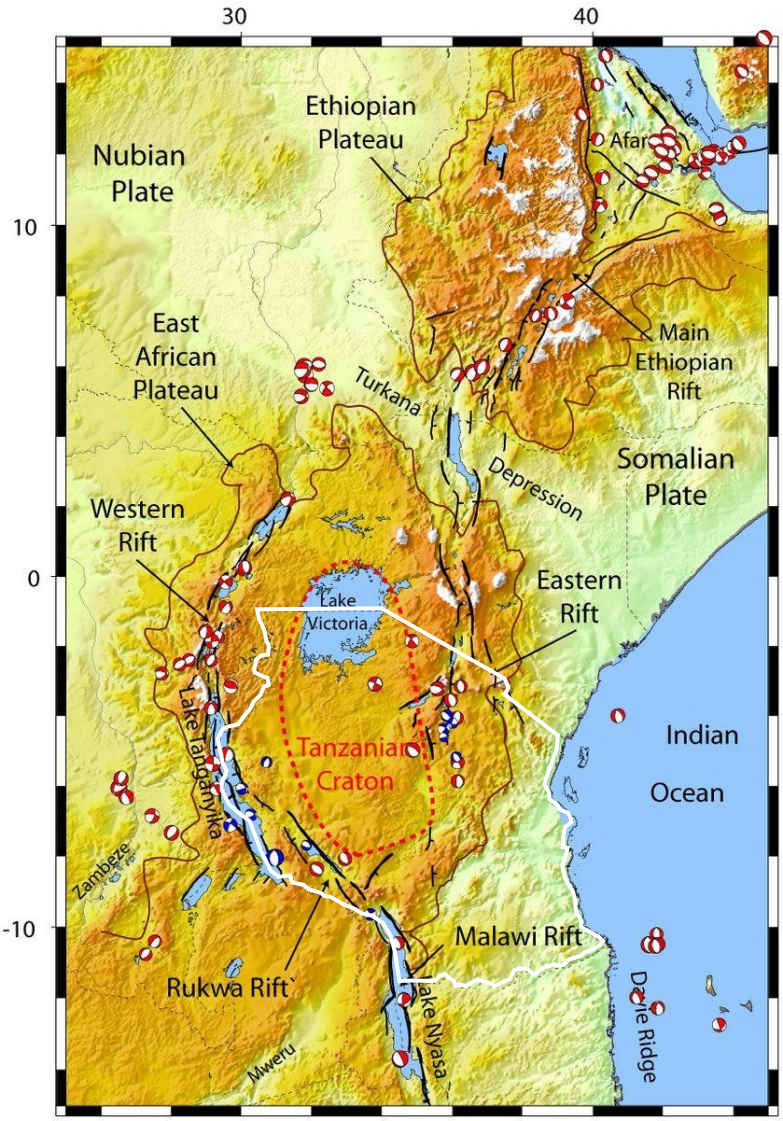


*Figure 1.1 The East African Rift System (modified after Benti et al., 2023). Tanzania, the study area, is outlined in white. The circles indicate the earthquake focal mechanisms describing the deformation in the Earth's crust (Stamps et al., 2014).*

The EARS is divided into two major branches, the western and the eastern branch. Tanzania is the only country in East Africa that is intersected by the two branches, whereas other countries are either intersected by the western or the eastern branch but not both. The eastern branch extends from the Afar region in Ethiopia in the north and continues south along the Paleoproterozoic Mozambique orogenic belt weak zones through Kenya and north Tanzania until it reaches SW Tanzania in the Mbeya region (Figures 1.1 and 1.2). The western branch extends from western Uganda to Mozambique along the weak zones of the Paleoproterozoic Ubendian Orogenic belt through the western part of Rwanda, Burundi and Tanzania where it intersects the eastern branch in the Mbeya region (Figure 1.2). From the Mbeya region, the two branches form the N-S trending Malawi rift that extends further south through Malawi until it ends in Mozambique (Figure 1.2).

In general, the EARS is floored by the Proterozoic high-grade metamorphic basement complex which has been covered by the Karoo and Cretaceous sedimentary rocks in places

(Figure 1.2), that were formed during the failed rift in the Mesozoic time (Ebinger et at., 1989). The Karoo and Cretaceous sedimentary formations are covered by the Cenozoic volcanic rocks of basaltic and trachytic compositions which are also covered by recent sedimentary rocks (Ebinger et al., 1989). The eastern branch is more prolific in magmatic activity due to significant thinning of the crust, enhanced upwelling of the asthenosphere, and lithospheric rupture (Ebinger, 2005; Ebinger et al., 2012). It is floored by the gneisses and granulites of the Neoproterozoic Mozambique belt and partly the Paleoproterozoic Usagaran belt in the SW Tanzania suggesting a predominance of reworked Archean crust (Fritz et al., 2013). The western branch is floored by the high-grade amphibolitic facies metamorphic basement of the Paleoproterozoic Ubendian belt and Mesoproterozoic Kibaran belt (Figure 1.2, Fritz et al., 2013). With the less thinning of the crust, the western branch is generally scant in magmatic activity except in a few places with localised active volcanoes such as the Nyiragongo volcano in the Democratic Republic of Congo (DRC) and at the triple junction and adjacent areas in the RVP in SW Tanzania, the focus of this study, where multiple volcanoes exist including the Ngozi, Rungwe, Kiejo, Mwakaleli and Tukuyu volcanoes and numerous monogenetic volcanic centres fed from deep magmatic sources (Fontijn et al., 2010).

The tectonic setup of the eastern branch is controlled by the preexisting N-S and NE-SW trending large-scale weak zones whereas the western branch is dominated by the pre-existing NW to NNW striking large-scale fault systems (Ebinger, 2005). These fault systems control the geometry of the rift forming a series of half-graben segments some developed to form the lakes (Figure 1.2). The current stress field of the EARS shows that the major fault systems of the EARS are intersected and reactivated by the ENE-WSW trending faults with strike-slip components (Ebinger et al., 2019) that have enhanced magmatic activity, fracture permeability of the rocks, and development of potential geothermal systems (e.g., Hinz et al., 2018).

The EARS geothermal potential has been estimated to be greater than 10 GWe (Benti et al., 2023) and been exploited only to a limited extent for power generation. As of 2023, the total geothermal installed energy capacity in the EARS was about 1200 MWe (Benti et al., 2023). Of these, 938 MWe are generated in the Olkaria geothermal field in Kenya (Gutiérrez-Negrín, 2024) and 7.3 MWe installed capacity in Aluto-Langano geothermal field in Ethiopia (Benti et al., 2023). Menengai with an estimated capacity of 105 MWe, also in Kenya, has 35 MWe installed and a 35 MWe unit is under construction. These resources have been developed in the northern sector of the eastern branch of the EARS (Figure 1.1) and are expected to have a much larger power potential than the geothermal resources in the western branch in Rwanda, Uganda, Malawi, Zambia and most of Tanzania. Unlike the eastern branch, the western branch of the EARS has no developed geothermal resources and only a few geothermal wells have been drilled, although numerous geothermal prospects have been identified and exploration has accelerated in the last few years. These differences depend on the fact that the eastern and western branch of the EARS host different types of geothermal systems. The eastern branch contains volcano-hosted, magmatically-heated high-temperature geothermal systems whereas the western branch mainly hosts low to medium-temperature geothermal systems which are heated by deep-circulation in faults. However, the Ngozi and Rungwe prospects in SW Tanzania are exceptions, as they host prospective high-temperature magmatically heated geothermal systems (Didas et al., 2023). These prospects are located at the intersection of the eastern (Usangu rift) and western (Rukwa rift) branch of the EARS and the northern part of the Malawi rift which is the

southern segment of the western branch of the EARS. This area is characterized by magmatic activity (Fontijn et al., 2010), low shear wave seismic velocity zone and thin lithosphere (O'Donnell et al., 2013). These characteristics are consistent with uprising asthenospheric mantle and localized melting beneath the RVP caused by thermal or compositional anomalies in the upper mantle, synrift or pre-rift lithospheric thining or a combination of the two (Accardo et al. 2017). The geological rationale for the difference is that the eastern branch has a relatively thick section of young volcanics likely to host fracture permeability overlying relatively shallow magma chambers whereas the western branch has relatively sparse and thin volcanics overlying fewer, less voluminous and much deeper magma chambers (Chorowicz, 2005).

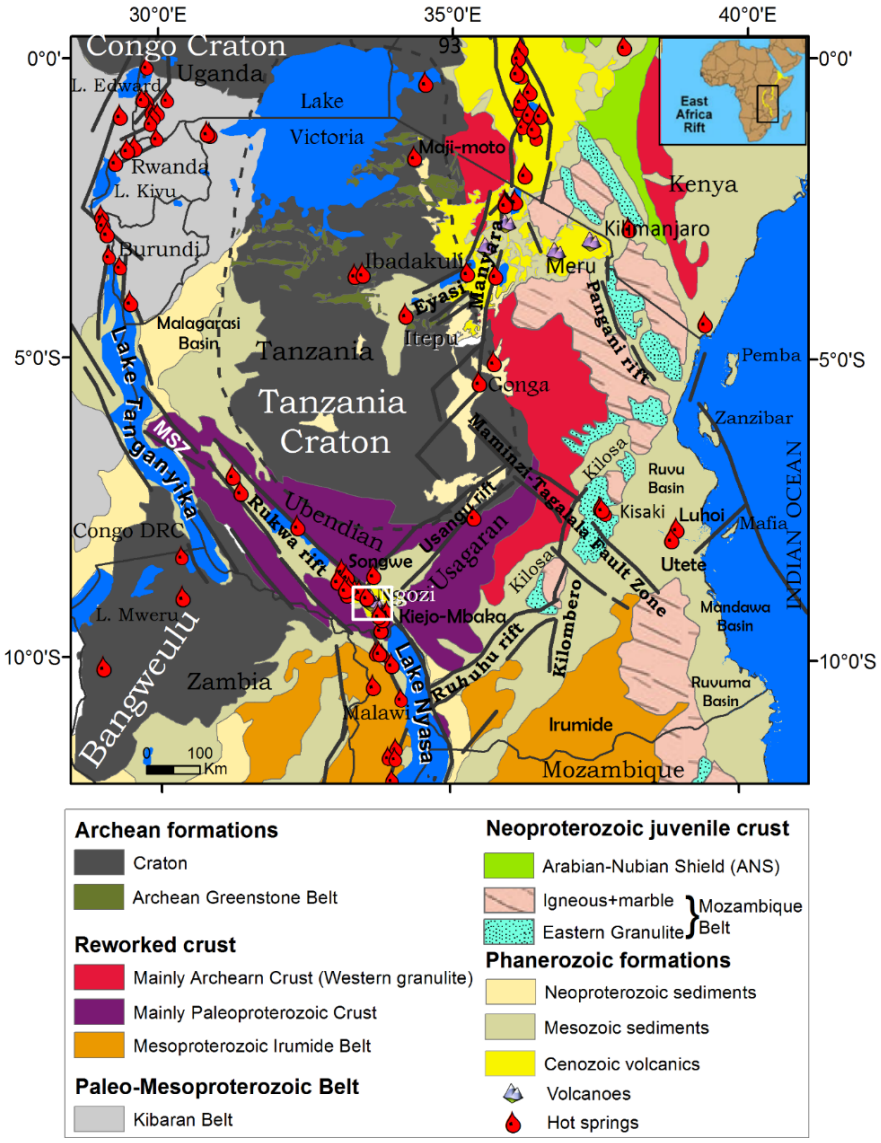


*Figure 1.2 Geological map of Tanzania modified from Fritz et al. (2013) and Didas et al. (2022) showing the main geological domains and hot springs distribution. The EARS margins are shown as thick black segment lines. The continuous thin gray lines define the political boundaries. MSZ: Mungese shear zone. The study area is indicated by a white square located at the triple junction of the east (Usangu rift), the west (Rukwa rift) branches of the EARS and its extension to the south along the Nyasa (Malawi) rift. The inset figure shows the location of the geological map of Tanzania on the African continent.*

## 1.4 Geothermal Systems in Tanzania

In Tanzania, most geothermal prospects are found within the western branch in Rukwa-Songwe rift basin, the triple junction and the Mbaka graben which are the northern part of the Malawi rift segment (Figure 1.2). The four most advanced prospects with estimated reservoir temperature ranging from 100℃ to over 230℃ are considered in this study (UNEP/ARGeo, 2016; Rizello et al., 2022; Asnin et al., 2022; Didas et al., 2023). The Ngozi and Rungwe prospects, are volcano-hosted, and probably magmatically-heated, located at the southwest triple junction of the EARS (Figure 1.2), potentially hosting a reservoir with a temperature greater than 230℃ (Alexander et al., 2016). The third one, Songwe, is located about 40 km northwest of Ngozi with an estimated reservoir temperature of 112℃ (Alexander et al., 2016). The fourth prospect, Kiejo-Mbaka, is located about 45 km south of the Ngozi and Rungwe prospects and has an estimated reservoir temperature of 140℃ (Rizzello et al., 2022). Ngozi, Rungwe, Songwe and Kiejo-Mbaka are the four flagship geothermal projects of the Tanzania Geothermal Development Company Limited (TGDC) that have reached the drilling stage to confirm the resource. Detailed surface studies were completed between 2016 and 2023. Geothermal prospects in the eastern branch in Tanzania are poorly defined due to lack of detailed surface studies. They are generally defined by regional studies and occurrences of the hot and thermal springs. The prospects include Lake Natron, Manyara, and Eyasi (Figure 1.2). Other geothermal prospects are located outside the EARS and generally host low-temperature systems. Such prospects include Ibadakuli and Majimoto (located in the Archean Tanzanian Craton), Kisaki and Luhoi (located in the Mesozoic sedimentary basin in the eastern part of Tanzania).

## 1.5 The study areas

The United Republic of Tanzania is located in East Africa. It is bordered by Uganda to the northwest; Kenya to the northeast; the Indian Ocean to the east; Mozambique and Malawi to the south; Zambia to the southwest; and Rwanda, Burundi, and the Democratic Republic of the Congo to the west. Geologically, Tanzania is composed of rocks with ages ranging from Archean to Cenozoic that have generally been intersected by the EARS which is splitting the African continent (Figure 1.2). The EARS has greatly influenced the distribution of potential sites for geothermal resources in Tanzania where most of the identified sites are located (Figure 1.2).

The RVP has been investigated in detail in this study. It is in the Mbeya region in SW Tanzania at the intersection of the eastern and western branch of the EARS. It comprises five major volcanoes, Ngozi, Rungwe, Kiejo, and Mwakaleli volcanoes as well as the highly eroded Tukuyu volcano and numerous monogenetic small volcanic eruption centres. The RVP is also the home of several geothermal prospects in Tanzania, Ngozi, Rungwe, Kiejo-Mbaka and Songwe prospects which form the focus of this study.

## 1.6 Previous geothermal work in the RVP

Geothermal exploration in the RVP dates back to 2006 when the German Federal Institute of Geosciences and Natural Resources (BGR) started the first detailed geoscientific studies

in the Ngozi and Songwe prospects. The second detailed surface study in the Ngozi prospect was done by the United Nations Environmental Programme (UNEP) in collaboration with TGDC and the Geothermal Development Company (GDC) of Kenya between 2015 and 2016. The EAGER-TGDC collaboration further assessed the Songwe prospect (Hinz et al., 2018). The Kiejo-Mbaka prospect was investigated in 2018 by ELC-Electroconsult in collaboration with TGDC, funded by the Icelandic International Development Agency (ICEIDA). The Rungwe prospect has been investigated recently within this PhD project during the detailed follow-up study of the Ngozi geothermal system (UNEP/ARGeo, 2016).

### 1.6.1 Ngozi and Rungwe prospects

The Ngozi and Rungwe geothermal prospects are 15 km apart at the triple junction of the EARS in Mbeya region, SW Tanzania. Since 2006 Ngozi has been identified by the TGDC as the flagship high-temperature geothermal prospect in Tanzania with a small reservoir interpreted below the Ngozi caldera Lake with a temperature >230℃ estimated from geothermometry of the chloride hot springs located on the bottom of the Ngozi caldera Lake (UNEP/ARGeo, 2016).

In the Ngozi prospect, previous research focused on the geothermal systems using 1D Occam inversion of MT/TEM data (Ochmann and Garofalo, 2013; UNEP/ARGeo, 2016). According to UNEP/ARGeo (2016), MT data from the Ngozi prospect have strong 3D effects manifested by 3D distortion parameters. To exclude these strong 3D effects at depths corresponding to the frequency that indicated the onset of 3D effects, the 1D Occam and layered MT inversion models, with static distortion constrained by TEM, were truncated at about 2000 m depth below surface. Later, Didas (2018) reprocessed the MT and TEM data from the Ngozi prospect and performed 1D joint inversion of the MT and TEM data and partially considered also the reliable deeper information below the clay cap. The study showed the existence of anomalies likely to be cooling intrusives at a depth between 3.5 and 4 km and about 2 km south of the Ngozi caldera. UNEP/ARGeo (2016) made the claim that Ngozi was hermetically sealed. Some subsequent interpretations considered an open connection from Ngozi to adjacent springs or to Ngozi from Rungwe within a northwest trending 4 km x 7 km fault zone which engulfs the Ngozi caldera (Didas and Hersir, 2021). The conclusion in Didas et al. (2023) concluded that separate systems at Ngozi and Rungwe are more likely.

On the other hand, the Rungwe prospect was given less attention due to lack of potential surface geothermal manifestations. The Rungwe prospect was interpreted in 2023 by Didas et al. (2023) as part of this PhD project thanks to additional MT survey data, soil temperature and carbon dioxide flux measurements acquired by TGDC over an area that extended from the Ngozi prospect to the southeast through the Rungwe volcano. The Rungwe geothermal system was imaged by the 3D MT resistivity model as a large up-doming of the conductive clay cap below the Rungwe volcano and is supported by the hot ground areas of >53℃ on the northwest and southeast flanks of the volcano.

In 2024 the United Nations Environmental Programme (UNEP) and the United States Energy Association (USEA) in collaboration with TGDC organised a Technical Review Meeting (TRM) in Mbeya region to discuss the two systems in the Ngozi and Rungwe prospect (Cumming et al., 2024). The TRM brought together a team of geothermal experts from East Africa, New Zealand and USA. The TRM concluded by supporting the findings

of Didas et al. (2023) that Ngozi and Rungwe are separate systems. Slim well drilling is planned in 2024 in the Ngozi and Rungwe prospects.

### 1.6.2 Songwe prospect

Songwe is a low-temperature geothermal prospect located about 40 km northwest of the Ngozi high-temperature prospect. The geothermal system is a deep circulation-fault controlled system with a reservoir temperature of 120℃ estimated from the geothermometry of the hot springs. The prospect has been investigated in several detailed surface study campaigns including the Geotherm group between 2006 and 2013 (Ochmann and Garofalo, 2013), UNEP in 2015 to 2016 (UNEP/ARGeo, 2016) and UK funded EAGER program in 2018 (Hinz et al., 2018). TGDC has developed several direct-use projects for agricultural and heating processes. Pilot projects in Songwe include an egg hatchery for chicken breeding, a hot swimming pool and a greenhouse. TGDC is planning a slim well drilling program to confirm the resource.

### 1.6.3 Kiejo-Mbaka prospect

The first detailed geothermal studies in Kiejo-Mbaka prospect were done in 2018 by ELC-Electroconsult in collaboration with TGDC, funded by ICEIDA (Hersir and Weisenberger, 2015). Before the 2018 study, the prospect was investigated by a regional study that included geochemical sampling of the hot springs that was performed by JICA in the whole country of Tanzania (JICA, 2014). The study by ELC-Electroconsult and TGDC (2017) revealed that the Kiejo-Mbaka prospect probably hosts a low-medium temperature fault-controlled deep circulation geothermal system associated with the Mbaka Fault with a reservoir temperature of 140℃ estimated from geothermometry of the hot springs. Their findings have been supported by additional MT data acquisition and 3D resistivity modelling of the MT data that was performed by Jacobs in collaboration with TGDC from 2022 to 2023 (Jacobs, 2023). For the details about the surface studies performed in the prospect and the geothermal system and geothermal conceptual models, see Rizello et al. (2022) and Jacobs (2023).

In 2020-21, TGDC drilled three shallow wells that reached a maximum depth of about 200 m and encountered warm shallow aquifers near the Mbaka border fault. One of the wells flows with a temperature of about 74℃ and artesian pressure (2 bar well-head pressure when filled with hot water) fed from a depth of about 70 m. Other wells are slightly colder. TGDC is planning a slim-wells drilling campaign in the prospect.

# 2 Methods

## 2.1 The Magnetotelluric method

### 2.1.1 The theoretical basis of the MT method

The Magnetotelluric (MT) method is a passive Electromagnetic (EM) exploration technique that utilizes a broad spectrum of the Earth's natural EM fields ranging from 10 kHz to less than 0.0001 Hz to investigate the spatial variations in the electrical resistivity of the subsurface at depths from less than a hundred metre to several kilometres (Chave and Jones, 2012). The natural EM field signals originate from two distinct sources: (1) low-frequency (1 Hz to <0.0001 Hz) EM signal due to the interaction of the solar wind (a continuous stream of plasma, carrying a weak magnetic field) and Earth's magnetic field (Parker, 1958); and (2) high-frequency signals (>1 Hz to 10 kHz) due to global lightning activities (e.g., Simpson and Bahr, 2005). These far and large-scale sources are treated as uniform plane waves propagating vertically in the highly resistive air and diffusively into the Earth which acts like a good conductor (Vozoff, 1972). The fluctuating magnetic field induces an electric current within the Earth, known as telluric current. The magnitude of the telluric current depends on the electrical conductivity of the subsurface. Based on Ampere's law, measurements of magnetic fluctuations at the Earth's surface determine the total electric current in the subsurface (Chave et al., 2012). The addition of electric field measurement at the Earth's surface provides the electrical conductivity below that point, and the transformation of electric and magnetic field data into the frequency domain helps to map the electrical conductivity as a function of depth and position. Because the EM fields are vectors, it is possible to measure three components of the magnetic field, and two horizontal components of the electric field on the surface of the Earth, where the vertical electric field vernishes due to the presence of the insulating atmosphere. When measurements are made in the 1 Hz to $10^4$ Hz frequency range, the method is referred to as the audio-frequency magnetotelluric (AMT) method. The low-frequency range of MT is typically applied for deep crustal-scale investigations while AMT is used to investigate shallow targets (Munoz et al., 2010). In this study, a frequency range of 320 Hz to 0.001 Hz was used to investigate the geothermal systems in the Ngozi and Rungwe prospects.

The MT method involves measuring the fluctuations of the naturally occurring electric and magnetic fields in orthogonal directions as means of determining the resistivity structure in the Earth's subsurface. The measurements at the surface of both the amplitude and phase of these fields are dependent on the electrical resistivity beneath the Earth's surface. In geothermal areas, the electrical resistivity variation is mainly influenced by several parameters including the conductivity of the rock matrix, permeability and the pore structure of the rock, the degree of fluid saturation, type of pore-fluid such as the content of water and steam, salinity of the pore fluid, surface or interface of conductivity and temperature (Hersir et al., 2021 and references therein). The shallower part of the geothermal system usually less than 2 km is typically dominated by the very low resistivity of the hydrothermally altered smectite clay cap or sedimentary deposition with high cation exchange capacity (CEC). In the geothermal reservoir below the clay cap where the rocks are porous and dominated by high-temperature hydrothermal clay alteration minerals such as chlorite and epidote, resistivity variation is controlled by pore-fluid, salinity of the pore fluid and temperature but

to a lesser degree by the alteration minerals (Lévy et al., 2018). At greater depths, magma chambers and partial melting of the rocks may be particularly conductive and will provide a resistivity contrast within the surrounding rocks (e.g., Ussher et al., 2000). The interpretation of the low-resistivity deeper bodies, however, should be integrated with other data sets as there have been a few cases in geothermal fields where low resistivity anomalies interpreted at great depth as magma chambers turned out to be graphitic bodies and ore minerals in Paleoproterozoic schist (e.g., Cumming, 2009). In some cases, seismic studies have identified magma reservoirs that were later found to have no difference in resistivity compared to the surrounding host rock. For example, at Newberry Volcano in the USA, the magma reservoir is relatively resistive ~50 Ωm made of dry rhyolitic melt, which matches the resistivity of the surrounding rhyolitic host rock (Martinez and Schultz, 2020). Therefore, in such cases, it is not possible to establish the presence of a magma reservoir based entirely on the resistivity contrast between the host rock and the melt.

### 2.1.2 Governing equations

The theory of the MT method is described by Maxwell's equations which relate the electric field **E** and magnetic field **B** as vector fields in any medium (Chave and Jones, 2012). For the derivation of the equations applied in the MT method, the reader is referred to Ward and Hohmann (1988), Simpson and Bahr (2005) and Chave and Jones (2012). The four Maxwell's equations are described below:

$$\nabla \cdot \mathbf{D} = \mathrm{q} \qquad \text{(Gauss's law for the electric field)}, \tag{2.1}$$

$$\nabla \cdot \mathbf{B} = 0 \qquad \text{(Gauss's law for the magnetic field)}, \tag{2.2}$$

$$\nabla \times \mathbf{E} = \frac{-(\partial \mathbf{B})}{(\partial \mathrm{t})} \qquad \text{(Faraday's law)}, \tag{2.3}$$

$$\nabla \times \mathbf{H} = \mathbf{j} \qquad \text{(Ampere's law)}. \tag{2.4}$$

where **D** is the electric flux density (C/m$^2$), **B** the magnetic flux density (T = V s/m$^2$), **E** the electric field (V/m), **H** the magnetic field (A/m), $q$ the electric charge density (C/m$^3$), $\boldsymbol{j}$ the electric current density (A/m$^2$) and $t$ is time (s).

Equation 2.1 is the Gauss's law for the electric field where the electric displacement **D** (in C/m$^2$) is solely due to a free electric charge density $q$ (in C/m$^3$).
Equation (2.2) is the Gauss's law for the magnetic field. It states that magnetic fields, defined by the magnetic induction **B** are always source-free, and no free magnetic poles exist.

*Faraday's law* in Equation (2.3) shows the coupling of an induced electric field **E** in a closed loop due to a time varying magnetic field **B** along the axis of the induced electric field.
Curl of magnetic field with a magnetic intensity **H** is caused by free electric current densities $\boldsymbol{j}$ (in A/m$^2$) and time varying electric displacements. This is expressed mathematically in Equation (2.4), and is also known as *Ampere's law*.

The expressions for *Faraday's* and *Ampere's laws* are initially decoupled. However, in the presence of a linear, isotropic medium the *material equations (constitutive relations)* can be introduced:

$$\boldsymbol{B} = \mu \boldsymbol{H}, \qquad 2.5$$

and

$$\boldsymbol{D} = \varepsilon \boldsymbol{E}, \qquad 2.6$$

Where $\varepsilon=\varepsilon_0\varepsilon_r$ is the dielectric permittivity, $\mu=\mu_0\mu_r$ is the magnetic permeability, with magnetic permeability of free space $\mu_0 = 4\pi \cdot 10^{-7}$ (H/m) and dielectric permittivity of free space $\varepsilon_0 = 8.85 \cdot 10^{-12}$ (F/m). Variations in $\mu_r$ and $\varepsilon_r$ are assumed negligible compared to variations in the bulk conductivity $\sigma$ of rocks. These constants are related via the speed of light, $c_0$ in free space ($c_0 = 1/\sqrt{\mu_0 \varepsilon_0}$).

Furthermore, current I of density **j** in *Ampere's law* (Equation 2.4), in the presence of an electric field can only flow if the medium has a conductivity $\sigma$ (in S/m) different from zero and can be expressed as:

$$\mathbf{j} = \sigma \mathbf{E} + \frac{(\partial \mathbf{D})}{(\partial t)} + \boldsymbol{j}^{ext} \qquad (2.7)$$

where $\sigma\mathbf{E}$ is the conduction current, also known as *Ohm's law*. The $\frac{(\partial \mathbf{D})}{(\partial t)}$ is the displacement current, which is generated by fluctuating electric fields. $\boldsymbol{j}^{ext}$ is extraneous current, or primary current, which is assumed to flow above Earth's surface.
Using the constitutive relations (2.5 and 2.6) and *Ohm's law*, Maxwell's equations (2.1 to 2.4) may be written as:

$$\nabla \cdot \mathbf{E} = \frac{\rho}{\epsilon} \qquad (2.8)$$

$$\nabla \cdot \mathbf{B} = 0 \qquad (2.9)$$

$$\nabla \times \mathbf{E} = \frac{-(\partial \mathbf{B})}{(\partial t)} \qquad (2.10)$$

$$\nabla \times \mathbf{H} = \mu\sigma \boldsymbol{E} + \mu\epsilon \frac{(\partial \boldsymbol{E})}{(\partial t)} \qquad (2.11)$$

***Helmoltz equations***

The Equations 2.8-2.11 can be rearranged to yield an expression for extracting information about the subsurface. Taking the curl of Equation (2.9) yields:

$$\nabla \times \nabla \times \mathbf{B} = \nabla \cdot (\nabla \cdot \mathbf{B}) - \nabla^2 \mathbf{B} = \nabla \times (\mu\sigma \mathbf{E} + \mu \frac{\epsilon \cdot (\partial \mathbf{E})}{(\partial t)}) = -\mu\sigma \frac{(\partial \mathbf{B})}{(\partial t)} - \mu\epsilon \frac{(\partial^2 \mathbf{B})}{(\partial t^2)} \qquad 2.12$$

Since $\nabla \cdot \boldsymbol{B} = 0$, Equation (2.12) simplifies to the equation of telegraphy, which describes the diffusive wave characteristics in a lossy ($\sigma > 0$) medium:

$$\nabla^2\mathbf{B} = \mu(\sigma\frac{(\partial\mathbf{B})}{(\partial t)} + \epsilon\frac{(\partial^2\mathbf{B})}{(\partial t^2)}) \qquad 2.13$$

The MT method works in the frequency domain. To convert Equation 2.13 into the frequency domain, the Fourier transformation conversion is applied. Assuming a harmonic time dependence $e^{i\omega t}$ for **B**, Equation (2.13) yields the *Helmholtz equation in the frequency domain*:

$$(\nabla^2 - \gamma^2)\mathbf{B} = 0 \qquad 2.14$$

where $\gamma$ denotes the complex wave number

$$\gamma^2 = i\omega\mu\sigma - \omega^2\mu\epsilon = k^2 - \kappa \qquad 2.15$$

The undamped wave part, travelling at a speed of $c = 1/\sqrt{\mu\varepsilon}$ is described by $\kappa$, whose wavelength is $\lambda=2\pi/\kappa$. In a conductive medium such as the Earth, the low frequencies utilized in MT make the propagation constant k (in $m^{-1}$) play a more important role since $\sigma \gg \epsilon\omega$. This notion is known as the *quasi-static* assumption and leads to the diffusion Equation for the **B**-field:

$$(\nabla^2 - k^2)\boldsymbol{B} = 0 \qquad 2.16$$

Following the method used above, and considering the case of absence of free current and electric charges, the diffusion Equation for the **E**-field can be derived in a similar fashion:

$$(\nabla^2 - k^2)\boldsymbol{E} = 0 \qquad 2.17$$

Equations (2.16) and (2.17) are fundamental for understanding the MT method. They describe the diffusive behaviour of electromagnetic waves in the frequency range of the MT method.
For a geographical coordinate system *{x,y,z}*, with *x,y and z* pointing north, east and vertically downwards, respectively, Equations (2.16) and (2.17) are not only dependent on the conductivity $\sigma$ and angular frequency $\omega$, but are also depth-dependent, i.e. $\boldsymbol{B}=\boldsymbol{B}(z)$. Therefore, the diffusion Equations have the following solution:

$$\boldsymbol{B}=\boldsymbol{B_0}e^{-ikz} + \boldsymbol{B_1}e^{ikz} \qquad 2.18$$

$$\boldsymbol{E}=\boldsymbol{E_0}e^{-ikz} + \boldsymbol{E_1}e^{ikz} \qquad 2.19$$

$\boldsymbol{B_0}, \boldsymbol{B_1}, \boldsymbol{E_0}, \boldsymbol{E_1}$ are the electromagnetic fields at the surface of the Earth (z=0). **B** and **E** have to vanish for $z \rightarrow \infty$ and, therefore, $\mathbf{B_1} = \mathbf{E_1} = 0$. Thus, the solution for Equations 2.18 and 2.19 simplifies to:

$$\boldsymbol{B}=\boldsymbol{B_0}e^{-ikz} \qquad 2.20$$

$$\boldsymbol{E}=\boldsymbol{E_0}e^{-ikz} \qquad 2.21$$

Where $k^2 = i\omega\mu\sigma$; hence,

$$k = (1+i)\sqrt{\frac{\omega\mu\sigma}{2}} \qquad 2.22$$

### 2.1.3 MT signal penetration depth

Equation (2.22) suggests the superposition of two characteristics of the field. The fields vary sinusoidally with depth due to the imaginary exponential term but also show a depth-dependent attenuation due to the real term. The inverse of the real part of k is known as the *skin depth* or *penetration depth* $(\delta)$ *of EM field,* which is defined as the distance in the direction of propagation, at which the amplitude of the electric field is decreased to 1/e of its original value, that is ~37% (Griffiths,1999), and can be estimated from the frequency of the EM signal and the resistivity of the material which the EM field passes through using the Equation 2.23 below.

$$\delta = \sqrt{\frac{2}{(\omega\mu\sigma)}} = 503\sqrt{\rho/f} \qquad [m] \qquad 2.23$$

where, $\rho$ is the resistivity of the subsurface [Ωm], f is the frequency of the Electromagnetic field [Hz].

From the formula, it is visible that the MT method is a frequency-sounding technique where the smaller the conductivity (high resistivity) is and/or the lower the frequency is, the deeper the EM field penetrates into the Earth. When an EM field of external origin enters the Earth, it diffuses downwards, but its penetration depth is limited as it attenuates. For an Earth of given resistivity distribution, a low-frequency harmonically oscillating EM field incident at the surface penetrates to a greater depth into the Earth than a high-frequency EM field.

The *skin depth* is a very important factor in MT survey design and interpretation. It is small in low resistivity formations and for high-frequency EM signals. Therefore, for greater depth of investigation, it is advisable to acquire MT data at long periods. It is to be noted here that the simple formulation in Equation 2.23 holds for a semi-infinite halfspace case, which is a very simple approximation of the true resistivity distribution in the Earth. For more realistic approximations, formulations for the skin depth must consider the resistivity distribution that would be 1D, 2D or 3D with an increasing degree of correspondence to reality. On the other hand, the use of this simplified formula is justified by the fact that it is often necessary to make a realistic estimate of the investigation depth to design a survey and therefore, before knowing the actual distribution of the electrical conductivity of the subsurface.

### 2.1.4 MT impedance, apparent resistivity, and phase

### Earth's model of uniform conductivity

The MT impedance, apparent resistivity and phase can be derived assuming Electromagnetic

field induction in the Earth's model of uniform conductivity. Expanding the curl operator in full notation, Equation (2.10) shows the following relationship between the components of the **E**- and **B**-fields:

$$\frac{(\partial Ez)}{(\partial y)} - \frac{(\partial Ey)}{(\partial z)} = -i\omega Bx \qquad 2.24$$

$$\frac{(\partial Ex)}{(\partial z)} - \frac{(\partial Ez)}{(\partial x)} = -i\omega By \qquad 2.25$$

$$\frac{(\partial Ey)}{(\partial x)} - \frac{(\partial Ex)}{(\partial y)} = -i\omega Bz \qquad 2.26$$

Since we assume that the ***B***-field propagates vertically downward in z-direction, the induced ***E***-field does not have a *z*-component ($E_Z = 0$). The *plane-wave assumption* states that the induced magnetic field only has horizontal components due to large distance to the source and that it is, therefore, valid for periods up to $10^5$s. This also implies that the $B_Z$ component is equal to 0. Therefore, $\frac{(\partial Ex)}{(\partial y)}$ and $\frac{(\partial Ey)}{(\partial x)}$ have to be zero, too, because there aren't horizontal changes in EM fields. The time derivative of, for example, the $B_x$-component at the surface of the Earth is equal to the spatial derivative of the $E_y$-component with respect to *z*. Equation (2.21) is the solution to the spatial derivative of $E_y$:

$$\frac{-(\partial Ey)}{(\partial z)} = kE_{y0}e^{-kz} = -i\omega B_x = -i\omega B_{x0}e^{-kz} \qquad 2.27$$

The *magnetotelluric impedance* ***Z*** (in units in Ω) is defined as the ratio of the electric and magnetic fields measured at the surface:

$$\boldsymbol{Z}(\omega) = \frac{\boldsymbol{E}_{x0}}{\boldsymbol{H}_{y0}} = -i\frac{\omega}{k} = -i\frac{\omega}{\sqrt{(i\omega\mu\sigma)}} = -\sqrt{(\frac{\omega}{\mu}\sigma)}\sqrt{i} \qquad 2.28$$

The ratio of the orthogonal components of the fields yields the same **Z** with an opposite sign. The *apparent resistivity* of the half-space, in units of Ωm, is defined as:

$$\rho = \frac{\mu}{\sigma}(|\boldsymbol{Z}|)^2 \qquad 2.29$$

In the frequency domain, ***Z****(ω)* is complex and has an associated phase $\phi$:

$$\phi = arg\sqrt{(\frac{\omega}{(\mu\sigma)})}\sqrt{i} = arg\sqrt{(\frac{\omega}{(\mu\sigma)})}e^{(i\pi/4)} = \pi/4 \qquad 2.30$$

Thus, the phase is a constant 45°, regardless of the resistivity of the underlying half-space. Schmucker and Weidelt (1975) introduced the complex Schmucker-Weidelt transfer function ***C***, which is directly related to the inverse of the propagation constant *k:*

$$\boldsymbol{C}: = \frac{1}{k} = \frac{\boldsymbol{Z}}{i\omega\mu_0} \qquad 2.31$$

## EM Induction in a layered (1D) Earth

Let's consider a horizontally layered Earth, where the conductivity only varies with depth along the *x*-axis. Each layer contains components of down-going and up-going energy, e.g., the x-component of the **E**-field in the n$^{th}$-layer can be expressed as:

$$E_{xn} = a_n(k_n, \omega)e^{(-k_{nz})} + b_n(k_n, \omega)e^{(+k_{nz})} \qquad 2.32$$

The magnetic field in the orthogonal *y*-direction would equate to:

$$B_n = \frac{k_n}{(i\omega)} E_{xn} \qquad 2.33$$

Therefore, the transfer function C for the n$^{th}$-layer is:

$$C_n(z) = E_{xn} \frac{(z)}{(i\omega B_{yn}(z))} \qquad 2.34$$

Wait (1954) noted that the transfer function can be analytically determined for each layer. Starting from the lowermost layer N, which is equal to a homogeneous half-space, Wait's recursive formula calculates each corresponding layer on top of the n$^{th}$-layer:

$$C_n(z_{n-1}) = \frac{k_n C_{n+1}(z_n) + \tanh(k_n(Z_n - Z_{n-1}))}{k_n(1 + k_n C_{n+1}(z_n) + \tanh(k_n(Z_n - Z_{n-1})))} \qquad 2.35$$

The apparent resistivity $\rho_a$ of the layered media can be expressed in terms of the complex transfer function **C** (compare to Equation 2.19):

$$\rho_a(\omega) = |C(\omega)^2|\mu_0\sigma \qquad 2.36$$

Accordingly, the phase $\phi$ is given as the inverse tangent of the ratio of the real and imaginary part of $\boldsymbol{C}$:

$$\phi(\omega) = \frac{\Im(C)}{\Re(C)} \qquad 2.37$$

In a two-layered model the phase will be above 45° if the top layer is less conductive than the bottom layer. Contrarily, the phase will be below 45°. For an n-layered Earth, the apparent resistivity curve has an asymptotic behaviour towards the shallowest and deepest layer at either end of the period range. The resolution of the middle layers depends strongly

on their thickness and their resistivity, and cannot necessarily be determined. Furthermore, conductive layers are more easily detected than resistive layers (Spies and Frischknecht, 1991). If $\rho_1$ and $\rho_2$ ($\rho_2>\rho_1$) are the resistivities of two layers, the resolution of the resistive layer is M times that of the conductive layer (Orange, 1989). It should also be mentioned that the entire information about the layered Earth is contained in the electric field E.

**EM Induction in a 2D Earth**

***B and E-polarizations***

Figure 2.1 illustrates a simplified two-dimensional (2D) model with a vertical resistivity boundary striking in the *x*-direction. The resistivity boundary may represent a geological fault or dyke. Electric currents on both sides of the interface must be conserved following the equation of continuity that assigns that the normal components of current density must be continuous on both sides. Ohm's law (Equation 2.7) can then be used to connect the current density to the electric field.

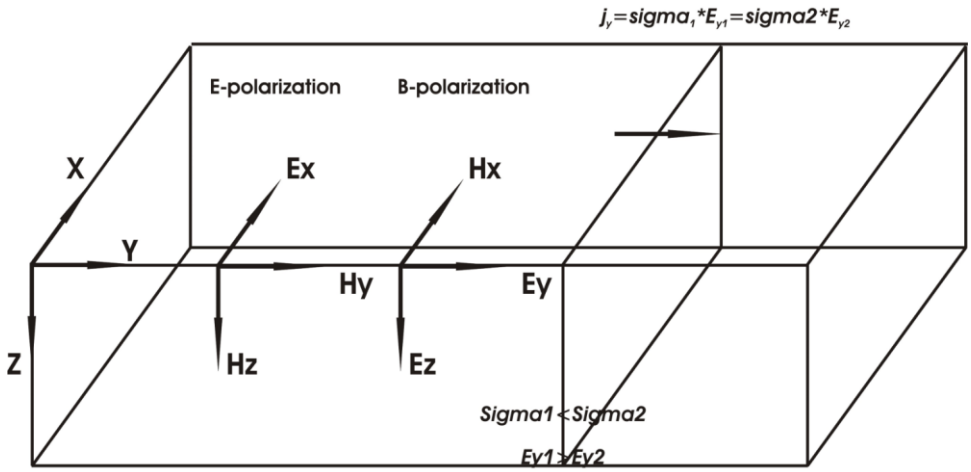


*Figure 2.1 Two-dimensional resistivity model with a lateral contact striking in x-direction. The resistivity boundary separates two regions of different conductivity $\sigma_1 \neq \sigma_2$. The **E**-field discontinuity arises from current preservation across the vertical contact.*

For the y-component:

$$j_{y_1} = \sigma_1 E_{y1} = \sigma_2 E_{y2} = j_{y_2} \qquad 2.38$$

The discontinuity in the resistivities causes a jump in the electric field normal to the boundary ($E_y$-component in Figure 2.1). The tangential components of the **E**-field in both the *y* and the *z*-direction are continuous: $E_{t1}=E_{t2}$. Due to the assumption of *homogeneous magnetic permeability*, the normal and tangential components of the magnetic field ***B*** are also continuous. The 2D assumption requires that the strike length is significantly longer than the skin-depth (Equation 2.23) and that all variations of the fields parallel to the strike are zero ( $\frac{\partial}{\partial x} = 0$).
Furthermore, the EM fields are orthogonal and can be *decoupled* into a component with the

E-field parallel to strike and the **B**-field parallel to strike. The *two modes* are referred to ***E***-polarization *(transverse electric (TE)-mode)* and ***B***-polarization *(transverse magnetic (TM)*-mode), respectively. The ***E***-polarization can be described through the following relationships:

$$\frac{\partial E_x}{\partial y} = \frac{\partial B_z}{\partial t} = i\omega B_z \qquad 2.39$$

$$\frac{\partial E_x}{\partial z} = \frac{\partial B_y}{\partial t} = i\omega B_y \qquad 2.40$$

***E***-polarization

$$\frac{\partial B_x}{\partial y} - \frac{\partial B_y}{\partial z} = \mu_0 \omega E_x \qquad 2.41$$

There is no discontinuous behaviour for the ***E***-polarization as the $E_y$-component does not exist in this mode.
In case of the ***B***-polarization, the currents are flowing perpendicular to the strike:

$$\frac{\partial B_x}{\partial y} = \mu_0 \sigma E_z \qquad 2.42$$

$$-\frac{\partial B_x}{\partial z} = \mu_0 \sigma E_y \qquad 2.43$$

***B***-polarization

$$\frac{\partial E_x}{\partial y} - \frac{\partial E_y}{\partial z} = i\omega B_x \qquad 2.44$$

At the ground-air boundary, $E_Z=0$. From the discussion above, it is clear that the discontinuity in the electric field is $\sigma_1/\sigma_2$ for the ***B***-polarization across the boundary. Therefore, the apparent resistivity $\rho_a$ has an offset of $(\sigma_1/\sigma_2)^2$ (Equation 2.38). Thus, the ***B***-polarization achieves a sharper resolution of the lateral resistivity boundary due to the jump in apparent resistivity. However, the resistivities close to the boundary are estimated too low for the less resistive region and too high for the more resistive region. The ***E***-polarization is more stable regarding the apparent resistivity estimates.

***Impedance tensor rotation***

To take into account the complex geometry of resistivity distrbution, the common practice is to measure both horizontal components of ***E*** and ***H***, *i*n order to find ***Z***. Therefore, the measure of these fields is done following the layout depicted in Figure 2.2.
During MT field data collection, the coordinates of measurement rarely coincide with the strike of a 2D structure. Therefore, the MT impedance tensor ***Z'*** contains non-zero components, unless it is rotated by an angle $\alpha$, which rotates it into a coordinate frame parallel and perpendicular to the strike of the resistivity boundary:

$$\boldsymbol{Z'} = \begin{pmatrix} Z'_{xx} & Z'_{xy} \\ Z'_{yx} & Z'_{YY} \end{pmatrix} = R \begin{pmatrix} 0 & Z'_{xy} \\ Z'_{yx} & 0 \end{pmatrix} R^T = R Z_{2D} R^T \qquad 2.45$$

where

$$R = \begin{pmatrix} \cos\alpha & \sin\alpha \\ -\sin\alpha & \cos\alpha \end{pmatrix} \qquad 2.46$$

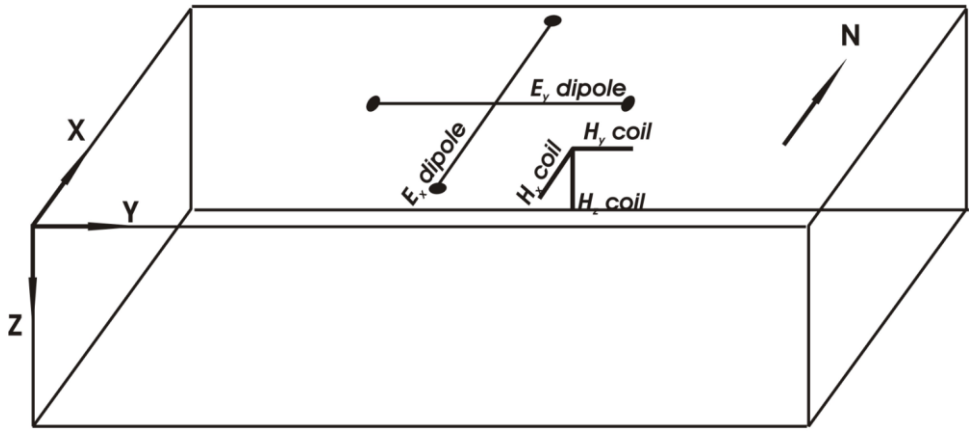


*Figure 2.2 Sketch of MT acquisition layout. E-field is measured by two horizontal electrical dipoles, while H-field is measured by three magnetometers aligned with x-y-z coordinates. Matching between N and x-coordinate is arbitrary.*

The components of the ***Z***-tensor change according to the dimensionality of the resistivity structures, as summarized in Table 2.1:

*Table 2.1 Entries of the impedance tensor **Z** vs dimensionality and isotropic conductivity distribution. The entries become increasingly independent for more complex dimensionality $Z_{\|}$ and $Z_{\perp}$ denote the E-parallel and E-perpendicular impedance, respectively.*

| | ***Dimensionality*** | | |
|---|---|---|---|
| | **1D** | **2D** | **3D** |
| ***Tensor components*** | $Z_{xx}=Z_{yy}=0$<br>$Z_{xy}=-Z_{yx}$ | $Z_{xx}=-Z_{yy}$<br>$Z_{xy}\neq Z_{yx}$ | $Z_{xx}\neq -Z_{yy}\neq Z_{xy}\neq Z_{yx}$ |
| ***Impedance tensor*** | $\begin{pmatrix} 0 & Z_n \\ -Z_n & 0 \end{pmatrix}$ | $\begin{pmatrix} 0 & Z_{\|\|} \\ Z_{\perp} & 0 \end{pmatrix}$ | $\begin{pmatrix} Z_{xx} & Z_{xy} \\ Z_{yx} & Z_{yy} \end{pmatrix}$ |

## 2.1.5 Data acquisition

The electric and magnetic field time series used in this study were acquired in the frequency range between 0.0001 Hz to 10 kHz using three broadband Phoenix MTU-5A systems (Phoenix, 2018) shown in Figure 2.3. MTU-5A consists of five channels, 2 electric field channels Ex and Ey, and 3 magnetic channels, Hx, Hy, and Hz. The instrument has a dynamic range of 130 dB with a powerline notch filter of >40 dB plus a selectable low pass, high pass, and band pass filter.

The magnetic field was measured by three low-noise broadband induction coils (MTC-150 and MTC-50H). The electric field was measured by Lead Chloride non-polarizing, broadband electrodes spaced between 70 and 100 m apart. Analog signals were amplified

and filtered before 24-bit digitization with three sampling rates of 2,400 Hz, 150 Hz and 15 Hz.


*Figure 2.3 Phoenix MTU-5A system (Phoenix, 2018) used for the data acquisition.*

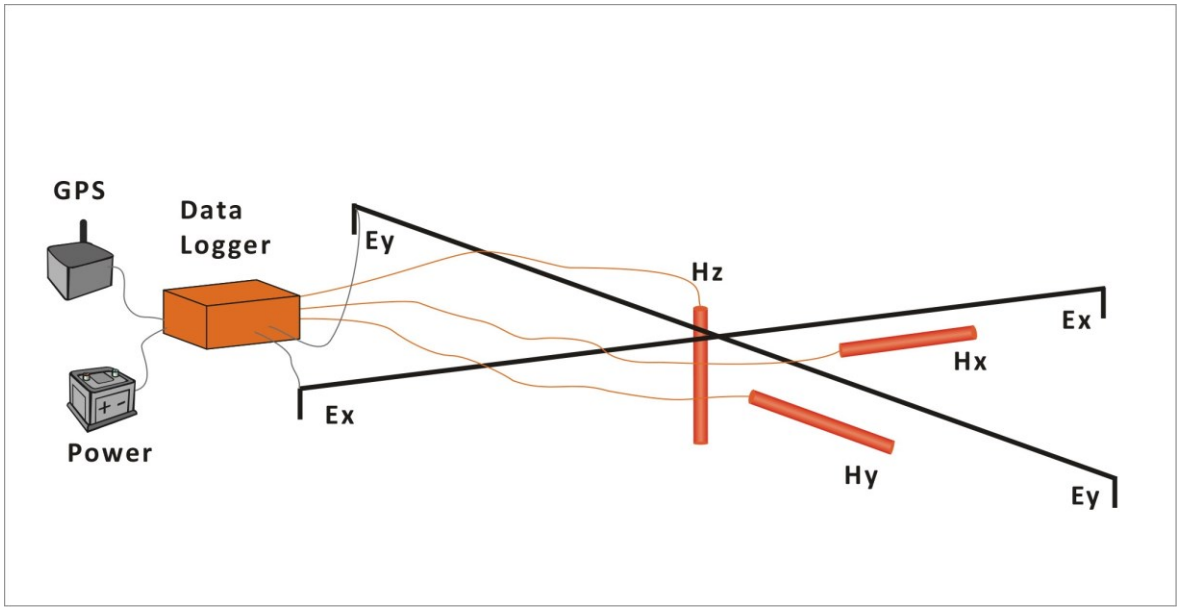


*Figure 2.4 The field setup of an MT station indicating relative electrode line and induction magnetometer positions (Hersir et al., 2021).*

A typical MT data acquisition field layout is shown in Figure 2.4. The electrode lines measure electrical potential differences typically along the North-South (Ex component) and East-West (Ey component) directions. Two magnetic sensors are oriented along the North-South (Hx) and East-West (Hy) geomagnetic directions (that may be easily referred to geographical coordinates once the geomagnetic declination is known) to measure the horizontal magnetic field while a third coil is installed vertically to measure the vertical magnetic field (Hz). In Tanzania, the magnetic declination is nearly 1° which implies that geomagnetic and geographical coordinates are almost identical.

MT data were collected at a total of 190 stations with a spacing ranging from 600 m to 2000 m over an area of approximately 700 km$^2$ across the Ngozi and Rungwe volcanoes within

the RVP. The data acquisition was carried out by TGDC crews and UNEP-supported GDC crews in several field campaigns which were conducted between 2015 and 2023.

The average recording time was about 18 hours, essentially deployed overnight when there is a minimum effect of non-planar electromagnetic fields (Chave and Jones, 2012).

### 2.1.6 Impedance tensor and magnetic transfer functions

The impedance tensor $\boldsymbol{Z}(\omega)$ and magnetic field Tipper $\boldsymbol{T}(\omega)$ are the fundamental MT transfer functions estimated at a given angular frequency $\omega = 2\pi f$ from the MT time series. Impedance tensor and Tipper contain information about the electrical structure of the Earth below each measurement site. The MT transfer functions in fact depend on the electrical resistivity distribution in an approximatively semispherical volume of Earth with a radius equal to the skin depth for the considered frequency of the EM signal. Actually, as explained by Simpson and Bahr (2005), this approximation is far too simple, because the conductivity structure of the Earth varies laterally as well as with depth. It is in fact deined an "adjustment length" which indicates the lateral distance up to which resistivity variations affect the MT impedance.

The time series of the two electric field components (Ex, Ey) and the three magnetic field components (Hx, Hy, and Hz) for each station were transformed into the frequency domain using the Fast Fourier Transformation method (Vozoff, 1991) using robust processing technique and editing the results (Egbert and Booker, 1986) in the SSMT2000 program (Phoenix Geophysics, 2005) and used to estimate the impedance tensor (**Z**):

$$\begin{pmatrix} E_x \\ E_y \end{pmatrix} = \begin{pmatrix} Z_{xx} & Z_{xy} \\ Z_{yx} & Z_{yy} \end{pmatrix} \begin{pmatrix} H_x \\ H_y \end{pmatrix} + \begin{pmatrix} \varepsilon_x \\ \varepsilon_y \end{pmatrix} \tag{2.47}$$

The magnetic field Tipper (the magnetic transfer function **T**) is defined by:

$$\mathrm{H_z} = \mathrm{T_x H_x} + \mathrm{T_y H_y} + \varepsilon_z \tag{2.48}$$

where $\varepsilon_{x,y,z}$ represent the incoherent noise not modelled by the linear relationships above.

The adopted SSMT2000 software (Phoenix Geophysics, 2005) uses an algorithm that performs an iterative coherence-based sorting of the Fourier-transformed data events and is based on two main processing steps (Jones and Jodicke, 1984). The first step transforms the five-time series from the time domain to the frequency domain. The Fourier transform is applied to the time series by calculating the amplitude and phase of the signal at a set of frequencies distributed according to 4 values per octave. The maximum and minimum value of frequencies depends on the sampling rate (which affects the highest frequency) and the length (affecting the lowest frequency) of the time series. Once the time series have been transformed into the frequency domain, the impedance and Tipper may be estimated for each chosen frequency as the second step.

In order to attempt to filter out noise-affected data, the software applies different processing schemes chosen by the user and based on multiple and partial coherency (Jones and Jodicke, 1984) that compare survey site channels with reference site channels (Gamble et al., 1979), and consider only data whose coherence is above a given value. Therefore, cultural noise at the survey site but not at the reference site might be reduced. Moreover, the software applies

a second stage of coherency processing that compares the telluric and magnetic results derived from the previous stage and selects data windows where electric and magnetic channels have acceptable coherence (see Equations 2.47 and 2.48).

The Tipper relates the vertical and horizontal components of the magnetic field alone and is sensitive to lateral changes in resistivity, particularly for vertically oriented contacts and long strike features which are excellent current channelers. In a purely layered earth (1D), the Tipper would be zero and it is therefore used for detecting 2D and/or 3D structures. The Tipper is a complex, frequency-dependent quantity consisting of both real and imaginary components. When plotted on a map as induction vectors, the Tipper provides information about the lateral distribution of conductors. The induction vector magnitude is proportional to the relative strength of the conductor, which generates the induced vertical magnetic field (John and Price, 1970). The real component of the induction vectors can be plotted using the Parkinson conversion (Parkinson, 1959), pointing towards conductors (used in this thesis, see Appendix C) or the Wiese convention (Wiese, 1962), pointing away from conductors.

The induction vectors provide information about the subsurface resistivity structure and are not affected by frequency-independent galvanic distortions caused by localized heterogeneities (Wannamaker et al., 1984).

In this thesis, most of the MT stations show non-zero Tipper values. The MT data have strong 3D effects manifested by 3D distortion parameters including the phase tensors (Caldwell et al., 2004) shown in Appendix B. Therefore, we have performed 3D inversion, incorporating both impedance and Tipper values to map both vertical and horizontal electrical resistivity contrasts. These resistivity anomalies include the Mbaka fault and other intrarift faults and fractures, sediment filling in local valleys, and the Ngozi-Rungwe fault zone. These fault systems have been interpreted to host prospective high-temperature geothermal reservoirs (Didas and Hersir, 2021; Rizello et al., 2022).

### 2.1.7 Remote reference technique and MT impedance estimation

MT measurements are affected by various types of noise, such as cultural sources (e.g., power lines, and trains) and atmospheric sources (e.g., lightning and wind vibrations). The remote reference technique, suggested by Gamble et al. (1979), involves measuring simultaneously at two separate locations: one within the survey area and another one far from the survey area several 10s to 1000s of km distant. The horizontal magnetic data from the survey area are then cross-correlated with the data from the remote station, and only correlated signals are emphasized. Sometimes, for surveys with more than one instrument running together, one station can be used as a remote station for the other(s) in case the separation is not too small and the noise is limited. This process helps to reduce the random and uncorrelated noise while preserving the natural MT signal. Magnetic remote reference is preferred over electric reference due to lower noise contamination and consistent correlation over large distances of the magnetic signals.

However, when the noise at the remote station is coherent with the noise at the survey area, the remote technique will not effectively remove the noise (Simpson and Bahr, 2005). Therefore, it is very important to make good selection of the remote site at an electromagnetically quiet and undisturbed location and to operate it continuously throughout the survey time. In case of power transmission lines, it can be advantageous to use multiple

remote reference stations, where a more distant one can be used to remove the effects of geomagnetically induced currents in the power lines within the long-period MT deadband.

In this study, because of many technical and practical and field logistic challenges (including local lightning, heavy rain, coherent noise), it was not possible to find a good location for a remote reference site for the 2015-2016 survey campaign. As a result, the raw data from 2015-2016 were not processed using remote referencing but whenever possible data from one of the MT sites in the area with better data quality were used as a local remote reference station. However, for the 2020-2022 MT survey campaign, the data were acquired together with the remote reference station that was used to reduce measurement noise.

### 2.1.8 Apparent resistivity and phase

The apparent resistivity and phase can be estimated from the MT impedance tensor. The apparent resistivity is a kind of an average between the different electrical resistivities of the subsurface which the diffusing EM field of varying frequencies travels through.

The phase angle $\varphi(\omega)$ represents the amount of time by which the harmonically oscillating electric field lags or leads the harmonically oscillating magnetic field. Considering $e^{-i\omega t}$ time dependence of the fields: i) the phase is 45° over a half-space; ii) for a 1D earth, the phase increases from 45° with $1/f$ if there is a resistivity decrease at depth, while it decreases with $1/f$ if there is a resistivity increase at depth. Also, for a semi-infinite halfspace, the apparent resistivity is the true resistivity. For a 1D Earth layered earth, at the high frequency limit the apparent resistivity is the true resistivity of the top layer and at the low frequency limit it is the true resistivity of the bottom bounding halfspace. The apparent resistivity takes on intermediate values elsewhere in the frequency (i.e. pseudo-depth) domain. Apparent resistivity and phase for the EM fields for the off-diagonal components (i.e., xy and yx), and for the diagonal components (i.e., xx, and yy) were calculated for ease of data visualization (Figure 2.5).

The apparent resistivity and phase for the off-diagonal impedance tensor elements (similar for the on-diagonal impedance tensor elements, xx and yy) are given by

$$\rho_{xy}(\omega) = \frac{1}{\mu_0 \omega}\left|Z_{xy}\right|^2 \quad \text{and} \quad \varphi(\omega) = \tan^{-1}\left(\frac{Im\{Z_{xy}\}}{Re\{Z_{xy}\}}\right) \tag{2.49}$$

$$\rho_{yx}(\omega) = \frac{1}{\mu_0 \omega}\left|Z_{yx}\right|^2 \quad \text{and} \quad \varphi(\omega) = \tan^{-1}\left(\frac{Im\{Z_{yx}\}}{Re\{Z_{yx}\}}\right) \tag{2.50}$$

where, *Im* means the imaginary component of the complex number and *Re* is the real component. Both apparent resistivity and phase are functions of an angular frequency ($\omega = 2\pi f$), and $\mu_0$ is the magnetic permeability in free space.

The phase angle can also be approximated as the slope of the resistivity curve when plotted against the period (Weidelt, 1972; Vozoff, 1990).

In the present study, apparent resistivity, phase and Tipper were computed for every MT station. The resulting apparent resistivities and phases were stored as Electrical Data Interchange (EDI) format, suitable for compatibility with geophysical inversion software.

Figure 2.3 shows an example of apparent resistivity and phase curves (xy- and yx-mode) at MT stations nz320 and nz342 measured in the Ngozi prospect.

MT station nz342 is possibly affected by the near-field effect only affecting the yx-mode. Since it affects the yx-mode only, we inferred that this issue was due to the mostly E-W trending 220 kV powerline. These observations are explained in Paper II. In such cases, the mode which is more affected by the near-field, is usually the one more parallel to the equivalent electrical dipole source, as reported by Pádua et al. (2002).

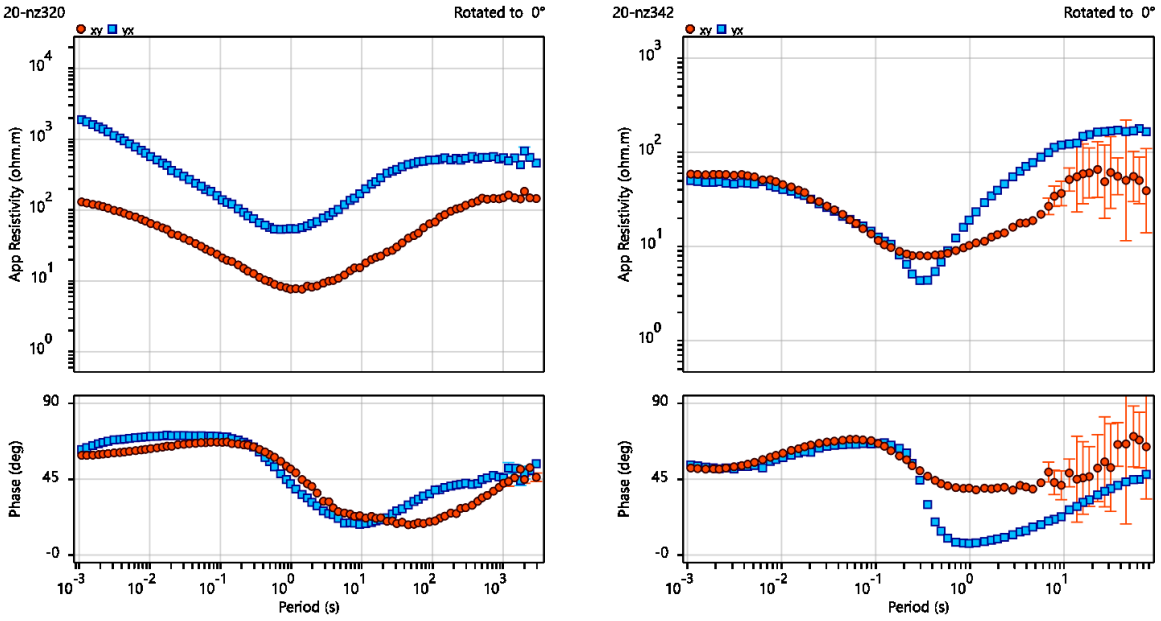


*Figure 2.5 Apparent resistivity and phase plotted against period which acts as a proxy for depth, for MT station nz320 and nz342, respectively. The nz320 MT data were acquired on the ridge of Ngozi volcano and are strongly affected by static shift distortion of more than a decade seen by the separation of the two apparent resistivity curves. Station nz342 was measured in the valley, north of Ngozi volcano and its yx mode was strongly affected by the 220 kV powerline, as revealed by the yx apparent resistivity mode slope exceeding 45° and phases approaching 0° from about 2 to 0.2 s. Please note that x and y refer to the geographic North and East directions, respectively. 'Rotated to 0°'at the top right of the apparent resistivity panels indicates that there has been no rotation of the data with respect to the geomagnetic coordinates.*

### 2.1.9 Directionality and Dimensionality of MT data

Before interpreting MT data, it is essential to analyze the dimensionality of the data in order to determine the appropriate inversion method and to understand the potential limitations of the models. The resistivity model for the Earth can be categorized as 1D, 2D, or 3D based on single or multiple MT stations parameters. For single MT station parameters, the resistivity pattern in the survey area can be categorized using parameters such as the Skew, a dimensionless parameter that shows how the MT data vary from the ideal 2D model computed from the impedances (see Equation 2.53 below), the amplitude of $Z_{xx}$ and $Z_{yy}$ relative to the amplitude of $Z_{xy}$ and $Z_{yx}$ in the principal axis rotation, from the split of the apparent resistivity curves as well as the Tipper magnitude. For multiple stations, phase tensors and induction arrows are emphasized more than impedance polar diagrams that tend

to be biased by static shift. Based on the assessment of these MT station parameters, a 1D, 2D or 3D inversion approach can be chosen to appropriately resolve the subsurface resistivity pattern. In a 1D Earth, resistivity only changes with depth. In a 2D Earth, resistivity varies with depth and in one principal horizontal direction (across the geoelectric strike direction). The horizontal angle perpendicular to that direction is called the electrical strike (see further in Hersir et al., 2021). In a 3D Earth, there is no specific strike direction and resistivity changes in all three principal directions. To better understand the variations in resistivity with depth in our study area, we conducted 1D and 3D inversion models of the resistivity distribution. We compared the results for a detailed investigation of the conductive smectite clay cap and reservoir geometries that were integrated with geological and geochemical results and identified potential areas for exploration drilling to confirm the presence of geothermal resources.

## 1D Earth case

In a 1D model, it is assumed that the Earth is a half-space made of multiple horizontal layers. In this case, the impedance tensor can be represented as follows:

$$\begin{pmatrix} E_x \\ E_y \end{pmatrix} = \begin{pmatrix} 0 & Z_{xy} \\ -Z_{xy} & 0 \end{pmatrix} \begin{pmatrix} H_x \\ H_y \end{pmatrix} \tag{2.51}$$

Only the orthogonal components of the magnetic and electric field are related, independent of the component orientations, and the diagonal components are zero. The off-diagonal components (Zxy and Zyx) are equal in magnitude but have opposite sign.

We used the TEMTD Linux-based software (Árnason, 2006b) to perform 1D joint inversion of the MT and TEM data using the arithmetic mean value of the off-diagonal components of the impedance tensor. The arithmetic mean was found to be more reliable and consistent compared to other invariants such as the determinant and the geometric mean. Therefore, it was chosen as the most suitable parameter for the inversion process. It provided stable and reasonable estimates for the resistivity values for each MT station, specifically for the $\rho_{xy}$ and $\rho_{yx}$ resistivities. The static shift distortion of MT data was corrected through the 1D joint inversion of MT and TEM data. This was achieved by applying a static shift correction factor, which shifted the apparent resistivity curve of the MT data to tie in with the apparent resistivity curve of the collocated TEM data.

We used a model composed of 50 layers with a noise floor for the response data set to be 3%. Damping factors were applied to smooth the output model, and the misfit of the model was evaluated using the Root-Mean-Square (RMS) factor. The highest RMS in the final fit was less than 2 for all soundings. Figure 2.64c illustrates a smooth 1D inversion result for site ng30Ar, representing the resistivity variations with depth in the study area.

## 2D Earth case

For 2D scenario, it is assumed that resistivity changes with depth and in one principal horizontal direction, i.e., orthogonal to the direction along which the conductivity is constant, the geoelectric strike. In this situation, the geoelectric strike direction, is determined by mathematically rotating the impedance tensor to align with the strike of the geoelectric structure that may be causing current channeling as discussed in subchapter 2.1.4. The impedance tensor can be expressed as:

$$\begin{pmatrix} E_x \\ E_y \end{pmatrix} = \begin{pmatrix} 0 & Z_{xy} \\ Z_{yx} & 0 \end{pmatrix} \begin{pmatrix} H_x \\ H_y \end{pmatrix} \quad (2.52)$$

In the case of a perfectly 2D scenario, only the magnetic and electric fields' orthogonal components are related, meaning that the diagonal components ($Z_{xx}$ and $Z_{yy}$) are equal to zero. This simplifying assumption can be applicable in many cases, but it must be carefully tested for each dataset. The methods for testing dimensionality and geoelectric strike direction are discussed in subchapter 2.1.10.

When the electric field is parallel to the electromagnetic strike, it is referred to as Transverse Electric (TE) mode or **E**-polarization whereas, Transverse Magnetic (TM) mode or **B**-polarization is when the magnetic field is parallel to the electromagnetic strike.

The inversion process is carried out on profiles perpendicular to the geoelectric strike after having rotated the measured coordinate system parallel and perpendicular to the geoelectric strike. We have not included the 2D inversion results in this thesis because the resistivity pattern is not generally 2D. The MT stations are 1D to a limited depth extent and are included in Appendix B to illustrate the implications of noise for the resolution of resistivity below individual stations.

### 3D Earth case

The Earth is generally 3D, therefore, resistivity varies with depth and in all horizontal directions. In a 3D Earth model, all the components of the impedance tensor are non-zero and, the diagonal elements of the impedance tensor $Z_{xx}$ and $Z_{yy}$ do not become zero simultaneously in any rotated coordinate system. Similarly, the off-diagonal elements of the impedance tensor $Z_{xy}$ and $Z_{yx}$ differ. Therefore, for a 3D Earth model, all the tensor elements are considered (Chave and Jones, 2012). The MT parameters are described by the impedance and induction terms in Equations 2.47 and 2.48.

In this thesis, a 3D resistivity modelling of MT data was performed using two software, the ModEM software (Egbert and Kelbert, 2012; Kelbert et al., 2014) and the GeoTools-RLM3D software developed by CGG (Mackie and Watts, 2012) by inverting the unrotated (i.e. aligned along the geomagnetic north that is practically parallel to the geographic North given the declination lower than 1° in the survey area) full impedance tensor elements ($Z_{xx}$, $Z_{yy}$, $Z_{xy}$, and $Z_{yx}$) together with the vertical to horizontal magnetic transfer functions from the 190 MT stations. The final inversion using GeoTools-RLM3D used all components of stations edited to reduce noise, whereas preliminary 3D MT inversions using ModEM utilized the generally lower noise on-diagonal impedance data. The two inversion codes produced similar results, however, GeoTools-RLM3D imaged a deep conductor not revealed by ModEM. The second paper in this thesis describes the modelling process and the results in detail.

## 2.1.10 MT dimensionality indicators

For MT data, dimensionality is dependent on frequency. At lower frequencies, the MT responses are influenced by changes in resistivity at both greater depth and greater distance from the station. Various parameters are used to assess the dimensionality, including Ellipticity, Skew, MT polarization (polar diagrams), Tipper induction arrows, phase tensor

analysis, and the apparent resistivities $\rho_{xx}(\omega)$ and $\rho_{yy}(\omega)$ spectra, which are compared directly to the $\rho_{xy}(\omega)$ and $\rho_{yx}(\omega)$ spectra in an appropriate rotation.

## Skew, Ellipticity and Phase tensor

The Skew (S) is a dimensionless parameter that shows how the MT data vary from the ideal 2D model as defined by Swift (1967) and is expressed by the following equation:

$$S = \left|\frac{Z_{xx} + Z_{yy}}{Z_{xy} - Z_{yx}}\right| \tag{2.53}$$

Ellipticity (E) is the ratio of the magnitude of the difference of the rotated diagonal elements to the sum of the rotated off-diagonal elements of the rotated impedance tensor as defined by Ranganayaki (1984) by the following equation:

$$E = \left|\frac{Z'_{xx} - Z'_{yy}}{Z'_{xy} + Z'_{yx}}\right| \tag{2.54}$$

According to Ranganayaki (1984) if E is < 0.1 the subsurface structure may be considered mainly as 1D.

Phase tensor analysis (Caldwell et al., 2004) on the other hand can help to characterize the 1D, 2D and 3D dimensionality and geoelectric strike direction without imposing the condition of 2D dimensionality of the subsurface. Like the Skew and Ellipticity, the phase tensors are sensitive to dimensionality of the subsurface but unlike Skew and Ellipticity, phase tensors are not affected by the static distortion.

To assess the subsurface dimensionality below the survey area, phase tensors are often represented as ellipses with principal phase values of the tensor represented by major and minor axes of the ellipse, respectively, coloured by the normalized Skew angle indicating the dimensional indicator. Plotting the phase tensor ellipses on a map reveals the strike direction and dimensionality of the subsurface. For 1D Earth, the phase tensor will plot as a circle. For 2D Earth, the phase tensor will plot as an ellipse with the major axis equal to the magnitude of the maximum value of the diagonal phase tensor elements. For 3D Earth, the phase tensor will be an ellipse and will align perpendicular to the most conductive direction. Usually, low Skew values of <0.2 indicate the resistivity geometry of the subsurface as 1D or 2D while a large Skew angle implies a 3D structure.

Our observed Skew values in the Ngozi and Rungwe prospects are generally large and imply a strong 3D effect. Appendix B provides phase tensor ellipses of MT data for the periods of 0.1 s, 1.0 s, 10 s and 100 s. At 10 s and longer periods, the data are typically 3D. Therefore, to resolve the 3D subsurface geometry, we performed the 3D inversion for the MT data in this study.

## Tipper

Based on the plane wave assumption the vertical magnetic fields are created by lateral conductivity gradients in the Earth's subsurface. The Tipper **T** (ω) is non-zero above non 1D conductivity structures, and zero above a 1D conductive structure (Berdichevsky and Dmitriev, 2008). Typically, Tippers are used to detect 2D and/or 3D conductivity structures (e.g., Samrock and Kuvshinov, 2013; Morschhauser et al., 2019; Hersir et al., 2021).

In this study, we estimated Tipper magnitudes by measuring the vertical component of the magnetic fields. The Tippers showed large values greater than zero, indicating that the subsurface in the study area is generally 2D or 3D.

### 2.1.11 Static shift analysis and correction techniques

The static shift effect is a phenomenon that has been recognized as an interpretation problem by many researchers for decades (e.g., Sternberg et al., 1988; Árnason et al., 2010). Generally, static shift originates from 3D structural effects that are on a scale too small to resolve given the frequency range and station spacing used in the survey. In areas with flat topography MT static shift is likely caused by near surface inhomogeneities typically produced by hydrothermal alteration in geothermal areas near the sounding site at a depth less than the minimum MT skin depth (e.g., Chave and Jones, 2012). In areas with rugged surfaces such as many volcanoes, the static shift is more likely to be caused by the topography (e.g., Stark et al., 2013) whereas the electric current flux is forced to spread out in topographic highs, thus lowering resistivity, and concentrating in topographic lows, thereby increasing resistivity (Árnason, 2015). Regardless the origin of the static shift, there are several approaches to explain and model statics. For example, the static shift caused by topography can be modelled by using the techniques of e.g., Jiracek (1990), Stark et al. (2013) and Árnason (2015) while static caused by inhomogeneities can be modelled using the approach by Pellerin and Hohmann (1990).

Practically, the static shift effect can be seen as a shift of one mode which could be detected by mode separation or both modes of the apparent resistivity curves of MT sounding data e.g., nz320 (Figure 2.5) across the entire frequency range (Park and Livelybrooks, 1989). Another way to evaluate the static shift effect is by observing the vertical shifts between the xy and yx apparent resistivity pseudo-sections. If not corrected for before or during inversion, the static shift can lead to incorrect resistivity values and a misleading pattern of resistivity, particularly with respect to adjacent stations not affected or differently affected by the static shift. While the static shift strongly affects the resistivity curve, it does not impact the phase curve. Likewise, the magnetic field Tipper is generally not affected by statics since it is only related to magnetic field components.

Various methods are employed to correct static shifts, with one of the most common techniques involves the use of active EM methods such as Transient Electromagnetic (TEM) measurements to provide an alternative constraint on near-surface resistivity. The MT apparent resistivity curves are then adjusted accordingly. One of the most effective methods involves correcting the shift by conducting a 1D joint inversion of the apparent resistivities of the collocated MT and TEM stations when the shallow structure is effectively 1D (e.g., Sternberg et al., 1988; Cumming and Mackie, 2010; Árnason et al., 2010; Árnason, 2015). Other methods for mitigating the effect of the MT static shift include 3D inversion of the MT phase tensor (Caldwell et al., 2004; Samrock et al., 2018), determination of the square root of the sum of the squared elements of the impedance (Rung-Arunan et al., 2022), averaging techniques (Tumbu and Mizunaga, 2020), and inverting for both 3D conductivity distribution and the elements of the distortion matrix (e.g. Avdeeva et al., 2015; Moorkamp et al., 2020; Soyer et al., 2021). Static shifts caused by topography can be corrected by modelling the topography in the survey area (Stark et al., 2013). However, static shift distortion is still an ongoing research topic and there is no general agreement on how to handle it.

Another simpler method for addressing static distortion in 3D MT inversion involves the following steps: First, finely discretize the upper part of the model. Then, reduce the regularization parameter in that part so that the structure in the upper zones can be arbitrarily rough while using more typical levels of regularization below. The upper zone becomes a scattering layer that can accommodate the effects of the static distortion. In this thesis, the static shift effects were assessed and corrected using TEM data and by modelling the topography in the starting model before 3D inversion was performed in the ModEM code (Egbert and Kelbert, 2012; Kelbert et al. 2014) and GeoTools-RLM3D software developed by CGG (Mackie and Watts, 2012). We found that the static shift is not only due to shallow conductors but also because of the rugged terrain. Therefore, it is important to isolate and understand the effect of terrain and increase confidence in interpreting the subsurface resistivity variations.

Based on the split between the two modes of apparent resistivity at 100 Hz in principal axis rotation, 45 MT stations had an apparent shift that differed by a factor of >2 times, at which point the geometry of the resistivity model was likely to be noticeably affected in this geothermal context. However, a >5 times apparent static was detected at only 15 stations (e.g., see Figure 2.5) which might significantly affect the interpretation if not adjusted. Moreover, based on correlations with the TEM data, the average shift was only times 0.88 (e.g., see Figure 2.6c), therefore, both modes were not commonly offset in the same direction. The sites located at the Rungwe and Ngozi volcanoes show large static shifts affecting the off-diagonal (xy and yx) components of the apparent resistivity curves throughout the frequency range (e.g., nz320 in Figure 2.5) probably caused by topography.

We estimated and corrected static shift distortion at stations with coincident TEM data. We used the Pellerin and Hohmann (1990) method to match the $Z_{xy}$ and $Z_{yx}$ impedances by shifting the two modes to a synthetic MT curve derived from the TEM data. This was part of a 1D joint inversion of the MT and TEM data using the TEMTD software, as shown in Figure 2.6 panels b and c.

Where TEM soundings were not available, we corrected MT stations for statics by aligning the apparent resistivity mode polarization with the topography at 100 Hz. We then adjusted it based on the expected topographic distortion based on Jiracek (1990). If an MT station was located on a ridge with its maximum polarization aligned with the ridge, we shifted the lower apparent resistivity mode to the higher mode in principal axis rotation. This evaluation at 100 Hz in a geothermal context is usually sufficient to isolate static distortion due to topography from the geological signal and from sources of noise such as capacity coupling (typically >300 Hz) or 50 Hz noise (UNEP/ARGeo, 2016).

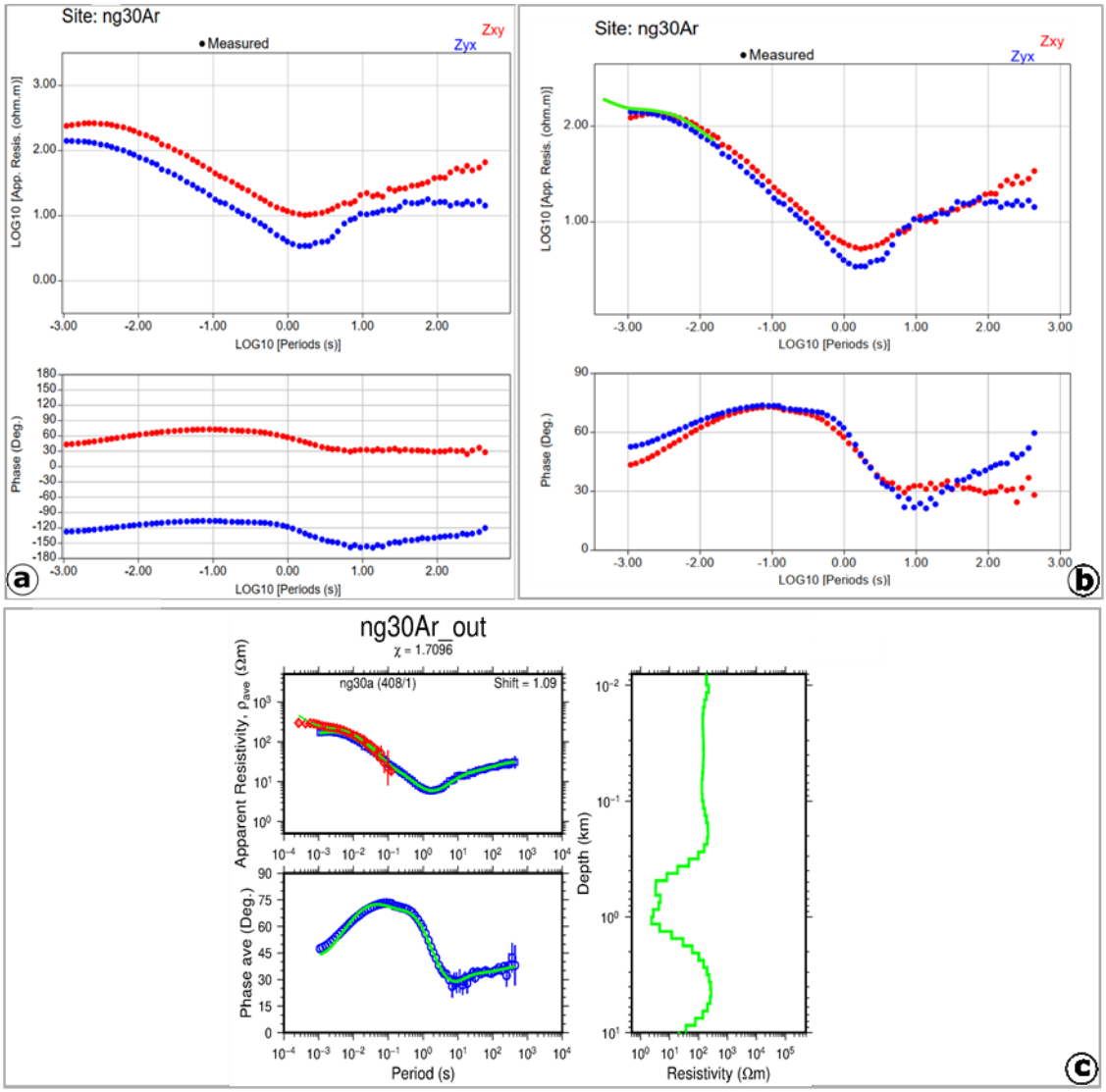


*Figure 2.6 A comparison between the field data affected by the static shift, and the static shift distortion corrected using TEM data and the 1D joint inversion result of MT and TEM data. **(a)** Field data for site ng30Ar affected by the static shift seen by the separation of the apparent resistivity curves, **(b)** MT sounding ng30Ar corrected for a static shift using TEM data. **(c)** Joint 1D Occam inversion of TEM and the average of the two modes of the MT data. The green curve to the right shows the resistivity Occam model vs. depth. The calculated responses of the resistivity model are given by the solid green lines in the two panels to the left. The shift multiplier is shown in the upper right-hand corner of the apparent resistivity panel.*

## 2.2 Transient Electromagnetic (TEM) method

The Transient Electromagnetic (TEM) method is a geophysical technique that uses a controlled and time-varying magnetic field to induce currents within the Earth, providing information about the resistivity of the subsurface. A primary magnetic field is created by an artificial steady current source transmitted through a wire loop or dipole placed on the

ground. When the transmitter current is abruptly terminated, eddy currents are induced in the ground, creating a secondary magnetic field. This secondary field diminishes over time, inducing a voltage in a receiver coil. The measurement of the voltage in the receiver coil provides resistivity information as a function of depth (Árnason, 1989).

Initially, after the transmitter current is terminated, the current in the ground is concentrated near the surface, and the measured signal predominantly reflects the resistivity of the uppermost layers. As time elapses, the current permeates deeper into the ground, and the measured signal provides insights into the resistivity of the deeper Earth layers. The depth of exploration is primarily determined by the product of the current and the area of the loop (transmitter moment) and the conductivity structure of the Earth. For more details, the reader is referred to Árnason (1989) and Spies and Frischknecht (1991).

In this study, the TEM method utilized the central loop configuration, employing a square transmitter loop and an inductive receiver coil coupled to the receiver unit. The transmission frequency was regulated by a controller unit that manages the current switching on and off in the loop. The receiver measured the decaying voltage after the termination of the current by the transmitter, ensuring the measurement of small secondary voltages in the absence of the primary field when the current was off.

TEM measurements are susceptible to distortions originating from cultural noise, instrumental noise from electronics, natural electromagnetic noise, and dimensional distortion, particularly related to topography (Stark et al., 2013). Some of these distortions can be mitigated through good site selection, repetitive stacking of measurements for each frequency, and the computation of averages.

Because the TEM method does not measure electric fields, it is not affected by the static shift. Therefore, to support the geothermal resistivity model, co-located TEM and MT soundings often provide an effective technique to correct for MT static shift (Sternberg et al., 1988; Pellerin and Hohmann, 1990; Árnason, 2015).

### 2.2.1 Data acquisition and analysis

The TEM data, used for correcting MT static distortion, were acquired using Zonge GDP32-12 and Zonge GDP32-24-bit multifunctional receiver TEM systems, the GT30 battery transmitter and 100 m or 200 m square transmitter loops during the 2015 and 2020 campaigns. The half-duty square wave current in the transmitter loop varied from 7 A to 21 A at 16 Hz, 4 Hz and 2 Hz. The time derivative of the vertical magnetic field was measured by a magnetic sensor coil at the centre of the loop. At most of the MT sites around the Rungwe volcano and the surrounding area, it was not possible to acquire TEM data because the terrain and logistical challenges of the prospect area made TEM data acquisition too expensive or impractical and, in any case, central loop TEM can be more distorted by rugged topography than MT (Stark et al., 2013).

The TemxZ software (Árnason, 2006a) was used to process the TEM data. The data from Zonge TEM equipment were analysed by omitting outliers, stacking and computing the apparent resistivity as a function of time after turn-off. The final output of the processed TEM data was *.inv files that were used for the 1D joint inversion with MT data using TEMTD software where the static shift factor was one of the parameters inverted for. Figure 2.4d illustrates the 1D joint inversion of MT and TEM data for station ng30Ar.

## 2.3 Data modelling and inversion approach

MT data forward and inverse modelling techniques are usually done after a thorough analysis of the data has been carried out, including dimensionality and directionality analysis and static shift evaluation and corrections. The modelling is done to obtain the conductivity distribution of the subsurface below an observation site in the survey area by converting the apparent resistivity as a function of period into a resistivity model as a function of depth and other spatial parameters in case of non-1D models. The MT forward modelling computes the impedances at a given observation site which are used to predict the MT responses in the model of the Earth's resistivity structure. MT inverse modelling involves the recovery of the resistivity pattern from the observed MT responses at specific locations and frequencies in the survey area. The inversion process involves several runs of forward modelling and comparisons of observed and predicted MT responses from one or more models of resistivity by minimizing the misfit between the observed data and predicted data from the model until a good fit is reached (e.g., Constable et al., 1987; Chave and Jones, 2012). To obtain a good fit between the observed and predicted MT responses the inversion procedure requires to be supplied with a starting model with some adjustments of inversion parameters and boundary conditions which are implemented through a direct application of a non-linear least square approach. Such a conversion procedure requires an algorithm called an inversion algorithm installed in the computer and for larger models, a powerful computer may be required. The inversion problem is non-unique meaning that more than one model can be produced that satisfies the constraints applied. However, synthetic modelling can be used to show the expected resolution and understand the reliability of certain features. For detailed information about solving the MT forward and inversion problems, the reader is referred to Chave and Jones (2012).

In this thesis, a 1D joint inversion of MT and TEM data was performed using the TEMTD software (Árnason, 2006b) for static correction, whenever possible. In performing the 3D inversion, two 3D inversion programs were used, the ModEM software (Egbert and Kelbert, 2012; Kelbert et al., 2014) and the GeoTools-RLM3D software developed by CGG (Mackie and Watts, 2012). The first 3D MT inversion was done using the ModEM software (Egbert and Kelbert, 2012; Kelbert et al., 2014) using the static shift corrected off-diagonal impedance tensor components and Tipper of MT data. The on-diagonal elements were not employed during 3D inversion using ModEM code (running on a local workstation) to limit the possible bias due to their much lower signal-to-noise ratio and save computer time in order to run tests with many different starting models and inversion parameters. The final 3D inversion model was obtained using unrotated full impedance tensor components and Tipper using the GeoTools-RLM3D software developed by CGG (Mackie and Watts, 2012) running on an external powerful multiprocessor parallel cloud. The details of the modelling process and the results obtained are discussed in paper II presented in this thesis.

## 2.4 Resistivity methods applied to geothermal exploration in Tanzania

The MT and TEM methods have been widely applied for geophysical exploration of geothermal systems in Tanzania since 2006. Employing TEM data for mitigating the static shift effects in MT has become a common practice. In particular, MT has been used in

characterizing the 3D resistivity distribution of the subsurface in several geothermal prospects including the high-temperature geothermal prospects in Ngozi and Rungwe regions (Alexander et al., 2016; Didas et al., 2023), as well as in low to medium-temperature prospects such as Kisaki, Luhoi (Armadillo et al., 2020), Kiejo-Mbaka (ELC and TGDC, 2017; Rizzello et al., 2022), Songwe (Alexander et al., 2016), Ibadakuli (TGDC, 2022), and Mount Meru (Josephat, 2023). Currently, an MT survey campaign is underway in the Natron prospect, located within the eastern branch of the EARS in northern Tanzania.

## 2.5 Resistivity pattern of geothermal systems

Geothermal systems are characterized by variable subsurface resistivity patterns, typically influenced by salinity, water content, porosity, fluid temperature, and hydrothermal alteration resulting from geothermal activity (Ussher et al., 2000; Hersir et al., 2021). Dry rocks above or surrounding the geothermal system which are unaffected by the system generally have high resistivity. Brine, with its high concentration of dissolved ions forming conductive electrolytes in the rock matrix of the reservoir, can reduce significantlythe bulk resistivity at temperatures up to 300℃ (Violay et al., 2012). In the context of geothermal fields at depths shallower than 2 or 3 km the presence of smectite clay related to hydrothermal alteration or sedimentary deposition, their cation exchange capacity has been identified as a key factor in determining low resistivity zones detected by methods like MT in geothermal systems (Lévy et al., 2018; Hersir et al., 2021).

For prospects characterized as high-temperature magmatically heated geothermal systems, the lowest resistivity indicates smectite clay cap rock above the resistive geothermal reservoir. A shallow magmatic heat source would in general be conductive below the geothermal reservoir. Therefore, the overall resistivity patterns of high temperature systems are influenced by shallow magmatic heat source, geothermal reservoir and conductive smectite cap rock. Low-medium temperature fault-controlled deep circulation systems can be identified by imaging the conductive smectite clay cap rock. For a fault-controlled deep circulation system, a conductor related to magma shallower than 10 km will in most cases not be detected by resistivity soundings.

The lower temperature part of the clay cap, is usually dominated by smectite which is unstable as the temperature increases above 80℃. It is converted into chlorite (in the case of basaltic rocks) or illite (for andesite and rhyolite rocks). The proportion of chlorite or illite to smectite increases with temperature from 80℃ to 180℃ resulting in the disappearance of the low temperature clay minerals, in particular, smectite or zeolites at about 220℃ (Árnason et al., 2000; Lévy et al., 2018). As the temperature increases the remaining small amount of smectite becomes highly resistive due to dehydration and above 240℃ chlorite/illite becomes dominant. Above the smectite-illite transition zone, the low resistivity is due to the higher cation exchange capacity in smectite than in the alteration minerals below. Because of its ability to reliably image temperature-dependent alteration patterns causing variation in resistivity in geothermal fields, the MT method has become the most important geophysical tool for characterizing the geometry of the geothermal reservoirs (Cumming, 2016a; Cumming and Mackie, 2010; Muñoz, 2014), and in combination with geological and geochemical information is used to develop the geothermal conceptual models used for targeting wells (e.g., Cumming, 2016b). The resistivity pattern of clay minerals has been used by several researchers to establish a relationship between temperature and permeability

of the system (e.g., Árnason et al., 2000; Ussher et al., 2000) assuming that the system is in equilibrium. Low permeability in the low resistivity zone above the reservoir is associated with a high content of smectite clay which usually deforms plastically under stress while illite and chlorite at high temperatures are more brittle and are available in large quantities above 50% are likely to form higher fracture permeability than smectite (Patrier et al., 1996; Lichoro, 2019).

It is important to keep in mind that fossil hydrothermal patterns due to cooling of the system can have similar resistivity as active geothermal systems as found in many cases. On the other hand, in some active geothermal fields, the low-resistivity clay cap and high-resistivity reservoir may have no significant resistivity contrast according to MT models (e.g., Pellerin et al., 1996; Melosh et al., 2012). Therefore, to define the boundaries of the geothermal reservoir in such cases might be difficult and sometimes a risk when developing a conceptual model for such a system. Common examples of non-smectite clay caps include the intermediate resistivity mixed-layer smectite-illite or chlorite clay cap (e.g., Pellerin et al., 1996) or the Tolhuaca geothermal field, Southern Chile (Melosh et al., 2012) where higher illite rich zones beneath the smectite zones act as the boundary of for some parts of the reservoir. Other similar examples include the Namora-I-Langit Geothermal Field which has a high resistivity chlorite-illite cap on its southwest edge (Cumming et al., 2000). Similarly, the low resistivity smectite zone in the EARS adjacent to Silali and other geothermal fields in Kenya that may be incorrectly interpreted as a geothermal clay cap is related to sediments and volcaniclastics deposited below the water table, whereas the geothermal fields are associated with a thinned and updomed low to moderate resistivity zone associated with clay cap (Lichoro, 2019).

## 2.6 Magnetic method

Magnetic measurements record the geomagnetic field and the total magnetization of rocks which is the vector sum of the induced and remanent magnetization. Furthermore, magnetic measurements also record magnetic diurnal variations caused by ionospheric and magnetospheric currents, which are subsequently eliminated from the data prior to interpretation using the magnetic base station data. Among all rock types, igneous, crystalline metamorphic rocks and banded iron formations that contain a significant amount of magnetite and pyrrhotite commonly have high total magnetization compared with sedimentary rocks and poorly consolidated sediments which have much lower magnetization (Reynold et al., 1990). Areas covered by igneous rocks, mafic and ultramafic rocks will produce higher magnitude anomalies compared to areas covered by felsic rocks (Hudson et al., 1999). Low magnetic anomalies can also be produced in regions where mineralized zones associated with strong epithermal, geothermal or hydrothermal silica alteration where magnetite has been altered to form non-magnetic sulphide minerals such as pyrite and chalcopyrite, molybdenite or galena. Low magnetic anomalies can also be produced by rocks that have undergone intense chemical weathering causing the conversion of magnetite into hematite due to the interactions of groundwater. The contrast in magnetic intensities between rocks is an important factor that has led to magnetic surveys being widely used to map the metamorphic basement rocks, igneous intrusions, dikes, lithological contacts, faults, folds and shear zones covered by sedimentary formations or thick weathered rock horizons.

In this thesis, the magnetic method is used for two main purposes: (i) in the first publication to infer and investigate the regional heat flux distribution of the crust throughout Tanzania in order to identify potential areas that may have geothermal resources and (ii) in the third publication to map surface and subsurface structures in the RVP. The primary objectives of the magnetic study in the RVP are to map the extent of known faults that are hidden below sediments and volcanics and to establish their relationships with the locations of seismic epicentres, hot springs, hot ground areas, and interpreted geothermal systems in the Songwe, Ngozi, Rungwe, and Kiejo Mbaka prospects. Our secondary goal is to expand the understanding of fault distribution within the RVP to predict the likely location of permeable zones and impermeable boundaries for potential geothermal resource targeting.

### 2.6.1 Aeromagnetic data processing

To estimate the distribution of regional heat flux in the crust in Tanzania, we utilized the total magnetic intensity (TMI) field aeromagnetic data collected by Geosurveys in 1977 and 1980. The data were collected along E-W flight lines spaced 1 km apart and 10 km tie lines spacing and draped at 120 m nominal ground clearance, covering a large part of Tanzania. In areas where no data were collected, such as over Lake Victoria, Kilimanjaro, and Uluguru mountains, we supplemented the TMI Earth Magnetic Anomaly Grid 2-arc-minute resolution (EMAG2) dataset. Additionally, we extended the coverage using EMAG2 data outside the political boundaries to resolve the extent of heat flux anomalies. EMAG2 is a free global satellite TMI dataset merged into a 2-arc-minute grid, upward continued 4 km above the geoid (Meyer et al., 2017). These data were draped to an elevation of 120 m using the ETOPO1 global relief model data with 1-arc-minute resolution (Amante and Eikin, 2009) and merged with the TMI of the 1977-1980 survey at a resolution of 250 m x 250 m. The resulting total TMI map is shown in Figure 2.7, top panel.

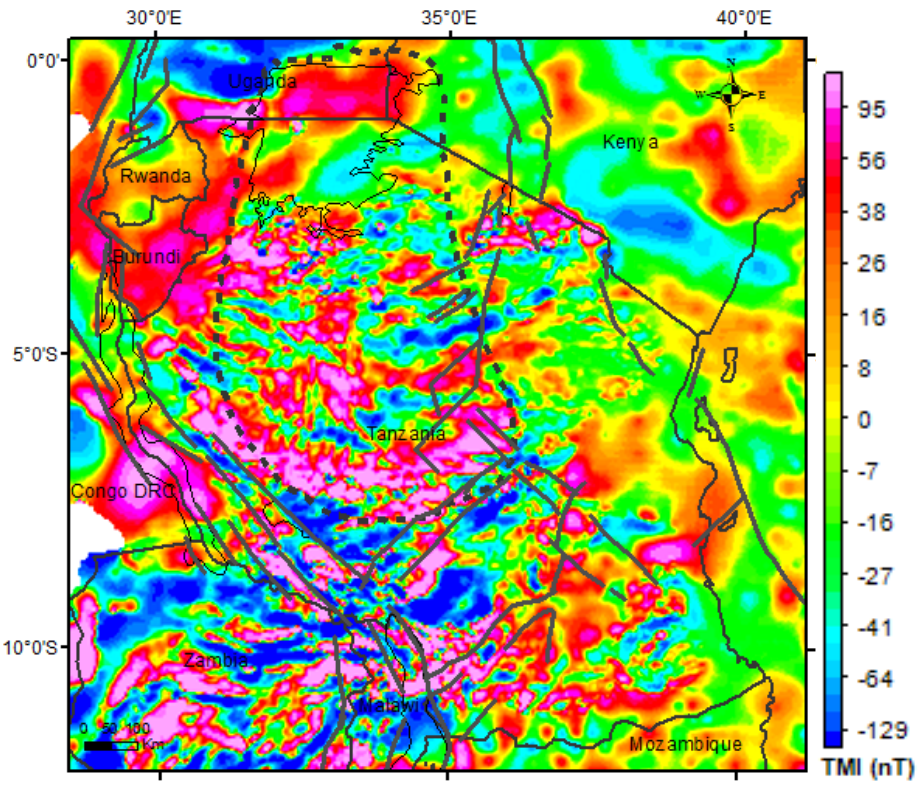

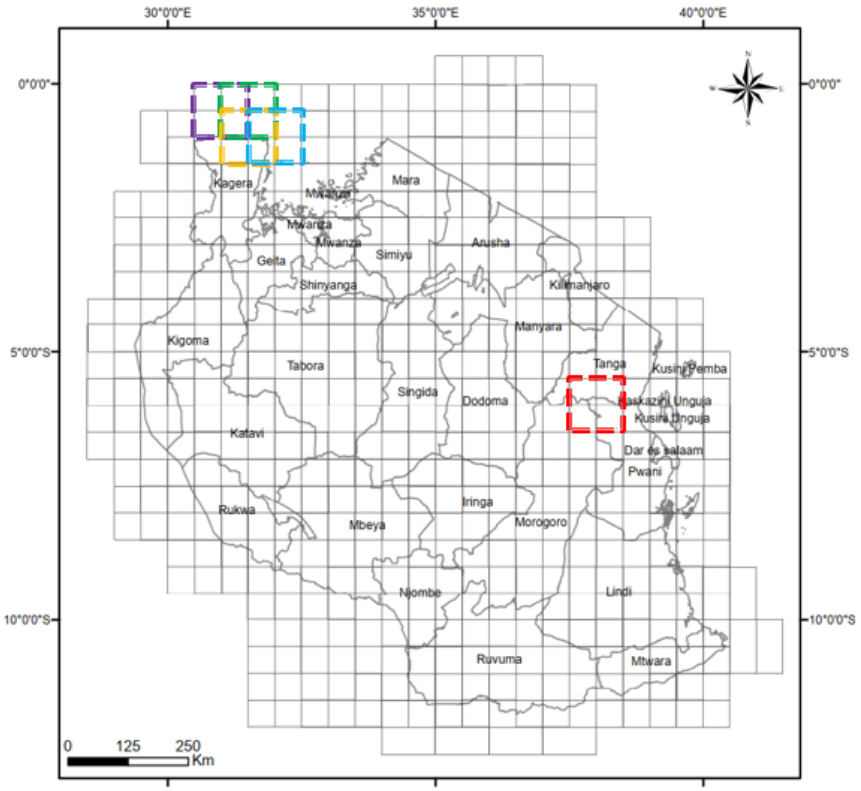


*Figure 2.7 Top panel: total field magnetic map of Tanzania merged from the 1970-1980 aeromagnetic survey and EMAG2 (Meyer et al., 2017) data set superimposed with the EARS main structures. Lower panel: distribution of 447 overlapping 50% square windows (e.g., red dotted window), each with a dimension of 110 x 110 km$^2$ (1°x1°) used in the computations of the power spectra. Purple, green, blue and yellow windows represent the overlaps.*

### 2.6.2 Curie point depth estimation

The depth to the bottom of the magnetic source (DBMS or $Z_b$) is assumed to be the Curie point depth (CPD) at which magnetic minerals in the Earth's crust reach their Curie temperature and at this temperature, rocks lose their permanent magnetism and become demagnetized. For magnetite, this is at 580 °C (Ross et al., 2006). The methods to estimate the depth of magnetic sources from magnetic anomalies can be grouped into two main categories: (1) power spectrum methods and (2) forward modelling and inversion methods. Power spectrum methods include using the power spectrum peak (Bhattacharyya and Leu, 1975; Connard et al., 1983), the centroid method (Okubo et al., 1985; Tanaka et al. 1999), and the modified centroid fractal method (Bansal et al., 2010). Forward modelling and inversion methods (Ross et al., 2006) are used to model individual magnetic anomalies to determine the depth to the magnetic sources. All these methods work in the wave number domain and focus on the long wavelength part of the spectrum related to deep magnetic sources, typically resolved using a large size window.

In this thesis, we used the centroid method to estimate the depth to the top (Zt) and depth to the centroid (Zo) of the magnetic body. We divided the area into overlapping windows and calculated the 2D radially averaged amplitude spectrum (RAAS) of the magnetic anomalies. Using Fast Fourier Transform (FFT), we analyzed the gridded TMI anomalies and extended each window to increase the resolution of our results. The window size was 110 km x 110

km, with a 50% overlap, totaling 447 windows (Figure 2.7, lower panel). It is important to note that using small windows may cause errors in estimating the depth to the magnetic source. Our window size of 110 km x 110 km can satisfactorily resolve the depth to the magnetic source down to a depth of 24.8 km. To validate results greater than 24.8 km, we recomputed using larger window sizes, for example, 220 km x 220 km, 400 m x 400 m and 500 m x 500 m.

The estimated depths to the top and centroid of the magnetic bodies were used to estimate the DBMS or $Z_b$, a proxy to the Curie point depth, using the approaches described by Okubo et al. (1985) and Tanaka et al. (1999). This procedure is discussed in detail in the first publication.

### 2.6.3 Geothermal gradient and heat flow estimations

The estimated DBMS or $Z_b$ in each window is used to determine the geothermal gradient by calculating the ratio of the Curie temperature of magnetite in the crust (~580 °C) to the depth of the base of the magnetic source (DBMS).

$$\text{Geothermal gradient} = \frac{(T_c)}{Z_b} \tag{2.55}$$

The surface heat flow in each window is calculated based on 1D steady-state conductive heat transfer (Equation 11) with boundary conditions $Z_b$ as CPD (Martos et al., 2017).

$$q_s = \lambda \frac{(T_c)}{Z_b} \tag{2.56}$$

where $q_s$ is the surface heat flow, $\lambda$ is the average thermal conductivity coefficient of the rocks (assumed as 2.5 W/m°C), $T_c$ is the Curie temperature of magnetite the most abundant magnetic mineral in the crust.

We use an average thermal conductivity of 2.5 W/m°C due to the dominance of Precambrian gneiss, granulite, and schist in Tanzania (Fritz et al., 2013, Figure 1.1), with conductivity values ranging between 2 and 3 W/m°C (Ray et al., 2015). This assumption of 1D variations of thermal conductivity and the use of a 1D heat flow equation is a simplifiedstandard approach adopted in similar crustal studies. In the case of strong 3D variations in lithospheric thermal conductivity, the estimates made using our simplified assumption will be affected and, therefore, should be used as just a first approximation of the true heat flow.

### 2.6.4 Structural interpretation from magnetic data in the RVP

The processed TMI data collected in RVP were analysed to remove the linear trend caused by flight lines which might introduce significant noise in the magnetic data. To remove the noise caused by survey lines, a microlevelling filter technique was applied to the TMI data. The resulting data were the corrected Total Magnetic Field Intensity (TMI), which was then gridded at a 250 m grid spacing using Geosoft Oasis Montaj software to create the TMI map. Subsequently, the reduction to the magnetic Pole (RTP) filtering technique (Baranov and Naudy, 1964) was applied to the TMI map to shift the anomalies over the source bodies and obtain interpretable magnetic anomaly maps that were consistent with the mapped geology

of the area. In addition to RTP, a 5 km low pass filter was applied to the RTP map to suppress the high-frequency anomalies and improve the quality of magnetic data that was used for the 2D forward modelling of the main magnetic anomalies.

The RTP and its low pass filtered map contain several anomalies originating from different sources, some of which are adjacent to each other, leading to interferences of the anomalies. There may also be overlain sources located at different depths, resulting in a weak anomaly along with a strong anomaly. To enhance the discontinuities in a signal and to delineate the outline of anomalous magnetic field sources such as geological boundaries and structures like faults, shear zones, and dikes, different edge detection filters were applied to the gridded RTP map.

The applied filters include the Analytic signal of the RTP (Roest et al., 1992), Tilt angle derivative (Miller and Singh, 1994), Total horizontal gradient (Cordell and Grauch, 1985), Vertical derivative (Cordell and Grauch, 1985), and the edge detection method that is based on the enhancement of the Total horizontal derivative of magnetic anomalies (Ferreira et al., 2013). The results of the filtered magnetic data were gridded to produce the maps.

We have used previously reported faults to consolidate the interpretation of the magnetic lineaments related to faults and define their lateral extent. In addition, we used the locations of seismic epicentres in the RVP compiled from several publications (e.g., Ebinger et al., 2019) and the International Seismological Centre catalogue (2023) within the time range from 1900 to 2019 to identify the magnetic lineaments related to active faults in the RVP. This approach has significantly improved the structural understanding of the area and has defined potential zones for geothermal resources when interpreted together with the available geothermal conceptual models of the Songwe, Ngozi, Rungwe and Kiejo-Mbaka prospects.

To understand the subsurface bodies which are likely causing the main magnetic anomalies in the RVP, the anomalies have been modelled using 2D forward modelling constrained by petrophysical and geochronology information derived from several publications (e.g., Marobhe, 1989; Fontijn et al., 2010; Sun et al., 2021) and the 3D MT resistivity model of the Ngozi and Rungwe prospects (Didas et al., 2023)

## 2.7 Gravity method

The gravity method involves measurements of variations in the Earth's gravitational field, which are caused by lateral variations of rock density. Practically, in gravity surveys, the different magnitude of gravity depends on latitude, elevation, topography of the surrounding terrain, earth tides, and density variations in the Earth's subsurface. Gravity contributions due to other factors than density are removed through data processing. Density variations in the Earth occur at different depths, the long wavelength regional anomalies are associated with deep sources and short wavelength residual anomalies are due to more local density variations in near-surface sources. In order to emphasize the interpretation of residual anomalies, the regional gravity anomaly is removed. The separation of the two gravity components can be done using different ways including (i) trend surface analysis which includes fitting and subtracting a low-order polynomial surface from the observed data and (ii) low pass filtering. In this study, low-pass filtering was employed. A detailed review of

the gravity method can be found in Telford et al. (1990), Blakely (1995) and Hinze et al. (2013).

### 2.7.1 Data analysis and modelling

We have used a new high-resolution (5' x 5' arc minute) Satellite-derived Free-air anomaly Earth's gravity field model compilation named SGG-UGM-2 (Figure 2.8a, Liang et al., 2020). In order to avoid the gravity effect related to the topography we preferred to use the gravimetric complete Bouguer anomalies reduced from Free-air anomaly. Our first task was to determine the density of the excess mass at a topography above sea level and use this density to calculate the Bouguer anomaly from the Free-air. In the GMSYS-3D extension of Geosoft Oasis Montaj, we employed the ETOPO1 elevation map (Figure 2.7b, Amante and Eakins, 2009), to calculate the effect of the topography assuming various densities of the underlying formations as 2.4, 2.5, 2.6, 2.7, 2.8, 2.9 and 3.0 g/cm$^3$. The Bouguer anomaly was obtained by subtracting each gravity effect response of the topography from the Free-air anomaly.

#### Density estimation

We used two different methods, Parasnis (Parasnis, 1951) and Nettleton (Nettleton, 1939), to estimate the correct Bouguer density.

In the Parasnis method, we determined the Bouguer density by performing a least square method using the slope of the best-fit line of the plot of the Free-Air anomalies (y-axis) against the topographic correction (x-axis). Our result showed a very low Bouguer density of ~0.7 g/cm$^3$, which may not have a physical meaning.

For the Nettleton approach, we established eight E-W profiles (Figure 2.8b), crossing topographic features, the western and eastern rift valleys, and plotted the Bouguer anomalies along each profile and compared them with the topography. The results for profiles 3 and 4 are shown in Figure 2.9, and for profile 1, 2 and 5 to 8, the results are shown in Appendix D. Our results indicated that a density between 2.8 and 3.0 g/cm$^3$ provided Bouguer anomaly with the least correlation with the topographic section. Based on these results, we chose to use a density of 2.8 g/cm$^3$ for our reductions, likely to be correlated with the density of the Paleoproterozoic crystalline metamorphic rocks, whereas the volcanics are likely to have lower density and the recent sediments having much lower density. However, we noticed a strong positive correlation along the western rift, possibly caused by the Lake waters and/or low-density sediment rift fill. In addition, a high Bouguer anomaly appeared within the boundaries of Lake Victoria. To address this, we conducted a simple modelling to reduce the effect, using sediment thicknesses from the CRUST1.0 Global model of Earth's Crust (Figure 2.6c, Laske et al., 2013). The densities of water, sediments, and basement were assumed to be 1.0 g/cm$^3$, 2.4 g/cm$^3$, and 3.0 g/cm$^3$, respectively (Armadillo et al., 2020; Rizzello et al., 2018). To validate the sediment thicknesses of the CRUST1.0 model, we compared it with wells drilled through the basement along the coastal region of Tanzania (Didas, 2016) and found good agreement. We observed that the CRUST1.0 model extrapolates thick sediments to the shoulders of the rift; therefore, we maintained the sediments along the rift zone while setting a zero-sediment thickness outside the rift zone.

To compensate for the overcorrected Bouguer anomaly (i.e., Bouguer anomaly computed with a density of 2.8 g/cm$^3$), we computed the contribution of the water and sediments using

density contrasts of 1.8 g/cm$^3$ and 1.4 g/cm$^3$, respectively, in reference to the density of the basement, with a density contrast set to zero below. Finally, we obtained the final Bouguer anomaly by compensating the overcorrection of the water and sediments to the original Bouguer anomaly.

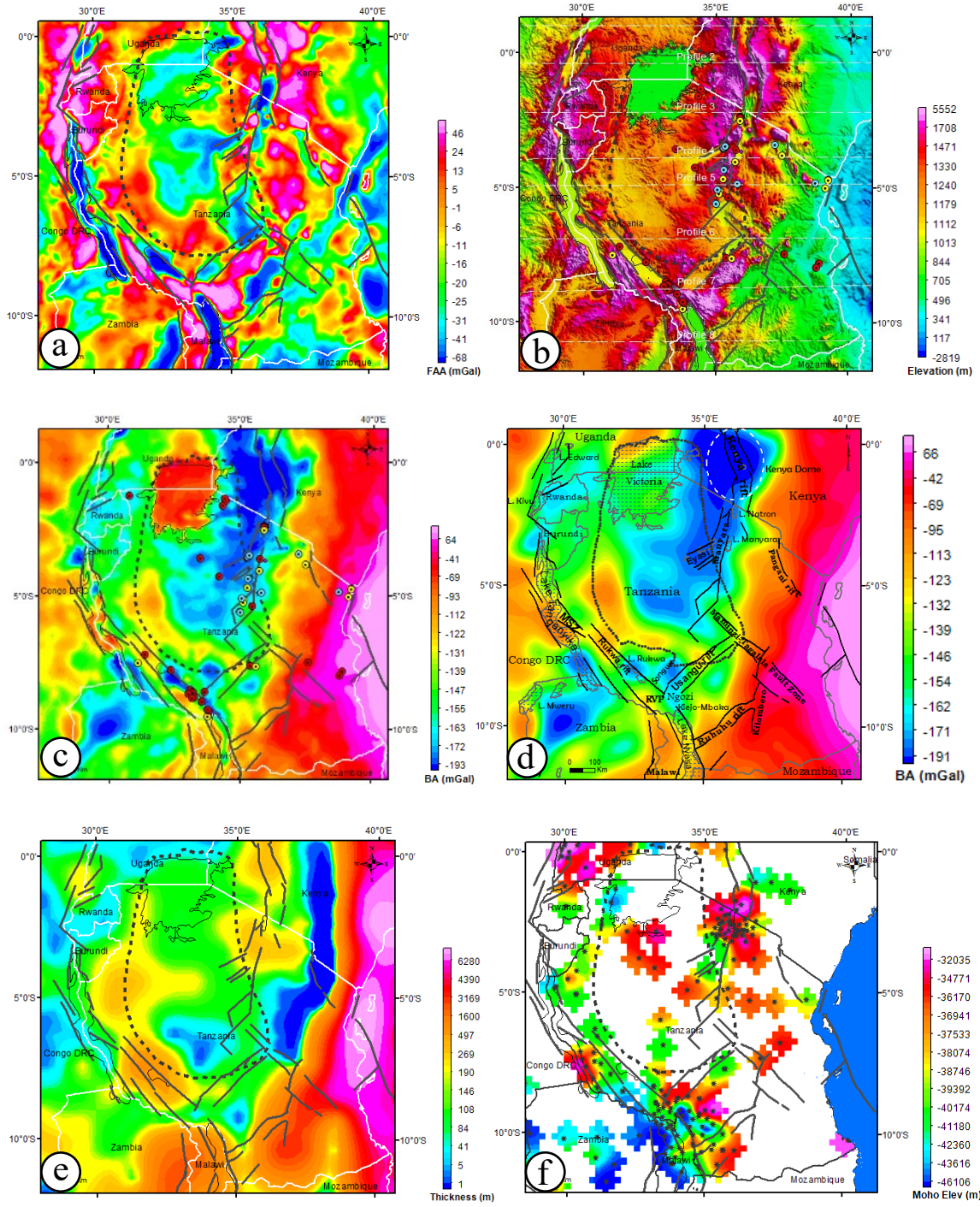


*Figure 2.8 Gravity data reductions: (a) Satellite-derived Free-air anomaly from Earth's gravity field model compilation named SGG-UGM-2 (Liang et al., 2020). (b) Elevation map from ETOPO1 (Amante and Eakins, 2009). (c) Bouguer gravity anomaly computed using a reduction density of 2.8 g/cm$^3$ before compensation for overcorrected Bouguer density. (d) 150 km low pass filtered Bouguer gravity anomaly map of the study area. (e) Sediment*

*thickness compiled CRUST1.0 (Laske et al., 2013). (f) Thicknesses of the crust from seismic receiver functions. The black dotted polygon and the black lines are the Archean Tanzania craton and major faults, respectively.*

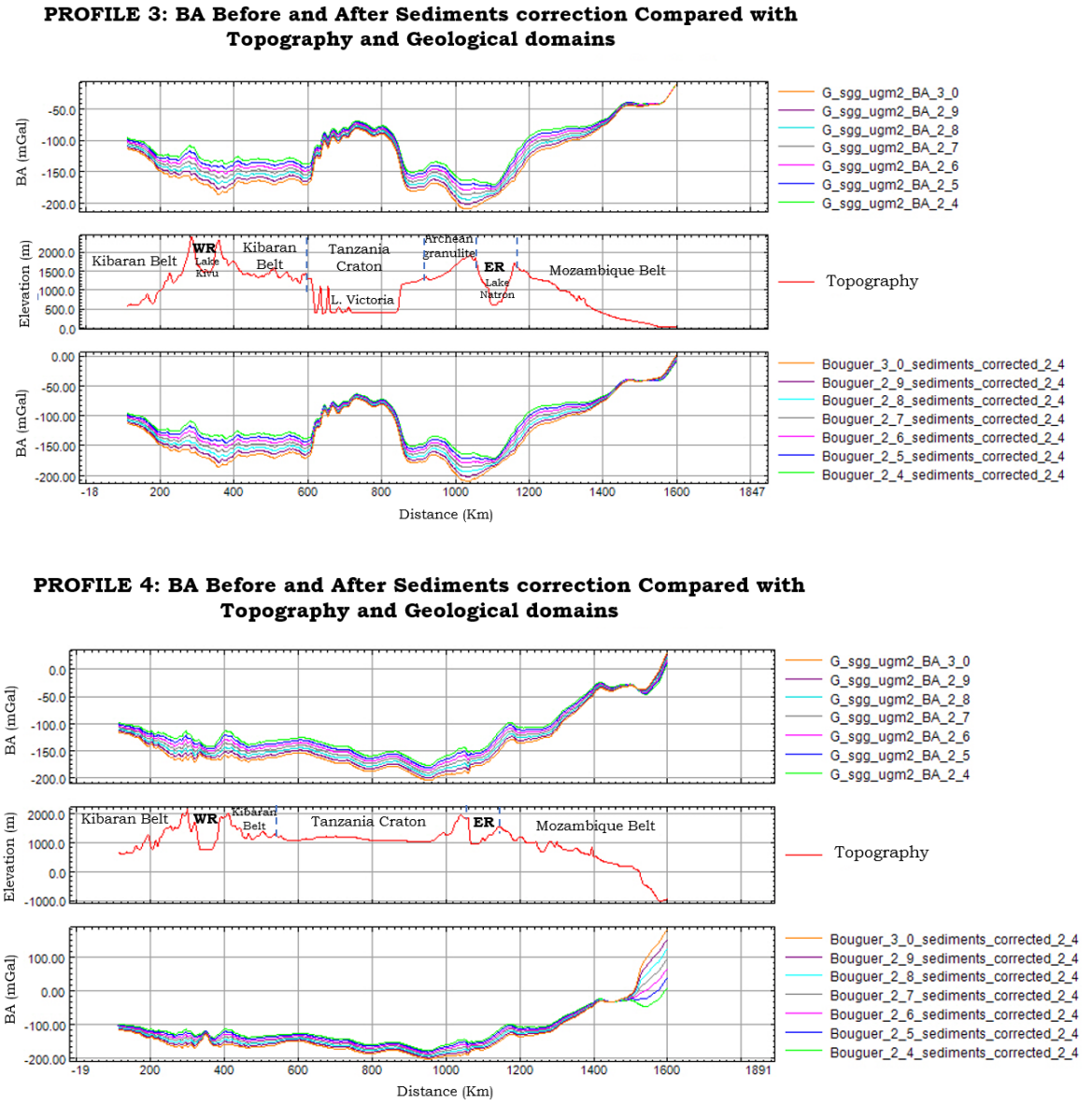


*Figure 2.9 Bouguer gravity anomalies using density varying from 2.4 g/cm$^3$ to 3.0 g/cm$^3$ along profile 3 and 4, compared with the topography and geological domains.* ***ER****: Eastern rift,* ***WR:*** *Western rift. For ages of the geological domains see Figure 1.2. In each profile, the top and bottom panel indicate the Bouguer gravity anomalies before and after correcting the effect of the water and sediments, respectively.*

## Estimation of Moho depth from Gravity data

To determine the Moho depth distribution in Tanzania, we conducted a constrained 3D inversion of the 150 km low-pass filtered Bouguer gravity anomaly map (refer to Figure 2.8d). We applied the low-pass filter to eliminate high-frequency anomalies related to shallow crust features, leaving only low-frequency anomalies possibly associated with the Moho surface.

We chose not to model the local anomalies along the rift axis, as this would require separating anomalies related to basement topography from those linked to magmatic intrusions within the basement, which is beyond the scope of this thesis. While the depth to Moho is typically defined by seismic methods, the limited areal extent of seismic surveys in the study area presents a challenge for Moho modelling. Therefore, gravity modelling serves as an alternative, with the Moho interface representing the density boundary where density transitions from 2.67 g/cm$^3$ to 3.30 g/cm$^3$.

Since the depth to Moho represents the crust-mantle intercept, we assigned a constant density contrast of 0.5 g/cm$^3$, corresponding to an average crustal and mantle density of 2.8 g/cm$^3$ and 3.3 g/cm$^3$, respectively. Given that gravity data inversion is susceptible to various factors such as data noise, geological heterogeneity, and non-uniqueness of solutions, effective regularization and the incorporation of a priori information are essential to minimize ambiguity. This is supported by previous studies (Kanda et al., 2019; Represas et al., 2012; Armadillo et al., 2020).

To constrain the depths to the crust where the Moho interface is found, we utilized a priori information on crustal thickness, compiled from seismic receiver functions by various authors (e.g., Tugume et al., 2012; Plasman et al., 2017; Borrego et al., 2018). We performed a 3D inversion of the gridded Bouguer gravity anomaly map as the reference model to ascertain the density distribution of subsurface structures, until achieving a fixed density contrast of 0.5 g/cm$^3$. During the inversion, the depth to Moho was constrained by the thickness of the crust based on seismic receiver functions.

The topography at the crust-mantle interface was derived by forward modelling Bouguer anomalies on the interface using techniques outlined by Parker (1972) and Blakely (1995) within the GMSYS-3D extension of Geosoft Oasis Montaj. Finally, we compared the results from the 3D inversion of gravity data with the crustal model from seismic receiver function analysis and the Global Moho depth (Laske et al., 2013).

# 3 Summary of results

## 3.1 Paper 1

The geothermal potential areas in Tanzania are generally located within the East African Rift System (EARS) manifested by the presence of surface geothermal manifestations. However, some areas in Tanzania remain unexplored due to limited accessibility. Semi-blind geothermal systems that cannot be identified based on the presence of surface geothermal manifestations may exist. To address these challenges, we employed the radially average power spectra of the total magnetic field using the centroid and de-fractal methods to estimate the regional crustal heat flux distribution in Tanzania. To evaluate the results against crustal thickness, 3D inversion of gravity data, constrained by existing Moho depth from seismic receiver functions, was utilized. By integrating the results with known geothermal prospects and surface geothermal manifestations, we were able to create a regional heat flux map of Tanzania highlighting the prospective geothermal areas. The overall findings of the study indicate the following:

- High heat flow values (over 100 $mW/m^2$) are located along the EARS and at the Proterozoic collision boundaries reactivated by the EARS. Newly identified areas with high heat flow values following the findings of this study include the western part of Tanzania between Lake Tanganyika and Lake Rukwa, where some pools of hot springs were found.

- In general, high heat flow anomalies align with known surface geothermal manifestations and shallow Moho depth in the range of approximately 30 to 35 km.

- A high heat flow anomaly is also observed in the central part of the Tanzanian craton, likely associated with the mantle plume imaged by seismic tomography.

- According to the results, the most promising areas for geothermal exploration in Tanzania include the EARS triple junction in the Rungwe volcanic province, the north Tanzania divergent zone, and the areas of the Proterozoic collision boundaries reactivated by the EARS.

## 3.2 Paper 2

Paper 2 investigates the subsurface resistivity pattern of the prospective high-temperature magmatically heated geothermal systems in Ngozi and Rungwe prospects. The study uses 190 MT soundings to develop a 3D MT resistivity model integrated with known faults, geothermometry of the hot springs, and hot ground areas. This aims to support the development of resource conceptual models of the systems. Previous surface studies in the Ngozi prospect revealed a small geothermal reservoir below the Ngozi caldera, supported by the geothermometry of the neutral chloride hot springs at the bottom of the Ngozi caldera Lake. However, MT soundings supporting this interpretation were missing inside the caldera until this study, when several MT soundings were measured inside it. On the other hand, the Rungwe volcano was previously considered less likely to host high-temperature geothermal systems due to lack of surface geothermal manifestations. However, this study discovered hot ground areas with temperatures exceeding 53°C on the northwest and southwest flanks of the Rungwe volcano. The 3D MT resistivity model provides further insights into these findings as follows:

- Ngozi and Rungwe prospects comprise two separate systems, a small reservoir located below the Ngozi caldera and a large reservoir located below Rungwe volcano.

- The systems are located within the NW-SE trending fault zone covered by an extensive conductive clay cap with variable thicknesses, demarcated to the west and east by the impermeable Precambrian Metamorphic basement, extending 30 km from the Kiejo area SE of the Rungwe volcano to the Ngozi caldera.

- A small geothermal reservoir is proposed below the Ngozi caldera by the present study.

- The second reservoir is interpreted to be large and located below the Rungwe volcano, supported by an updomed base of the conductive clay cap below the volcano, typical of a boiling geothermal reservoir. Additional evidence for the existence of a geothermal reservoir at Rungwe includes hot ground areas with temperatures >53°C mapped to the northwest and southeast of the volcano.

- The absence of geothermal surface manifestations directly over the inferred Rungwe upflow zone is consistent with the effective sealing of the proposed underlying geothermal reservoir by the clay cap. The scarcity of thermal manifestations on the up-dip margins of the low-resistivity clay cap can be explained by the coincidence of the base of the clay cap with impermeable Precambrian formations and by structural boundaries.

- An inferred magma chamber heating the Ngozi and Rungwe geothermal systems is imaged at a depth of ~6 km as a deep conductor located between the Ngozi and Rungwe volcanoes.

- Combining the interpreted results, this implies that the Rungwe volcano has the highest geothermal resource potential where proposed drilling sites might intersect the interpreted high-temperature reservoir.

## 3.3 Paper 3

Paper 3 focuses on the Rungwe Volcanic Province (RVP) in SW Tanzania, where aeromagnetic data are used to investigate surface and subsurface structures. The structures include faults and intrusions, which are mostly concealed by thick volcanic and sedimentary layers, sitting on top of Precambrian metamorphic rock. The magnetic lineaments are interpreted along with known faults and seismic epicentres in order to distinguish between magnetic features that are not related to the known faults and concealed active faults. For the purpose of identifying zones of probable high permeability that can be targeted for geothermal drilling, the identified faults are combined with known surface geothermal manifestations and existing geothermal models in the Songwe, Ngozi, Rungwe and Kiejo geothermal prospects. The main outcome is an updated structural map based on an interpretation of aeromagnetic data, constrained by 2D-forward modelling of magnetic anomalies, together with the distribution of previously reported faults, seismic epicentres, 3D magnetotelluric resistivity models, and surface geothermal manifestations. This updated structural map may be used to support geothermal resource targeting in the RVP. The findings indicate the following:

- Magnetic anomalies in the RVP, including the prominent Mbeya anomaly, are related to the high magnetic susceptibility or remanent magnetism of Precambrian rocks and Cretaceous carbonatite intrusions buried in the rift under a varying thickness of non-magnetic sediments and volcanic rocks.

- Magnetic lineaments are related to structures controlling the geometry of the Precambrian rocks and concealed dikes and the thickness of the sediments and volcanics.

- The recent Ngozi and Rungwe trachyte volcanics have relatively low magnetic susceptibility comparable to the low susceptibility of the sediments in the rift basins.

- The revised neotectonic structural map shows prominent NW, NE and NS-trending magnetic lineaments that correlate with previously reported faults and alignments of seismic epicentres in the study area and with the regional trend of the rift segments. The NE-trending magnetic lineaments are consistent with interpretations of the current stress field in the RVP.

- The main volcanoes in the RVP, Ngozi, Rungwe and Kiejo, are aligned with the NW-trending linear magnetic feature joining the Lupa and Livingstone rift border faults. This lineament is intersected and frequently displaced by the NE and NS-trending lineaments, suggesting that the NE to NS-striking structures are younger.

- The Rungwe and Ngozi volcanoes, numerous monogenetic eruption centres and the Mwakaleli caldera which originated ca. 2 Ma ago following an ignimbrite eruption are located within a zone of low-intermediate magnitude magnetic features forming a basin-like structure surrounded by magnetic high anomalies of the Precambrian basement structures.

- We interpret the intersections between the NW-trending intrarift faults and the NS and NE-trending faults as favourable locations for wells to target higher permeability

within the geothermal resource conceptual models previously constructed using 3D MT resistivity imaging integrated with supporting geoscience data.

# 4 General Summary and Conclusions

The results of this PhD project provide a clearer picture of the geothermal potential areas in Tanzania and in particular the Ngozi and Rungwe geothermal prospects than previously known. The results are based on geophysical methods that are integrated with results from geochemical and geological surveys that provide constraints on the developed geothermal resource conceptual model. The following summary and conclusions can be drawn from this study.

1. Zones with high heat flux in Tanzania are found along the East African Rift System and Proterozoic collision zones that have been affected by the EARS.

2. The RVP is characterized by zones of varying magnetic values indicating rocks with different magnetic susceptibilities. The trachytic Ngozi, Rungwe and Mwakaleli volcanoes are characterized by relatively low magnetic values compared to the low magnetic values of the non-magnetic sedimentary formations within the rift segments.

3. The Ngozi, Rungwe and Mwakaleli volcanoes and several monogenetic volcanic eruption centres are enclosed by a zone of low-intermediate magnitude magnetic features forming a basin-like structure surrounded by magnetic high anomalies of the Precambrian basement structures. This zone suggests an area with the following properties: (i) a hydrothermally affected area that has destroyed the magnetism of the rocks, (ii) oxidized rocks due to meteoric water that has converted magnetite into hematite and limonite non-magnetic minerals or (iii) area covered by non-magnetic sedimentary rocks covered by trachytic rocks with low magnetic susceptibility values.

4. There are two types of prospective geothermal systems in the RVP, (1) magmatically heated high temperature systems in the Ngozi and Rungwe prospects and (2) low-medium temperature deep circulation fault-controlled geothermal systems in the Songwe and Kiejo-Mbaka prospects.

5. A large geothermal reservoir is proposed below the Rungwe volcano, supported by an updoming conductive clay cap and hot ground areas on its northwest and southeast flanks. The second, smaller reservoir is proposed below Ngozi caldera and is estimated to be >230℃.

6. The Ngozi and Rungwe geothermal reservoirs are interpreted as magmatically heated geothermal systems with a shallow magma chamber located between the Ngozi and Rungwe volcanoes. The 3D MT resistivity model images this magma chamber as a conductive body at a depth of ~6 km.

7. The Ngozi and Rungwe geothermal reservoirs are likely hosted in four rock formations and possibly combinations of: (i) the old basalt, (ii) the neck of the

volcanic intrusion (iii) faulted red sandstone overlying the Precambrian basement or (iv) the Faulted Precambrian basement rocks.

8. The Rungwe and Ngozi geothermal reservoirs are limited by faults and impermeable basements to the east and west, respectively. The combination of faults, the impermeable basement and the thick clay cap act as important barriers to the geothermal systems as manifested on the surface except below the Ngozi caldera Lake where the clay cap is very small or lacking leading to the discharge of the neutral chloride hot springs.

9. The RVP is characterised by four structural trends, the NW-SE, NE-SW, ENE-WSW, and N-S trending fault systems illustrated in a revised neotectonic structural map generated in this study by combining the magnetic lineaments supported by previously reported faults and alignments of seismic epicentres. The structural trends are consistent with the trends of the rift segments and the current stress field of the rift. The NW-SE lineaments are aligned with the Rukwa rift, the NE-SE are consistent with the Usangu rift and the N-S lineaments are aligned with the Malawi rift. The ENE-WSW fault system is consistent with the current active rift stress fields with strike-slip components.

10. Ngozi, Rungwe and Kiejo volcanoes, the main volcanoes in the RVP, are aligned with the NW-trending linear magnetic feature joining the Lupa and Livingstone rift border faults. This magnetic feature is frequently displaced by the NE and NS-trending lineaments, suggesting that the NE to NS-striking structures are younger.

11. This study suggests that the intersections between the NW-trending intrarift faults and the NS and NE-trending faults are considered favorable locations for wells to target high permeability within the geothermal conceptual models previously constructed using 3D MT resistivity imaging integrated with other geoscientific data. The suggested fault intersections based on magnetic mapping are important locations which should be confirmed through ground mapping with Lidar support of subtle features that may be associated with very recent fault movement.

# 5 Further research

To advance the result of this research project, several follow-up works are suggested:

1. A geophysical investigation of the RVP, particularly the Kiejo, Mwakaleli, and Tukuyu volcanoes, to explore geothermal resources beneath these unexplored areas, leveraging the newly imaged prospective geothermal system below Rungwe volcano.

2. Acquisition of additional MT data east of the Rungwe volcano to define the extent of the prospective geothermal system imaged below the Rungwe volcano.

3. Advancing the study by conducting a gravity survey supported with the location of known faults, seismic epicentres, and findings from this project to map the subsurface structure in the RVP.

4. For detailed imaging of geothermal systems and subsurface structures in the Ngozi and Rungwe prospects, a 3D joint inversion of MT and gravity data is recommended, enhancing the precision of targeting geothermal wells.

5. Micro-seismic monitoring to map active fault zones and model the magma chamber imaged by MT data, which is interpreted as the potential heat source for the geothermal systems in the Ngozi and Rungwe prospects.

6. Carry out detailed structural mapping assisted by remote sensing techniques such as Lidar to map active faults in the RVP.

7. Seasonal monitoring of the hot ground areas at the flanks of the Rungwe volcano to track variations in these areas over time.

8. A better definition of the geothermal resource in the Ngozi and Rungwe prospects includes:
   i) Modifying the UNEP (2016) proposed locations of the slim wells to target the up-doming resistivity pattern;
   ii) Assessing well targets and the resource area using conceptual model isotherms, including cold water influx through vents and gaps in the low resistivity cap in the P90 conceptual model;
   iii) Adding high-value datasets such as MT data set, ground mapping of active faults; and
   iv) Assessing the likelihood of outcomes based on comparative analysis of Ngozi and Rungwe with analogous drilled geothermal prospects in the EARS and worldwide.

# References


Accardo, N., Gaherty, J., Shillington, D., Ebinger, C., Nyblade, A., Mbogoni, G., Kamihanda, G., 2017. Surface wave imaging of the weakly extended Malawi Rift from ambient-noise and teleseismic Rayleigh waves from onshore and lake-bottom seismometers. Geophysical Journal International, 209(3), 1892–1905.

Armadillo, E., Rizzello, D., Pasqua, C., Pisani, P., Ghirotto, A., Didas, M., et al., 2020. Geophysical constraints on the Luhoi (Tanzania) geothermal conceptual model. Geothermics 87, 101875. https://doi.org/10.1016/j.geothermics.2020.101875.

Árnason, K., 2015. The static shift problem in MT soundings. In: Proceedings of the World Geothermal Congress 2015, Melbourne, Australia.

Árnason, K., Eysteinsson, H., Hersir, G.P., 2010. Joint 1-D inversion of TEM and MT data and 3-D inversion of MT data in the Hengill area, SW Iceland. Geothermics, 39, 13-34.

Árnason, K., Karlsdóttir, R., Eysteinsson, H., Flóvenz, Ó.G., Gudlaugsson, S.T., 2000. The Resistivity Structure of High-Temperature Geothermal Systems in Iceland. Proc. World Geotherm. Congr. 2000, 923–928, Kyushu - Tohoku, Japan.

Árnason, K., 2006a. TemX, short manual. Short manual. ÍSOR, Iceland Geosurvey. Unpublished, 11 pp.

Árnason, K., 2006b. TEMTD, A Programme for 1D inversion of central-loop TEM and MT data. Short manual. ÍSOR, Iceland Geosurvey. Unpublished, 17 pp.

Árnason, K., 1989. Central loop transient electromagnetic sounding over a horizontally layered earth (No. OS-89032/JHD-06). Reykjavik: Orkustofnun.

Alexander, K., Cumming, W.B., Malini, L., 2016. Technical review of the geothermal potential of Ngozi and Songwe geothermal prospects. In: Proceedings of the 6th African Rift Geothermal Conference. Addis Ababa, Ethiopia.

Amante, C., Eakins, B.W., 2009. ETOPO1 1 arc-minute global relief model: procedures, data sources and analysis. NOAA Technical Memorandum NESDIS NGDC-24. National Geophysical Data Center, Marine Geology and Geophysics Division, Boulder, Colorado. https://repository.library.noaa.gov/view/noaa/1163

Avdeeva, A., Moorkamp, M., Avdeev, D., Jegen, M., Miensopust, M., 2015. Threedimensional inversion of magnetotelluric impedance tensor data and full distortion matrix, Geophysical Journal International, 202(1), 464–481.

Bansal, A.R., Gabriel, G., Dimri, V.P., 2010. Power law distribution of susceptibility and density and its relation to seismic properties: an example from the German continental deep drilling program. J. Appl. Geophys. 72, 123–128. https://doi.org/10.1016/j.jappgeo.2010.08.001.

Baranov, V., Naudy, H., 1964. Numerical calculation of the formula of reduction to the magnetic pole. Geophysics, 29, 67-79. https://doi.org/10.1190/1.1439334.

Benti, E.N., Woldegiyorgis, A.T., Geffe A.C., Gurmesa, S.G., Chaka D.M., Mekonnen, S.Y., 2023. Overview of geothermal resources utilization in Ethiopia: Potentials, opportunities, and challenges. Scientific African 19 (2023) e01562. https://doi.org/10.1016/j.sciaf.2023.e01562.

Bhattacharya, B.K., Leu, L.K., 1975. Analysis of magnetic anomalies over Yellowstone national park: mapping of curie point isothermal surface for geothermal reconnaissance. J. Geophys. Res. 80, 4461–4465. https://doi.org/10.1029/JB080i032p04461.

Blakely, R.J., 1995. Potential Theory in Gravity & Magnetic Applications. Cambridge Univ. Press.

Borrego, D., Nyblade, A.A., Accardo, N.J., Gaherty, J.B., Ebinger, C.J., Shillington, D.J., et al., 2018. Crustal structure surrounding the northern Malawi rift and beneath the Rungwe Volcanic Province, East Africa. Geophys. J. Int. 215, 1410–1426. https://doi.org/10.1093/gji/ggy331.

Caldwell, T.G., Bibby, H.M., Brown, C., 2004, The magnetotelluric phase tensor, Geophysical Journal International, v. 158, p. 457–469.

Chave, A., Jones, A., 2012. The Magnetotelluric Method: Theory and Practice. Cambridge University Press. https://doi.org/10.1017/CBO9781139020138. A. Chave and A. Jones (eds.).

Chorowicz, J., 2005. The East African rift system. J. Afr. Earth Sci., 43(1-3) 379-410.

Cumming, W., Colvin, A., Haizlip, J., 2024. USEA-USAID Team Report: Ngozi Geothermal Prospect Technical Review Meeting. TGDC internal report (Unpublished report), 89 pp.

Cumming, W., 2016a. Geophysics and resource conceptual models in geothermal exploration and development. Geotherm. Power Gener. 33–75. https://doi.org/10.1016/B978-0-08-100337-4.00003-6 (Chapter 3).

Cumming, W., 2016b. Resource conceptual models of volcano-hosted geothermal reservoirs for exploration well targeting and resource capacity assessment: construction, pitfalls and challenges. GRC Trans. 40, 2016.

Cumming, W., Mackie, R., 2010. Resistivity imaging of geothermal resources using 1D, 2D and 3D MT inversion and TDEM static shift correction illustrated by a glass mountain case history. In: Proceedings of the World Geothermal Congress, Bali, Indonesia.

Cumming, W., 2009, Geothermal resource conceptual models using surface exploration data. Proceedings, 34th Workshop on Geothermal Reservoir Engineering, Stanford University, Stanford, CA.

Cumming, W., Nordquist, G.A., Astra, D., 2000. Geophysical Exploration for Geothermal Resources – An Application of Combined MT-TDEM, vol.19. Society of Exploration Geophysics, 1071 – 1074 (extended abstracts).

Constable, S.C., Parker, R.L., Constable, C.G., 1987. Occam's inversion: A practical algorithm for generating smooth models from EM sounding data, Geophysics, 52, p. 289-300

Cordell, L., Grauch, V.J.S., 1985. Mapping basement magnetization zones from aeromagnetic data in the San Juan Basin, New Mexico. The Utility of Regional Gravity and Magnetic Anomaly Maps, pp. 181–197.Didas, M. M., Armadillo, E., Hersir, G. P., Cumming, W., Rizzello, D., Benediktsdóttir, Á., Geirsson, H., 2023. New MT surveys and 3D resistivity imaging beneath the Ngozi-Rungwe volcanoes at the triple rift junction of the East African Rift System in SW Tanzania: Support for integrated interpretations of geothermal conceptual models. Geothermics, 118, 102893 https://doi.org/10.1016/j.geothermics.2023.102893.

Didas, M. M., Armadillo, E., Hersir, G. P., Cumming, W., Rizzello, D., 2022. Regional thermal anomalies derived from magnetic spectral analysis and 3D gravity inversion: Implications for potential geothermal sites in Tanzania. Geothermics, 103, 10243. https://doi.org/10.1016/j.geothermics.2022.102431.

Didas, M.M., Hersir, G.P., 2021. 1D joint inversion of MT and TEM data from Ngozi geothermal prospect, southwest Tanzania. An integrated interpretation of geoscientific results. Proceedings of the World Geothermal Congress 2020+1, Reykjavik, Iceland.

Didas, M.M., 2018. 1D Joint Inversion of MT and TEM Data from Ngozi Geothermal Prospect, SW-Tanzania – An Integrated Interpretation of Geoscientific Results. Orkustofnun, Grensásvegur 9, IS-108 Reykjavík, Iceland. UNU-GTP Reports 2018. Report 13, 46.

Didas, M.M, 2016. Geophysical Investigation of the Subsurface Structures of the Mandawa Basin, Southeast Coastal Tanzania. University of Dar es Salaam, p. 170. MSc. Thesis, unpublished.

Ebinger, C.J., Oliva, S.J., Pham, T.Q., Peterson, K., Chindandali, P., Illsley-Kemp, F., et al., 2019. Kinematics of active deformation in the Malawi rift and Rungwe Volcanic Province, Africa. Geochem., Geophy., Geosys., 20, 3928–3951. https://doi.org/10.1029/2019GC008354.

Ebinger, C., 2012. Evolution of the Cenozoic East African rift system: Cratons, plumes, and 20 continental breakup. Regional Geology and Tectonic. Phanerozoic Rift Systems and 21 Sedimentary Basins, eds D. G. Roberts and A. W. Bally (Amsterdam: Elsevier), 22, 133-156

Ebinger, C., 2005. Continental break-up: The East African perspective. Astronomy & Geophysics, 46 (2), 2.16–2.21. https://doi.org/10.1111/j.1468-4004.2005.46216.x.

Ebinger, C.J., Deino, A.L., Drake, R.E., Tesha, A.L., 1989. Chronology of volcanism and rift basin propagation – Rungwe Volcanic Province, East Africa. J. Geophys., Research 94, 15785–15803. https://doi.org/10.1029/JB094iB11p15785.

Egbert, G.D., Kelbert, A., 2012. Computational recipes for electromagnetic inverse problems. Geophys., J. Int., 189(1), 251–267. https://doi.org/10.1111/j.1365-246X.2011.05347.x.

ELC and TGDC, 2017. Surface Exploration and Training in Kiejo-Mbaka Geothermal Area, Tanzania. TGDC internal unpublished technical report, p. 98.

Fritz, H., Abdelsalam, M., Ali, K., Bingen, B., Collins, A., Fowler, A., et al., 2013. Orogen styles in the East African orogen: a review of the Neoproterozoic to Cambrian tectonic evolution. J. Afr. Earth Sci. 86, 65–106. https://doi.org/10.1016/j.jafrearsci.2013.06.004.

Fontijn, K., Ernst, G.G.J., Elburg, M.A., Williamson, D., Abdallah, E., Kwelwa, S., Mbede, E., Jacobs, P., 2010. Holocene explosive eruptions in the Rungwe Volcanic Province, Tanzania. JVG Research 196, 91–110. https://doi.org/10.1016/j.jvolgeores.2010.07.021.

Gamble, T.D., Goubau, W.M., Clarke, J., 1979. Magnetotellurics with a remote magnetic reference. Geophysics 44, 53–68. https://doi.org/10.1190/1.1440923.

Griffiths, D.J., 1999. Introduction to Electrodynamics, 3rd Edition, Prentice Hall, New Jersey, 576 pp.

Gutiérrez-Negrín, C.A.L., 2024. Evolution of worldwide geothermal power 2020–2023. Geothermal Energy (2024) 12:14. https://doi.org/10.1186/s40517-024-00290-w.

Hersir, G.P., Guðnason, E.Á., Flóvenz, Ó.G., 2021. Geophysical exploration techniques. Compr. Renew. Energy 7, 26–79. https://doi.org/10.1016/B978-0-12-819727-1.00128-X.

Hersir, G.P., Weisenberger, T.B., 2015. Rungwe Volcanic Region, SW-Tanzania - A Proposal for Surface Exploration Studies, Supported by ICEIDA/NDF. Iceland GeoSurvey, short report ÍSOR-15048, 11p.

Hinze, W.J., Frese, V.R.R., Saad, A.H., 2013. Gravity and Magnetic Exploration: Principles, Practices, and Applications. Cambridge University Press 2013.

Hinz, N., Cumming, W., Sussman, D., 2018. Exploration of fault-related deep circulation geothermal resources in the western branch of the East African rift system: examples from Uganda and Tanzania. In: Proceedings of the 7th African Rift Geothermal Conference. Kigali, Rwanda.

Hudson, M.R., Mikolas, Marlo, Geissman, J.W., Allen, B.D., 1999. Paleomagnetic and rock magnetic properties of Santa Fe Group sediments in the 98th Street core hole and correlative surface exposures, Albuquerque Basin, New Mexico: New Mexico Geological Society 50th field conference, Albuquerque Basin, Guidebook, p. 355–361.

Jacobs, 2023. Summary of Technical Assistance to TGDC - Oct 2023. Unpublished report, 46 pp.

Jiracek, G., 1990. Near-surface and topographic distortions in electromagnetic induction. Surv. Geophys. 11, 163–203. https://doi.org/10.1007/BF01901659 v.

Jones, F. W., and Price, A.T., 1970. The perturbations of alternating geomagnetic fields by conductivity anomalies, Geophysical Journal of the Royal Astronomical Society, v. 20, 317-334.

Jones A.G., Jodicke H., 1984. Magnetotelluric transfer function estimation improvement by a coherence-based rejection technique. 54th Annual International Meeting, Soc. of Expl. Geophys. Josephat S., 2023. Major and Trace Elements Geochemistry of Natural Waters in Meru, Tanzania. Master Thesis, University of Iceland, 74 pp.

Kanda, I., Fujimitsu, Y., Nishijima, J., 2019. Geological structures controlling the placement and geometry of heat sources within the Menengai geothermal field, Kenya as evidenced by gravity study. Geothermics 79 (2019) 67–81. https://doi.org/10.1016/j.geothermics.2018.12.012.

Kelbert, A., Meqbel, N., Egbert, G.D., Tandon, K., 2014. ModEM: a modular system for inversion of electromagnetic geophysical data. Comput. Geosci. 66, 40–53. https://doi.org/10.1016/j.cageo.2014.01.010.

Laske, G., Masters, G., Ma, Z., Pasyanos, M.E. 2013. Update on CRUST1.0: A 1-degree Global Model on Earth's Crust. Poster EGU2013-2658.

Lévy, L., Gibert, B., Sigmundsson, F., Flóvenz, Ó.G., Hersir, G.P., Briole, P., Pezard P.A., 2018. The role of smectites in the electrical conductivity of active hydrothermal systems: electrical properties of core samples from Krafla volcano, Iceland. Geophys. J. Int., 215(3), 1558–1582. https://doi.org/10.1093/gji/ggy342.

Liang, W., Li, J., Xu, X., Zhang, S., Zhao, Y., 2020. A high-resolution earth's gravity field model SGG-UGM-2 from GOCE, GRACE, satellite altimetry, and EGM2008. Geodesy Surv. Eng. 6, 860–878. https://doi.org/10.1016/j.eng.2020.05.008.

Lichoro, M.C., 2019. Regional geothermal characterization of northern Kenya rift from resistivity and gravity. PhD thesis, University of Iceland, pp 169.

Mackie, R., Watts, M.D., 2012. Detectability of 3-D sulphide targets with AFMAG. SEG 2012 Expanded Abstracts 1–4. https://doi.org/10.1190/segam2012-1248.1.

Marobhe, I.M., 1989. Interpretation of aerogeophysical anomalies of southwestern Tanzania, Geol. Surv. Fin. Bull. 350, 72.

Bowles-Martinez, E., & Schultz, A., 2020. Composition of magma and characteristics of the hydrothermal system of Newberry Volcano, Oregon, from magnetotellurics. Geochemistry, Geophysics, Geosystems, 21, e2019GC008831. https://doi.org/10.1029/2019GC008831.

Martos, Y.M., Catalán, M., Jordan, T.A., Golynsky, A., Golynsky, D., Eagles, G., Vaughan, D.G., 2017. Heat flux distribution of Antarctica unveiled. Geophys. Res. Lett. 44 (22), 11417–11426. https://doi.org/10.1002/2017GL075609.Melosh, G., Moore, J., Stacey, R., 2012. Natural Reservoir Evolution in the Tolhuaca Geothermal Field, Southern Chile. Proc. Work. Geotherm. Reserv. Eng. 37, 217–223.

Meyer, B., Saltus, R., Chulliat, A., 2017. EMAG2: Earth Magnetic Anomaly Grid (2-Arcminute Resolution) Version 3. National Centers for Environmental Information, NOAA. https://doi.org/10.7289/V5H70CVX.

Miller, H.G, Singh, V.J., 1994. Potential Field tilt - A new concept for location of potential field sources. Applied Geophysics, 32, 213-217.

Moorkamp, M., Avdeeva, A., Basokur, A., Erdogan, E., 2020. Inverting magnetotelluric data with distortion correction: stability, uniqueness and trade-off with model structure, Geophysical Journal International, 222(3), 1620–1638.

Morschhauser, A., Grayver, A., Kuvshinov, A., Samrock, F., Matzka, J., 2019. Tippers at island geomagnetic observatories constrain electrical conductivity of oceanic lithosphere and upper mantle, Earth, Planets and Space, 71(1), 1–9.

Munoz, G, Ritter O, Moeck, I., 2010. A target-oriented magnetotelluric inversion approach for characterizing the low enthalpy Groß Schönebeck geothermal reservoir. Geophys J Int 183:1199–1215.

Nettleton, L.L., 1939. Determination of Density for Reduction of Gravimeter Observations. Annual Meeting, Oklahoma City, Oklahoma, 176-183.

Ochmann, N., and Garofalo, K., 2013. Geothermal Energy as an Alternative Source of Energy for Tanzania, Final Technical Report of Phase II (2010-2013), Technical Cooperation with United Republic of Tanzania, GEOTHERM-Project 2002.2061.6, Unpublished Report, 156 pp.

O'Donnell, J., Adams, A., Nyblade, A., Mulibo, G., Tugume, F., 2013. The uppermost mantle shear wave velocity structure of eastern Africa from Rayleigh wave tomography: Constraints on rift evolution. Geophysical Journal International, 194(2), 961–978.

Okubo, Y., Graf, R.J., Hansen, R.O., Ogawa, K., Tsu, H., 1985. Curie point depths of the island of Kyushu and surrounding area, Japan. Geophysics 50, 481–489. https://doi.org/10.1190/1.1441926.

Orange, A.S., 1989. Magnetotelluric exploration for hydrocarbons. Proc. IEEE, 77, 287-317.

Nettleton, L.L., 1939. Determination of Density for Reduction of Gravimeter Observations. Geophysics 4, 176–183. doi:10.1190/1.1437088.

Pádua, M.B., Padilha, A.L., Vitorello, Í., 2002. Disturbances on magnetotelluric data due to DC electrified railway: A case study from southeastern Brazil. Earth Planet, 54, 591–596 (2002). https://doi.org/10.1186/BF03353047.

Parasnis, D.S., 1951. A study of rock densities in English Midlands. Geophys J Int 6:252–271.

Park, S.K., and Livelybrook, D.W., 1989: Quantitative interpretation of rotationally invariant parameters in Magnetotellurics. Geophysics, 54, 1484-1490.

Parker, E.N., 1958. Dynamics of the interplanetary gas and magnetic fields, Astrophysical Journal, 128, p. 664.
Parker, R.L. 1972. The Rapid Calculations of Potential Anomalies. Geophys. J. R. Astr. Soc. 31, (1972), 447-455.
Patrier, P., Papapanagiotou, P., Beaufort, D., Traineau, H., Bril, H., Rojas, J., 1996. Role of permeability versus temperature in the distribution of the fine (< 0.2 μm) clay fraction in the Chipilapa geothermal system (El Salvador, Central America), J. Volc. Geotherm. Res., 72, 101–120.
Pellerin, L., and Hohmann, G.W., 1990: Transient electromagnetic inversion: A remedy for magnetotelluric static shifts. Geophysics, 55-9, 1242-1250.
Pellerin, L., Johnston, J., Hohmann, G., 1996. A numerical evaluation of electromagnetic methods in geothermal exploration. Geophysics 61, 121 – 130 61, 121–130.
Phoenix Geophysics, 2005. Data Processing user guide, SSMT2000, NPIPlot, MTEditor, synchro time series View. Phoenix Geophysics, Ltd, Toronto, Canada.
Phoenix, 2018. Phoenix Geophysics, website: http://www.phoenix-geophysics.com/home.
Plasman, M., Tiberi, C., Ebinger, C., Gautier, S., Albaric, J., Peyrat, S., Gama, R., 2017. Lithospheric low-velocity zones associated with a magmatic segment of the Tanzanian Rift, East Africa. Geophys. J. Int. 210, 465–481. https://doi.org/10.1093/gji/ggx177.
Ranganayaki, R.P., 1984. An interpretive analysis of magnetotelluric data. Geophysics, 49, 1730-1748.
Ray, L., Forster, H.J., Forster, A., Fuchs, S., Naumann, R., Appelt, O., 2015. Tracking the thermal properties of the lower continental crust: measured versus calculated thermal conductivity of high-grade metamorphic rocks (Southern Granulite Province, India). Geothermics 55, 138–149. https://doi.org/10.1016/j. geothermics.2015.01.007.
Represas, P., Catalao, J., Montesinos, F.G., Madeira, J., Mata, J., Antunes, C., Moreira, M., 2012. Constraints on the structure of Maio Island (Cape Verde) by a three-dimensional gravity model: imaging partially exhumed magma chambers. Geophys. J. Int. 190, 931–940. https://doi.org/10.1111/j.1365-246X.2012.05536.x,
Rizzello, D., Armadillo E., Pasqua, C., Pisani, P., Principe C., Lelli M., Didas, M., Giordan, V., Mnjokava, T., Kabaka, K., Tumbu, L., Marini L., 2022. Assessment of the Kiejo-Mbaka geothermal field by three-dimensional geophysical modelling. Geomech. Geophys. Geo-energ. Geo-resour. 8, 143. https://doi.org/10.1007/s40948-022-00456-5.
Rizzello, D., Armadillo, E., Pasqua, C., Pisani, P., Mnjokava, T., Mwano, J., Didas, M., Tumbu, L., 2018. Three-dimensional geophysical modelling of Kiejo-Mbaka geothermal field, Tanzania. In: Proceedings of the ARGEO-C7 Geothermal Conference. Kigali, Rwanda, p. 14.
Roest, W. R., Verhoef, J., Pilkington, M., 1992. Magnetic interpretation using the 3-D analytic signal. Geophysics, 57(1), 116–125.
Ross, H.E., Blakely, R.J., Zoback, M.D., 2006. Testing the use of aeromagnetic data for the determination of Curie depth in California. Geophysics 71, L51–L59. https://doi.org/10.1190/1.2335572.
Rung-Arunwan, T., Siripunvaraporn, W., Utada, H., 2022. The effect of initial and prior models on phase tensor inversion of distorted magnetotelluric data, Earth, Planets and Space, 74(1), 1–24.

Samrock, F., Grayver, A. V., Eysteinsson, H., Saar, M. O., 2018. Magnetotelluric image of transcrustal magmatic system beneath the Tulu Moye geothermal prospect in the Ethiopian Rift, Geophysical Research Letters, 45(23), 12–847.

Samrock, F., Kuvshinov, A., 2013. Tippers at island observatories: Can we use them to probe electrical conductivity of the earth's crust and upper mantle?, Geophys. Res. Lett., 40, 824–828.

Schmucker, U., Weidelt, P., 1975. Electromagnetic Induction in the Earth. Laboratoriet for anvendt geofysik Aarhus Universitet, Lectures Notes.

Simpson, F., Bahr, K., 2005. Practical magnetotellurics, Cambridge University Press.

Spies, B.R., Frischknecht, F.C., 1991. Electromagnetic sounding. In Nabighian, M.N., ed., Electromagnetic methods in applied geophysics, v. 2: Society of Exploration Geophysicists, p. 285 – 425.

Soyer, W., Mackie, L.R, Hallinan, S., Miorelli, F., Pavesi, A., Garanzini, S., Sagala, B., Siagian, H., 2021. Geophysics over high enthalpy fields: lessons from RLM-3D magnetotelluric and joint inversions. In: Proceedings of the World Geothermal Congress 2020+1 Reykjavik, Iceland.

Stamps, D. S., Flesch, L.M., Calais, E., Ghosh, A., 2014, Current kinematics and dynamics of Africa and the East African Rift System, J. Geophys. Res. Solid Earth, 119. https://doi.org/10.1002/2013JB010717.

Sternberg, B.K., Washburne, J.C., Pellerin, L., 1988. Correlation for the static shift in magnetotellurics using transient electromagnetic soundings. Geophysics 53, 1459–1468. https://doi.org/10.1190/1.1442426.

Stark, M.A., Soyer, W., Hallinan, S., Watts, M.D., 2013. Distortion Effects on Magnetotelluric sounding Data Investigated by 3D Modeling of High-resolution topography. GRC Transactions, 37.

Sun, K., Zhang, L., Zhao, Z., He, F., He, S., Wu, X., Qiu, L., Ren, X., 2021. Geochronology, petrography and Sr-Nd-Hf isotopes of Mbalizi carbonatite, southwestern Tanzania. J. Afr. Earth Sci. 184, 104308. https://doi.org/10.1016/j.jafrearsci.2021.104308.

Swift, C.M., 1967. A magnetotelluric investigation of electrical conductivity anomaly in the southern United States. PhD Thesis. Massachusetts Institute of Technology, Cambridge, MA

Tanaka, A., Okubo, Y., Matsubayashi, O., 1999. Curie point depth based on spectrum analysis of the magnetic anomaly data in East and Southeast Asia. Tectonophysics 306, 461–470. https://doi.org/10.1016/S0040-1951(99)00072-4.

Telford, W.M., Geldart, L.P., Sherif, R.E., 1990. Applied geophysics: Cambridge University Press.

TGDC, 2022. Ibadakuli geothermal prospect: Geophysical report results from 3D Inversion of Magnetotelluric data integrated with geological and geochemical results. TGDC internal report (Unpublished), 39 pp.

Tugume, F., Nyblade, A., Julia, J., 2012. Moho depths and Poisson's ratios of Precambrian crust in East Africa: evidence for similarities in Archean and Proterozoic crustal structure. Earth planet. Sci. Lett. 355, 73–81. https://doi.org/10.1016/j.epsl.2012.08.041.

Tumbu, L., 2019. Multi-dimensional Resistivity Imaging from Magnetotelluric Data and its Geological Interpretation in Kiejo-Mbaka Geothermal Field, South-West

Tanzania. Master Thesis, Kyushu University, Department of Earth Resources Engineering, 133 pp.
UNEP/ARGeo, 2016. Geothermal resource assessment report Ngozi and Songwe Geothermal Prospects, Tanzania. Unpublished report, 695 pp.
Ussher, G., Harvey, C., Johnstone, R., Anderson, E., 2000. Understanding the resistivities observed in geothermal systems, in Poceedings World Geothermal Congress, pp. 1915–1920, Kyushu Japan.
Vozoff, 1991. Magnetotellurics: Principles and practice, Earth Planetary Science, v. 99, p. 441-471.
Vozoff, V., 1990. Magnetotellurics: Principles and practice, Earth Planetary Science, v. 99, p. 441-471.
Wannamaker, P.E., Hohmann, G.W., SanFilipo, W.A., 1984, Electromagnetic modeling of three-dimensional bodies in layered earths using integral equations, Geophysics, 49, 60-74.
Ward, S., Hohmann, G., 1988. Electromagnetic theory for geophysical applications (Vol.1): Society of Exploration Geophysicists
Weidelt, P., 1972. The inverse problem of geomagnetic induction, Journal of Geophysics, v. 38, p. 257-289
Wiese, H., 1962, Geomagnetische Tiefentellurik Teil II: Die Streichrichtung der Untergrundstrukturen des elektrischen Widerstandes, erschlossen aus geomagnetischen Variationen (Strike direction of underground structures of electric resistivity, inferred from geomagnetic variations), Pure and Applied Geophysics, 52, 83-103.

# Paper I

**Regional thermal anomalies derived from magnetic spectral analysis and 3D gravity inversion: Implications of potential geothermal sites in Tanzania**

**Makoye M. Didas,** Egidio Armadillo, Gylfi Páll Hersir, William Cumming, Daniele Rizzello.

The paper published in Geothermics: https://doi.org/10.1016/j.geothermics.2022.102431

Geothermics 103 (2022) 102431

Contents lists available at ScienceDirect

Geothermics

journal homepage: www.elsevier.com/locate/geothermics

# Regional thermal anomalies derived from magnetic spectral analysis and 3D gravity inversion: Implications for potential geothermal sites in Tanzania

Makoye Mabula Didas [a,f,g,*], Egidio Armadillo [b], Gylfi Páll Hersir [c], William Cumming [d], Daniele Rizzello [e]

[a] Tanzania Geothermal Development Company Ltd (TGDC), P. O. Box: 14801, Ursino House No. 25, Dar es Salaam, Tanzania
[b] Applied Geophysics Laboratory, University of Genoa, Italy
[c] gylfi.pall@outlook.com, Iceland
[d] Cumming Geoscience, Santa Rosa, CA, USA
[e] Tellus S.A.S., Italy
[f] Faculty of Earth Sciences, University of Iceland, Sturlugata 7, Reykjavík 101, Iceland
[g] GRÓ-GTP, Urðarhvarfi 8 (B), Kópavogi 203, Iceland

ARTICLE INFO

*Keywords:*
East African rift system
Aeromagnetic data
Gravity data
Centroid method
Curie point depth
Moho depth
Heat flow

ABSTRACT

Tanzania is one of the several countries intersected by the East African Rift System (EARS) endowed by a geothermal potential that has been explored only to a limited extent. Here we present the first heat flux map over the region based on the Curie point depth (CPD) estimation from aeromagnetic data. We have estimated the base of magnetic sources as a proxy for the CPD from the radially average power spectra of the total magnetic field using the centroid and the de-fractal methods. Our results show that the CPDs range ca. 11 to 43 km and are comparable to, but more detailed than global CPD estimates. The heat flow has then been computed assuming a constant thermal conductivity. In order to evaluate the results against crustal thickness, we have inverted the gravimetric regional field data constrained by the existing Moho depth from seismic receiver functions. Our analysis has revealed high heat flow values (over 100 mW/m$^2$) along the EARS and at the Proterozoic collision boundaries that have been reactivated by the EARS. In general, the high heat flow anomalies coincide with known surface geothermal manifestations and shallow Moho depth in the range ca. 30 to 35 km. A high heat flow anomaly is also found in the central part of the Tanzanian craton, likely related to the mantle plume imaged by seismic tomography. The most interesting areas for geothermal exploration in Tanzania, according to our results, are the EARS triple junction in the Rungwe volcanic province, the north Tanzania divergent zone and the areas of the Proterozoic collision boundaries reactivated by the EARS.

## 1. Introduction

Understanding the thermal structure of the Earth's crust is essential in geothermal exploration and development. Although the *in-situ* crustal thermal gradient can be measured directly by drilling deep boreholes (Nyblade et al., 1990; Nyblade and Pollack et al., 1993; Nyblade, 1997), estimation of the thermal gradient and heat flow at a regional scale using direct methods alone suffers from many drawbacks such as high cost, non-uniform distribution, limited investigation depth and disturbed temperatures due to shallow groundwater circulation. One of the most commonly used indirect method to characterize regional heat flow is based on estimation of the depth to the base of the magnetic sources (DBMS) from spectral analysis of the total magnetic intensity anomalies. In many cases, DBMS can be used as a proxy for the Curie point depth (CPD) in the Earth's crust. The CPD is the depth at which magnetic minerals, principally magnetite, in the Earth's crust lose their magnetic properties when temperature increases above their Curie temperature of about 580°C (Hunt et al., 1995). Once the CPD has been estimated over an area, it can be used to map the geothermal gradient and the heat flux, assuming mean values for the thermal conductivity.

Aside from uncertainty in the computation of DBMS from magnetic spectra, significant sources of uncertainty in the estimation of

* Corresponding author at: Tanzania Geothermal Development Company Ltd (TGDC), P. O. Box: 14801, Ursino House No. 25, Dar es Salaam, Tanzania.
*E-mail address:* geodidas@ymail.com (M.M. Didas).

https://doi.org/10.1016/j.geothermics.2022.102431
Received 16 August 2021; Received in revised form 14 April 2022; Accepted 21 April 2022
Available online 4 May 2022

temperature gradient in this study include the assumption that the DBMS is controlled only by temperature (at the CPD) and the assumption that heat transfer from CPD to the surface is only by 1D conduction. In addition to temperature, the DBMS can be controlled by lateral variations in lithology with differing magnetic properties (Bansal et al., 2011; Ross et al., 2006). The assumption of 1D conduction may not be valid where the lithosphere thins in rift zones, likely causing significant 2D, 3D or transient conductive and/or convective heat transfer, for example in geothermal reservoirs. Therefore, it is important to interpret the DBMS/CPD and geothermal gradient estimates in the context of alternative constraints provided by the tectonic setting, hydrologic regime, temperature measurements from deep boreholes, crustal

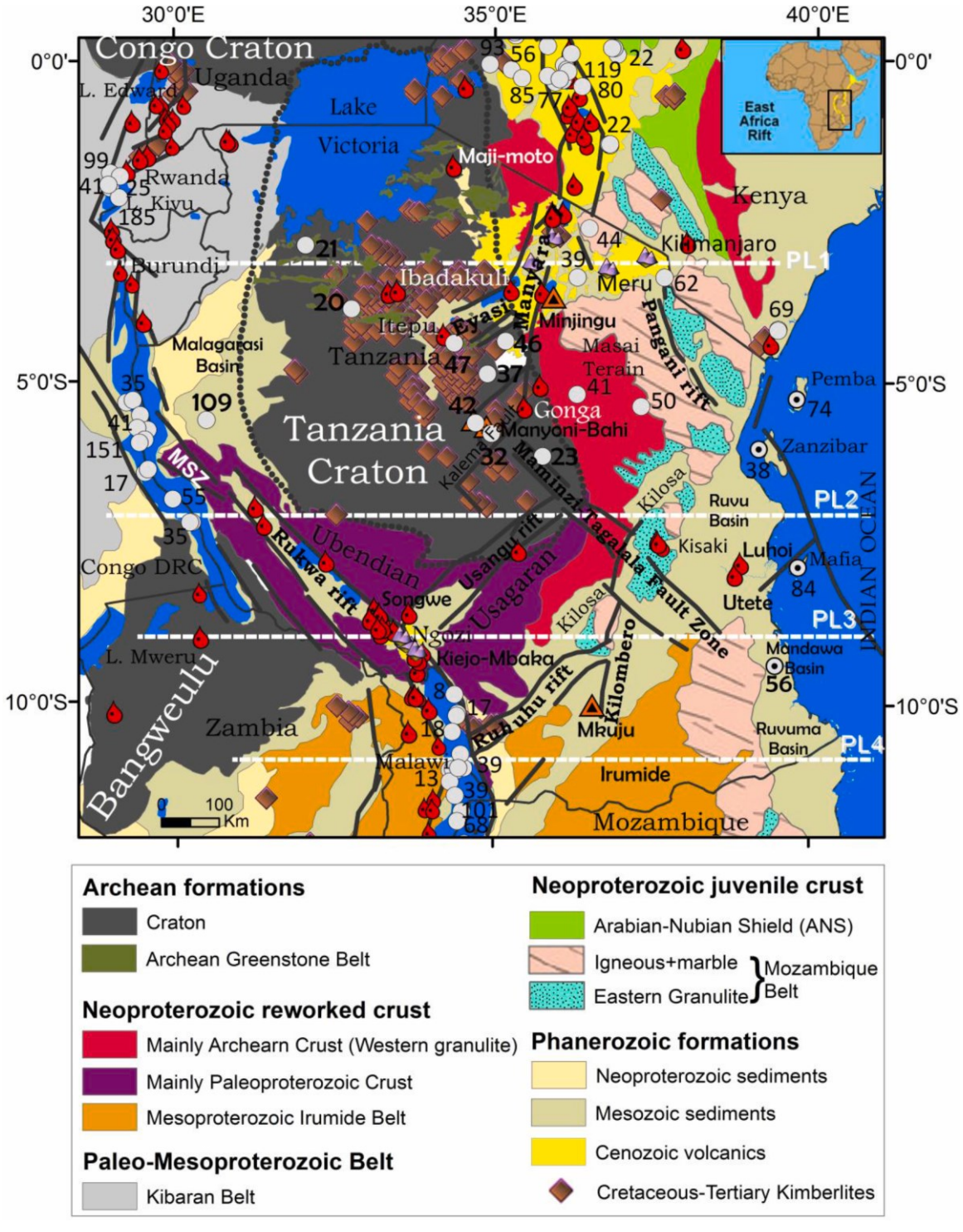


**Fig. 1.** Geological map of Tanzania and neighbouring countries showing the main geological domains with the EARS margins shown as thick black segment lines. The white numbered circles are boreholes and the numbers displayed are the heat flux in $mW/m^2$. The red drops are hot springs. The brown diamonds are the Cretaceous-Tertiary Kimberlite pipes. Map modified from Fritz et al. (2013). The continuous thin black lines define the political boundaries. The white dotted lines are selected profiles for the integrated interpretation of the results shown in Fig. 9.

boundaries derived from seismic and gravity measurements, and the properties of geologic formations, including their magmatic age, radiogenic heating, thermal conductivity and magnetic parameters. In spite of such complications, similar CPD and thermal gradient estimates have been used to complement borehole thermal data worldwide where deep boreholes are unavailable or leave very wide gaps, for example in: northeast Japan (Okubo and Matsunaga, 1994); Yellowstone National Park, U.S.A. (Bhattacharya and Leu, 1975); Kyushu Island, Japan (Okubo et al., 1985); east and southeast Asia (Tanaka et al., 1999); the African-Eurasian convergence zone in southwest Turkey (Dolmaz et al., 2005); south-central Europe (Chiozzi et al., 2005); California, U.S.A. (Ross et al., 2006). More recent examples include Australia (Kumar et al., 2021); East Africa beneath the Malawi rift zone (Njinju et al., 2019); Western U.S.A. (Bouligand et al., 2009); Greenland (Martos et al., 2018); Yukon, Canada (Witter et al., 2018); Antarctica (Martos et al., 2017, 2019; Dziadek et al., 2021); in the Adriatic Sea, Eastern Italy (Kelemework et al., 2021); Colombian Caribbean (Quintero et al., 2019) and Mexico (Carrillo-de la Cruz et al., 2020a, 2021).

Tanzania is one of the several countries intersected by the East African Rift System (EARS) with geothermal potential that has been explored only to a limited extent (Hochstein et al., 2000; Mnjokava et al., 2015). A first attempt to study the regional heat flow in Tanzania was made on the basis of several shallow boreholes (70–300 m deep), sparsely scattered in the craton and the surrounding Proterozoic orogenic belts (Nyblade and Pollack, 1993; Nyblade, 1997). The results indicate heat flow ranges of 60-74, 39–62 and 20–47 $mW/m^2$ in the Mesoproterozoic Kibaran belt, Neoproterozoic Mozambique belt and in Archean Tanzanian craton, respectively. Heat flow of 56 $mW/m^2$ was obtained from an onshore deep hydrocarbon exploration well and 51-87 $mW/m^2$ further east offshore (Nyblade, 1997). An inferred average, maximum and minimum surface heat flow value of $106 \pm 51$, $68 \pm 47$, and $53 \pm 19$ $mW/m^2$ in the eastern rift (largely in the Kenyan rift), western rift and the surrounding shield, respectively, was estimated from shallow boreholes (Fadaie and Ranalli, 1990). Location and values of the direct available measurements are shown in Fig. 1. Note that the locations are very scattered and focused on known anomalous areas. Therefore, these measurements cannot be used to obtain a representative regional heat flux map. Also, these data may be strongly biased by shallow water circulation (Nyblade et al., 1990; Nyblade and Pollack, 1993). In recent years, the geothermal potential of Tanzania has been investigated through several internationally funded projects focusing on a few promising prospect areas (Hersir et al., 2015; Kabaka et al., 2016): the Songwe, Kiejo-Mbaka and Luhoi low-medium temperature geothermal systems (Hinz et al., 2018; Armadillo et al., 2020; Rizzello et al., 2018) and the high-temperature Ngozi prospect (Kalberkamp et al., 2010; Alexander et al., 2016; Didas and Hersir, 2021). However, a regional heat flux map covering the whole of Tanzania and the associated detailed tectono-thermal interpretations are still lacking.

The goal of this study is to produce a heat flux map of Tanzania by integrating the existing direct measurements with CPD estimations from the DBMS to assess geothermal development potential in the context of the geology of the region. The geology of Tanzania is dominated by the Tanzania Archean Craton which is bordered by Proterozoic orogenic belts associated with Gondwana amalgamation and is crosscut by the Cenozoic EARS (Fig. 1). Mesozoic sediments cover the Neoproterozoic belt to the east. To support a new DBMS computation, we have merged two magnetic data sets, the total intensity aeromagnetic data acquired in Tanzania from 1977 to 1980 (Stendal et al., 2004) and magnetic data from the 2 arc-minute Earth Magnetic Anomaly Grid (EMAG2) described by Meyer et al. (2017). Using the centroid method of Okubo et al. (1985) and Tanaka et al. (1999) and the de-fractal method (Salem et al., 2014), we have computed the DBMS from spectral analyses of magnetic anomalies. Heat flow is then estimated by assuming conduction from the CPD to the surface, assuming a reasonably close match of the DBMS to the CPD. To further constrain the potential for new geothermal prospects, we have integrated existing crustal thickness estimations from passive seismic data with 3D gravity inversion to obtain the Moho interface and better constrain how the CPD, heat flow and known geothermal sites are correlated with seismic and tectonic information. To provide a validation benchmark, we have compared the heat flow estimates from CPD to the geothermal gradient found in deep hydrocarbon exploration wells and analysed the relationship between the heat flow anomalies and the location of uranium deposits.

## 2. Geological and tectonic setting

The geology of Tanzania consists of Archean cratonic nuclei also known as the Tanzanian craton (Borg and Krogh, 1999; Manya and Maboko, 2003) which is surrounded by the Proterozoic orogenic belts formed as a result of widespread continental collisions during Gondwana amalgamation (Boniface et al., 2012; Thomas et al., 2016). The last collision is marked by the north-south trending Neoproterozoic Pan African orogenic belt (Mozambique belt) that forms the East African orogen (Fig. 1, Meert and Lieberman, 2008; Boniface, 2019). In Permo-Triassic time, the East African orogen was overprinted by phases of post-orogenic extension which resulted in the formation of deep intracratonic NE-SW trending Karoo basins (Fig. 1) and initiation of coastal basins (Nicholas et al., 2007). In the Jurassic-Cretaceous some of the Karoo rifts were reactivated leading to the successful rifting that separated Madagascar from East Africa and to the development of the continental passive margin along the western coast of the Indian Ocean (Reeves and De Wit, 2000; Bumby and Guiraud, 2005). From Neogene to the present, the craton and the Proterozoic orogenic belts are overprinted by the EARS (Saria et al., 2014; Asefa and Ayele, 2020).

### 2.1. The Archean Tanzanian craton

The Tanzanian craton extends from central Tanzania to south Uganda and Kenya and adjoins the Congo craton to its north (Fig. 1). It is composed of orthogneiss basement dated >3600 Ma intruded by large granitoid plutons dated between 2610 and 2815 Ma (Kabete et al., 2012b; Thomas et al., 2016). The emplacement of granitic bodies was coeval with the basaltic volcanic rocks erupted in an intra-oceanic setting (Manya, 2001; Manya and Maboko, 2003), metamorphosed to greenschist facies (Tanzania greenstone belts) that hosts world-class gold deposits (Kabete et al., 2012a). During the Cretaceous and Tertiary, over 360 Kimberlite pipes intruded the Tanzanian craton (Stiefenhofer and Farrow, 2004), including the youngest known Kimberlite (>30 Ma) located in the western side of the craton (Fig. 1, Brown et al., 2012). The craton margins are tectonically sutured to adjacent formations by Proterozoic orogenic belts. The NW-SE trending Paleoproterozoic Ubendian belt limits the craton to the southwest (Manya, 2011; Boniface and Appel, 2017). The NE-SW trending Paleoproterozoic Usagaran belt borders it to the south (Thomas et al., 2016), the Mesoproterozoic Kibaran belt limits it to the west and the N-S trending Neoproterozoic Mozambique belt borders it to the east (Fritz et al., 2013; Thomas et al., 2016; Boniface, 2019). The Ubendian belt lies along a successful branch of a Mesoproterozoic rift that opened to form ocean basins between the Tanzanian craton and Bangweulu block (Boniface, 2019). From Neogene onwards, the eastern branch of the EARS has impinged across the eastern and southern margins of the Tanzanian craton (Ebinger et al., 1997; Saria et al., 2014; Ebinger et al., 2017).

### 2.2. Proterozoic orogenic belts

The Paleoproterozoic Ubendian-Usagaran orogenic belts are comprised of medium to high-grade metamorphic rocks, granitic and gabbroic intrusions, and volcanic rocks (Lenoir et al., 1994; Mruma, 1995) formed as a result of subduction and tectonic collision events caused by Gondwana amalgamation in Tanzania (Boniface, 2019). The Neoproterozoic Mozambique belt comprises juvenile rocks including the nappes of anorthosite-gabbro suites with emplacement ages between

700 and 900 Ma. They had subsequently been metamorphosed to amphibolite to granulite facies between 620 and 550 Ma (Möller et al., 2000; Kröner et al., 2003; Thomas et al., 2014), corresponding to the tectono-thermal events of the East African Orogen (Sommer and Kröner, 2013) resulting from the closure of the Mozambique Ocean between 850 and 620 Ma (Fritz et al., 2013; Mole et al., 2018). The East African Orogen extends from southern Israel, Sinai and Jordan in the north to Mozambique and Madagascar in the south (Stern, 1994; Fritz et al., 2013). The late Paleozoic–Mesozoic Karoo sedimentary basins developed in the Paleo-Mesoproterozoic crust (Wopfner, 2002) and the Mozambique belt which is overlaid by the Mesozoic passive-margin coastal sedimentary basins (Fig. 1, Kent et al., 1971). The Paleozoic-Mesozoic sediments have a significant role in the geology of geothermal prospects including a clay cap and/or reservoir in Songwe (Alexander et al., 2016; Hinz et al., 2018), Ngozi (Alexander et al., 2016), Kiejo-Mbaka (Rizzello et al., 2018) and Luhoi (Armadillo et al., 2020) prospects. From Neogene onwards, the EARS has disrupted the Proterozoic orogenic belts.

### 2.3. Mesozoic rifting

The Mesozoic rift consists of the deep intracratonic NE-SW trending Karoo Basins (e.g., Ruhuhu, Kilombero and Kilosa basins, Fig. 1) and the southeast coastal Basins of Tanzania (Nicholas et al., 2007). They were formed as a result of the breakup of Gondwanaland from Permian to Late-Cretaceous (Bumby and Guiraud, 2005) and the development of the passive continental margin along the western margin of the Indian Ocean (Kent et al., 1971; Bussert et al., 2009). The coastal and offshore sedimentary basins consist of marine and terrestrial sediments over 4000 m thick (Didas, 2016) that host a potential hydrocarbon system (Kagya, 1996), with discoveries of natural gas totaling more than 57 TCF (TPDC, 2021).

### 2.4. The East Africa rift system (EARS)

The Cenozoic EARS consists of two branches, the western rift with scant magmatic eruption products (Ebinger, 1989) and the eastern branch with much more prolific magmatic eruption activity (Foster et al., 1997; Ebinger et al., 2017). The eastern branch starts at the Afar

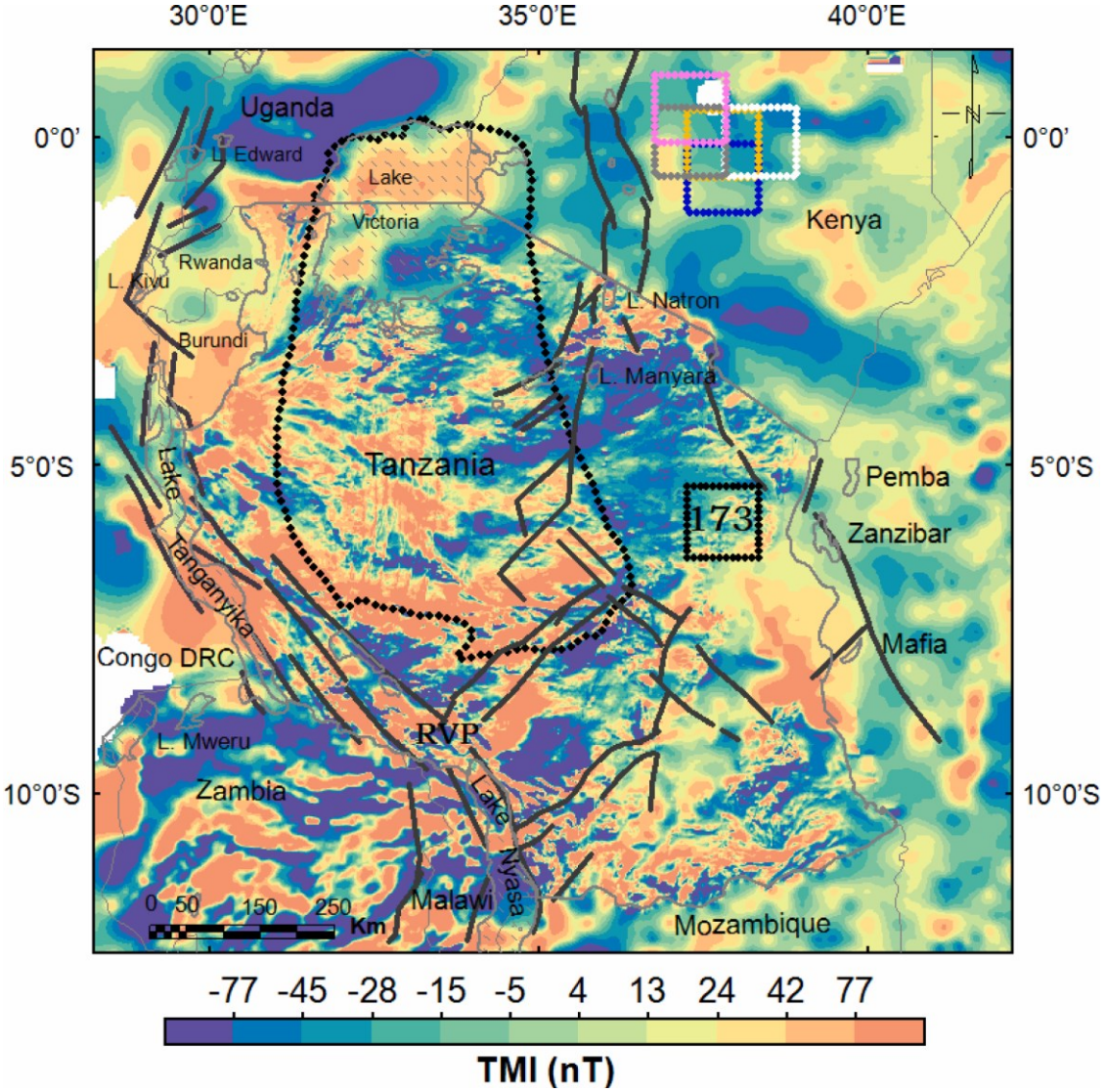


**Fig. 2.** TMI map of Tanzania and neighbouring countries merged from EMAG2 (Meyer et al., 2017) and 1977-1980 surveys (Stendal et al., 2004). The area was divided into 447 overlapping square windows, each with a dimension of 110 × 110 km$^2$ (1°x1°) used for the computations of the power spectra. The purple, grey, yellow, blue and white windows in the NE (upper right) corner represent how the windows overlap at 50%. The black square shows the location of window 173 with the computed 1D radially power spectrum shown in Fig. 3. The Tanzanian craton is outlined with a dotted black line. Thick black segment lines indicate the EARS.

triple junction in southeast Eritrea and north Ethiopia and is developed mostly within the Neoproterozoic Mozambique belt (Fig. 1). The rift stretches to the south through Ethiopia, Kenya and north Tanzania where it forms the north Tanzania divergent zone (NTDZ) defined by the Manyara and Eyasi rift zones that extends into the Archean craton (Fig. 1). The western branch stretches from northern Uganda within the Ruwenzori belt and extends south along pre-existing structures in the Mesoproterozoic Kibaran belt and further south along the Ubendian-Craton suture through the Irumide belt in Malawi and central Mozambique (Fig. 1, Ebinger et al., 1989). South of the Tanzanian craton and southwest of the Ubendian belt, the EARS has reactivated Karoo aged faults within the Mesozoic Karoo rifts (Le Gall et al., 2004). In Tanzania, the eastern and western branches of the EARS converge in the Mbeya area forming a triple junction within the Rungwe Volcanic Province (RVP, Fontijn et al., 2012), and then form the N-S trending Malawi rift which extends further south to Malawi and Zambia where it terminates. Recent seismological studies (e.g., O'Donnell et al., 2013; Mulibo and Nyblade, 2016) have proposed inferred extension of the eastern branch through the Neoproterozoic Mozambique belt crossing the Tanzanian coastal basins.

## 3. Geophysical data and methods

### 3.1. Aeromagnetic data

We have used the total magnetic intensity (TMI) airborne anomaly data (Fig. 2) collected by Geosurveys in 1977 and 1980 along E-W flight lines spaced 1 km apart, sampled every 50 m and draped at 120 m nominal ground clearance over large parts of Tanzania (Stendal et al., 2004). No data were collected over Lake Victoria and the Kilimanjaro and Uluguru mountains to the north, northeast and east, respectively. Hence, we have used the TMI Earth Magnetic Anomaly Grid 2-arc-minute resolution (EMAG2) dataset as a supplement for the uncovered areas. EMAG2 are open-source global TMI datasets compiled from satellite, ship, and airborne magnetic measurements and merged into a 2-arc-minute grid upward continued at 4 km above the geoid (Meyer et al. (2017). These data were draped to an elevation of 120 m using the ETOPO1 global relief model data with 1-arc-minute resolution (Amante and Eakins, 2009) and merged with the TMI of the 1977–1980 survey (Fig. 2). The two magnetic grids have been merged using the Knit Grids utilities in the Seequent Geosoft Oasis Montaj package. Along the suture line, the mismatch in the grid values is corrected by adjusting the grids on either side of the path, propagating the correction required at each suture point in a circle whose radius is equal to the user-defined correction width. This method provides smooth blending without over-smoothing high-frequency variations which may occur along the suture path. The final grid was sampled at 250 m spacing.

### 3.2. Curie point depth (CPD) estimation methodologies

The depth to the bottom of the magnetic sources (DBMS) can be used as a proxy for the Curie point depth (CPD), where temperature becomes so high that magnetic minerals in the Earth's crust lose their magnetic properties (Okubo et al., 1985). The most common magnetic mineral in the Earth's crust is magnetite, an oxide of iron but other metals influence the magnetic properties of minerals, including copper, cobalt, manganese, magnesium and nickel, causing the Curie temperature to vary from 440 to 580°C (Hunt et al., 1995). However, because magnetite is the dominant magnetic mineral, its Curie temperature of ~ 580°C is usually assumed to be the reference temperature for the CPD (Hunt et al., 1995; Ross et al., 2006). The assumption of DBMS as a proxy for CPD may be biased for many reasons. For instance, DBMS may be related to a contrast in lithology such as sub-horizontal detachment faults or unconformity or contact between young volcanic rocks overlying weakly magnetic thick sedimentary rocks (Bansal et al., 2011; Ross et al., 2006) or its computation could be distorted by the window size of the data used to compute the power spectrum (Ravat et al., 2007). Therefore, additional independent geothermal, geological and geophysical data are usually needed to verify the correspondence between DBMS and CPD (Okubo et al., 1985).

There are several methods to estimate the DBMS from magnetic anomalies, as described for instance in Carrillo-de la Cruz et al. (2020a) and Kelemework et al. (2021). In this study, we have used the centroid method (Okubo et al., 1985; Tanaka et al., 1999) and evaluated the results against the de-fractal method (Salem et al., 2014). All the methods work in the frequency domain and use the low wavenumbers (long wavelength) part of the spectrum, assuming that they are related to the deep magnetic sources (Spector and Grant, 1970; Bhattacharya and Leu, 1975).

The theoretical 2D spectrum of the total magnetic field for a random and uncorrelated distribution of magnetization ($P_t$) is presented by Blakely (1995) as a function of magnetization power spectrum ($P_m$), top depth ($Z_t$) and bottom depth ($Z_b$) of the anomalous body.

$$P_t(k_x, k_y, Z_t, Z_b) = 4\pi^2 C_m^2 P_m(k_x, k_y) |\Theta_m|^2 |\Theta_f|^2 e^{-2|k|Z_t}\left(1 - e^{-|k|(Z_b - Z_t)}\right)^2 \quad (1)$$

In Eq. (1), $C_m$ is a proportionality constant that depends on the direction of magnetization and geomagnetic field, $k_x$, $k_y$ are the wavenumbers in 2π radian/km in the x and y directions, respectively. Their Euclidean norm k is expressed as $|\mathbf{k}| = \sqrt{k_x^2 + k_y^2}$, and $Z_t$ and $Z_b$ are the depths to the top and bottom, respectively, of the magnetic source assumed to be a slab. Finally, $\Theta_m$ and $\Theta_f$ are the directional factors related to the magnetization and geomagnetic field, respectively. When the 1D radially averaged power is computed, the terms $\Theta_m$, $\Theta_f$ and $P_m(k_x, k_y)$ become constant. Hence, the power spectrum is expressed as:

$$P(k, Z_t, Z_b) = A_1 e^{-2|k|Z_t}\left(1 - e^{-|k|(Z_b - Z_t)}\right)^2 \quad (2)$$

where, P is the 1D power spectrum and $A_1$ is a constant.

In terms of centroid depth $Z_0$, (i.e., the midpoint between the top and bottom of the magnetic source) Eq. (2) can be written as (Okubo et al., 1985; Tanaka et al., 1999):

$$P(k, Z_t, Z_o, Z_b) = A_2 e^{-|k|Z_0}\left(e^{-|k|(Z_t - Z_0)} - e^{-|k|(Z_b - Z_0)}\right) \quad (3)$$

where $A_2$ is a constant.

For low wavenumbers of the radially averaged amplitude spectra Eq. (3) can be written as (Tanaka et al., 1999):

$$\ln\left(\frac{P(k)^{\frac{1}{2}}}{k}\right) = A_3 - |k|Z_0 \quad (4)$$

where $A_3$ is constant. The centroid depth $Z_0$ can, therefore, be calculated from the slope of the low wavenumber segment of the spectrum.

For the depth to the top of the magnetic source $Z_t$, which normally is obtained in the medium to high wavenumber range of the spectrum, Eq. (3) can be written as (Spector and Grant, 1970),

$$\ln(P(k))^{\frac{1}{2}} = A_4 - |k|Z_t \quad (5)$$

where, $A_4$ is a constant.

Then the approach of Okubo et al. (1985) and Tanaka et al. (1999) is used to calculate the DBMS or $Z_b$.

$$\text{DBMS} = (2Z_o - Z_t) \quad (6)$$

where, $Z_o$ is the centroid depth of the magnetic source and $Z_t$ is the depth of the top.

In the de-fractal method, Salem et al. (2014) assumed that the observed amplitude $A_F$ spectrum may be corrected considering the fractal sources using the relationship:

$$A_R(K_x, K_y) = A_F(K_x, K_y)\, K^{\alpha/2} \quad (7)$$

where K is the norm of the wavenumber and α is the fractal parameter. The method evaluates $Z_t$, $Z_b$ and α computing the forward modeling and evaluating the match between the modeled and corrected spectrum, albeit with high fractal parameter α values tending to overcorrect the spectrum (Carrillo-de la Cruz et al., 2020b).

In this study, we have estimated CPD using both the centroid method (Okubo et al., 1985; Tanaka et al., 1999) and the de-fractal method (Salem et al., 2014). For the centroid method computations, we have used the frequency domain algorithms available in the MagMap Seequent Geosoft Oasis Montaj package. For the de-fractal method computations, we have used the MAGCPD package (Carrillo-de la Cruz et al., 2020b).

### 3.3. CPD computations by the centroid method

We have applied the centroid method (Okubo et al., 1985; Tanaka et al., 1999) to square windows of dimension 110 km × 110 km (ca. 1° × 1°) running over the study area with 50% overlap. The CPD estimation has been performed on a total of 447 windows. In the case of windows with resulting DBMS larger than 25 km (8% of the total), we have used larger size windows of dimension 220 km × 220 km (ca. 2° × 2°).

The size of the windows has been chosen on the basis of the following

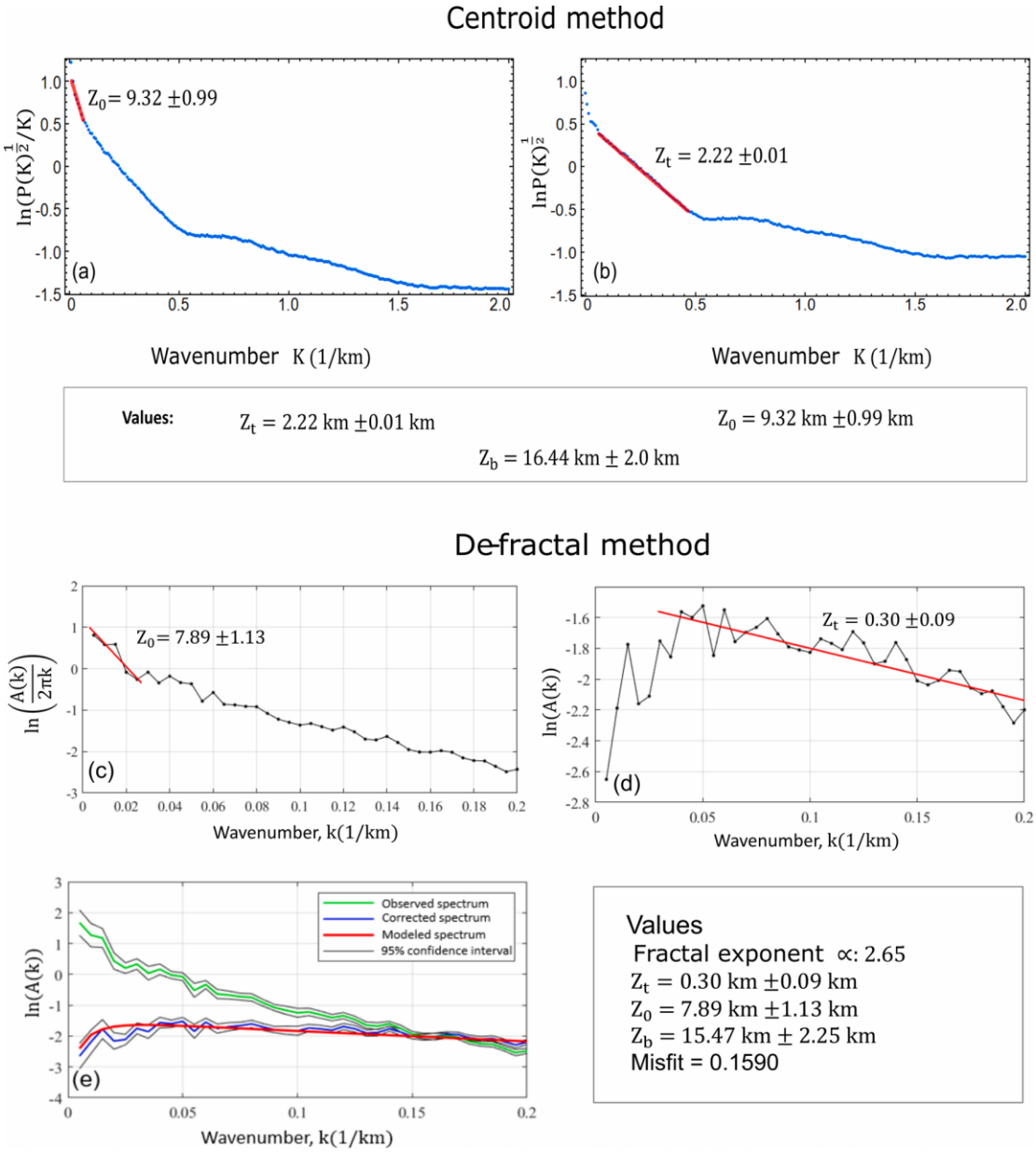


**Fig. 3.** 1D radially averaged power spectrum and computed parameters for window 173, indicated with black square in Fig. 2. (a) the mean centroid depth ($Z_0$), (b) mean top depth ($Z_t$) of the magnetic sources, over the window, respectively, as estimated from the slope of the interpolated red line. Its corresponding CPD ($Z_b$) is 16.44 ± 2.0 km. Images (c-e) indicate the same parameters in a large window (200 km) centered at the same location as 173 and computed using de-fractal method. The two methods reproduce similar CPD results. For the de-fractal method, the 2.65 fractal parameter produced a good match and minimum misfit between the observed and modeled spectra. The error between the corrected and modeled spectrum is computed as 95% confidence interval represented by the greyish curves in panel 3e.

considerations:

(i) As small as possible window size is essential in order to detect the expected short CPD wavelength variations across the EARS.
(ii) The 110 km window size was used in a similar work by Njinju et al. (2019), who applied the same methodology along the Malawi Rift, just to the south of Tanzania.
(iii) It has been proposed recently by Kelemework et al. (2021) that for the centroid method the window size should be between 3–5 times the average depth of investigation. We, therefore, expect reliable results for CPD depth up to 22 (110/5) to 36.6 (110/3) km, that is up to about 30 km using the 110 km size window, while for the 220 km size window we expect reliable results up to at least CPD of 44 km.

The optimum window size is still a matter of scientific discussion (e.g., Blakely, 1995; Maus et al., 1997; Ravat et al., 2007; Bouligand et al., 2009; Bansal et al., 2011; Li et al., 2013; Abraham et al., 2014; Nwankwo, 2014; Andres et al., 2018) and is in general unique for each area (Kumar et al., 2020; Ravat et al., 2007). It is small over tectonically active areas with high heat flow and large in stable regions such as the cratonic areas (Ravat et al., 2007; Kelemework et al., 2021). A typical approach is to choose a window large enough to show a clear peak in the very low wavenumber band of the spectrum (e.g. Ravat et al., 2007). We tested different window sizes, such as 500, 400, 300, 250, 220, 110 km. However, the peak was never been clearly detected, possibly because of the presence of a uniformly magnetized layer, a spectral peak represented by a single point, presence of layered sources (Blakely, 1995; Ravat et al., 2007) or the method used to generate the power spectrum (Bansal et al., 2006). The absence of a spectral peak has also been reported by Ravat et al. (2007) and Bouligand et al. (2009) and no peak is visible in the spectra shown in Carrillo-de la Cruz et al. (2020a). Our final choice of a 110 km window is justified because temperature gradients measured in deep petroleum exploration wells are in the range of 22–58 °C/km in different geologic settings of Tanzania (Fig. 6a). Assuming a Curie temperature of 580°C, this range implies a maximum CPD of 26.4 km. Because this value is <30 km our 110 km window size (approximately 4 times the maximum CPD) seems to be suitable.

The selection of the wavenumber bands for the computation of $Z_t$ and $Z_0$ in each window was based on a physical inspection of the spectra of the respective window (e.g. Bansal et al., 2011). After the reconnaissance of the evident linear features in each plot, a straight line was fitted based on the least-squares method. Therefore, the wavenumber band where the fit is performed varies from plot to plot for each window. Fig. 3a,b show an example of linear fitting for window 173. Considering all the windows, the centroid depths $Z_o$ were estimated from the slope of the spectrum in the wavenumber range 0.0079-0.079 1/km, while the average depths to the top of the magnetic sources $Z_t$ were estimated within the wavenumber range 0.0794-0.5 1/km.

We have also to underline that, in estimating the depths to the top and bottom of the magnetic sources, the centroid method assumes a random and uncorrelated distribution of the magnetic sources (e.g. Spector and Grant, 1970). This hypothesis has been questioned by many authors who have suggested that a fractal/scaling distribution of the magnetic sources would be more realistic (Pilkington and Todoeschuck, 1990, 2004; Maus and Dimri, 1995; Salem et al., 2014). Hence, a scaling exponent has been proposed to be applied to the power spectrum to account for the random magnetization and geological variability (Bansal and Dimri, 1999, 2001, 2005, 2010; Pilkington and Todoeschuck, 1993; Maus and Dimri, 1995; Dimri 2000; Dimri et al., 2003; Bansal et al., 2006). Kelemework et al. (2021) have observed that the centroid method assumption of random and uncorrelated distribution of the sources usually overestimates the CPD. Therefore, the results from this method could be interpreted as a likely deeper limit of the DBMS estimates of the CPD (Fig. 5b). Therefore, the centroid method continues to be used (e.g. Njinju et al., 2019; Dziadek et al., 2021) since it avoids the arbitrary choice of the fractal parameter and is relevant to cases where a deeper range of the CPD is of interest, for example, in areas of cratonic crust like much of Tanzania.

### 3.4. CPD computations by the de-fractal method

In order to overcome the simplifying assumption of random and uncorrelated magnetic sources, we have applied the de-fractal method (Salem et al., 2014; Carrillo-de la Cruz et al., 2020a) to square windows of 300 and 200 km size covering the study area with 50% overlap. The size of the windows in this approach is larger than in the previous one, because according for instance to Kelemework et al. (2021), it must be larger than minimum 5 times the expected CPD. Since the use of 300 and 200 km windows gave very similar results, we consider here the results obtained with the use of the 200 km size window, giving the higher lateral resolution (Fig. 5a).

The fractal exponent of the de-fractal method allows the user to take into account different magnetization distributions linked to different geological conditions (e.g., Bouligand et al., 2009; Carrillo-de la Cruz et al., 2021). On the other hand, the major drawback with this approach is that the choice of the fractal parameter is not straightforward. Li et al. (2019) have observed that the fractal exponent and Curie depth are so strongly inter-connected that they cannot be reliably estimated independently. In the de-fractal approach (e.g. Carrillo-de la Cruz et al., 2020a) the strategy is to choose the fractal parameter that gives the best fit between the observed and the modeled spectrum computed from the current estimation of the top and bottom of the magnetized layer (see Fig. 3c–e for example). Therefore, this approach is also subjective because of the broad minimum fitting errors that often occur by applying a range of fractal exponents and because of the correlation between the fractal parameter and the CPD that affects forward modeling (Li et al., 2019).

Generally speaking, the CPD estimations we have obtained using the de-fractal method (Fig. 5a) show similar patterns as using the centroid method (Fig. 5b), but the centroid method gives generally deeper CPD than the de-fractal method (see Figs. 3 and 5). The tendency of the de-fractal method to overcorrect the spectra and produce erroneously small Curie depths has been widely reported (Li et al., 2019; Kelemework et al., 2021). Therefore, the DBMS and CPD estimates using the de-fractal method can be considered to be biased to shallow depths at lower confidence than the centroid method estimates, in the context of a region dominated by cratonic crust but bordered by rifting.

### 3.5. Evaluation of the CPD errors

The errors of the centroid and top depths of the magnetic sources, $\Delta Z_0$ and $\Delta Z_t$, have been computed from the slope error of the linear fit (e.g., Ravat et al., 2007; Kelemework et al., 2021). Uncertainty of the depth to the bottom of the magnetic sources ($\Delta Z_b$) has been computed using the standard propagation error formula (e.g. Martos et al., 2019):

$$\Delta Z_b = \sqrt{4\Delta Z_0^2 + \Delta Z_t^2} \quad (8)$$

The resulting statistical errors of the centroid and top depths of the magnetic sources have been found to be in the range of 0.24–1.05 and 0.01–0.34 km, respectively. The corresponding error of the DBMS, $\Delta Z_b$, is in the range 0.5–2.1 km. This approach and similar magnitude errors have been obtained by many authors, e.g. 0.16–2.16 km in Coahuila, Mexico (Carrillo-de la Cruz et al., 2020a), less than 2 km beneath Thwaites Glacier in West Antarctica (Dziadek et al., 2021) and 0.53 km in Soutpansberg Basin, South Africa (Nyabeze and Gwavava, 2016). The same computations applied to the de-fractal method have yielded very similar results.

All the spectral methods and the estimates of fitting error have limitations that must be considered when interpreting the accuracy of the results with respect to both DBMS and CPD. Errors in choosing the

correct wavenumber band over which a linear fit is calculated may produce unpredictable errors that are very difficult to evaluate. Also, depth estimation is very sensitive to small variations of the fractal parameter. Moreover, depth estimations may be biased by sources at different depths which may affect the top depth estimations due to strong overlapping of the related spectral components (Hussein et al., 2013; Kelemework et al. (2021)). Uncertainties derived from these problems could be quantitatively estimated using Bayesian inversion (where parameters related to the thickness of magnetic sources are expressed in probability terms) because of its capability to incorporate prior information such as measurements from deep wells (Mather and Fullea, 2019; Audet and Gosselin, 2019; Lösing et al., 2020). However, the CPD uncertainty computed using the Bayesian approach requires very large window sizes 15-30 times larger than the deepest possible magnetic base in the study area (Mather and Fullea, 2019). Moreover, it is likely that factors other than curve fitting, like the separation of DBMS from CPD where deep lithology lacks magnetic sources (Kumar et al., 2021), cumulatively contribute greater uncertainty to the CPD estimate. Therefore, the errors in CPD are expected to be much greater than the estimated fitting errors and are likely to be of the order of many kilometers (e.g. Ravat et al., 2007; Mather and Fullea, 2019).

To address this uncertainty, the thermal gradient derived from the CPD estimates has been interpreted in the context of other data sets, including geothermal gradient and heat flux estimated from deep wells, resistivity distribution from magnetotelluric surveys, phase velocity variations from seismic tomography, tectonic setting of the regions and Moho elevations from seismic and gravity inversions.

### 3.6. Geothermal gradient and heat flow estimations

The estimated DBMS can be used to determine the temperature distribution at depths and consequently the geothermal gradient (Okubo et al., 1985). Firstly, we have assumed a proxy between the DBMS and CPD. The geothermal gradient $\frac{\partial T}{\partial z}$ has been calculated in each window as the ratio of the Curie temperature ($T_c$) of magnetite (580°C) in the crust and the estimated depth to the base of the magnetic source (DBMS) or $Z_b$ assumed to be the Curie point depth (CPD) in each window.

$$\frac{\partial T}{\partial z} = \frac{\mathbf{T_c}}{\mathbf{Z_b}} \tag{9}$$

The surface heat flow $\mathbf{q_s}$ in each window is computed under the assumption that 1D steady-state conductive heat transfer dominates (e.g. Martos et al., 2017).

$$\mathbf{q_s} = \lambda \frac{\mathbf{T_c}}{\mathbf{Z_b}} \tag{10}$$

Where, $\lambda$ is the average thermal conductivity coefficient of the rock. We choose to use an average thermal conductivity of 2.5 W/m°C because the basement rocks in Tanzania are dominantly the Precambrian gneiss, granulite and schist (Fritz et al., 2013, Fig. 1) with a conductivity range between 2 and 3 W/m°C (Ray et al., 2015).

### 3.7. Gravity data analysis

We have used gravity inversion to obtain Moho depth estimates over the large areas not covered by seismic data. The Moho depth estimates are used to compare the CPD and the associated geothermal gradients and heat flow derived from aeromagnetic data against crustal thickness. We use the new high resolution (5' x 5' arc minute) satellite-derived Free-Air gravity field model compilation SGG-UGM-2 (Liang et al., 2020) as our gravity data. In order to remove the gravity effect related to the topography we have computed the complete Bouguer anomaly using the ETOPO1 elevation map (Amante and Eakins, 2009), assuming Bouguer densities in the range 2.4 to 3 × $10^3$ kg/$m^3$. As a final reference value, we have chosen 2.8 × $10^3$ kg/$m^3$ because it showed the least correlation with the topography and is representative of the widespread exposure of crystalline rocks in the region.

The use of a Bouguer density of 2.8 × $10^3$ kg/$m^3$ will overcorrect the gravity over areas where there is a significant thickness of sediments and/or water. We, therefore, have taken into account the density reductions due to water (in the lakes and the Indian Ocean) and sediments using the sediment thicknesses compilation from the CRUST1.0 Global model (Laske et al., 2013), verified against wells drilled to the basement along the coastal region of Tanzania (Didas, 2016). The densities of water and sediments were assumed to be 1, and 2.4 × $10^3$ kg/$m^3$, respectively. Finally, we obtained the Bouguer anomaly compensated for water and sediments. To downweight the effects of the shallow intra-crustal density variations, we have applied a 150 km low pass filter.

The final gridded Bouguer anomaly (Fig. 4) indicates a broad zone of gravity low along the eastern rift axis and the surrounding area which extends south to the Archean Tanzanian craton. This anomaly is probably caused by a combination of features including the pre-existing thick crust caused by Precambrian tectonic collisions (Nyblade and Pollack, 1992), thickening of the crust due to Neoproterozoic collisional events during the formation of the Mozambique belt (Simiyu and Keller, 2001; Fritz et al., 2013), Cenozoic low density volcanoclastic rocks with thickness reaching 2 km on the rift flanks (Baker et al., 1988), crustal thickening due to intrusions near Moho (Hay et al., 1995) and the low density mantle beneath the apex of the Kenyan dome (Simiyu and Keller, 1997). The gravity low in the craton follows the trend of the area with Kimberlite pipes, indicating thick crust.

### 3.8. Estimation of Moho depth from gravity data

To infer the Moho depth distribution in Tanzania, we performed a constrained 3D inversion of the 150 km wavelength cut-off low pass filtered Bouguer gravity anomaly corrected for the sediments (Fig. 4). We used the GM-SYS 3D Geosoft Seequent software package. Forward modelling is based on a combination of Fast-Fourier Transform and space-domain algorithms to calculate the total response of the model (Parker, 1973). The inversion for solving the Moho depths is based on the procedure proposed by Parker and Huestis (1974) which assumes a simplified model of fixed densities of the crust and mantle. The algorithm solves iteratively for the thickness of a single layer representing the crust. This simplification in the model probably introduces the greatest departure from reality. The optimal solution is obtained when modeled Bouguer anomaly is close to the measured Bouguer anomaly within a given error. We assigned a constant density contrast of 0.5 × $10^3$ kg/$m^3$ to the crust/mantle boundary, assuming average crustal and mantle densities of 2.8 and 3.3 × $10^3$ kg/$m^3$, respectively. Since the inversion of gravity data is strongly affected by the non-uniqueness of the solutions, addition of *an a priori* constraint is needed to reduce the ambiguity (Kanda et al., 2019; Represas et al., 2012). As *an a priori* constraint, we have used the crustal thickness derived from seismic receiver functions compiled from several authors (Last et al., 1997; Dugda et al., 2005; Wölbern et al., 2010; Tugume et al., 2012; Kachingwe et al., 2015; Hodgson et al., 2017; Plasman et al., 2017; Borrego et al., 2018). The seismic receiver function crustal depth estimations have been gridded (Fig. 5d) to form a starting model for the gravity inversion and were used as a reference model during the inversion. The final crustal elevation model we have obtained is shown in Fig. 7 and described in paragraph 4.2. The final RMS error is 1.4 mGal. Finally, we have validated our results against the Global Moho depth by Laske et al. (2013). There is a good first-order match between our inversion and the global model over the areas covered by the receiver functions since our model has used receiver functions as constraints. In the large areas where receiver functions estimations from the global data set are not available, our model shows more detail. Note that the low pass filtering applied to the Bouguer gravity anomaly used for the

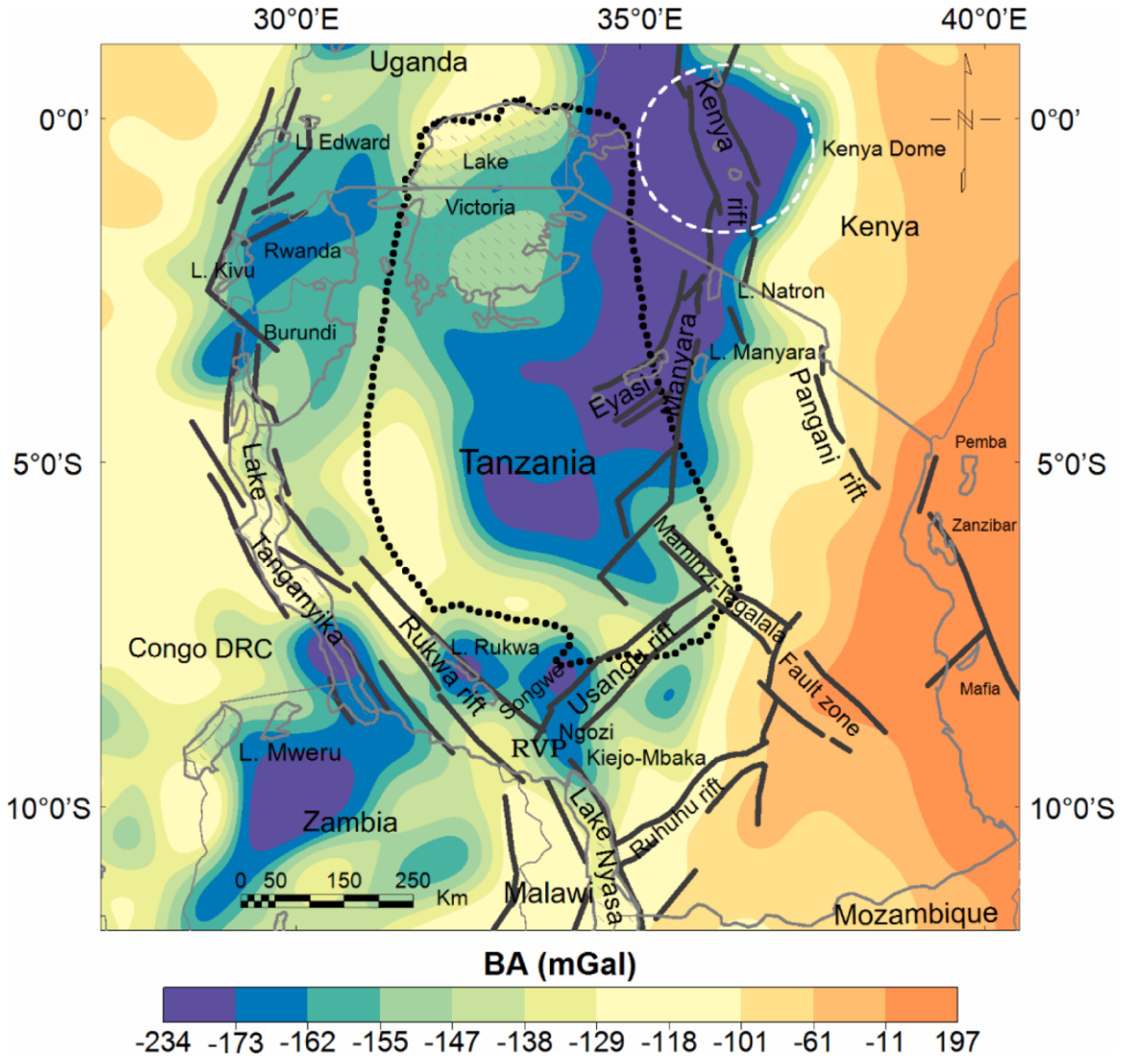


**Fig. 4.** The 150 km low pass filtered Bouguer gravity anomaly map, used here for the inversion. The dashed white ellipse indicates the Kenyan dome. The Tanzanian craton is outlined with a dotted black line. Thick black segment lines indicate the EARS.

inversion may have affected short-wavelength contributions from Moho, expected for instance along the rift axis.

## 4. Results

### *4.1. Curie point depth, geothermal gradient, heat flow and the geology of Tanzania*

Overall results of the CPD, geothermal gradient and heat flow estimated from magnetic data are shown in Figs. 5 and 6. As a reference, in Fig. 5c we have reported the Global CPD estimated by Li et al. (2017). Our estimated CPDs range between 11 and 43 km beneath the geoid (Fig. 5a,b), the geothermal gradient ranges between 14 and 53 °C/km (Fig. 6a) while the heat flow values range between 34 and 132 mW/m$^2$ (Fig. 6b). As indicated in Fig. 5a,b, shallow CPDs are observed along the eastern branch of the EARS from Kenya through northern Tanzania where they terminate at the Eyasi rift as it diverges into the Archean Tanzanian craton (anomaly 2, Fig. 5a,b). In the western branch, shallow CPDs are seen southwest in the Rungwe volcanic province (RVP) and in the Rukwa rift. The northern part of the Malawi rift is characterized by shallow values of CPDs which increase partially to the south in Lake Nyasa. Other parts of the western rift valley associated with shallow CPDs are the central and southern parts of the Tanganyika rift basin and areas around Lake Kivu in Rwanda through northwest Burundi.

Apart from the EARS, shallow CPDs generally follow the Proterozoic continental-continental collision boundaries (anomalies 2, 3, 4, 5, 8 & 9) from the northeast through south: (i) at the Neoproterozoic collision boundaries between the Archean crust (Western Granulite) and the Neoproterozoic Mozambique belt (anomaly 2), (ii) along collision boundaries between the southern margin of the Archean Tanzanian craton and the Paleoproterozoic Usagaran-Ubendian belts (anomaly 4 & 5), (iii) at the collision boundary between Mesoproterozoic Irumide and Paleoproterozoic Usagaran belts (anomaly 8), (iv) at the collision boundary between the Irumide belt and Mozambique belt defined by the Ruhuhu and Kilombero rifts (anomaly 9). An unexpected pervasive zone of shallow CPDs in the Tanzanian craton (anomaly 1, Fig. 5a,b) is found south of Lake Victoria including the Ibadakuli geothermal site with the 65°C hot springs, where there is no surface expression of intense faulting related to the EARS. However, this anomaly is also observed in the global CPD (Fig. 5c, Li et al., 2017) and is related to a relatively shallow Moho depth (Fig. 5d) and the deeper low phase velocity from seismic tomography (Mulibo and Nyblade, 2013). The area is known for the world-class gold and diamond deposits hosted in meta-basalts and Cretaceous Kimberlites pipes, respectively. Geochemical studies of the hot springs indicate the absence of a shallow magmatic heat source and, therefore, they have been classified as being a result of a deep circulation

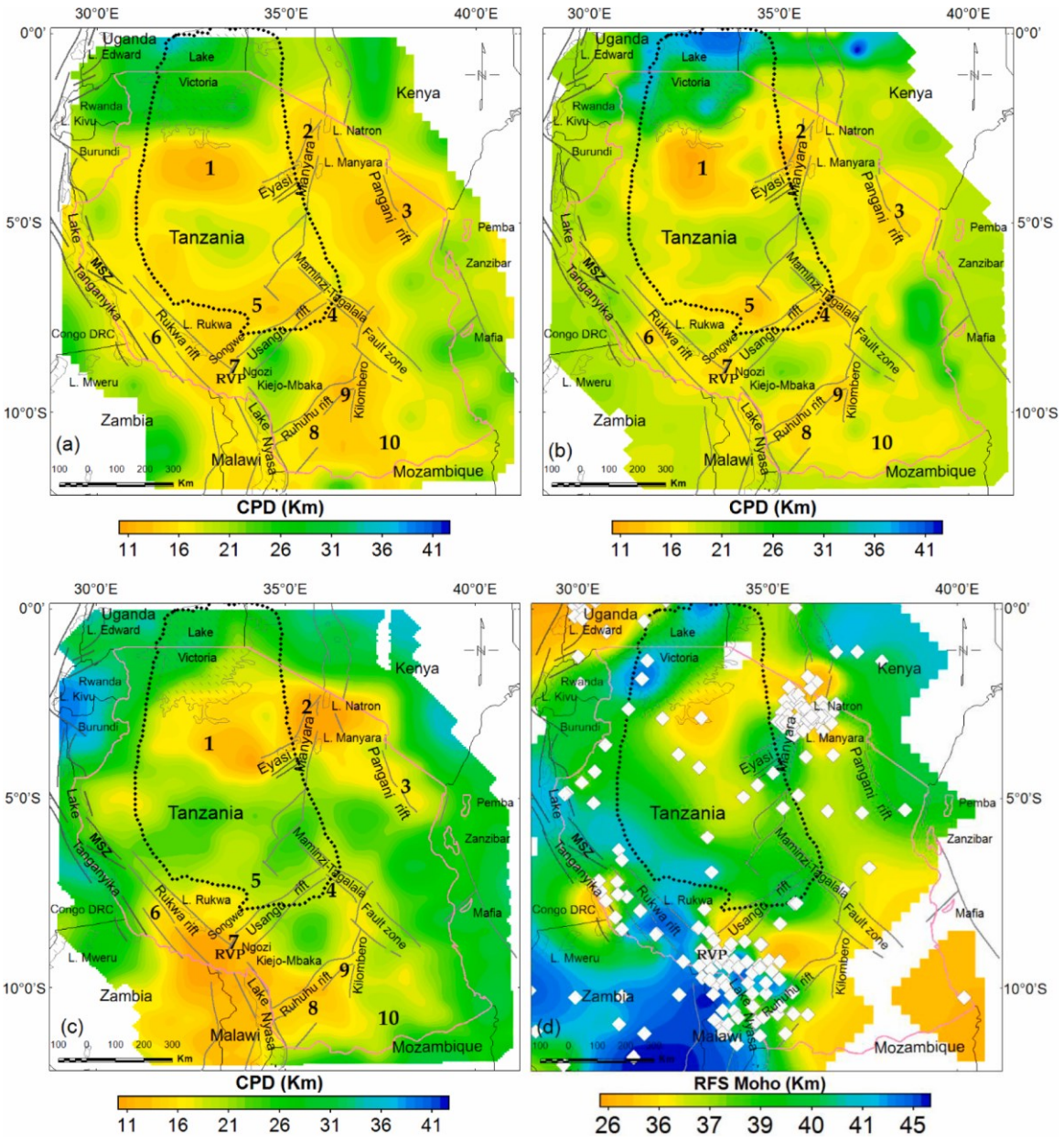


**Fig. 5.** Comparison of the CPD estimations from (a) Defractal method using 200 km widow sizes, (b) Centroid method using 110 km window sizes, (c) Global CPD map (Li et al., 2017), (d) Moho depth estimates from seismic receiver function used as constraints for 3D gravity inversion. Thick black segment lines indicate the extent of the EARS. White diamonds are the seismic stations. The numbers represent the heat flow anomalies discussed in chapter 5.

of a fault-controlled geothermal system (Hochstein et al., 2000; Hinz et al., 2018; TGDC, 2020) except the hot springs at the floor of the Ngozi caldera in the RVP which indicate magmatic affinity (Alexander et al., 2016).

The deepest CDP of 43 km in Tanzania is observed far away from the Proterozoic collision boundaries. High CPD values in nearby countries are observed in southeast Uganda and along the eastern shoulder of the rift in Kenya. A clear similarity between the CPD from this study in Fig. 5a and the Global CPD (Fig. 5c, Li et al., 2017) is observed but with additional information in the current results. Most of the low CPDs relate with zones under an extensional regime (Stamps et al., 2018) including anomalies 2, 3, 5, 6 and 7. A good correlation is also observed between the very low seismic phase velocity from seismic tomography (Mulibo and Nyblade, 2013) and the shallow CPD south of Lake Victoria and the associated high geothermal gradient and high heat flow.

### 4.2. Moho depths from 3D inversion of Bouguer gravity anomalies

The Moho depths based on a 3D inversion of Bouguer gravity data shown in Fig. 7 indicate a depth variation from 19 km offshore to 49 km beneath the Kenyan dome. From the Kenyan dome, large Moho depths extend to the south, following the western shoulder of the eastern rift into the Tanzanian craton. South of the craton, deep Moho is observed at the Proterozoic Ubendian-Usagaran mobile belts. From the offshore anomaly, the shallow Moho depth extends to the coastal area and southwards.

The localized shallow Moho expected beneath the eastern branch of the EARS based on seismic studies and magma encountered in geothermal wells in Menengai in the Kenyan rift (Mbia et al., 2015) is not resolved by the gravity inversion because of the filtering. However, zones of relatively shallow Moho depths of 36 km are observed to the north and south of the Kenyan dome while in the western branch

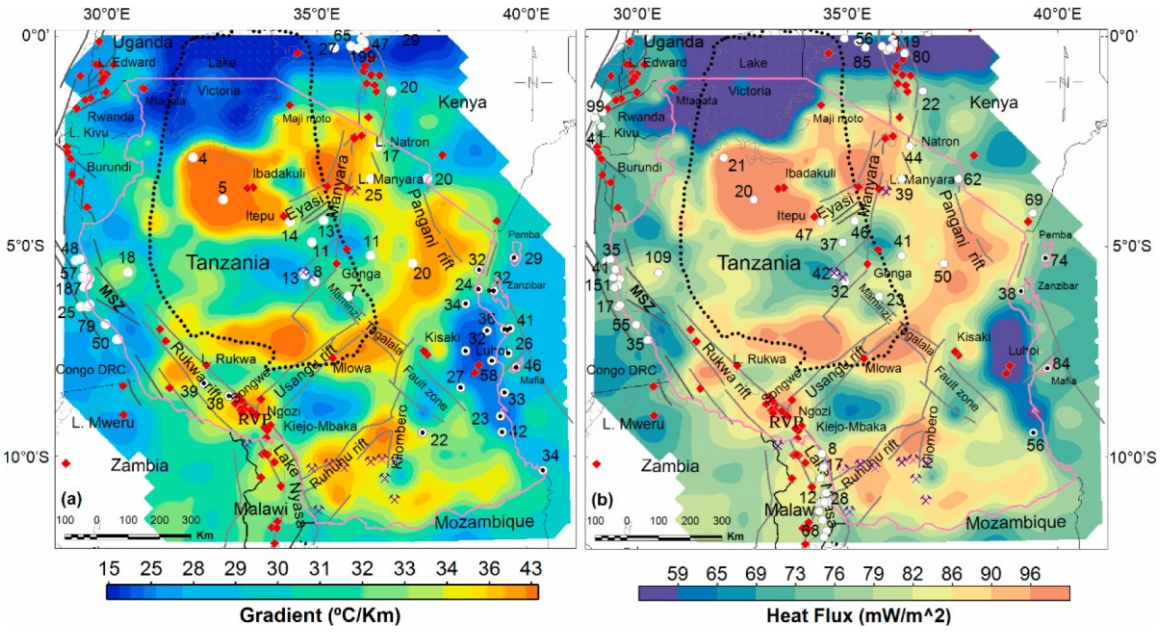


**Fig. 6.** Maps of estimated geothermal parameters from the radially averaged power spectrum of magnetic anomalies superimposed on structures. (a) Geothermal gradient map derived from Fig. 5a, (b) Heat flow map. White circles and white circles with a black dot are the shallow and deep hydrocarbon exploration wells, respectively. The numbers displayed are the numbers of available measured geothermal gradient or heat flow values from boreholes. The red diamonds are the hot springs and the crossed-pickaxe symbols indicate Uranium deposits. The maps are generated using minimum curvature gridding with a grid cell size of 2 km x 2 km.

shallow Moho depths are observed northwest and southeast of the Rukwa rift extending further south through western Malawi with an offset parallel to the rift axis. Below Lake Tanganyika, shallow Moho depths are revealed at the northern and central parts of the Lake. The Moho depths in the craton range from 45 km beneath the central part to 35 km in the southwest parallel to the northwest-trending Paleo-proterozoic Ubendian mobile belt. Localized zones with great Moho depths of 44 km are identified beneath the Ibadakuli, Maji-moto hot springs and below Lake Victoria.

## 5. Discussions

In order to better compare our results with existing information, we present several profiles across different geological and tectonic domains in Fig. 9. For each profile, we show in the upper panel the topography and the geological domains (see also Fig. 1). In the lower panel, we show our CPD estimates (magenta line), the global CPD estimation (blue) by Li et al. (2017), our gravimetric Moho (orange), the seismic Moho (green) from the global model of Laske et al. (2013) and the seismic Moho (black) from our compilation of existing receiver functions. Locations of the profiles are shown in Fig. 8. Profiles PL1 to PL4 are aligned EW in order to intersect the main structural features of the region and they include many locations of crustal thickness estimations derived from the seismic receiver functions (white diamonds). We have labelled the high heat flow anomalies 1 to 10 on the map and on the profiles. Below, we discuss each of these ten anomalies separately.

The Global CPD (Li et al., 2017) and the current CPD study are in fairly good agreement onshore, while offshore the global CPD is generally deeper in the mantle. We consider our estimation to be more reliable since it is based on the manual selection of frequency ranges to be linearly interpolated for each window while the procedure of Li et al. (2017) is necessarily automatic.

The gravity Moho is on average relatively deeper than the global seismic Moho. However, it is generally in good agreement with the receiver function Moho since the gravity Moho inversion has been constrained by the receiver function Moho. Both the gravimetric and global seismic crustal thickness estimations may be biased. Our gravimetric Moho depth estimation could be affected by density variations in the sediments and in the crust that have been assumed to be homogeneous. The seismic receiver function depth estimations may be affected by strong 3D effects and too short acquisition time.

### 5.1. Thermal structures beneath the Archean Tanzanian Craton

Overall, Archean cratons are known worldwide as the coolest landmasses on Earth associated with low heat production, low heat flow and low geothermal gradient compared to the surrounding Proterozoic mobile belts along which continental rifts subsequently develop (e.g., Lee and Uyeda, 1965; Lysak, 1987; Nyblade and Pollack, 1993). Therefore, deep CPD estimates and associated low heat flow values are expected beneath the craton lithosphere. Although Nyblade et al. (1990) have suggested that such a model generally applies to the Tanzanian Craton, our results indicate an unexpectedly high heat flow anomaly south of Lake Victoria and its southern region (anomaly 1, profiles P1, PL1 in Figs. 8 and 9). Our estimation is confirmed by the global CPD estimation by Li et al. (2017), unexpected shallow Moho estimations from seismic receiver function (Kachingwe et al., 2015) and low resistivity at a depth greater than 5 km (TGDC, 2020).

The rocks exposed in this area, including Meso-Archean meta-basalts (greenstone belts) and Neo-Archean Tonalite-trondhjemite-granodiorite (TTG) intrusions, are associated with a very shallow CPD of ~11 km and resulting high heat flow values of ~132 mW/m$^2$. The Ibadakuli geothermal site is in this area and is associated with hot springs with a maximum surface temperature discharge of 65°C. Two geothermal sites namely Itepu and Maji-moto are 120 km and 230 km to the southeast and northeast of this anomaly, respectively, with a surface temperature discharge of 60°C from a hot spring at the Maji-moto area (Hochstein et al., 2000). Seismological studies (e.g., Mulibo and Nyblade, 2013) demonstrate that the African mantle superplume which is responsible for the formation of the EARS is located below this heat flow anomaly. Once the plume reaches the base of the cratonic lithosphere, it forms two convective cells which spread to the east and west to open up the western and eastern branches of the EARS. Prior to the current plume activity, this area experienced widespread Kimberlite volcanism during Cretaceous to Tertiary times (Stiefenhofer and Farrow, 2004; Brown et al., 2012) indicating that this part of the craton was thermally

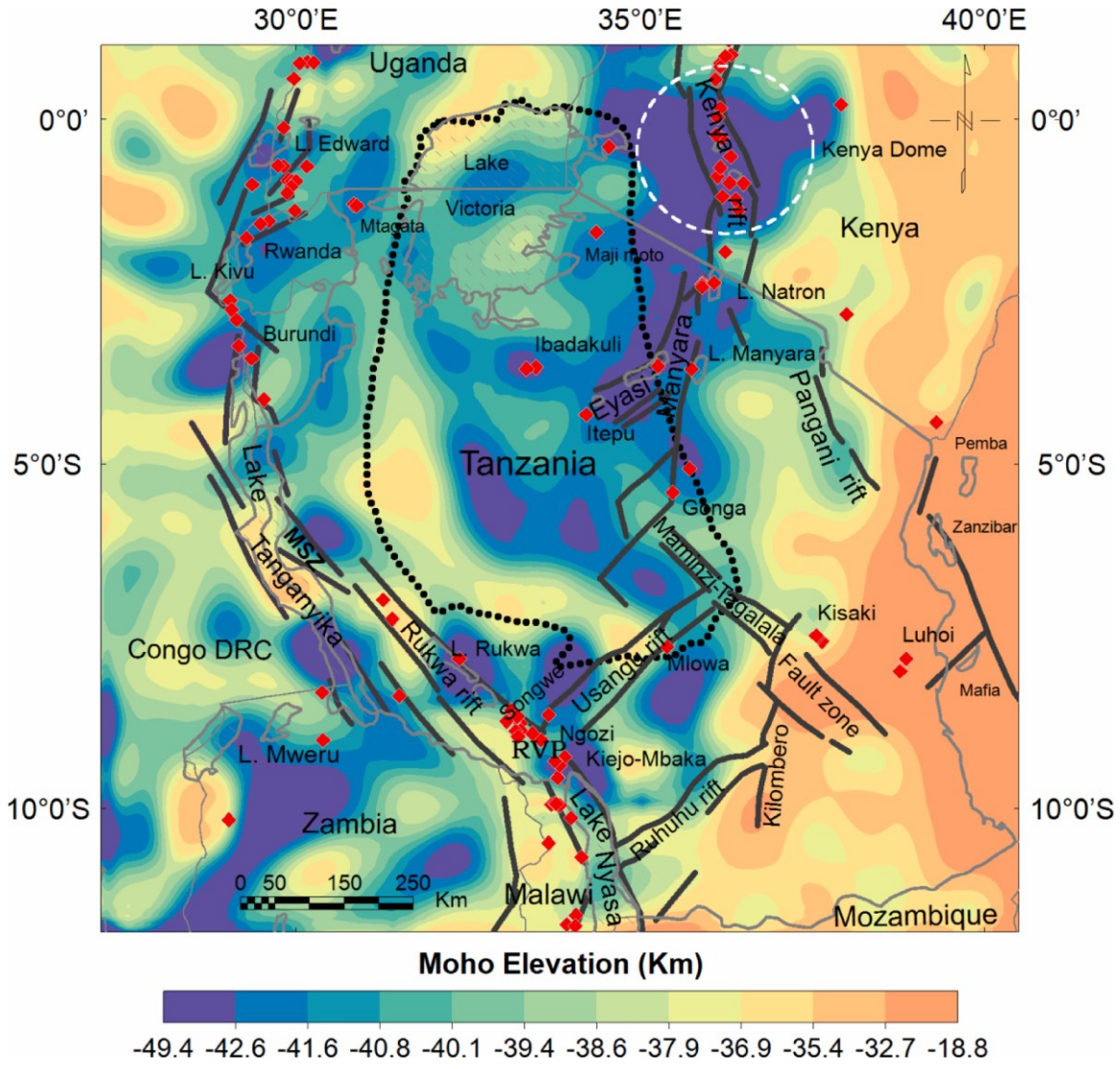


**Fig. 7.** Moho elevation map based on 3D inversion of Bouguer gravity data superimposed on hot spring locations (red diamonds). The main faults in the area are indicated by thick black lines. The black dotted polygon marks the boundary of the Archean Tanzanian craton. The stripped polygons are the lakes. The map is generated using the minimum curvature gridding with a grid cell size of 1 km × 1 km.

reactivated by the upwelling mantle superplume. The heat flow anomaly is associated with a relatively thin crust (see profiles P1 and PL1) of ~34 km from seismic studies (Kachingwe et al., 2015) that could be the result of intense heating caused by the hot mantle plume beneath the cratonic lithosphere as it extends towards the eastern and western branches of the EARS. Also, an abrupt decrease in average apparent resistivity from >1000 to about 100 Ωm at 1000 s period (corresponding to a depth of greater than 5 km) from magnetotelluric data at the Ibadakuli prospect (TGDC, 2020) may indicate a possible conductive anomaly at depth perhaps resulting from a high deep thermal gradient caused by the upwelling of the mantle superplume.

However, our estimated heat flow anomaly is not supported by the mean heat flow value of 34 ± 4 mW/m$^2$ as reported by Nyblade et al. (1990), Nyblade and Pollack (1993) and Nyblade (1997) and derived from shallow boreholes in the region (Fig. 6b). We suspect that the heat flow from shallow boreholes is not representative of the regional heat flow patterns, possibly because most of the boreholes were originally drilled for mineral exploration or groundwater consumption purposes. Therefore, the standard procedures for heat flow measurements have probably not been implemented. Temperature profiles of the boreholes also show borehole logs affected by cold-water inflow at a depth of 100–150 m (Nyblade, 1997), therefore, contributing to low surface heat flow. The other possible explanation is that the deep thermal perturbation associated with mantle superplume and rifting beneath the craton appears not yet to be conducted to the surface although it does along the rift axis.

We have also investigated the possibility that radiogenic heat production from granites rich U-Th-K could locally create significant heat. However, the two economically viable Uranium deposits in Manyoni district (Singida region) and Bahi district in Dodoma region (Kasoga et al., 2015) in the central part of the craton have no correlation with the location of the observed high heat flow values identified in this study, indicating low radiogenic heat contribution in the craton. Similarly, the high K (mean $KO_2$=4.95wt%) Archean granites in Mara region (area around the Maji-Moto hot spring) reported by Mshiu and Moboko (2012) do not correlate with high heat flow anomalies in this study. The lack of significant positive correlations between the areas with known radiogenic sources and heat flow zones suggests a minimum regional radiogenic heat contribution in the craton. However, at a local scale it may have a significant effect and, therefore, should not be completely ruled out. Gas geochemistry from Ibadakuli and the Maji-moto hot springs indicate the abundance of helium gas of continental origin

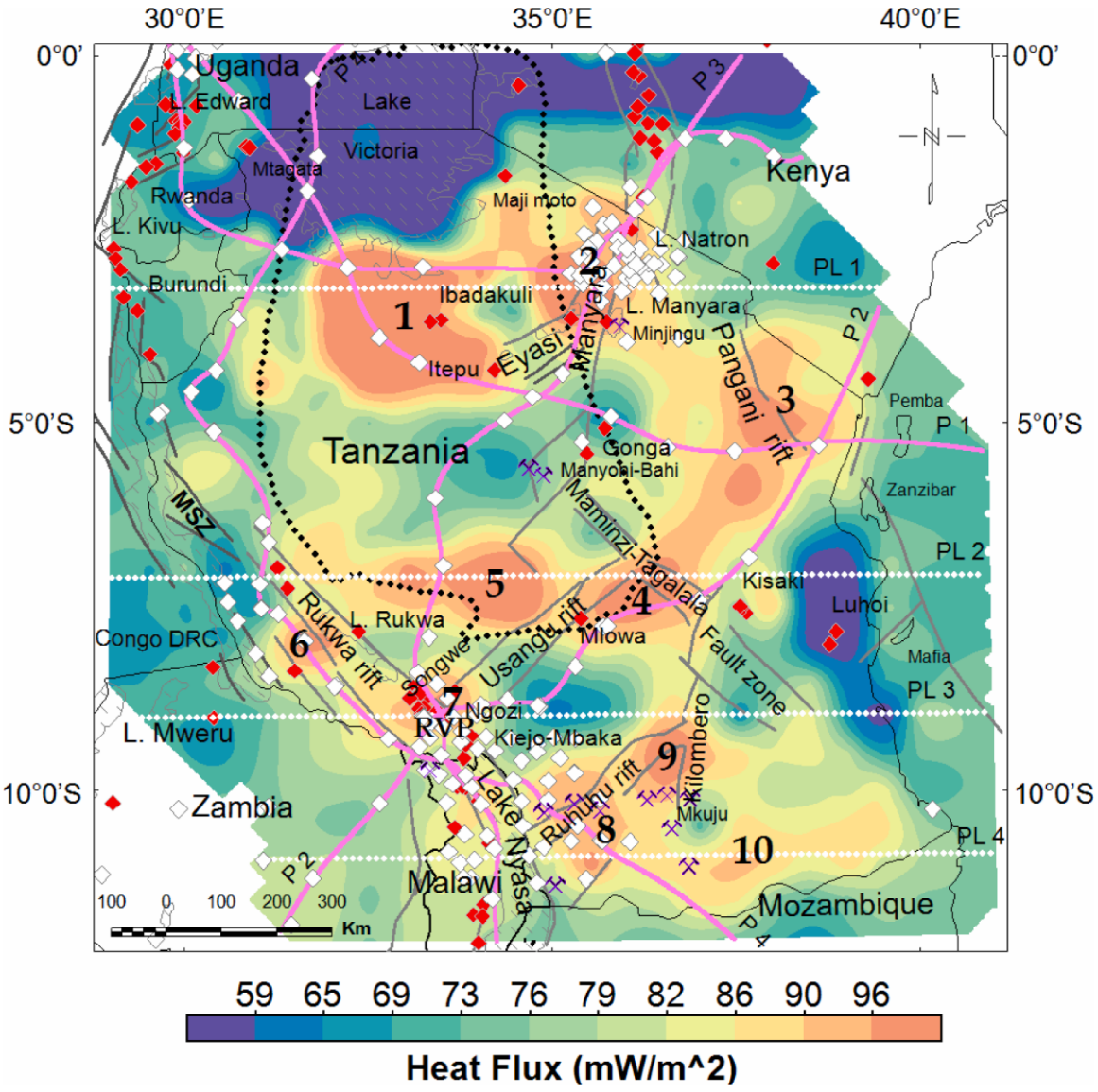


**Fig. 8.** Heat flow map superimposed on seismic stations (white diamonds), hot springs (red diamonds) and areas with Uranium deposits (crossed-pickaxe). The pervasive high heat flow zone south of Lake Victoria in the craton is very consistent with the Archean mid-oceanic ridge defined by the Mesoarchean greenstone belts (green polygons in Fig. 1) which were reactivated in Cretaceous by over 300 Kimberlite volcanisms and the uprising mantle superplume at the onset of the active EARS. The outline of the craton is marked with a black dotted polygon. The white dotted (PL) and pink coloured (P) lines are the selected profiles shown in Fig. 9. The numbers represent the heat flow anomalies discussed below.

accounting for about 36 mmol/mol and 13 % of the gas volume, respectively, derived from the decay of radiogenic elements in the crystalline basement of Archean crust (Hochstein et al., 2000; TGDC, 2020). Chandrasekhar et al. (2014) estimated the power capacity from these granites and assumed that each cubic kilometer of such granite has the capacity to generate about 42 × $10^{15}$ kWh of electricity with a temperature of 180°C at 5 km depth assuming the thermal gradient to be 40 °C/km and an average heat flow of 75 mW/$m^2$.

Although Kimberlite volcanism is usually associated with low crustal temperature, the large number of ~300 Kimberlite pipes present in the area may cause a significant thermal perturbation if heat is still preserved at depth. Hu et al. (2000) have suggested that residual heat flow may be preserved for millions of years after the ending of the deformation activity and is more dependent on the age of the last tectonothermal activity than the age of the province. Sclater et al. (1980) concluded that it takes about 800 Ma for the heat flow on the continents to decrease to the constant value of 46 mW/$m^2$. Therefore, based on our results, heat flow anomaly 1 is intruded by Kimberlites but also the small heat flow area to the south of anomaly 1 is intruded by a similar cluster of Kimberlite pipes. Therefore, the lack of consistency between the Kimberlites and the heat flow anomalies indicates the absence of direct heat contribution from the Cretaceous-Tertiary Kimberlite volcanism.

We, therefore, suggest that the thermal-mechanical instability in the craton was caused by the Cenozoic to present-day upwelling mantle superplume. It is likely that, due to the low permeability of the craton and the presence of shallow cold aquifers, the increase in deep heat flow interpreted beneath anomaly 1 is not widely manifested at the surface in the form of hot springs except at Ibadakuli area.

### 5.2. *Thermal structures beneath the Proterozoic mobile belts*

Generally speaking, the high heat flow anomalies follow the collision boundaries between the Paleo-Proterozoic Ubendian-Usagaran belt with the Archean Tanzanian craton to the south, and along a collision boundary between the Archean crust, also known as the western granulite (Fritz et al., 2013), with the Neoproterozoic Mozambique belt to

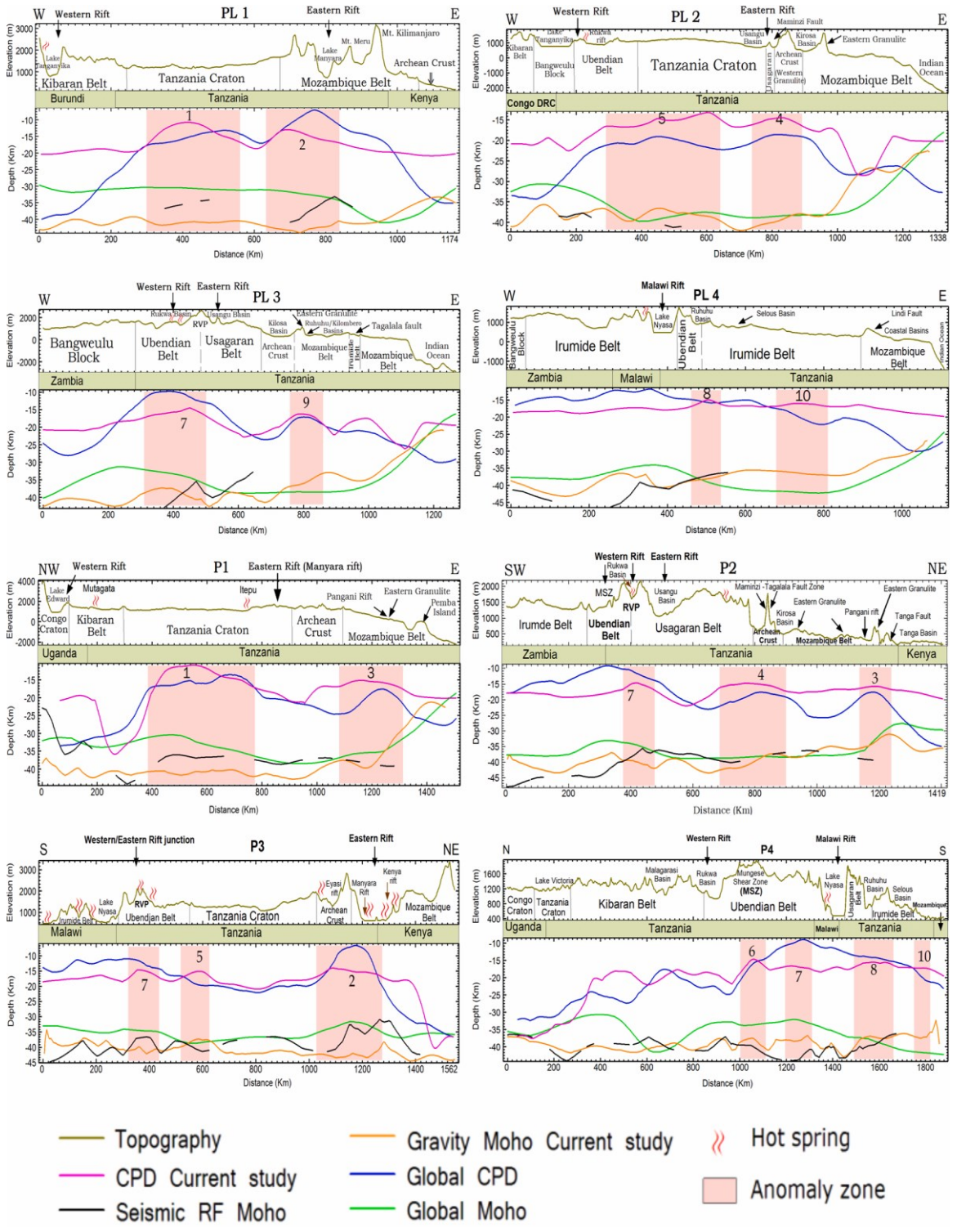


**Fig. 9.** Comparisons of the estimated CPD and gravity Moho with the global CPD (Li et al., 2017), global seismic Moho (Laske et al., 2013), seismic Moho from receiver functions and geological domains. The numbers are the locations of the high heat flow anomalies indicated in Fig. 8. Profile locations are shown in Figs. 1 and 8.

the east (Fig. 8). Moreover, high heat flow anomalies occur further south at the collision boundary between the Mesoproterozoic Irumide belt and the Neoproterozoic Mozambique belt. The heat flow is higher where the collision boundary is overprinted by the active EARS indicating thermal reactivation of the collision boundaries of the Proterozoic belts. These boundaries include: (i) Anomaly 2 (see profiles P3 and PL1), the area around the NTDZ which overprints the collision boundary between the Neoproterozoic Mozambique belt and the Archean western granulite. (ii) Anomaly 3 (profiles P1 and P2) along the Neoproterozoic Mozambique belt reactivated by the EARS which form the northwest-southeast Pangani rift. The elevated heat flow that demarcates the north, east and south boundaries of the Masai block is linked to the NTDZ, Pangani fault and the curving Neoproterozoic collision boundary, respectively, characterized by low density and low

seismic velocity (Ebinger et al., 2017; Tiberi et al., 2019). (iii) Anomaly 4 (profiles P2 and PL2) at the collision boundary between Paleoproterozoic Usagaran belt with the Archean craton overprinted by the south extension of the EARS (i.e., Maminzi fault and Usangu rift intersection zone). (iv) Anomaly 5 (profiles P3 and PL2) at the collision boundary between the Paleoproterozoic Ubendian belt with the Tanzanian craton overprinted by Kalema fault, the poorly developed eastern branch of the EARS. (v) Anomaly 6 (profile P4) at the collision boundary between the Ubendian and Bangweulu block marked by the Mungese shear zone. (vi) Anomaly 7 (profiles P2, P3, P4 and PL3) at the collision boundary between the Paleoproterozoic Usagaran-Ubendian belts overprinted by the east and west branches of the EARS at the Rungwe volcanic province. (vii) Anomaly 8 (profile P4 and PL4) at the collision boundary between the Paleoproterozoic Usagaran and Mesoproterozoic Irumide belts overprinted by the eastern branch of the EARS which form the Ruhuhu rift. (viii) Anomaly 9 at the collision boundary between the Neoproterozoic Mozambique belt and the Mesoproterozoic Irumide belt overprinted by the eastern branch of the EARS at the intersection between Kilombero and Ruhuhu basins which adjoins the central Malawi rift zone.

Our findings reveal that, besides the tectonic processes indicated by the seismic activity (O'Donnell et al., 2013), the Proterozoic sutures are affected by thermal processes, as indicated by the current shallower CPD, high heat flow and elevated geothermal gradient. The results also underlie the role played by the EARS in controlling tectonothermal processes at the Proterozoic collision boundaries.

### 5.3. Thermal structures beneath the Karoo Basins

High heat flow anomalies are present in the Permo-Triassic Karoo rift basins, particularly along the Ruhuhu-Kilombero Rift zone (anomaly 8 & 9, profiles P4 and PL3, PL4), and south of the Selous basin (anomaly 10, profile PL4) that is partially covered by the Karoo sediments. However, anomaly 9 appears to fit at the contact between the Paleoproterozoic Usagaran and Mesoproterozoic Irumide belts overprinted by the eastern branch of the EARS which Le Gall et al. (2004) suggest propagates through the Ruhuhu basin. Anomaly 8 is at the collision boundary between the Neoproterozoic Mozambique mobile belt and the Mesoproterozoic Irumide belt overprinted by the EARS in the Ruhuhu basin which adjoins the central Malawi rift. The huge Uranium deposit at Mkuju area in Selous basin, south Tanzania lies between anomaly 9 and 10. However, since these anomalies correspond to an updoming of the Moho elevation, we consider them to be a result of the mantle elevation rather than the radiogenic heat production from Uranium deposits. Moreover, there is no information about the existence of surface geothermal manifestations in this area with helium-rich hot springs which could be linked to radiogenic sources. Therefore, we interpret elevated heat flow values as being due to the recent reactivation by the EARS of the crustal extension and consequently elevated mantle associated with the Permo-Triassic rifting event. Crustal thickness studies from analysis of the seismic receiver function generally indicate that the Karoo Basins are characterized by a relatively thinner crust (30-38 km) compared to the thicker crust (46-50 km) in the surrounding area (Kachingwe et al., 2015; Borrego et al., 2018). This suggests that crustal thinning existed during Permo-Triassic rifting and is still preserved. A relatively high heat flow anomaly in Tanga (east of anomaly 3, profiles P1 and P2) is located at the intersection between Pangani and Tanga major faults probably reactivated by the EARS.

### 5.4. Thermal structures below Mesozoic sedimentary basins

In general, the southeast coastal sedimentary basins of Tanzania (Mandawa and Ruvuma basins) which form the passive continental margin are characterized by the lowest regional heat flow values (profiles PL2, PL3). The thick sedimentary cover of >4 km (Didas, 2016) should not affect the estimation of the bottom of the magnetic source and our low estimations are confirmed by the global estimation by Li et al. (2017). The progressive thinning of the crust towards the coast, imaged both by the seismic and gravimetric models has, therefore, been thermally compensated. Some known geothermal systems with shallow reservoirs (e.g. the Luhoi system along the Lindi fault zone) and the anomalously high bottom hole temperature of some deep oil wells have been explained as local anomalies formed by relatively deep hot fluid upwelling along faults (Armadillo et al., 2020).

However, the relatively high heat flow anomalies located offshore are probably caused by magmatic intrusions forming sills or dykes within the sedimentary section. Hot volcanic sill or dykes emplaced within Campanian sandstones were encountered in Mafia-1 well in Mafia island (Mpanda, 1997).

### 5.5. Thermal structures beneath the EARS

Our results indicate the highest heat flow of 90–104 $mW/m^2$ (anomaly 2) at the eastern branch of the EARS from the Manyara rift towards the south to the three rift segments of the NTDZ (see profile P3). The Kenyan rift would be expected to have the highest heat flow in East Africa. Therefore, the low heat flux, and moderate CPD in the eastern branch in Kenya is probably due to inadequate resolution caused by using a large data window size. A window size of 50 km × 50 km would resolve the anomaly below the Kenyan rift. Shallow CPD of 15 km has been estimated from magnetic data by Kuria et al. (2010) in the Olkaria geothermal field and validated using temperature logs from deep wells. Similarly, high heat flow is seen along the western branch at the southern triple junction in the Rungwe volcanic province (anomaly 7) where the eastern and western branches of the EARS converge (Fontijn et al., 2012). From this triple junction, the rift propagates to the south along the Malawi rift which is characterized by low to moderate heat flow. The high heat flow values in the EARS are due to the thinning of the crust and mantle elevation caused by the active crustal extension. This observation is supported by the minimum crustal thickness estimations along the rift axis from seismic receiver functions (Wölbern et al., 2010; Tugume et al., 2012; Laske et al., 2013; Hodgson et al., 2017; Plasman et al., 2017; Borrego et al., 2018), shallow low seismic velocity zone (Mulibo and Nyblade, 2013; Ebinger et al., 2017; Grijalva et al., 2018; Tiberi et al., 2019) and low-density zone (Tiberi et al., 2019).

The Ngozi geothermal area located at the southern triple junction (in the Rungwe volcanic province) where the eastern and western branches of the EARS intersect, is characterized by high heat flow values of ~98 $mW/m^2$. Na-K geothermometry from the hot springs (66–89°C) indicated a high temperature geothermal system with a reservoir temperature greater than 230°C heated by a magmatic body located within a depth range of 5–7 km below the Ngozi caldera (Alexander et al., 2016; Didas and Hersir, 2020). The Ngozi area is bordered by some geothermal systems characterized by a lack of apparent magmatic contribution to the water and gas chemistry, including the 140°C reservoir in the Kiejo-Mbaka prospect located about 50 km to the southeast (Rizzello et al., 2018) and the 120°C reservoir in the Songwe prospect (Alexander et al., 2016) located about 50 km northwest. Further south of the Ngozi prospect, the Malawi rift is characterized by numerous hot springs with measured temperatures of up to 80°C aligned with the rift margin (e.g., Njinju et al., 2019). At a regional scale, the Ngozi and Songwe prospects are linked to the same heat flow anomaly with the peak located at the Ngozi-Rungwe volcanoes, while the Kiejo-Mbaka prospect seems to form an independent system. In fact, it is considered to be an extensional domain play fault-controlled system with lateral leakage (Rizzello et al., 2018).

Unlike the magma-rich eastern branch of the EARS (Foster et al., 1997) associated with numerous fumaroles and hot springs and the poorly magmatic Malawi rift (Ebinger et al., 2019), associated with many hot springs, the poorly magmatic Lake Tanganyika rift has very few surface geothermal manifestations (ARGeo, 2021) and is generally

characterized by relatively elevated but discontinuous heat flow zones (anomalies to the west and further northwest of anomaly 6, respectively). The central heat flow anomaly (northwest of anomaly 6) is the largest and corresponds to the contact between the Paleoproterozoic Ubendian and Mesoproterozoic Kibaran mobile belts which is reactivated by the EARS by the Mungese shear zone which extends southeast in the Rukwa rift. The highest heat flow values of 154 mW/m$^2$, measured from shallow boreholes drilled at the bottom of Lake Tanganyika, are within this anomaly and confirm our estimations. Along the Malawi rift, our results indicate a region of relatively high heat flow at the northern part of Lake Nyasa corresponding to the hot springs and uniform distribution of relatively deep CPDs in the central part associated with low heat flow. According to Njinju et al., 2019, the regions of highest heat flow (70-82 mW/m$^2$) in the Malawi rift zone are concentrated within the Permo-Triassic Karroo rift basins that, in Tanzania, correspond to anomaly 8 and 9 which lie along the Ruhuhu basin at the Proterozoic collision boundaries, as already mentioned.

The low heat flow between anomalies 2 and 3, associated with the dormant volcanoes, Mt. Kilimanjaro and Mt. Meru in northeast Tanzania, may be a computational artefact related to the resolution in the data window that includes the volcanoes and the surrounding areas and/or it may be related to extensive alteration of the rocks that eliminated magnetic minerals. Neither the Kilimanjaro nor Meru volcanoes demonstrate shallow CPD or elevated thermal anomalies (e.g., profile PL 1 in Fig. 9) and there are no surface geothermal manifestations other than the volcanoes itself. The question is whether the surrounding lithosphere is thick and cold, or if the volcanoes are associated with localized deep structures enhancing the rise of local plumes. The former is supported by the large crustal thickness based on seismic receiver function analysis. Thick crust between 37 and 40 km is common beneath the areas surrounding the volcanoes compared to the relatively thinner crust between 29 and 32 km along the rift axis (Last et al., 1997; Dugda et al., 2005; Plasman et al., 2017).

## 6. Conclusion

We have used the inversion of the radially averaged power spectra of the magnetic anomalies to estimate the Curie point depth of the magnetic sources, geothermal gradient and surface heat flow in Tanzania. We found that the high heat flow anomalies often correspond to shallow Moho and are generally found where the Proterozoic collision boundaries underwent tectonic and thermal reactivation by the EARS.

High heat flow is observed along the EARS at the north Tanzania divergence zone (NTDZ) of the eastern branch, while in the western branch it is observed in the Rukwa rift and at the Rungwe Volcanic Province (RVP) located at the triple junction of the eastern and western branches of the EARS and Malawi rift. The high heat flow values in the RVP and in the NTDZ are due to Cenozoic magmatism in the EARS which is caused by thinning of the crust and mantle elevation as a result of crustal extension.

The unexpectedly wide zone of high heat flow to the south of Lake Victoria in the Archean craton is associated with the African mantle superplume which originates from the mantle-core boundary to the base of the craton where it forms two convective cells that drive the opening of the eastern and western branches of the EARS. Radiogenic heat production from Uranium deposits and K-rich granites in the area do not appear to contribute significantly to the regional heat flow. Low heat flow values are seen in the central part of the Archean craton and away from the suture zones of the Proterozoic mobile belts.

Our findings have revealed unexplored geothermal potentials along i) the Proterozoic collision boundaries reactivated by the EARS, ii) the RVP and iii) NTDZ.

## CRediT authorship contribution statement

**Makoye Mabula Didas:** Conceptualization, Methodology, Software, Formal analysis, Writing – original draft, Writing – review & editing. **Egidio Armadillo:** Conceptualization, Methodology, Data curation, Resources, Writing – review & editing. **Gylfi Páll Hersir:** Funding acquisition, Project administration, Writing – review & editing, Supervision, Resources, Conceptualization. **William Cumming:** Resources, Writing – review & editing, Supervision, Conceptualization. **Daniele Rizzello:** Supervision, Writing – review & editing.

## Declaration of Competing Interest

The authors declare that they have no known competing financial interests or personal relationships that could have appeared to influence the work reported in this paper.

## Acknowledgments

This research was financially supported by the GRÓ Geothermal Training Programme in Iceland (GRÓ GTP) under the auspices of UNESCO (formerly UNU-GTP). It is a part of the PhD programme of the first author carried out at the University of Iceland. Their support is greatly acknowledged. The aeromagnetic data were provided by the Geological Survey of Tanzania (GST) in collaboration with the Tanzania Geothermal Development Company (TGDC) as a part of the geothermal exploration database in Tanzania. The public data, Global CPD are from https://www.nature.com a product work by Li et al. (2017), SRTM-DEM data are the product of USGS available at https://lpdaac.usgs.gov and the Crustal thickness from https://igppweb.ucsd.edu/~gabi/crust1.html the product of Laske et al. (2013). The Tanzania Geothermal Development Company (TGDC) is thanked for its continuous support in facilitating this work as well as the PhD study of the first author. We thank Juan Luis Carrillo-de la Cruz for providing MAGCPD software used for CPD estimations. We are thankful to PhD committee members, Ásdís Benediktsdóttir and Halldór Geirsson for useful discussions, insights and reviews during this study. Finally, Dr. Craig Miller is acknowledged for his careful review of the manuscript; constructive and most useful comments.

## References

Alexander, K., Cumming, W.B., Malini, L., 2016. Technical review of geothermal potential of ngozi and songwe geothermal prospects. In: Proceedings of the 6th African Rift Geothermal Conference. Addis Ababa, Ethiopia.

Andres, J., Marzan, I., Ayarza, P., Martí, D., Palomeras, I., Torne, M., Campbell, S., Carbonell, R., 2018. Curie point depth of the Iberian Peninsula and surrounding margins. A thermal and tectonic perspective of its evolution. J. Geophys. Res. Solid Earth 123, 2049–2068. https://doi.org/10.1002/2017JB014994.

Armadillo, E., Rizzello, D., Pasqua, C., Pisani, P., Ghirotto, A., Didas, M., et al., 2020. Geophysical constraints on the Luhoi (Tanzania) geothermal conceptual model. Geothermics 87, 101875. https://doi.org/10.1016/j.geothermics.2020.101875.

Asefa, J., Ayele, A., 2020. Complex tectonic deformation in circum-Tanzania craton: East African rift system. J. Afr. Earth Sci. 170, 103893 https://doi.org/10.1016/j.jafrearsci.2020.103893.

Audet, P., Gosselin, M.J., 2019. Curie depth estimation from magnetic anomaly data: are-assessment using multitaper spectral analysis and Bayesian inference. Geophys. J. Int. 218, 494–507. https://doi.org/10.1093/gji/ggz166.

Baker, B.H., Mitchell, J.G., Williams, L.A.J., 1988. Stratigraphy, geochronology and volcano-tectonic evolution of the Kedong-Naivasha-Kinangop region, Gregory rift valley, Kenya. J. Geol. Soc. Lond. 145, 107–116. https://doi.org/10.1144/gsjgs.145.1.0107.

Bansal, A.R., Dimri, V.P., 1999. Gravity evidence for mid crustal domal structure below Delhi fold belt and Bhilwara super group of western India. Geophys. Res. Letters 26, 2793–2795. https://doi.org/10.1029/1999GL005359.

Bansal, A.R., Dimri, V.P., 2001. Depth estimation from the scaling power spectral density of nonstationary gravity profile. Pure Appl. Geophys. 158, 799–812. https://doi.org/10.1007/PL00001204.

Bansal, A.R., Dimri, V.P., 2005. Depth determination from nonstationary magnetic profile for scaling geology. Geophys. Prospect. 53, 399–410. https://doi.org/10.1111/j.1365-2478.2005.00480.x.

Bansal, A.R., Dimri, V.P., Sagar, G.V., 2006. Depth estimation from gravity data using the maximum entropy method (MEM) and multi taper method (MTM). Pure Appl. Geophys. 163, 1417–1434. https://doi.org/10.1007/s00024-006-0080-8.

Bansal, A.R., Gabriel, G., Dimri, V.P., 2010. Power law distribution of susceptibility and density and its relation to seismic properties: an example from the German

continental deep drilling program. J. Appl. Geophys. 72, 123–128. https://doi.org/10.1016/j.jappgeo.2010.08.001.
Bansal, A.R., Gabriel, G., Dimri, V.P., Krawczyk, C.M., 2011. Estimation of the depth to the bottom of magnetic sources by a modified centroid method for fractal distribution of sources: an application to aeromagnetic data in Germany. Geophysics 76, 11–22. https://doi.org/10.1190/1.3560017.
Bhattacharya, B.K., Leu, L.K., 1975. Analysis of magnetic anomalies over yellowstone national park: mapping of curie point isothermal surface for geothermal reconnaissance. J. Geophys. Res. 80, 4461–4465. https://doi.org/10.1029/JB080i032p04461.
Blakely, R.J., 1995. Potential Theory in Gravity & Magnetic Applications. Cambridge Univ. Press.
Bouligand, C., Glen, J.M.G., Blakely, R.J., 2009. Mapping Curie temperature depth in the western United States with a fractal model for crustal magnetization. J. Geophys. Res. 114, B11104. https://doi.org/10.1029/2009JB006494.
Boniface, N., Appel, P., 2017. Stenian - Tonian and Ediacaran metamorphic imprints in the southern Paleoproterozoic Ubendian Belt, Tanzania: constraints from *in situ* monazite ages. J. Afr. Earth Sci. 133, 25–35. https://doi.org/10.1016/j.jafrearsci.2017.05.005.
Boniface, N., Schenk, V., Appel, P., 2012. Paleoproterozoic eclogites of MORBtype chemistry and three Proterozoic orogenic cycles in the Ubendian belt (Tanzania): evidence from monazite and zircon geochronology, and geochemistry. Precambrian Res. 192-195, 16–33. https://doi.org/10.1016/j.precamres.2011.10.007.
Boniface, N., 2019. An overview of the Ediacaran-Cambrian orogenic events at the southern margins of the Tanzania craton: implication for the final assembly of Gondwana. J. Afr. Earth Sci. 150, 123–130. https://doi.org/10.1016/j.jafrearsci.2018.10.015.
Borg, G., Krogh, T., 1999. Isotopic age data of single zircons from the Archean Sukumaland greenstone belt, Tanzania. J. Afr. Earth Sci. 29, 301–312. https://doi.org/10.1016/S0899-5362(99)00099-8.
Borrego, D., Nyblade, A.A., Accardo, N.J., Gaherty, J.B., Ebinger, C.J., Shillington, D.J., et al., 2018. Crustal structure surrounding the northern Malawi rift and beneath the Rungwe Volcanic Province, East Africa. Geophys. J. Int. 215, 1410–1426. https://doi.org/10.1093/gji/ggy331.
Brown, R.J., Manya, S., Buisman, I., Fontana, G., Field, M., Mac Niocaill, C., Stuart, F.M., 2012. Eruption of Kimberlite magmas: physical volcanology, geomorphology and age of the youngest kimberlitic volcanoes known on earth (the upper Pleistocene/Holocene Igwisi Hills volcanoes, Tanzania). Bull. Volcanol. 74 (7), 1621–1643. https://doi.org/10.1007/s00445-012-0619-8.
Bumby, A.J., Guiraud, R., 2005. The geodynamic setting of the Phanerozoic basins of Africa. J. Afr. Earth Sci. 43, 1–12. https://doi.org/10.1016/j.jafrearsci.2005.07.016.
Bussert, R., Heinrich, W.D., Aberhan, M., 2009. The Tendaguru formation (late Jurassic to early cretaceous, Southern Tanzania): definition, palaeoenvironments, and sequence stratigraphy. Foss. Rec. 12, 141–174. https://doi.org/10.1002/mmng.200900004.
Carrillo-de la Cruz, J.L., Prol-Ledesma, R.M., Gomez-Rodríguez, D., Rodríguez-Díaz, A. A., 2020a. Analysis of the relation between bottom hole temperature data and Curie temperature depth to calculate geothermal gradient and heat flow in Coahuila. Mexico. Tectonophysics 780, 228397. https://doi.org/10.1016/j.tecto.2020.228397.
Carrillo-de la Cruz, J.L., Prol-Ledesma, R.M., Veľ azquez-Sanchez, P., Gomez- Rodríguez, D., 2020b. MAGCPD: a MATLAB-based GUI to calculate the Curie point- depth involving the spectral analysis of aeromagnetic data. Earth Sci. Inf. 13, 1539–1550. https://doi.org/10.1007/s12145-020-00525-x.
Carrillo-de la Cruz, J.L., Prol-Ledesma, M.R., Gabriel, G., 2021. Geostatistical mapping of the depth to the bottom of magnetic sources and heat flow estimations in Mexico. Geothermics 97, 102225. https://doi.org/10.1016/j.geothermics.2021.102225.
Chandrasekhar, V., Omenda, P., Chandrasekharam, D., 2014. High heat generating granites of Tanzania. In: Proceedings of the 5th African Rift Geothermal Conference Arusha. Tanzania.
Chiozzi, P., Matsushima, J., Okubo, Y., Pasquale, V., Verdoya, M., 2005. Curie-point depth from spectral analysis of magnetic data in Central–Southern Europe. Phys. Earth Planet. Inter. 152 (4), 267–276. https://doi.org/10.1016/j.pepi.2005.04.005.
Didas, M.M, 2016. Geophysical Investigation of the Subsurface Structures of the Mandawa basin, Southeast Coastal Tanzania. University of Dar es Salaam, p. 170. MSc. Thesis (unpublished.
Didas, M.M., Hersir, G.P., 2020. 1D joint inversion of MT and TEM data from Ngozi geothermal prospect, southwest Tanzania. An integrated interpretation of geoscientific results. In: Proceedings of the World Geothermal Congress 2020+1. Reykjavik, Iceland.
Dimri, V.P., Dimri, V.P., 2000. Crustal fractal magnetization. Application of Fractals in Earth Sciences. A. A. Balkema/Oxford and IBH Publishing Co., pp. 89–95. ISBN 9789054102847.
Dimri, V.P., Bansal, A.R., Srivastava, R.P., Vedanti, N., Mahadevan, T.M., Arora, B.R., Gupta, K.R., 2003. Scaling behaviour of real earth source distribution: Indian case studies. Indian Continental Lithosphere: Emerging Research Trends. Geological Society India Memoir, pp. 431–448, 53.
Dolmaz, M.N., Ustaomer, T., Hisarli, Z.M., Orbay, N., 2005. Curie point depth variations to infer thermal structure of the crust at the African-Eurasian convergence zone, SW Turkey. Earth Planets Space 57, 373–383. https://doi.org/10.1186/BF03351821.
Dugda, M.T., Nyblade, A.A., Julia, J., Langston, C.A., Ammon, C.J., Simiyu, S., 2005. Crustal structure in Ethiopia and Kenya from receiver function analysis: implications for rift development in eastern Africa. J. Geophys. Res. 110, (B)01303. https://doi.org/10.1029/2004JB003065, 2005.
Dziadek, R., Ferraccioli, F., Gohl, K., 2021. High geothermal heat flow beneath Thwaites Glacier in West Antarctica inferred from aeromagnetic data. Commun. Earth Environ. https://doi.org/10.1038/s43247-021-00242-3.
Ebinger, C.J., Poudjom, Y., Mbede, E., Foster, F., Dawson, J., 1997. Rifting archean lithosphere: the Eyasi–Manyara–Natron rifts, East Africa. J. Geol. Soc. Lond. 154, 947–960. https://doi.org/10.1144/gsjgs.154.6.0947.
Ebinger, C., 1989. Tectonic development of the western branch of the East Africa rift system. Bull. Seismol. Soc. Am. 101, 885–903. https://doi.org/10.1130/0016-7606(1989)101<0885:TDOTWB>2.3.CO;2.
Ebinger, C.J., Oliva, S.J., Pham, T.-Q., Peterson, K., Chindandali, P., Illsley-Kemp, F., et al., 2019. Kinematics of active deformation in the Malawi rift and Rungwe Volcanic Province, Africa. Geochem. Geophys. Geosyst. 20, 3928–3951. https://doi.org/10.1029/2019GC008354.
Ebinger, C.J., Keir, D., Bastow, I.D., Whaler, K., Hammond, J.O.S., Ayele, A., Hautot, S., 2017. Crustal structure of active deformation zones in Africa: implications for global crustal processes. Tectonics 36, 3298–3332. https://doi.org/10.1002/2017TC004526.
Fadaie, K., Ranalli, G., 1990. Rheology of the lithosphere in the East African rift system. Geophys. J. Int. 102, 445–453. https://doi.org/10.1111/j.1365-246X.1990.tb04476.x.
Fontijn, K., Williamson, D., Mbede, E., Ernst, G.G.J., 2012. The Rungwe volcanic province, Tanzania-a review. J. Afr. Earth Sci. 63, 12–31. https://doi.org/10.1016/j.jafrearsci.2011.11.005.
Foster, A., Ebinger, C., Mbede, E., Rex, D., 1997. Tectonic development of the northern Tanzania sector of the East African rift system. J. Geol. Soc. Lond. 154, 689–700. https://doi.org/10.1144/gsjgs.154.4.0689.
Fritz, H., Abdelsalam, M., Ali, K., Bingen, B., Collins, A., Fowler, A., et al., 2013. Orogen styles in the East African orogen: a review of the Neoproterozoic to Cambrian tectonic evolution. J. Afr. Earth Sci. 86, 65–106. https://doi.org/10.1016/j.jafrearsci.2013.06.004.
Grijalva, A., Nyblade, A.A., Homman, K., Accard, N.J., Gaherty, J.B., Ebinger, C.J., Mulibo, G., 2018. Seismic evidence for plume-and craton-influenced upper mantle structure beneath the Northern Malawi rift and the Rungwe Volcanic Province, East Africa. Geochem. Geophys. Geosyst. 19 (10), 3980–3994. https://doi.org/10.1029/2018GC007730.
Hay, D.E., Wendlandt, R.F., Keller, G.R., 1995. The origin of Kenya rift plateau-type flood phonolites: integrated petrologic and geophysical constraints on the evolution of the crust and upper mantle beneath the Kenya rift. J. Geophys. Res. 100, 5435–5444. https://doi.org/10.1029/94JB03036.
ARGeo. (n.d.). Home, 2021. ARGeo AGID Database August 2021. https://agid.theargeo.org/.
Hersir, G.P., Kristinsson, S.G., Mnjokava, T., 2015. Tanzania Visit in January 2015. Assessment of Areas for Surface Exploration Studies and Training Needs. Internal Report Prepared for TGDC with Funding from ICEIDA. Iceland GeoSurvey, Report number ÍSOR-2015/025. 48pp.
Hinz, N., Cumming, W.B., Sussman, D., 2018. Exploration of fault-related deep-circulation geothermal resources in the western branch of the East African rift system: examples from Uganda and Tanzania. In: Proceedings of the 7th African Rift Geothermal Conference. Kigali, Rwanda.
Hochstein, M.P., Temu, E.B., Moshy, C.M.A, 2000. Geothermal resources of Tanzania. In: Proceedings of the World Geothermal Congress. Kyushu-Tohoku, Japan.
Hodgson, I., Illsley-Kemp, F., Gallacher, R.J., Keir, D., Ebinger, C.J., Mtelela, K., 2017. Crustal structure at a young continental rift: a receiver function study from the Tanganyika Rift. Tectonics 36 (12), 2806–2822. https://doi.org/10.1002/2017TC004477.
Hu, S., He, L., Wang, J., 2000. Heat flow in the continental area of China: a new data set. Earth Planet. Sci. Lett. 179 (2), 407–419. https://doi.org/10.1016/S0012-821X(00)00126-6.
Hunt, C.P., Moskowitz, B.M., Banerjee, S.K., 1995. Magnetic properties of rocks and minerals. Rock Physics & Phase Relations: A Handbook of Physical Constants, vol. 3. T. J. Ahrens, Ed., Washington, DC, USA: AGU Ref. Shelf, pp. 189–204. https://doi.org/10.1029/RF003p0189.
Hussein, M., Mickus, K., Serpa, L.F., 2013. Curie point depth estimates from aeromagnetic data from death valley and surrounding regions, California. Pure Appl. Geophys. 170 (4), 617–632. https://doi.org/10.1007/s00024-012-0557-6.
Kabaka, K.T., Mnjokava, T.T., Kajugus, S.I., 2016. Geothermal development in Tanzania, a country update. In: Proceedings of the 6th African Rift Geothermal Conference. Addis Ababa, Ethiopia.
Kabete, J.M., Groves, D.I., McNaughton, N.J., Mruma, A.H., 2012a. A new tectonic and temporal framework for the Tanzanian shield: implications for gold metallogeny and undiscovered endowment. Ore Geol. Rev. 48, 88–124. https://doi.org/10.1016/j.oregeorev.2012.02.009.
Kabete, J.M., McNaughton, N.J., Groves, D.I., Mruma, A.H., 2012b. Reconnaissance SHRIMP U–Pb zircon geochronology of the Tanzania craton: evidence for Neoarchean granitoid–greenstone belts in the central Tanzania region and the Southern East African Orogen. Precambrian Res. 216–219, 232–266. https://doi.org/10.1016/j.precamres.2012.06.020.
Kachingwe, M., Nyblade, A., Julia, J., 2015. Crustal structure of precambrian terranes in the southern African subcontinent with implications for secular variation in crustal genesis. Geophys. J. Int. 202, 533–547. https://doi.org/10.1093/gji/ggv136.
Kagya, M.L., 1996. Geochemical characterization of Triassic petroleum source rock in the Mandawa basin, Tanzania. J. Afr. Earth Sci. 23, 73–88. https://doi.org/10.1016/S0899-5362(96)00053-X.
Kalberkamp, U., Schaumann, G., Ndonde, P.B., Chiragwile, S.A., Mwano, J.M, GEOTHERM Working Group, 2010. Surface exploration of a viable geothermal

resource in Mbeya area, SW Tanzania. In: Part III: Geophysics. Proceedings of the World Geothermal Congress 2010. Bali, Indonesia.
Kanda, I., Fujimitsu, Y., Nishijima, J., 2019. Geological structures controlling the placement and geometry of heat sources within the Menengai geothermal field, Kenya as evidenced by gravity study. Geothermics 79, 67–81. https://doi.org/10.1016/j.geothermics.2018.12.012.
Kasoga, K.F., Mwalongo, D.A., Sawe, S.F., Nyaruba, M.M., Dammalapati, U., 2015. Ambient gamma dose rate measurements at Manyoni uranium deposits, Singida, Tanzania. In: Proceedings of SAIP2015. ISBN: 978-0-620-70714-5.
Kelemework, Y., Fedi, M., Milano, M., 2021. A review of spectral analysis of magnetic data for depth estimation. Geophysics 86 (6), J33. https://doi.org/10.1190/geo2020-0268.1.
Kent, P.E., Hunt, J.A., Johnstone, D.W., 1971. The Geology and Geophysics of Coastal Tanzania. Her Majesty's Stationary Office (HMSO), London. Geophysical Paper N. 6. ISBN 0118801384.
Kröner, A., Muhongo, S., Hegner, E., Wingate, M., 2003. Single-zircon geochronology and Nd isotopic systematics of Proterozoic high-grade rocks from the Mozambique Belt of southern Tanzania (Masasi area): implications for Gondwana assembly. J. Geol. Soc. 160, 745–757. https://doi.org/10.1144/0016-764901-170.
Kumar, R., Bansal, A.R., Ghods, A., 2020. Estimation of depth to bottom of magnetic sources using spectral methods: application on Iran's aeromagnetic data. J. Geophys. Res. Solid Earth 125 (3). https://doi.org/10.1029/2019JB018119.
Kumar, R., Bansal, A.R., Betts, P.G., Ravat, D., 2021. Re-assessment of the depth to the base of magnetic sources (DBMS) in Australia from aeromagnetic data using the defractal method. Geophys. J. Int. 225, 530–547. https://doi.org/10.1093/gji/ggaa601.
Kuria, Z.N., Woldai, T., van der Meer, F.D., Barongo, J.O., 2010. Active fault segments as potential earthquake sources: inferences from integrated geophysical mapping of the Magadi fault system, Southern Kenya rift. J. African Earth Sci. 57-4, 345–359. https://doi.org/10.1016/j.jafrearsci.2009.11.004.
Last, R., Nyblade, A., Langston, C., Owens, T., 1997. Crustal structure of the east African plateau from receiver functions and Rayleigh wave phase velocities. J. Geophys. Res. Solid Earth 102, 24469–24483. https://doi.org/10.1029/97JB02156.
Laske, G., Masters, G., Ma, Z., Pasyanos, M.E. 2013. Update on CRUST1.0: A 1-degree Global Model on Earth's Crust. Poster EGU2013-2658.
Le Gall, B., Gernigon, L., Rolet, J., Ebinger, C., G loaguen, R., Nilsen, O., Mruma, A., 2004. Neogene-Holocene rift propagation in central Tanzania: morphostructural and aeromagnetic evidence from the Kilombero area. Bull. Geol. Soc. Am. 116 (3-4), 490–510. https://doi.org/10.1130/B25202.1.
Lee, W.H., Uyeda, S., 1965. Review of heat flow data. Terr. Heat Flow 8, 87–190. https://doi.org/10.1029/GM008p0087.
Lenoir, J.L., Liegois, J.P., Theunissen, K., Klerkx, J., 1994. The Palaeoproterozoic Ubendian shear belt in Tanzania: geochronology and structure. J. Afr. Earth Sci. 19 (3), 169–184. https://doi.org/10.1016/0899-5362(94)90059-0.
Li, C.-F., Wang, J., Lin, J., Wang, T., 2013. Thermal evolution of the North Atlantic lithosphere: new constraints from magnetic anomaly inversion with a fractal magnetization model. Geochem. Geophys. Geosyst. 14 (12), 5078–5105. https://doi.org/10.1002/2013GC004896.
Li, C-F., Lu, Y., Wang, J., 2017. A global reference model of curie-point depths based on EMAG2. Sci Rep. 7, 45129. https://doi.org/10.1038/srep45129.
Li, CF., Zhou, D., Wang, J., 2019. On application of fractal magnetization in Curie depth estimation from magnetic anomalies. Acta Geophys. 67, 1319–1327. https://doi.org/10.1007/s11600-019-00339-6.
Liang, W., Li, J., Xu, X., Zhang, S., Zhao, Y., 2020. A high-resolution earth's gravity field model SGG-UGM-2 from GOCE, GRACE, satellite altimetry, and EGM2008. Geodesy Surv. Eng. 6, 860–878. https://doi.org/10.1016/j.eng.2020.05.008.
Lösing, M., Ebbing, J., Szwillus, W., 2020. Geothermal heat flux in Antarctica: assessing models and observations by Bayesian inversion. Front. Earth Sci. https://doi.org/10.3389/feart.2020.00105.
Lysak, S.V., 1987. Terrestrial heat flow of continental rifts. Tectonophysics 143 (1–3), 31–41. https://doi.org/10.1016/0040-1951(87)90076-X.
Manya, S., 2011. Nd-isotopic mapping of the Archaean–Proterozoic boundary in southwestern Tanzania: Implication for the size of the Archaean Tanzania Craton. Gondwana Res 20 (2011), 325–334. https://doi.org/10.1016/j.gr.2011.01.002.
Manya, S., 2001. Geochemical Investigation of Archaean Greenstones in the Rwamagaza Area, North-Western Tanzania. University of Dar-es-Salaam. M.Sc. Thesis.
Manya, S., Maboko, M.A.H., 2003. Dating basaltic volcanism in the Neoarchean Sukumaland Greenstone Belt of the Tanzania Craton using Sm–Nd method: implications for the geological evolution of the Tanzania Craton. J. Afr. Earth Sci. 121, 35–45. https://doi.org/10.1016/S0301-9268(02)00195-X.
Martos, Y.M., Catalan, M., Jordan, T.A., Golynsky, A., Golynsky, D., Eagles, G., Vaughan, D.G., 2017. Heat flux distribution of Antarctica unveiled. Geophys. Res. Lett. 44 (22), 11417–11426. https://doi.org/10.1002/2017GL075609.
Martos, Y.M., Jordan, T.A., Catalan, M., Jordan, T.M., Bamber, J.L., Vaughan, D.G., 2018. Geothermal heat flux reveals the Iceland hotspot track underneath Greenland. Geophys. Res. Lett. 45 (16), 8214–8222. https://doi.org/10.1029/2018GL078289.
Martos, Y.M, Catalán, M., Galindo-Zaldivar, J., 2019. Curie depth, heat flux, and thermal subsidence reveal the Pacific mantle outflow through the Scotia Sea. J. Geophys. Res. Solid Earth 124, 10735–10751. https://doi.org/10.1029/2019JB017677.
Mather, B., Fullea, J., 2019. Constraining the geotherm beneath the British Isles from Bayesian inversion of Curie depth: integrated modelling of magnetic, geothermal, and seismic data. Solid Earth 10, 839–850. https://doi.org/10.5194/se-2019-9.
Maus, S., Dimri, V.P., 1995. Potential field power spectrum inversion for scaling geology. J. Geophys. Res. 100 (B7), 12605–12616. https://doi.org/10.1029/95JB00758.
Maus, S., Gordon, D., Fairhead, J.D., 1997. Curie temperature depth estimation using a self-similar magnetization model. Geophys. J. Int. 129, 163–168. https://doi.org/10.1111/j.1365-246X.1997.tb00945.x.
Meert, J.G., Lieberman, B.S., 2008. The Neoproterozoic assembly of Gondwana and its relationship to the Ediacaran-Cambrian radiation. Gondwana Res 14, 5–21. https://doi.org/10.1016/j.gr.2007.06.007.
Meyer, B., Saltus, R., Chulliat, A., 2017. EMAG2: Earth Magnetic Anomaly Grid (2-Arcminute Resolution) Version 3. National Centers for Environmental Information, NOAA. https://doi.org/10.7289/V5H70CVX.
Mbia, P.K., Mortensen, A.K., Oskarsson, N., Hardarson, B.S., 2015. Sub-surface geology, petrology and hydrothermal alteration of the menengai geothermal field, Kenya: case study of wells MW-02, MW-04, MW-06 and MW-07. In: Proceedings of the World Geothermal Congress 2015. Melbourne, Australia.
Mnjokava, T., Kabaka, K., Mayalla, J., 2015. Geothermal development in Tanzania – a country update. In: Proceedings of the World Geothermal Congress 2015. Melbourne, Australia.
Mole, D.R., Barnes, S.J., Taylor, R.J., Kinny, P.D., Fritz, H., 2018. A relic of the Mozambique Ocean in south-east Tanzania. Precambrian Res. 305, 386–426. https://doi.org/10.1016/j.precamres.2017.10.009.
Möller, A., Mezger, K., Schenk, V., 2000. U-Pb dating of metamorphic minerals: PanAfrican metamorphism and prolonged slow cooling of high pressure granulites in Tanzania, East Africa. Precambrian Res. 104, 123–146. https://doi.org/10.1016/S0301-9268(00)00086-3.
Mpanda, S., 1997. Geological Development of the East African Coastal Basin of Tanzania. Stockholm University, Sweden. Ph.D. ThesisISBN:91-22-01756-9.
Mruma, A.H., 1995. Stratigraphy and palaeodepositional environment of the Palaeoproterozoic volcano-sedimentary Konse Group in Tanzania. J. Afr. Earth Sci. 21 (2), 281–290. https://doi.org/10.1016/0899-5362(95)00065-2.
Mshiu, E.E., Maboko, M.A.H., 2012. Geochemistry and petrogenesis of the late Archaean high-K granites in the southern Musoma-Mara Greenstone Belt: their influence in evolution of Archaean Tanzania Craton. J. Afr. Earth Sci. 66, 1–12. https://doi.org/10.1016/j.jafrearsci.2012.03.002.
Mulibo, G.D., Nyblade, A.A., 2013. The P and S wave velocity structure of the mantle beneath eastern Africa and the African superplume anomaly. Geochem. Geophys. Geosyst. 14 (8), 2696–2715. https://doi.org/10.1002/ggge.20150.
Mulibo, G.D., Nyblade, A.A., 2016. The seismotectonics of southeastern Tanzania: implications for the propagation of the eastern branch of the east African rift. Tectonophysics 674, 20–30. https://doi.org/10.1016/j.tecto.2016.02.009.
Nicholas, C.J., Pearson, P.N., McMillan, I.K., Ditchfield, P.W., Singano, J.M., 2007. Structural evolution of southern coastal Tanzania since the Jurassic. J. Afr. Earth Sci. 48, 273–297. https://doi.org/10.1016/j.jafrearsci.2007.04.003.
Njinju, E.A., Kolawole, F., Atekwana, E.A., Stamps, D.S., Atekwana, E.A., Abdelsalam, M. G., Mickus, K.L., 2019. Terrestrial heat flow in the Malawi rifted zone, East Africa: Implications for tectono-thermal inheritance in continental rift basins. J. Volcanol. Geotherm. Res. 387, 106656 https://doi.org/10.1016/j.jvolgeores.2019.07.023.
Nyabeze, P.K., Gwavava, O., 2016. Investigating heat and magnetic source depths in the Soutpansberg Basin, South Africa: exploring the Soutpansberg Basin geothermal field. Geotherm. Energy 4, 1–20. https://doi.org/10.1186/s40517-016-0050-z.
Nyblade, A.A., 1997. Heat flow across the East African plateau. Geophys. Res. Lett. 24 (16), 2083–2086. https://doi.org/10.1029/97GL01952.
Nyblade, A.A., Pollack, H.N., 1993. A global analysis of heat flow from Precambrian terrains: implications for the thermal structure of Archean and Proterozoic lithosphere. J. Geophys. Res. 98, 12207–12218. https://doi.org/10.1029/93JB00521.
Nyblade, A.A., Pollack, H.N., 1992. A gravity model for the lithosphere in western Kenya and northeastern Tanzania. Tectonophysics 212, 257–267. https://doi.org/10.1016/0040-1951(92)90294-G.
Nyblade, A.A., Pollack, H.N., Jones, D.L., Podmore, F., Mushayandebvu, M., 1990. Terrestrial heat flow in east and southern Africa. J. Geophys. Res. 95, 17371–17384. https://doi.org/10.1029/JB095iB11p17371.
Nwankwo, L.I., 2014. Discussion on: "Spectral analysis of aeromagnetic data for geothermal energy investigation of Ikogosi warm spring – Ekiti State, southwestern Nigeria". Geotherm. Energy 2, 11. https://doi.org/10.1186/s40517-014-0011-3.
O'Donnell, J., Adams, A., Nyblade, A.A., Mulibo, G.D., Tugume, F., 2013. The uppermost mantle shear wave velocity structure of eastern Africa from Rayleigh wave tomography: constraints on rift evolution. Geophys. J. Int. 194, 961–978. https://doi.org/10.1093/gji/ggt135.
Okubo, Y., Matsunaga, T., 1994. Curie point depth in northeast Japan and its correlation with regional thermal structure and seismicity. J. Geophys. Res. 99 (B11), 22363–22371. https://doi.org/10.1029/94JB01336.
Okubo, Y., Graf, R.J., Hansen, R.O., Ogawa, K., Tsu, H., 1985. Curie point depths of the island of Kyushu and surrounding area, Japan. Geophysics 50, 481–489. https://doi.org/10.1190/1.1441926.
Parker, R.L., 1973. The rapid calculation of potential anomalies. Geophys. J. Int. 31 (4), 447–455. https://doi.org/10.1111/j.1365-246X.1973.tb06513.x.
Parker, R.L., Huestis, S.P., 1974. The inversion of magnetic anomalies in the presence of topography. J. Geophys. Res. 79 (11), 1587–1593. https://doi.org/10.1029/JB079i011p01587.
Pilkington, M., Todoeschuck, J.P., 1993. Fractal magnetization of continental crust. Geophys. Res. Lett. 20 (7), 627–630. https://doi.org/10.1029/92GL03009.
Pilkington, M., Todoeschuck, J.P., 1990. Stochastic inversion for scaling geology. Geophys. J. Int. 102 (1), 205–217. https://doi.org/10.1111/j.1365-246X.1990.tb00542.x.
Pilkington, M., Todoeschuck, J.P., 2004. Power-law scaling behavior of crustal density and gravity. Geophys. Res. Lett. 31 (9), L09606. https://doi.org/10.1029/2004GL019883.

Plasman, M., Tiberi, C., Ebinger, C., Gautier, S., Albaric, J., Peyrat, S., Gama, R., 2017. Lithospheric low-velocity zones associated with a magmatic segment of the Tanzanian Rift, East Africa. Geophys. J. Int. 210, 465–481. https://doi.org/10.1093/gji/ggx177.

Quintero, W., Campos-Enŕquez, O., Hernandez, O., 2019. Curie point depth, thermal gradient, and heat flow in the Colombian Caribbean (northwestern South America). Geotherm. Energy 7 (1). https://doi.org/10.1186/s40517-019-0132-9.

Ravat, D., Pignatelli, A., Nicolosi, I., Chiappini, M., 2007. A study of spectral methods of estimating the depth to the bottom of magnetic sources from near-surface magnetic anomaly data. Geophys. J. Int. 169 (2), 421–434. https://doi.org/10.1111/j.1365-246X.2007.03305.x.

Reeves, C., De Wit, M., 2000. Making ends meet in Gondwana: retracing the transforms of the Indian Ocean and reconnecting continental shear zones. Terra Nova 12, 272–280. https://doi.org/10.1046/j.1365-3121.2000.00309.x.

Ray, L., Förster, H.J., Förster, A., Fuchs, S., Naumann, R., Appelt, O., 2015. Tracking the thermal properties of the lower continental crust: measured versus calculated thermal conductivity of high-grade metamorphic rocks (Southern Granulite Province, India). Geothermics 55, 138–149. https://doi.org/10.1016/j.geothermics.2015.01.007.

Represas, P., Catalão, J., Montesinos, F.G., Madeira, J., Mata, J., Antunes, C., Moreira, M., 2012. Constraints on the structure of Maio Island (Cape Verde) by a three-dimensional gravity model: imaging partially exhumed magma chambers. Geophys. J. Int. 190, 931–940. https://doi.org/10.1111/j.1365-246X.2012.05536.x.

Rizzello, D., Armadillo, E., Pasqua, C., Pisani, P., Mnjokava, T., Mwano, J., Didas, M., Tumbu, L., 2018. Three-dimensional geophysical modelling of Kiejo-Mbaka geothermal field, Tanzania. In: Proceedings of the ARGEO-C7 Geothermal Conference. Kigali, Rwanda, p. 14.

Ross, H.E., Blakely, R.J., Zoback, M.D., 2006. Testing the use of aeromagnetic data for the determination of Curie depth in California. Geophysics 71, L51–L59. https://doi.org/10.1190/1.2335572.

Salem, A., Green, C., Ravat, D., Singh, H.K., East, P., Fairhead, J., Morgen, D.S., Biegert, E., 2014. Depth to Curie temperature across the central Red Sea from magnetic data using the de-fractal method. Tectonophysics 624–625, 75–86. https://doi.org/10.1016/j.tecto.2014.04.027.

Saria, E., Calais, E., Stamps, D.S., Delvaux, D., Hartnady, C.H., 2014. Present-day kinematics of the East African rift. J. Geophys. Res. 119 (4), 1–17. https://doi.org/10.1002/2013JB010901.

Sclater, J.G., Jaupart, C., Galson, D., 1980. The heat flow through oceanic and continental crust and the heat loss of the Earth. Rep. Geophys. Space Phys. 18, 269–311. https://doi.org/10.1029/RG018i001p00269.

Simiyu, S.M., Keller, G.R., 2001. An integrated geophysical analysis of the upper crust of the southern Kenya rift. Geophys. J. Int. 147, 543–561. https://doi.org/10.1046/j.0956-540x.2001.01542.x.

Simiyu, S.M., Keller, G.R., 1997. Integrated geophysical analysis of the East African plateau from gravity and recent seismic studies. in stress and stress release in the Lithosphere, eds Fuchs, K., Altherr, R., Muller, B. & C., Prodehl Tectonophysics 278, 291–314. https://doi.org/10.1016/S0040-1951(97)00109-1.

Sommer, S., Kröner, A., 2013. Ultra-high temperature granulite-facies metamorphic rocks from the Mozambique Belt of SW Tanzania. Lithos 170, 117–143. https://doi.org/10.1016/j.lithos.2013.02.014.

Spector, A., Grant, F., 1970. Statistical models for interpreting aeromagnetic data. Geophysics 35 (2), 293–302. https://doi.org/10.1190/1.1440092.

Stamps, D.S., Saria, E., Kreemer, C., 2018. A geodetic strain rate model for the east African rift system. Sci. Rep. 8, 732. https://doi.org/10.1038/s41598-017-19097-w.

Stendal, H., Frei, R., Muhongo, S., Rasmussen, T.M., Mnali, S., Petro, F., Temu, E.B., 2004. Gold potential of the Mpanda mineral field, SW Tanzania: evaluation based on geological, lead isotopic and aeromagnetic data. J. Afr. Earth Sci. 38, 437–447. https://doi.org/10.1016/j.jafrearsci.2004.04.005.

Stern, R.J., 1994. Arc assembly and continental collision in Neoproterozoic East African Orogen: implications for the consolidation of Gondwanaland. Ann. Rev. Earth Planet. Sci. 22, 319–351. https://doi.org/10.1146/annurev.ea.22.050194.001535.

Stiefenhofer, J., Farrow, D.J., 2004. Geology of the Mwadui kimberlite, Shinyanga district, Tanzania. Lithos 76, 139–160. https://doi.org/10.1016/j.lithos.2004.04.017.

Tanaka, A., Okubo, Y., Matsubayashi, O., 1999. Curie point depth based on spectrum analysis of the magnetic anomaly data in East and Southeast Asia. Tectonophysics 306, 461–470. https://doi.org/10.1016/S0040-1951(99)00072-4.

TGDC-Tanzania Geothermal Development Company, 2020. Geoscientific Investigation Report for the Ibadakuli Geothermal Prospect, Tanzania. TGDC-Tanzania Geothermal Development Company, p. 44. TGDC Technical internal report (unpublished.

Thomas, R.J., Spencer, C., Bushi, A.M., Baglow, N., Boniface, N., de Kock, G., Horstwood, M.S., et al., 2016. Geochronology of the central Tanzania Craton and its southern and eastern orogenic margins. Precambrian Res. 277, 47–67. https://doi.org/10.1016/j.precamres.2016.02.008.

Thomas, R.J., Bushi, A.M., Roberts, N.M., Jacobs, J., 2014. Geochronology of granitic rocks from the Ruangwa region, southern Tanzania – links with NE Mozambique and beyond. Precambrian Res. 100, 70–80. https://doi.org/10.1016/j.jafrearsci.2014.06.012.

Tiberi, C., Gautier, S., Ebinger, C., Roecker, S., Plasman, M., Albaric, J., Deverch, J., et al., 2019. Lithospheric modification by extension and magmatism at the craton-orogenic boundary: North Tanzania divergence, East Africa. Geophys. J. Int. 216, 1693–1710. https://doi.org/10.1093/gji/ggy521.

TPDC-Tanzania Petroleum Development Company, 2021. Gas Discoveries. TPDC-Tanzania Petroleum Development Company. https://www.tpdc.co.tz/gasdiscoveries.php.

Tugume, F., Nyblade, A., Julia, J., 2012. Moho depths and Poisson's ratios of Precambrian crust in East Africa: evidence for similarities in Archean and Proterozoic crustal structure. Earth planet. Sci. Lett. 355, 73–81. https://doi.org/10.1016/j.epsl.2012.08.041.

Witter, B.J., Miller, A.C., Friend, M., Colpron, M., 2018. Curie point depths and heat production in Yukon, Canada. In: Proceedings of the 43rd Workshop on Geothermal Reservoir Engineering.

Wölbern, I., Rumpker, G., Schumann, A., Muwanga, A., 2010. Crustal thinning beneath the Rwenzori region, Albertine rift, Uganda, from receiver-function analysis. Int. J. Earth Sci. 99, 1545–1557. https://doi.org/10.1007/s00531-009-0509-2.

Wopfner, H., 2002. Tectonic and climatic events controlling deposition in Tanzanian Karoo basins. J. Afr. Earth Sci. 34, 167–177. https://doi.org/10.1016/S0899-5362(02)00016-7.

## Further readings

Abraham, E.M, Lawal, K.M., Ekwe, A.C., Alile, O., Murana, K.A., Lawal, A.A., 2014. Spectral analysis of aeromagnetic data for geothermal energy investigation of Ikogosi Warm Spring - Ekiti State, southwestern Nigeria. Geothermal Energy 2, 1–21. https://doi.org/10.1186/s40517-014-0006-0.

Amante, C., Eakins, B.W., 2009. ETOPO1 1 arc-minute global relief model: procedures, data sources and analysis. NOAA Technical Memorandum NESDIS NGDC-24. National Geophysical Data Center, Marine Geology and Geophysics Division, Boulder, Colorado. https://repository.library.noaa.gov/view/noaa/1163.

, UN Environment Africa Geothermal Inventory Database (AGID). https://agid.theargeo.org/countries.php.

Laske, G., Masters, G., Ma, Z., Pasyanos, M.E., 2013. Update on CRUST1.0 - A 1- degree global model of Earth's crust. EGU General Assembly 15, EGU2013–2658. Retrieved from http://meetingorganizer.copernicus.org/EGU2013/EGU2013-2658.pdf.

Plasman, M., Tiberi, C., Ebinger, C., Gautier, S., Albaric, J., Peyrat, S., Gama, R., 2017. Lithospheric low-velocity zones associated with a magmatic segment of the Tanzanian Rift, East Africa. Geophys. J. Int. 210 (1), 465–481. https://doi.org/10.1093/gji/ggx177.

# Paper II

**New MT surveys and 3D resistivity imaging beneath the Ngozi-Rungwe volcanoes at the triple rift junction of the East African Rift System in SW Tanzania: Support for integrated interpretations of geothermal conceptual models.**

**Makoye M. Didas,** Egidio Armadillo, Gylfi Páll Hersir, William Cumming, Daniele Rizzello, Ásdís Benediktsdóttir, Halldór Geirsson.

The paper published in Geothermics: https://doi.org/10.1016/j.geothermics.2023.102893

Geothermics 118 (2024) 102893

Contents lists available at ScienceDirect

Geothermics

journal homepage: www.elsevier.com/locate/geothermics

# New MT surveys and 3D resistivity imaging beneath the Ngozi-Rungwe volcanoes at the triple rift junction of the East African Rift System in SW Tanzania: Support for integrated interpretations of geothermal conceptual models

Makoye Mabula Didas [a,f,g,*], Egidio Armadillo [b], Gylfi Páll Hersir [c], William Cumming [d], Daniele Rizzello [e], Ásdís Benediktsdóttir [h], Halldór Geirsson [f]

[a] Tanzania Geothermal Development Company Ltd (TGDC), P. O. Box: 14801, Ursino House No. 25, Dar es Salaam, Tanzania
[b] Applied Geophysics Laboratory, DISTAV, University of Genoa, Italy
[c] Independent Researcher, Reykjavik, Iceland, formerly at Iceland GeoSurvey (ÍSOR), Urdarhvarf 8, Kopavogur IS-203, Iceland
[d] Cumming Geoscience, Santa Rosa, CA, USA
[e] Tellus S.A.S., Italy
[f] Faculty of Earth Sciences, University of Iceland, Sturlugata 7, Reykjavík 101, Iceland
[g] GRÓ GTP, Urdarhvarf 8, Kópavogur IS-203, Iceland
[h] Reykjavík Energy, Bæjarhálsi 1, 110 Reykjavík, Iceland, formerly at Iceland GeoSurvey (ÍSOR), Urdarhvarf 8, Kopavogur IS-203, Iceland

ARTICLE INFO

*Keywords:*
Rungwe Volcanic Province
Magnetotelluric
3D MT inversion
Ngozi-Rungwe Fracture Zone
Rungwe-Ngozi Conductive Anomaly
Usangu Conductive Anomaly

ABSTRACT

The geothermal system related to the Ngozi and Rungwe volcanoes, SW Tanzania, lies at the intersection of the west and east branches of the East African Rift System and has been investigated by many geoscientists for decades. Here we present a 3D electrical resistivity model based on 190 magnetotelluric resistivity soundings that have been integrated with geochemical and geological results to support the development of the geothermal resource conceptual model presented here. The model includes two separate reservoirs, a larger system located beneath the Rungwe volcano and a smaller chloride water reservoir located under the Ngozi caldera, which contains a neutral chloride hot spring with geothermometry >230°C. An extensive conductive clay cap with variable thickness extends along the 30 km long NW-SE trending Ngozi-Rungwe Fault Zone from the Kiejo area SE of the Rungwe volcano to the Ngozi caldera. The absence of geothermal surface manifestations directly over the inferred Rungwe upflow zone is consistent with effective sealing of the proposed underlying geothermal reservoir by the clay cap. The scarcity of thermal manifestations on the up-dip margins of the low-resistivity clay cap can be explained by coincidence of the base of the clay cap with impermeable Precambrian formations and by structural boundaries. This interpretation implies that the area with the highest geothermal resource potential is the Rungwe volcano where proposed drilling sites might intersect the proposed high-temperature reservoir.

## 1. Introduction

The Ngozi geothermal prospect which is the northern part of the combined Ngozi-Rungwe prospect area considered in this study, has previously been interpreted as a high-temperature magmatically heated geothermal system (Alexander et al., 2016; Didas and Hersir, 2021) that has been considered to be the most promising geothermal prospect in Tanzania (Kajugus et al., 2021). The combined prospect lies within the Rungwe Volcanic Province (RVP) (Fontijn et al., 2012), located in the Mbeya Region at the triple rift junction formed by the intersection of the south-Rukwa-north-Malawi (Nyasa) and south Usangu rift basins which are the west and east branches of the East African Rift System (EARS) in southwest Tanzania (Figs. 1 & 2). The RVP is characterised by the Neogene-Quaternary effusive and eruptive volcanic rocks from four volcanic eruption centres (Fig. 3): Tukuyu, Rungwe, Ngozi and Kiejo volcanoes (Harkin, 1960; Ebinger et al., 1989; Fontijn et al., 2012, 2013). The area is affected by enhanced regional heat flux according to recent results derived from regional magnetic spectral analysis and 3D

* Corresponding author at: Tanzania Geothermal Development Company Ltd (TGDC), P. O. Box: 14801, Ursino House No. 25, Dar es Salaam, Tanzania.
*E-mail address:* geodidas@ymail.com (M.M. Didas).

https://doi.org/10.1016/j.geothermics.2023.102893
Received 7 March 2023; Received in revised form 1 December 2023; Accepted 6 December 2023
Available online 15 December 2023

gravity inversion (Didas et al., 2022). Due to the triple rift intersection, the RVP rocks are affected by three families of very recent fractures and faults (Fontijn et al., 2010a; Delvaux et al., 2010) that may control secondary permeability and fluid flow.

Based on geological, geochemical and geophysical data, previously identified prospects within the RVP have been assessed as hosting an inferred cumulative geothermal resource capacity of up to 191 megawatt electric (MWe) at an optimistic 10% level of confidence (UNEP/ARGeo, 2016; ELC, TGDC, 2017; EAGER, 2018). The previously assessed geothermal prospects include Songwe to the northwest, the Ngozi prospect in the centre, and Kiejo-Mbaka to the southeast (Fig. 2). Geothermometry from hot springs indicated reservoir temperature of 232 ± 13°C in Ngozi (Alexander et al., 2016), 140 ± 13°C in Kiejo-Mbaka (Rizzello et al., 2022) and 112 ± 16°C in Songwe (Alexander et al., 2016; Asnin et al., 2022). Therefore, Ngozi is considered a likely high-temperature volcano-hosted, magmatic geothermal prospect

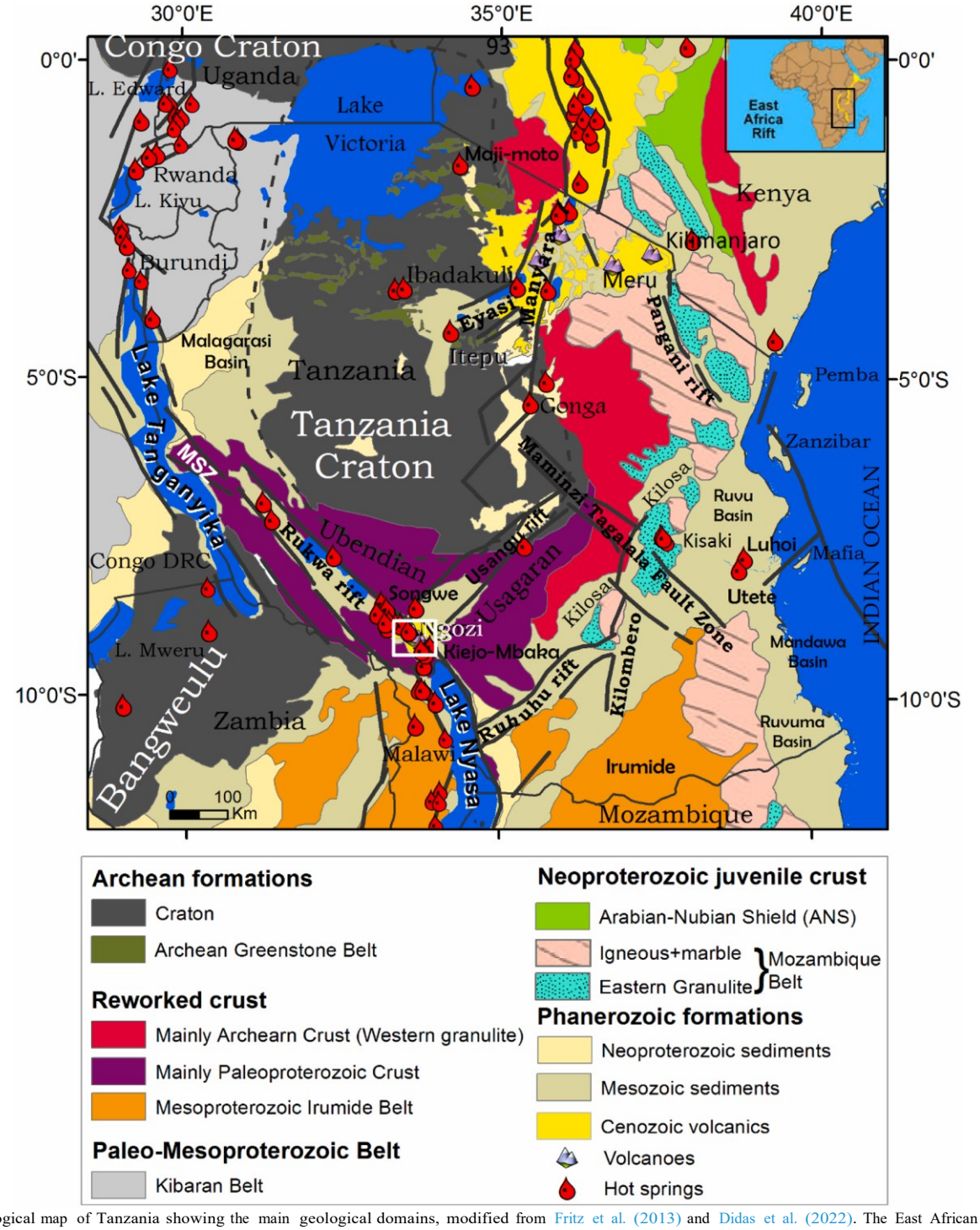


**Fig. 1.** Geological map of Tanzania showing the main geological domains, modified from Fritz et al. (2013) and Didas et al. (2022). The East African Rift System (EARS) margins are indicated by heavy dark gray segmented lines and political boundaries by gray continuous lines. The study area is indicated by a white square located at the intersection of the east (Usangu rift), the west (Rukwa rift) branches of the EARS and its extension to the south along the Nyasa (Malawi) rift. The dotted polygon indicates the outline of the Archean Tanzania Craton. The inset figure shows the location of the map.

(Kraml et al., 2008; Alexander et al., 2016) while Songwe and Kiejo-Mbaka are low to medium-temperature, fault-related deep circulation prospects (Alexander et al., 2016; Hinz et al., 2018; Rizzello et al., 2022). Capacity estimates for inferred geothermal resources using a Monte Carlo volumetric assessment approach indicated more than 140 MWe at Ngozi (Didas and Hersir, 2021) and 13 MWe at Kiejo-Mbaka (ELC, TGDC, 2017) at a 10% level of confidence. A capacity assessment using power density and analogy approaches (Cumming, 2016c) indicated about 38 MWe at Songwe (EAGER, 2018) at a 10% level of confidence. A drilling programme financially supported by the Geothermal Risk Mitigation Facility (GRMF) and the Government of Tanzania is planned for 2024 to directly test the existence of a geothermal resource and more confidently assess its capacity, first at the Ngozi prospect and subsequently at Kiejo-Mbaka and Songwe.

The primary surface geothermal manifestations in the study area are the underwater thermal springs located at the bottom of the Ngozi caldera Lake (Alexander et al., 2016; Jolie, 2019), with the highest measured temperature discharge of 89°C (Ochmann and Garofalo, 2013). The geochemical assessments by Ochmann and Garofalo (2013) and Alexander et al. (2016) concluded that the deep reservoir component of the spring water has an overall NaCl composition, with a relatively high Cl anion content of 7610 ± 1090 mg/kg, a Na cation content of 4970 ± 570 mg/kg and a TDS (Total Dissolved Solids) of 15,800 ± 2300 mg/kg supporting an estimate of a source temperature of 232 ± 13°C. The geochemistry model for the deep reservoir is that it is recharged by a mix of magmatic water from below the caldera and meteoric waters possibly coming from the Ngozi highlands (Ochmann and Garofalo, 2013) and the western highlands of the Elton plateau (Fig. 3, this study). Such high concentrations of Na and Cl and the related high TDS in the interpreted Ngozi reservoir fluid are typical of the geothermal reservoir fluids in convergent plate boundaries but it is unusual in the continental rift zone of East Africa. For example, in comparison with the Olkaria geothermal system, NaCl fluids prevail over $NaHCO_3$ fluids, but reservoir chloride content is much lower than in Ngozi, with a median of 373 ± 185 mg/kg (Karingithi et al., 2010). The low to medium-temperature $NaHCO_3$ hot springs found 8–12 km to the west and 12–14 km to the northwest of Ngozi caldera (Figs. 3 and 4) have been interpreted as meteoric water conductively heated through the cap of the Ngozi geothermal system to temperatures ranging from 120°C to 130°C (Alexander et al., 2016). Thermal springs and areas of hot ground that have recently been identified in the Rungwe volcano area (Figs. 3 and 4) have not yet been fully analysed but indicate at least conductive heating of meteoric water by high temperature below the Rungwe volcano and possibly condensate derived from steam leaking from a geothermal reservoir.

The regional geoscience studies that have included the Ngozi-Rungwe geothermal prospect have mostly focused on the tectonic and volcanological evolution of the western branch of the EARS and the volcanism of the RVP at the triple junction (Ebinger et al., 1989; Delvaux et al., 1992; Ebinger et al., 1993 a, b; Delvaux and Hanon, 1993; Delvaux et al., 1998; Gibert et al., 2002; Fontijn et al., 2010a, 2010b, 2012, 2013; Ebinger et al., 2019). Previous geoelectrical soundings were carried out mainly for groundwater investigations (Mnzava et al., 2004; DECON, SWECO and Inter-Consult, 2005). Geothermal exploration studies have either focused on a narrow range of data (Walker, 1969; Hochstein et al., 2000) or have considered volcanic centres separately (Kraml et al., 2008, 2010; Delvaux et al., 2010; Ochmann and Garofalo, 2013; Alexander et al., 2016). However, a comprehensive conceptual model that includes a resistivity model of the entire Ngozi-Rungwe area had not been completed prior to the current study.

Here we report on the first resistivity model of the Ngozi-Rungwe geothermal system(s) based on the three-dimensional (3D) inversion of magnetotelluric (MT) data. The 3D inversion takes into account the 3D geometry of the subsurface resistivity and the resulting effects in the MT data and, therefore, supports more reliable resolution of resistivity at depths below the clay cap than could be achieved using the previous one-dimensional (1D) models (Kalberkamp et al., 2010; Alexander et al., 2016; Didas and Hersir, 2021). The inversion includes 98 MT sounding stations acquired from 2015 to 2016 (Alexander et al., 2016) and 92 new soundings, measured in 2020 (Didas and Hersir, 2021) and 2022 as a part of this study to fill the large data gaps within the Ngozi caldera as well as over the Rungwe volcano and the surrounding areas (Fig. 4). A total of 98 Transient Electromagnetic (TEM) measurements have also been made to constrain the topographic and shallow resistivity effects

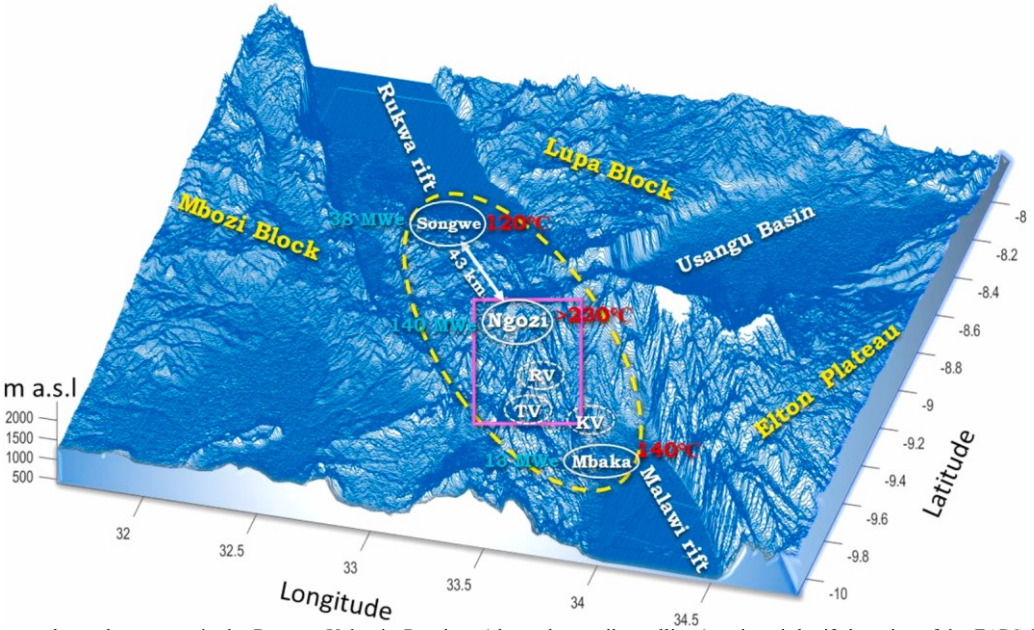


**Fig. 2.** Location of the geothermal prospects in the Rungwe Volcanic Province (shown by a yellow ellipse) at the triple rift junction of the EARS. The purple rectangle represents the study area. Previously published estimates of reservoir temperatures and resource capacities at a 10% likelihood are indicated in red and blue, respectively (see references in the text). The four main volcanoes are indicated as Ngozi, TV (Tukuyu volcano), RV (Rungwe volcano) and KV (Kiejo volcano). As horizontal scale, the white arrow shows the distance between Ngozi and Songwe geothermal prospects.

on the MT data (e.g. the static shift). The objective of our study is to model the resistivity structures at a greater depth than could be reliably attained using 1D resistivity models (Kalberkamp et al., 2010; Alexander et al., 2016; Didas and Hersir, 2021) to resolve and to better understand the structural and geothermal characteristics of the entire Ngozi-Rungwe prospect.

## 2. Geological and structural setting

The Mbeya triple rift junction consists of three major rift basins, the NW Rukwa rift, the NE Usangu rift and the SE to NS Malawi rift which stretches to the south through Malawi and terminates in Zambia (Figs. 1–3). The triple rift junction is formed at the intersection of the three Proterozoic belts which form the basement: the NW trending Paleoproterozoic Ubendian belt, the NE trending Paleoproterozoic Usagaran and the SW trending Mesoproterozoic Irumide belts which are disrupted by the EARS (Fig. 1). The Proterozoic basement is covered by the Karoo and Cretaceous sedimentary rocks which are overlain by the Neogene volcanic rocks related to the development of the EARS (Fig. 3) forming the RVP.

### 2.1. Proterozoic basement

The geology of the Ngozi-Rungwe area is floored by the Paleoproterozoic metamorphic basement mainly comprised of medium to high-grade metamorphic rocks, granitic and gabbroic intrusions, and volcanic rocks (Lenoir et al., 1994; Mruma, 1995). The Paleoproterozoic metamorphic basement is intruded locally by carbonatite pipes along Songwe scarp, presumed to have been emplaced during the Cretaceous time (Ebinger et al., 1989). The basement rocks are exposed west of the Rungwe volcano and north of the Ngozi caldera (Fig. 3) and belong to the Ubendian orogenic belt formed as the result of subduction and tectonic collision events caused by the Gondwana amalgamation in Tanzania (Boniface, 2019). These metamorphic rocks are expected to be low permeability except where disrupted by intrusions and/or a fault geometry susceptible to permeable fracturing, likely focusing deep upflow zones and bounding geothermal reservoirs hosted in the overlying volcanic and sedimentary rocks. These rocks are expected to have higher resistivity and density than overlying volcanic and sedimentary rocks and probably higher magnetic susceptibility, possibly excepting some lava flows and intrusions.

### 2.2. Karoo and Cretaceous sediments

Cretaceous and Karoo-aged sedimentary rocks overlie the Precambrian basement, with sandstone outcrops to the southwest, west and northwest of the RVP (Fig. 3). The Permian-Triassic Karoo Supergroup (~200–300 Ma) formed in rift valleys (Catuneanu et al., 2005; Dypvik et al., 1990) and is generally exposed in limited areas along the western rift margin (Fig. 3), suggesting that Tertiary faulting and subsidence commenced in late Miocene or early Pliocene time (Ebinger et al., 1989). The Karoo Supergroup primarily consists of alternating mudstone, siltstone, sandstone and basal conglomerate units. These sedimentary rocks are overlain by the Cretaceous red sandstone group ~66–145 Ma (Ebinger et al., 1989, 1993b). This Cretaceous group comprises a succession of red sandstones and mudstones (Roberts et al., 2004). Miocene-Holocene lacustrine and fluvial sediments (old and young lake beds sequence) comprise white to tan-white sandstone and siltstone containing pebbles and boulders of metamorphic basement overlaying the Cretaceous sandstone (Ebinger et al., 1989). They outcrop to the NW in the Rukwa basin, to the SE in the Malawi rift, to the east in the Usangu basin and they have been found in a shallow borehole south of the Rungwe volcano (Fig. 4). These sediments reveal the extent of the lakes which once occupied the rift basin (Fontijn et al., 2012). In the RVP the Karoo, Cretaceous and possibly more recent sediments are overlain by the young volcanic formation (Fontijn et al., 2012). Sediments

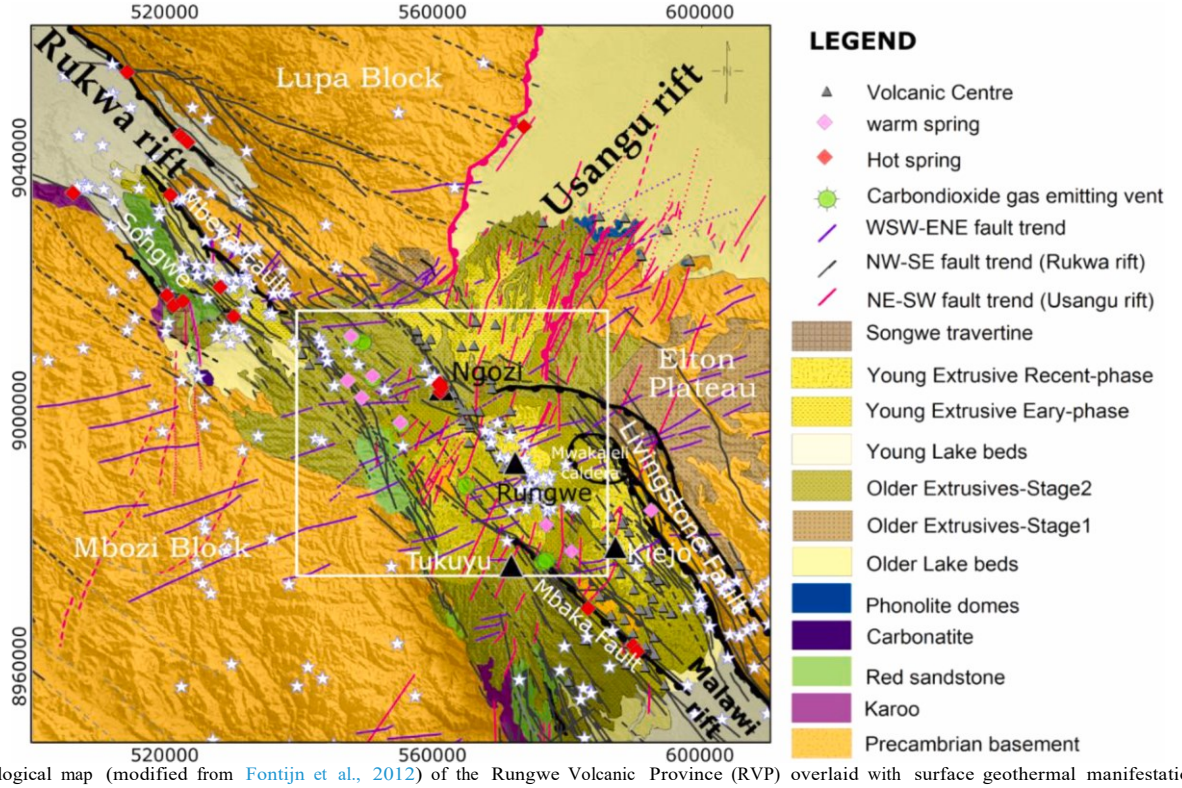


**Fig. 3.** Geological map (modified from Fontijn et al., 2012) of the Rungwe Volcanic Province (RVP) overlaid with surface geothermal manifestation and the active/recent faults grouped in three different groups compiled from many authors (Ebinger et al., 1989 and 1993b; Delvaux and Hanon, 1993; Delvaux et al., 2010; Fontijn et al., 2012; Alexander et al., 2016; Rizzello et al., 2022). White stars represent seismic epicenters according to Ebinger et al. (2019). Bold black and pink lines indicate en-echelon border fault segments. The white rectangle outlines the study area.

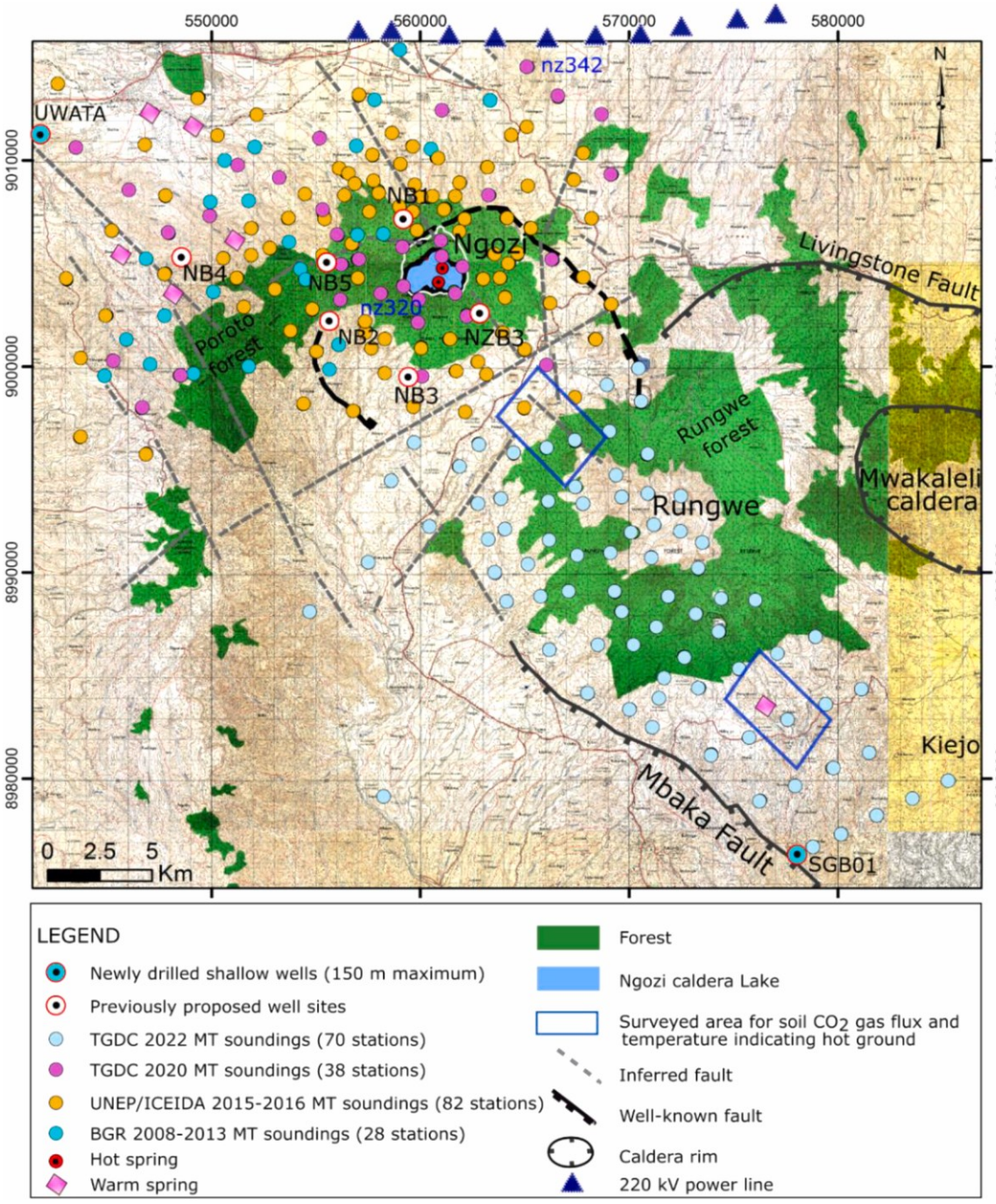


**Fig. 4.** Topographic map showing the spatial distributions of MT stations according to survey campaigns. The five locations considered by Alexander et al. (2016) for slim wells (NB1-2-3-4-5) are indicated by white circles with a black dot. NZB3 slim well was proposed in 2018 by Didas (2018).

containing smectite clay are expected to be imaged as electrically conductive bodies, as reported by Rizzello et al. (2022) in the vicinity of Kiejo and Rungwe volcanoes to the west of the Mbaka fault, by Hinz et al. (2018) to the northwest of the Ngozi volcano, and by Alexander et al. (2016) to the west of the Ngozi volcano.

### 2.3. *Neogene-Quaternary volcanic eruptive history*

Volcanism in the RVP began in the Early Miocene, between 19 and 17 Ma prior to or concurrently with the development of the rift border faults forming phonolite domes in the Usangu Basin (Ebinger et al., 1989; Ivanov et al., 1999; Rasskazov et al., 2003). The Late Cenozoic activity is subdivided into three stages (Ebinger et al., 1989, 1993b; Fontijn et al., 2012) based on field relationship (Harkin, 1960) and radiometric ages of volcanic rocks (Ebinger et al., 1989, 1993b; Ivanov et al., 1999).

Stage 1 (Late Miocene ~9.2–5.4 Ma), was dominated by effusive eruptions of basaltic magma and phonolitic magma together with the emplacement of widespread phonolitic ignimbrites from the largely eroded Mwakaleli caldera (Figs. 3 & 4) also known as Katete volcano, east of Rungwe volcano (Harkin, 1960; Ebinger et al., 1989; Fontijn et al., 2012) which was partly reactivated in the second stage at 2.35 ± 0.04 Ma (Ebinger et al., 1989). Volcanic rocks of the first stage mostly occur at the rift shoulders to the south of the Lupa block and west of the Elton plateau (Fig. 3).

Stage 2 (Late Pliocene-Early Pleistocene ~3.0–1.6 Ma) produced the

old extrusives, with effusive dominated activity from the largely eroded Tukuyu volcano (2.35–1.34 Ma, Ivanov et al., 1999) and several eruptive centres spread around the RVP with emplacement of basalts and phonolites (Harkin, 1960) (Figs. 2 and 3).

Stage 3 (Mid-Pleistocene - present) corresponds to the young extrusives (Harkin, 1960; Fontijn et al., 2010b). The oldest rocks from this stage are found in the NW and N parts of the region, towards the Rukwa and Usangu Basins, respectively (Fig. 3). The most recent formations are concentrated around the three large volcanoes, Rungwe, Ngozi, and Kiejo (Fontijn et al., 2010a, 2010b, 2013; Fig. 2). Ngozi had a major Plinian-style eruption ca. 10 ka and an ignimbrite-forming eruption within the last 1 ka, while Rungwe had at least five moderately explosive to Plinian-style eruptions within the Late Holocene (Fontijn et al., 2010b, 2013). The most voluminous one was the ~4 ka Plinian-style Rungwe Pumice eruption of a trachytic composition (Fontijn et al., 2011, 2013). This was accompanied by a series of small eruptive centres (volcanic cones, domes and eruption craters) observed in the area (Ebinger et al., 1989; Delalande et al., 2015). The Kiejo activity started in the mid-Pleistocene with the oldest lava flow dated at 0.42 ± 0.03 Ma (Ebinger et al., 1989). The most recent eruption of the Kiejo volcano is a tephrite basaltic lava flow dated to approximately 200 years ago (Harkin, 1960; Fontijn et al., 2012).

### 2.4. Structures

The RVP and the Ngozi-Rungwe prospect are characterized by three main sets of faults; the Rukwa NW-SE major trend, the NNE-SSW Malawi rift trend and the NE-SW Usangu faults that have been mapped at a regional scale by Ebinger et al. (1989, 1993b), Fontijn et al. (2010b, 2012), and Delvaux and Hanon (1993), and at a local scale during detailed geothermal assessment studies (Delvaux et al., 2010; Hinz et al., 2018; Rizzello et al., 2022). The NE and NW trending faults are considered to have been reactivated by the recent stress regime at the triple junction (Delvaux et al., 1992; Fontijn et al., 2010b), which changed from extension to strike-slip compression (intermediate compression vertical component) and transtension at ~0.6 Ma ago caused by strike-slip reactivation of the border faults (Delvaux et al., 1992; Ring et al., 1992). A partially mapped 4 km wide and 7 km long NW trending fault zone forming a graben-like structure transects the Ngozi dome, connects several volcanic edifices northwest and southeast of the Ngozi caldera, and cuts the Ngozi caldera Lake (Didas and Hersir, 2021). Fontijn et al. (2012) interpreted the same fault zone as a narrow NW-SE buried rift fault truncated by the NE-SW trending faults southeast of the Ngozi caldera. Most of the faults in the RVP are concealed by the thick Quaternary volcanics including the narrow NNE-SSW trending fault zone which transects the Ngozi caldera inferred from the distribution of the hot springs and the corresponding Ngozi Lake floor temperature pattern (Kraml et al., 2008; Jolie, 2019).

The N50°W striking prominent Mbaka fault, which transects south of the study area, was developed at 2.5 Ma and served as a conduit for basaltic magmas during the second stage of the volcanic activity of the RVP (Ebinger et al., 1993b). The detailed magnetotelluric investigations in the Mbaka area to the south of the studied area (Rizzello et al., 2022), have shown that the Mbaka fault represents the western flank of the narrow Mbaka horst, that uplifted the Precambrian basement to the east of the fault.

Microseismic data were collected from a temporary array of 15 broadband seismometers deployed in the RVP from August 2013 to October 2015 (Ebinger et al., 2019), and the detected events plotted as white stars in Fig. 3. Only 3 earthquakes occurred beneath Ngozi and 31 under Rungwe volcano at depths of 5 to 18 km (Fig. 3). They occurred throughout the observation period, rather than in swarms. There might have been more micro-earthquake activity during the time of the temporary network as the magnitude of completeness was $M_L$ 1.9 (Ebinger et al., 2019). The majority of the epicentres are aligned along the NW trending structures. The focal mechanism solutions are consistent with the current extension direction of about N65°E (Ebinger et al., 2019). There is no permanent network of local seismic stations in the RVP. Moreover, the area is not seismically active with magnitude >4 earthquakes that could be detected by the teleseismic network and used to further constrain the Rungwe-Ngozi geothermal interpretation.

## 3. Previous geothermal studies

Early geothermal exploration in this area includes a regional study carried out from 1976 to 1979 by the Swedish Consulting Group (SWECO) with a main focus on geochemical analysis of hot and warm springs located 7 km west and 12 to 43 km northwest of Ngozi (see Figs. 3 and 4 for location) (SWECO, 1978). The SWECO study suggested potential high-temperature prospects in the RVP that eventually encouraged further geothermal investigation to assess geothermal conceptual models.

In 2006-2009 and 2010-2013, the Federal Institute of Geosciences and Natural Resources (BGR) in cooperation with geoscientists of the Government of Tanzania carried out two phases of detailed surface geological, geochemical and geophysical investigations with support from the Federal Ministry for Economic Cooperation and Development of Germany within the framework of the GEOTHERM technical corporation programme (Kraml et al., 2008, 2010; Kalberkamp et al., 2010; Delvaux, 2010; Ochmann and Garofalo, 2013). The GEOTHERM studies included 28 MT and 48 TEM soundings north and west of Ngozi caldera (Fig. 4), geological mapping, a bathymetry survey in the Ngozi caldera Lake and geochemical sampling and analysis of the hot springs. Three chloride hot springs with temperature discharges of 89°C, 76°C and 66°C with a flow rate of 44 L/s connected by a north-south trending fault were mapped on the bottom of the Ngozi caldera Lake, suggesting a discharge from a geothermal reservoir with a temperature of >200°C (Kraml et al., 2008, 2010). The chemical composition of the Lake Ngozi water indicates that the Ngozi hot springs discharge a mixture of local meteoric water interpreted as infiltrating the Poroto forest (Fig. 4) and hydrothermal-magmatic water. This model was supported by stable water isotope evidence that agreed with the indications given by the concentrations of major anions and the NaCl chemical composition of the Ngozi reservoir fluid.

In 2015, investigators from Iceland GeoSurvey (ÍSOR), funded by Icelandic International Development Agency (ICEIDA – presently: The Ministry for Foreign Affairs (MFA) in Iceland – Directorate for International Development Cooperation) and the Nordic Development Fund (NDF), assessed the geothermal potential of three prospect areas in Tanzania, namely, Lake Natron, Kisaki and Luhoi (Hersir et al., 2015). Subsequently, Luhoi (Hersir et al., 2015; Armadillo et al., 2020) and Kiejo-Mbaka (Hersir and Weisenberger, 2015; Rizzello et al., 2022), as well as the Ngozi prospect together with Songwe (Hinz et al., 2018; Alexander et al., 2016) were proposed as the most promising geothermal prospects in Tanzania.

Between 2015 and 2016 the United Nations Environmental Programme (UNEP), the African Development Bank (AfDB) and ICEIDA, funded detailed surface studies for geothermal resource assessment in Ngozi and Songwe which was implemented by UNEP in collaboration with the Tanzania Geothermal Development Company (TGDC) together with the support from ÍSOR and Geothermal Development Company of Kenya (GDC) (Alexander et al., 2016).

In July 2015, 53 MT and 34 TEM stations were acquired, supplemented in 2016 by an additional 52 MT, 50 TEM (Fig. 4) and 132 gravity stations. Based on these new data sets, Alexander et al. (2016) concluded that Songwe and Ngozi are separate geothermal systems, with Ngozi interpreted as a possible high-temperature volcano-hosted geothermal system with cation geothermometry indicating a temperature of 232 ± 13°C and Songwe interpreted as a low-medium temperature fault-controlled deep-circulation geothermal system with a silica geothermometry indicating a temperature of 112 ± 16°C. The study also concluded that the hot springs at the bottom of the Ngozi Lake were

discharged from a neutral chloride geothermal reservoir, most likely located below the Ngozi caldera and hosted mainly in old volcanic rocks and the Ngozi volcanic neck and intrusion that penetrated the Proterozoic basement. The depth to the top of the reservoir was estimated to be at least 500 m below the surface of the water of the Ngozi caldera Lake. Based on the co-existence of biotite and hauyne in the trachytic pumice from Rungwe volcano (Fontijn et al., 2013), a possible shallow trachytic magma heat source was assumed below the Ngozi caldera at a depth of 5 to 7 km, although this could not be imaged by the geophysical data.

Alexander et al. (2016) noted that most of the MT data were affected by prominent 3D effects at depths greater than ~2 km. Therefore, to limit 3D bias in the 1D resistivity models, the lowest MT frequencies associated with depths greater than 2 km were not included in the 1D MT inversions. As a result, any magmatic heat source that might exist at 5 to 7 km depth could not be reliably resolved using 1D MT inversion and, because of the gap in good quality MT data coverage near the summit of the Ngozi volcano, even a 3D inversion of the available MT data would be unlikely to resolve such a magma body. According to their final integrated conceptual model at a 50% level of confidence, the geothermal system in Ngozi area was likely confined below the caldera with an area of 2.9 $km^2$ whereas at a more optimistic 10% level of confidence, the estimated area of 12 $km^2$ extends outside the caldera rim, mainly to the west.

Alexander et al. (2016), proposed locations for five vertical exploratory slim holes (NB1-2-3-4-5 in Fig. 4) to be drilled through the clay cap to collect temperature data but not to directly test the most likely reservoir extent due to access restrictions.

In 2017, the Government of Tanzania, through the Ministry of Energy (formally known as Ministry of Energy and Minerals), and TGDC contracted Norton Rose Fulbright (NRF) in consortium with Carbon Counts and Scientific and Engineering Power Consultants (SEPCO) to assess the potential geothermal resources in Ngozi, Songwe, Kiejo-Mbaka, Luhoi and Lake Natron (Norton Rose Fulbright, 2017). NRF recommended that the drilling targets proposed by Alexander et al. (2016) should be shifted closer to Ngozi caldera, based on more optimistic access assumptions.

In 2018, Didas and Hersir (2021) reprocessed the available MT-TEM resistivity data set, performed new 1D MT-TEM joint inversions and integrated the resulting resistivity models with the geochemical and surface geological data. These authors hypothesized that the reservoir may be hosted within a 4 km wide by 7 km long NW-SE trending fault zone spanning from the southeast of Ngozi caldera in the vicinity of the Rungwe volcano to the northwest of the Ngozi caldera. However, the lack of MT data inside the caldera still limited the resolution of the subsurface resistivity structures of the area.

The uncertainty in the extent of the proposed Ngozi geothermal reservoir is illustrated by the contrasting models given by Delvaux et al. (2010), Alexander et al. (2016) and Didas and Hersir (2021). These MT interpretations are limited by their use of 1D inversions that are unreliable at depths of investigation below the bottom of the low resistivity clay cap, about 2 km, because of 3D effects at frequencies that would reflect the resistivity pattern at greater depths. A 3D inversion would have been problematic because of the large gap in suitably low-noise MT data near the Ngozi caldera. Moreover, the previous studies did not investigate the contribution of the Rungwe volcano to the geothermal system. Therefore, in this study, 38 MT stations which were partially funded by GRÓ-GTP were acquired in 2020 inside the Ngozi caldera and the surrounding area, and 70 more MT stations in 2022 to extend MT coverage to Rungwe. These have been combined with the earlier MT data in a 190 station MT data set (Fig. 4) to support the inversion of a 3D resistivity model for the entire Ngozi-Rungwe prospect area.

## 4. Data and methods

In this work, the magnetotelluric (MT) method was applied to image the subsurface resistivity structures of the study area. MT is a passive method using the naturally occurring electromagnetic field caused by the interactions between the solar wind and the magnetosphere and lightning discharges from the equatorial regions (Chave and Jones, 2012). It has a depth of penetration from less than a hundred metres to many hundreds of kilometres (Chave and Jones, 2012). MT is widely used to investigate geothermal systems, especially to map the electrically conductive clay zone that caps the geothermal reservoir and to detect shallow magmatic heat sources as detected in the Ethiopian rift in the EARS (Didana et al., 2015; Samrock et al., 2021; Samrock et al., 2023), Kirishima volcano Kyushu Island, Japan (Aizawa et al., 2014) and southeast of the Tibetan Plateau (Ye et al., 2018). The impermeable cap that prevents the buoyant hot geothermal upflow from rapidly exhausting the system to the surface is generally formed by a layer of rock with sufficient smectite clay content with high cation exchange capacity to reduce both permeability and resistivity (Ussher et al., 2000; Cumming, 2016a; Levy et al., 2018; Armadillo et al., 2020; Hersir et al., 2022). A clay cap can form below the flanks of a volcano by low-temperature hydrothermal alteration of lavas and tuffs to smectite clay or smectite clay can be deposited as a sedimentary layer in basins adjacent to volcanoes. Regardless of origin, low-resistivity smectite clay and mixed-layer clays transform to more resistive clays like chlorite and illite at 180 to 250°C (Ardid et al., 2021; Ussher et al., 2000; Muñoz, 2014). Rocks hosting geothermal fluids forming the reservoir are usually characterised by relatively high resistivity values between 20 and 100 Ωm (Anderson et al., 2000). A pattern of low resistivity over high resistivity is ambiguous if considered in isolation but, when interpreted in the context of an integrated conceptual model that considers all geoscience and thermodynamic constraints, it can be correlated with the overall permeability distribution of a geothermal reservoir (Hersir et al., 2022; Cumming, 2016a; Cumming, 2016b). In rift-hosted volcanic systems, the heat source is usually interpreted to be a shallow-lying hot intrusive body or a shallow magma chamber that, in a few cases, has been characterised by anomalously low resistivity e.g. in the Ethiopian rift in EARS (Didana et al., 2015; Samrock et al., 2021).

### 4.1. Data

The MT data comprise 190 stations distributed over an area of ~700 $km^2$. Station spacing varies from 600 m around the Ngozi caldera to 2000 m south of Rungwe volcano (Fig. 4). Examples of field data are shown in Fig. 5. The dataset includes four geothermal exploration campaigns in 2015 and 2016 (carried out by UNEP/ICEIDA), and in 2020 and 2022 (carried out by TGDC). A total of 28 MT soundings were also acquired in 2008 and 2010 (Kalberkamp et al., 2010) on the north flank of Ngozi. However, because the data from the 2008 and 2010 MT campaigns were noisy and lacked vertical magnetic field data, the 2015 and 2016 MT surveys were designed to replace the earlier MT data. The MT data acquired in 2020 covered the 5 km in diameter gap inside the Ngozi caldera and the proximal area where Alexander et al. (2016) inferred the location of the upflow of the geothermal reservoir. The 2022 campaign extended the survey area SE, in order to investigate the contribution of the Rungwe volcano area to the geothermal system.

### 4.2. MT impedance and magnetic transfer function estimation

The impedance tensor $\mathbf{Z}$ was estimated in the frequency domain by first applying the Fast Fourier Transform (FFT) method (Bendat and Piersol, 1971) to the time series records (two electric field components $E_x$, $E_y$ and three magnetic field components $H_x$, $H_y$ and $H_z$ aligned along the NS, EW and vertical direction, respectively). At a given site, the frequency-dependent impedance tensor $\mathbf{Z}$ is defined as:

$$\mathbf{E} = \mathbf{ZH} = \begin{pmatrix} E_x \\ E_y \end{pmatrix} = \begin{pmatrix} Z_{xx} & Z_{xy} \\ Z_{yx} & Z_{yy} \end{pmatrix} \begin{pmatrix} H_x \\ H_y \end{pmatrix}$$

The apparent resistivity and phase for the xy mode (similar for the

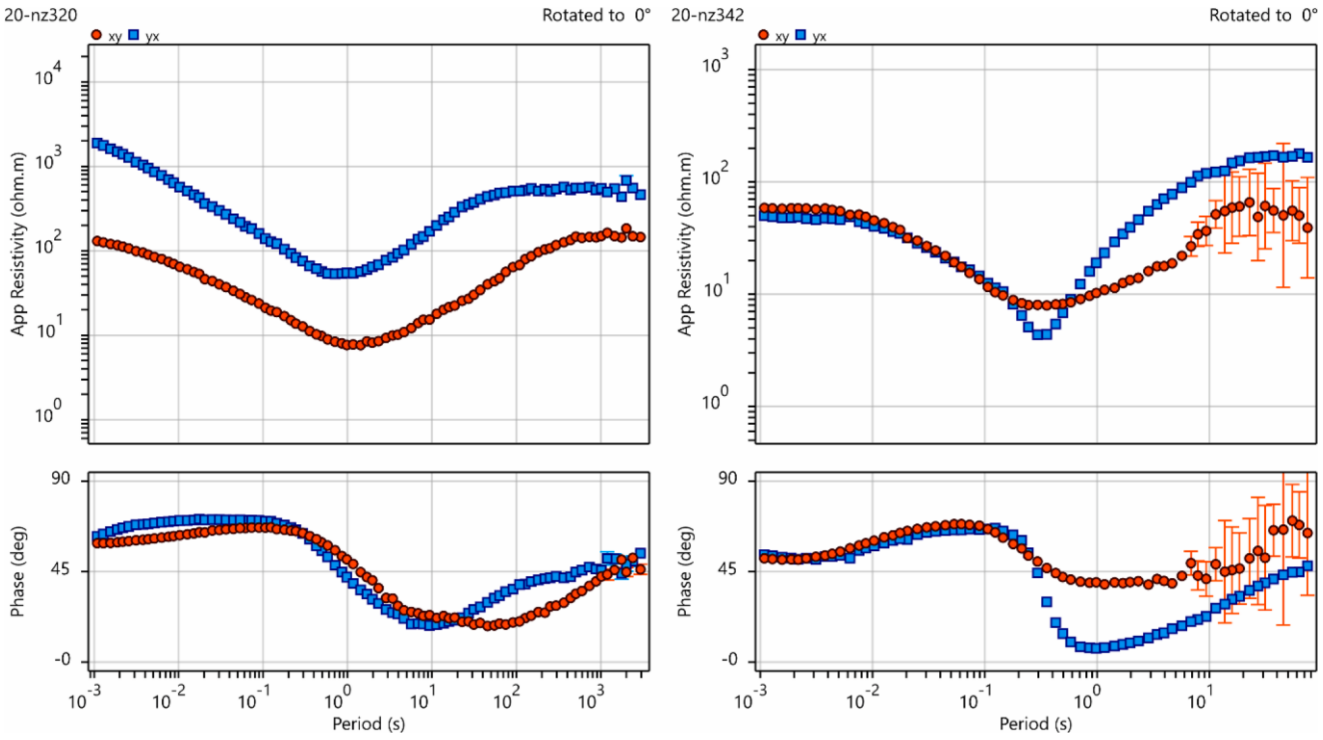


**Fig. 5.** Examples of field data. Left panels: Field data for site nz320 (see location in Fig. 4) affected by static shift distortion of more than a decade seen by the separation of the two apparent resistivity curves. Right panels: Field data for station nz342 located northeast of the Ngozi caldera (Fig. 4), strongly affected by the 220-kV powerline, showing the yx apparent resistivity mode slope exceeding 45° and phases approaching 0° from about 2 to 0.2 s.

yx, xx and yy modes) are given by:

$$\rho_{xy}(\omega) = \frac{1}{\mu_0 \omega} |Z_{xy}|^2$$

$$\varphi_{xy}(\omega) = \tan^{-1}\left(\frac{\mathrm{Im}\{Z_{xy}\}}{\mathrm{Re}\{Z_{xy}\}}\right)$$

Both the apparent resistivity and phase are functions of the angular frequency ($\omega = 2\pi f$), and $\mu_0 = 4\pi$ x 10 $^{7}Hm^{1}$ is the magnetic permeability in free space.

The frequency-dependent geomagnetic transfer function, or "tipper" (**T**) is defined by:

$$\mathbf{H_z} = \mathbf{TH_{hor}} = T_x H_x + T_y H_y$$

The tipper relates the horizontal components of the magnetic field to the vertical one and is sensitive to lateral changes in resistivity.

The MT impedances for the 2015-2016 GDC-TGDC data have been estimated by applying the robust scheme of Sutarno (2008) using single-site processing without a remote reference (Gamble et al., 1979). The remote reference needed to reduce the effect of cultural and incoherent noise (Chave and Jones, 2012) was not used for the 2015-2016 data because of many problems with acquisition and processing at the reference station including local lightning, heavy rain and coherent noise (UNEP/ARGeo, 2016; Alexander et al., 2016). For the 2020-2022 TGDC data, the MT impedances and vertical transfer functions were estimated using the remote reference scheme of Gamble et al. (1979) extended to the robust processing method of Chave and Thompson (1989) and Rizzello and Armadillo (2023). As a result, a data set consisting of the impedance and tipper in the nominal frequency range of 320 to 0.001 Hz was obtained for 190 MT stations; their location is given on Fig. 4.

Some stations located on the north side of the Ngozi caldera show strong influence on the yx (east-west) mode of the apparent resistivity and phase caused by the 220 kV regional power line and have typical signs of coherent distortion (the power line is shown on Fig. 4). The power line trends approximately E-W across the northeast part of the study area and is connected to the Mwakibete switching substation to the north (Fig. 4). The distortion is characterized by the yx apparent resistivity mode slope exceeding 45° and phases approaching 0° (see e.g. Iliceto and Santarato, 1999; Pellerin et al., 2003; Chave and Jones, 2012) from about 2 to 0.2 s (see Fig. 5 right panels). The effect is small at sites located at the Ngozi dome and is not observed to the south. Therefore, the affected Zyx data were excluded in the inversion.

### 4.3. *Three-dimensional magnetotelluric modelling*

#### 4.3.1. *Model discretization*

For the inversion, we used GeoTools-RLM3D software developed by CGG (Mackie and Watts, 2012). We have adopted a 3D resistivity model made by a total of 2.92 million cells, consisting of 97 × 209 cells in X-and Y- directions extending from -68.76 km to +68.76 km in S-N (X) direction and from -82.76 km to +82.76 km in E-W (Y) direction. The top of the model is located at the highest elevation point in the area (3000 m a.s.l). The minimum horizontal cell size is 250 m over the survey area, increasing exponentially beyond it towards the edges of the model up to 18,850 m in both X-and Y-directions (Fig. 6 top panel). In the vertical (Z) direction, the grid consists of 144 layers. The bottom of the grid is located at a depth of 233 km. The uppermost 84 layers are used to model the topography and they have grid cell thicknesses of 25 m. Below, the thickness increases exponentially with depth. A detail of the modelled topography is shown in a zoomed-in NW-SE trending profile across the Ngozi and Rungwe volcanoes in Fig. 6 middle panel. The topographic data are the 30 m SRTM DEM from the Aster global dataset of the USGS (2009, https://lpdaac.usgs.gov).

#### 4.3.2. *Inversion*

An initial homogeneous half-space model of 50 Ωm was adopted after some testing. The Ngozi Lake was assigned the fixed resistivity of 1.9 Ωm measured by Ochmann and Garofalo (2013) and Delalande et al.

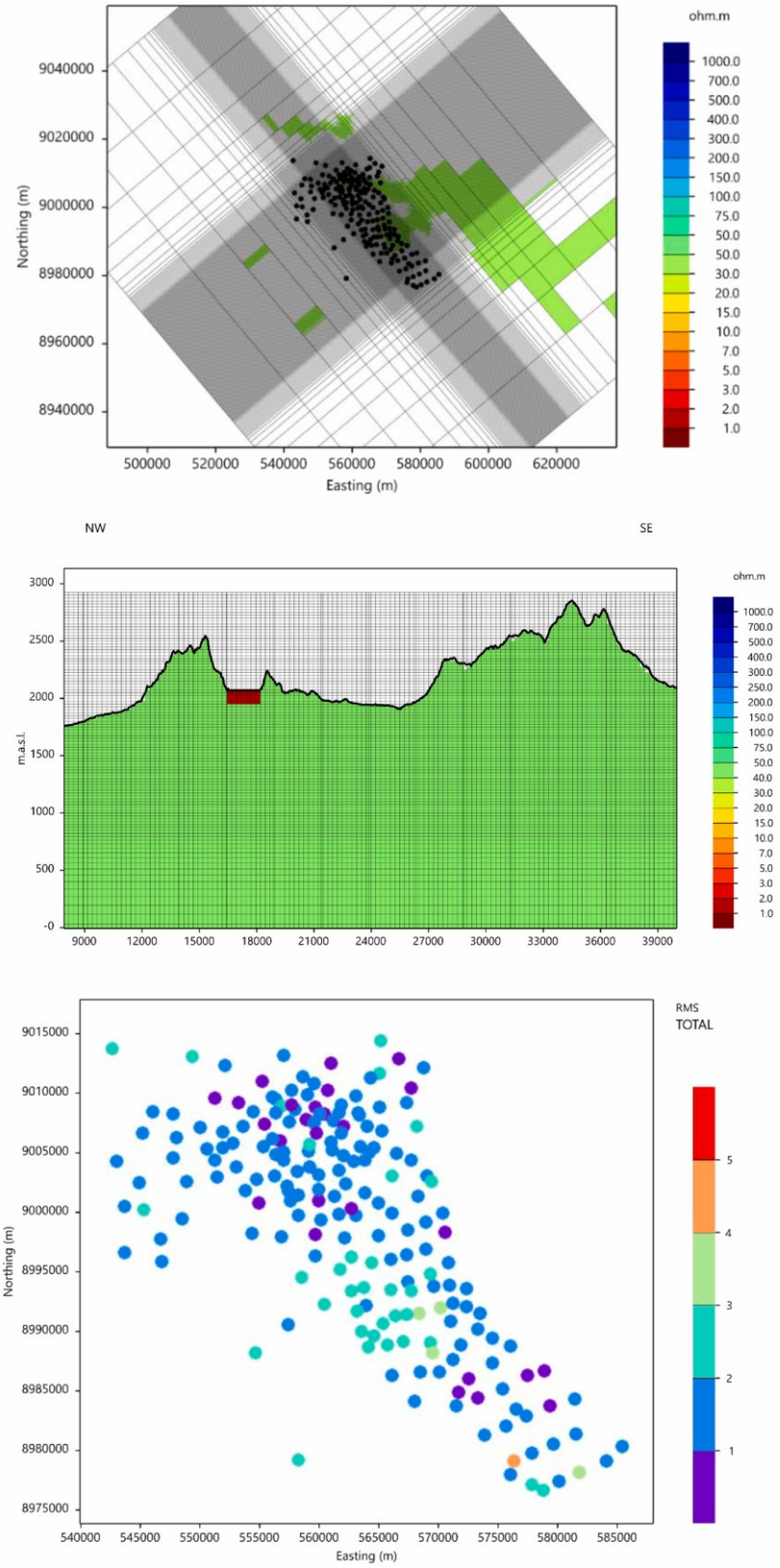


**Fig. 6.** Top panel: Horizontal section of the starting model grid (50 Ωm homogeneous earth half-space with topography); the MT stations are indicated as black dots. Middle Panel: NW-SE trending vertical section of the starting model grid through the Ngozi and Rungwe volcanoes showing the topography above 0 km elevation with 5 times vertical exaggeration; a fixed resistivity of 1.9 Ωm has been assigned to the Ngozi caldera Lake (red squares). Lower panel: Misfit map of total (impedance and tipper) normalized RMS of the final resistivity model for each station shown as coloured symbols.

(2015). The orientation of the model axis was N40°W in order to keep the number of the model cells as few as possible. This is different from the principal components of the field-layout during the data measurement which was NS. We inverted for the unrotated full impedance tensor elements (Zxx, Zyy, Zxy and Zyx), jointly with the vertical to horizontal magnetic transfer functions from the 190 MT stations. The final model has a resulting normalized Root Mean Square (nRMS) error of 1.7; nRMS values at each station are mapped in Fig. 6 lower panel. Examples of the comparisons of the observed data and inversion responses are shown in Fig. 7.

Impedance and tipper data were sampled in the period range from 0.003 to 1000 s, for a total of 23 periods with a density of 4 periods per decade (e.g. see Fig. 7). As an absolute error floor, we used 5% of the geometrical mean of the off-diagonal MT impedance elements (defined as $0.05 * \sqrt{|Z_{xy}| * |Z_{yx}|}$), 10% of the geometrical mean of the diagonal MT impedance elements (defined as $0.1 * \sqrt{|Z_{xx}| * |Z_{yy}|}$) and an absolute error of 0.02 for the geomagnetic transfer functions (tipper).

During the inversion, the galvanic distortions were automatically corrected via simultaneous inversion of a 2 × 2 real galvanic distortion matrix (Soyer et al., 2021).

$$\mathbf{Z_c}(f) = \mathbf{CZ}(f) = \begin{pmatrix} C_{11} & C_{12} \\ C_{21} & C_{22} \end{pmatrix} \begin{pmatrix} Z_{xx}(f) & Z_{xy}(f) \\ Z_{yx}(f) & Z_{yy}(f) \end{pmatrix}$$

Where Z is the 2 × 2 complex impedance tensor between the undistorted horizontal electric field and the magnetic field in frequency (f) domain, and C is the real-valued, frequency independent 2 × 2 distortion matrix.

## 5. Results

The final 3D resistivity model is presented here as horizontal depth slices (Fig. 8) and vertical cross-sections (Figs. 9 & 10) superimposed on the main faults compiled from different sources (Ebinger et al., 1989 and 1993b; Delvaux and Hanon, 1993; Delvaux et al., 2010; Fontijn et al., 2012; UNEP/ARGeo, 2016; Rizzello et al., 2022). Generally speaking, the subsurface resistivity structure of the Ngozi-Rungwe geothermal prospect area reflects the characteristic hydrothermal alteration of a high-temperature geothermal system as described by e.g. Lévy et al. (2018), Ussher et al. (2000) and Anderson et al. (2000).

A shallow high resistivity zone labelled **R1** in the 3D resistivity cross-sections shown in Figs. 9 and 10 is mainly correlated with unaltered and dry rocks near the surface. Its resistivity is typically of the order of hundreds of Ωm, with a maximum thickness of ~700 m at the Ngozi and Rungwe volcanoes.

Slice maps from 1600 m a.s.l to 400 m a.s.l (Fig. 8) show a wide and thick low resistivity (1-15 Ωm) layer below **R1**. It is elongated along the NW-SE direction over an area of approximately 8 km x 52 km passing through the Rungwe and Ngozi volcanoes. Therefore, we name it the Rungwe-Ngozi Conductive Anomaly (**RNCA**). To the NW of Ngozi, another shallow low resistivity layer trends NE-SW parallel to the

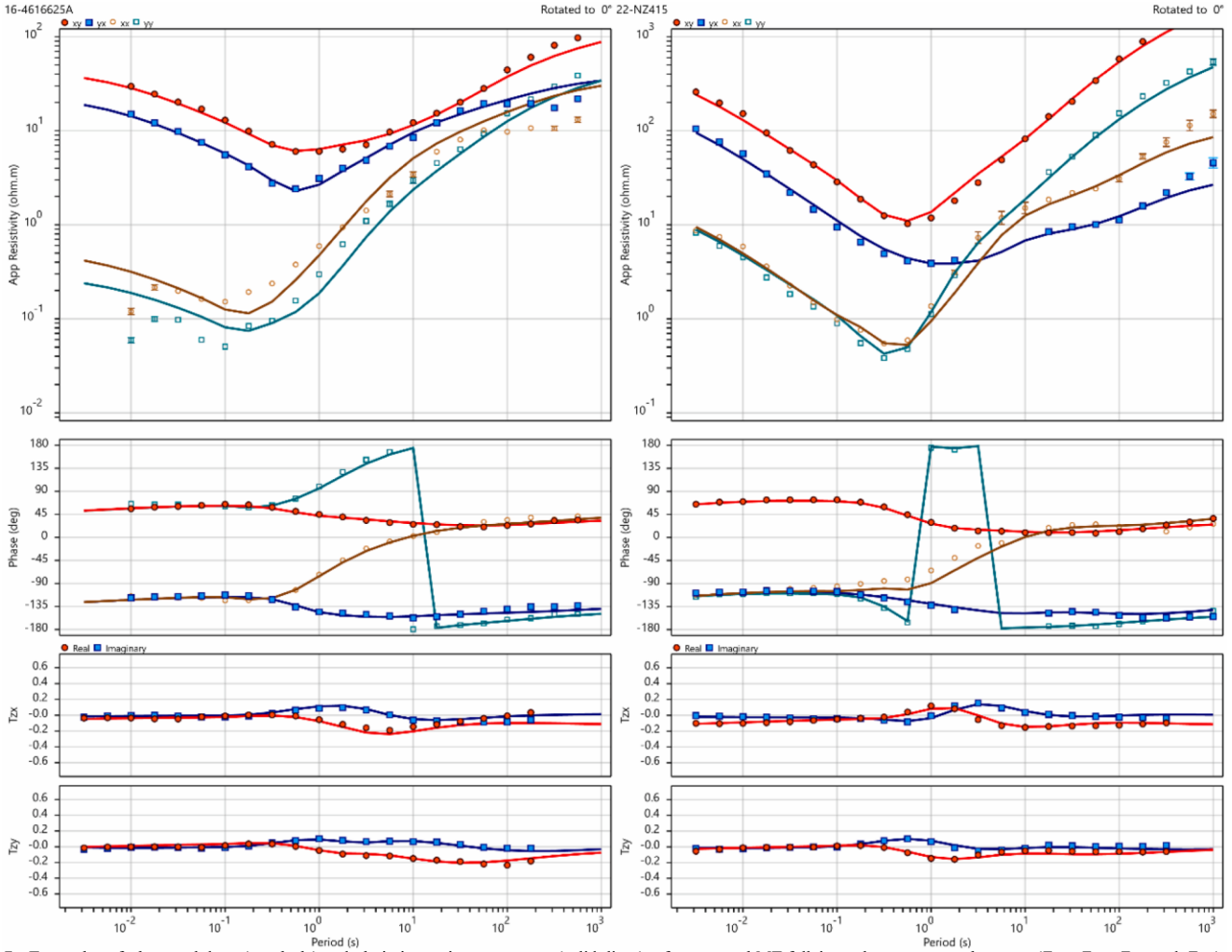


**Fig. 7.** Examples of observed data (symbols) and their inversion responses (solid lines) of unrotated MT full impedance tensor elements (Zxx, Zyy, Zxy and Zyx) and tipper functions. Left and right panels are stations nz314 and nz415, respectively.

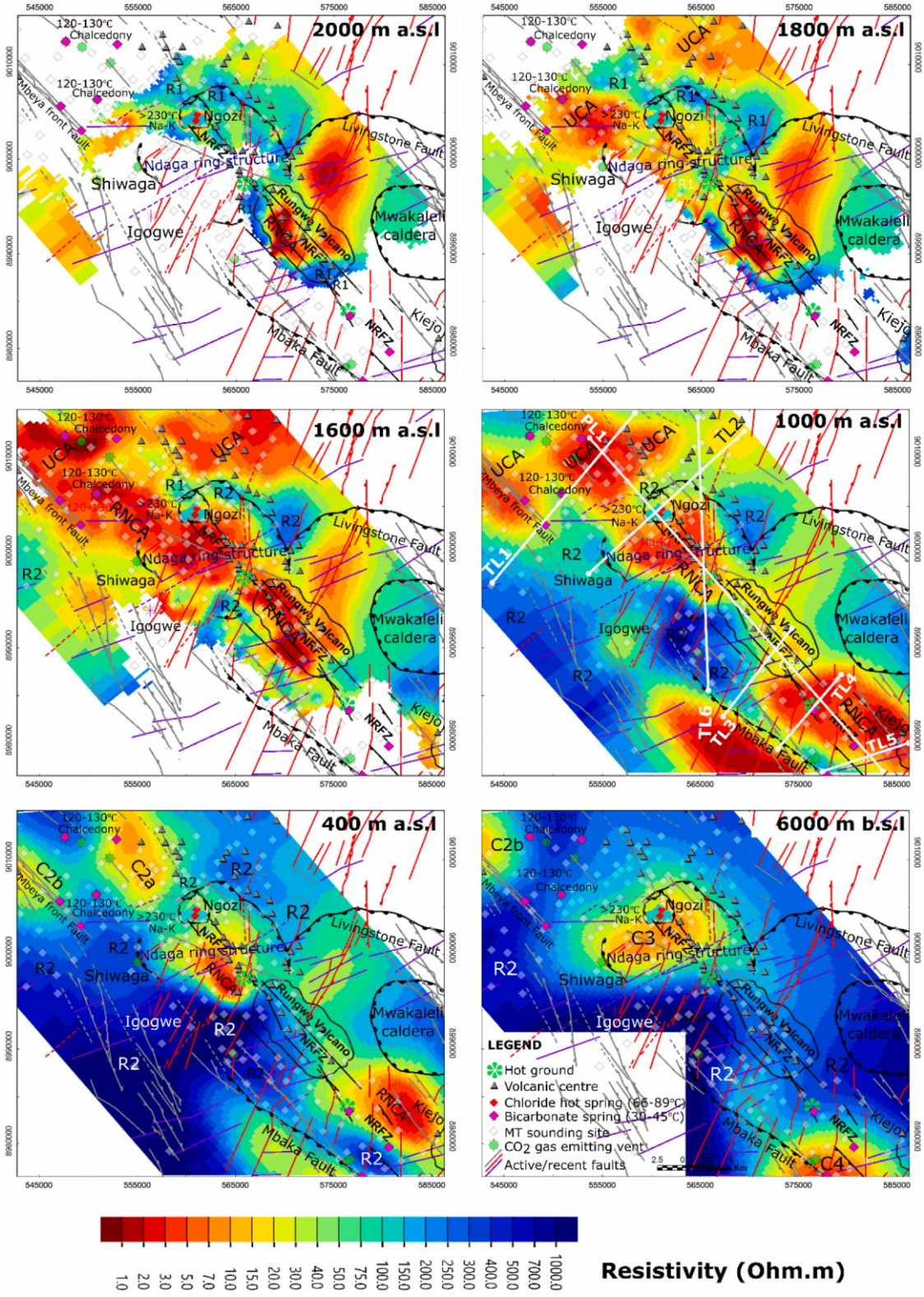


**Fig. 8.** Horizontal resistivity depth slices at 2000 m a.s.l down to 6000 m b.s.l superimposed with warm/hot springs, faults and volcanic eruption centres compiled from several authors (Ebinger et al., 1989, 1993b; Delvaux and Hanon, 1993; Delvaux et al., 2010; Alexander et al., 2016) and hot ground areas mapped in this study. **RNCA** and **UCA** represent the conductive clay caps sealing the inferred geothermal systems within the Ngozi-Rungwe fault zone (**NRFZ**) and the sub-parallel transition zones **C2a-b**, respectively. **R1** represents the surficial resistivity feature. **R2** represents the highest resistivity domains below **RNCA** and **UCA** and to the SW and NE. **C3** and **C4** are the possible magmatic heat sources. White lines in panel 1000 m a.s.l indicate the vertical cross-sections shown on Figs. 9 and 10.

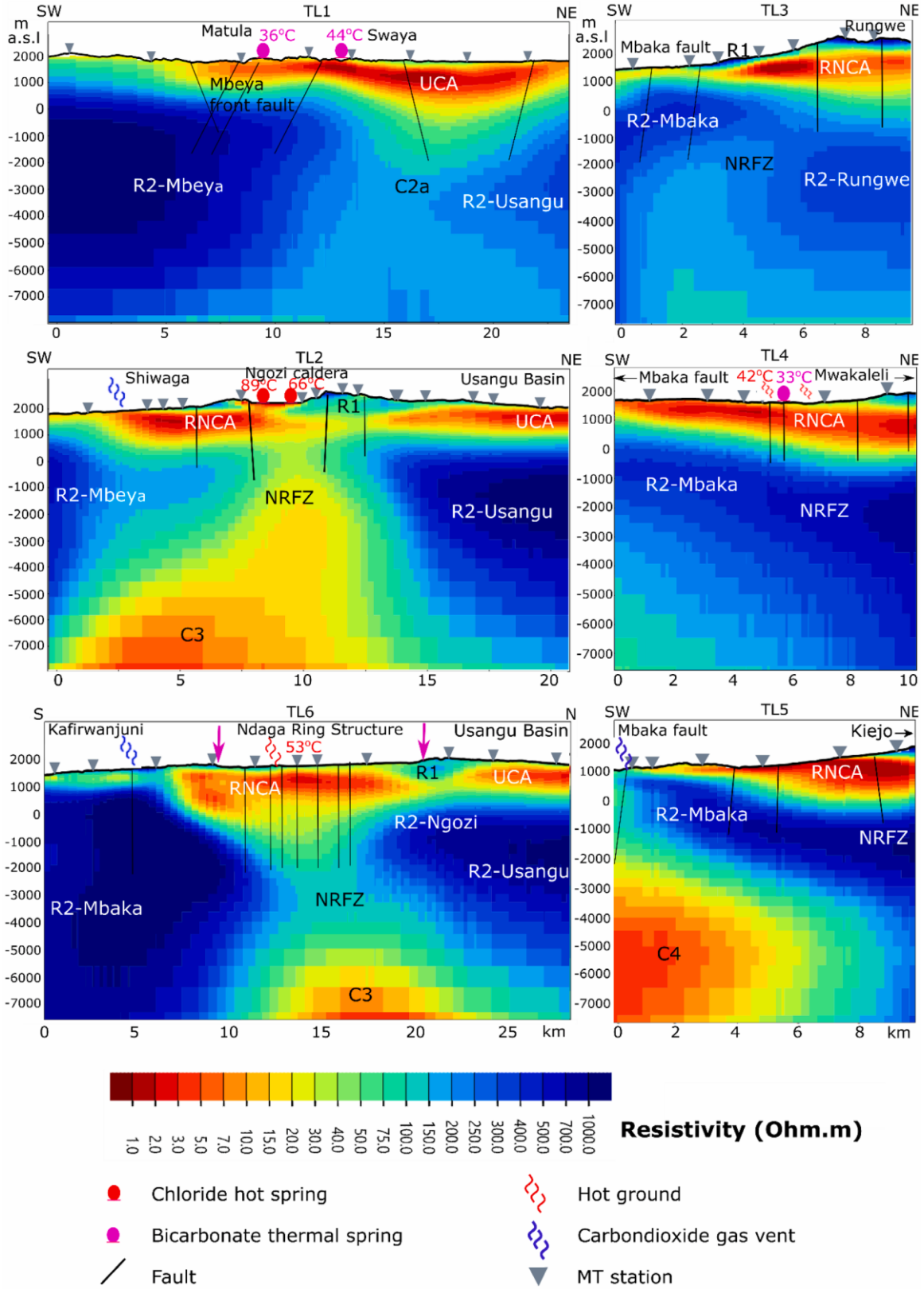


**Fig. 9.** Resistivity cross-sections TL1-TL6 crossing the NW-trending **NRFZ**; for location see Fig. 8. The black lines indicate the intersection of the cross-sections with the mapped faults in Fig. 8. In general, **RNCA** thickens at the flanks of the Rungwe volcano. The hot ground anomalies detected by the soil temperature survey at a depth of 70 cm to the north and south of the Rungwe volcano are shown in profiles TL6 and TL4, respectively.

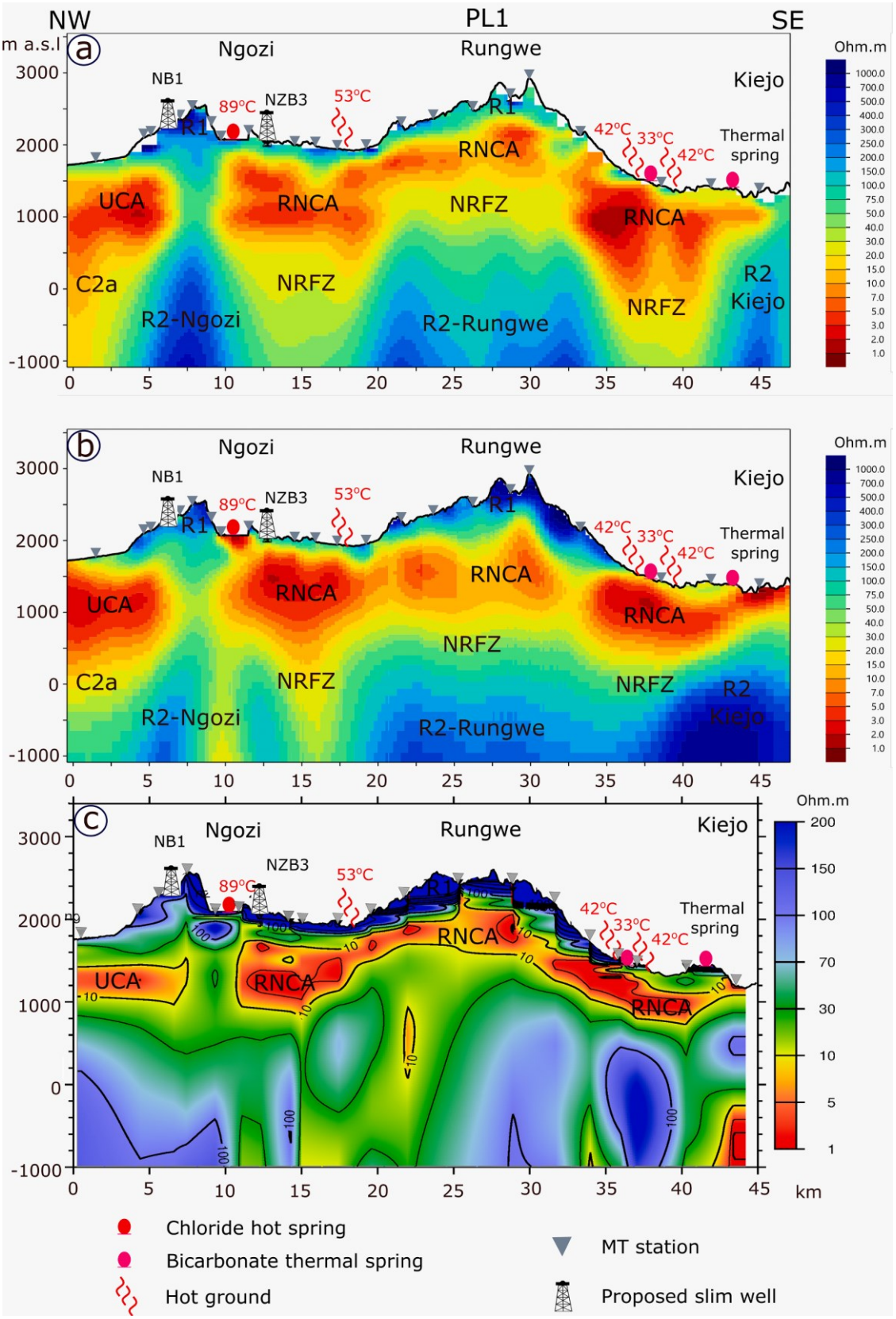


**Fig. 10.** Resistivity cross-section PL1 along the **NRFZ** NW-SE trending fault zone. The 3D inversion results of the off-diagonal components and tipper using ModEM software (uppermost panel), the 3D inversion results of the full tensor impedance elements and tipper using GeoTools-RLM3D software (middle panel) and the 1D inversion results (lowermost panel) are shown for comparisons (note that the colour scale for the two 3D cross-sections is the same). For further figure legend see Fig. 8. NB1 and NZB3 denote proposed well locations by Alexander et al. (2016) and Didas and Hersir (2021), respectively. The location of the cross-section and the MT stations are shown in Fig. 8, slice 1000 m a.s.l.

Usangu rift basin, where warm springs and cold $CO_2$ gas vents are located. We name this shallow conductor the Usangu Conductive Anomaly (**UCA**).

As illustrated in the cross-sections in Fig. 9, the tops of the **RNCA** and **UCA** low resistivity layers are at a depth ranging from a few metres to 700 m below the surface, and their thickness varies from 200 m to 1500 m. **RNCA** layer is about 500 m thick beneath the Rungwe volcano and reaches a maximum thickness of 1500 m at the flanks of the Kiejo and Rungwe volcanoes (see, section TL3 and TL4 in Fig. 9, PL1 in Fig. 10). However, the conductive layer is absent below the east and north flanks of the Ngozi caldera (TL2 in Fig. 9 and PL1 in Fig. 10). At the Rungwe volcano, **RNCA** forms a dome-like shape (PL1 in Fig. 10) which is only partially resolved to the east in the vicinity of the Mwakaleli caldera due to limited MT data coverage (TL3 and TL4 in Fig. 9). This up doming geometry of **RNCA** is missing below the Ngozi caldera and the surrounding area where this conductor is generally flat.

Below the **RNCA** conductor, resistivity increases with depth, reaching roughly 1000 Ωm below 3000 m depth (see sections TL1, TL4 and TL5 in Fig. 9, PL1 in Fig. 10). Wide transition zones showing moderate resistivity of about 15-200 Ωm are separated by resistive background **R2** (TL1, TL2, TL3 and TL6 in Fig. 9). Another two sub-parallel wide transition zones labelled **C2a**, and **C2b** in the figures occur below conductor **UCA** to the north of Ngozi caldera (Fig. 8, slices 400 m a.s.l and 6000 m b.s.l). These transition zones form column-like anomalies (see profiles TL1 in Fig. 9 and PL1 in Fig. 10) that have been observed for instance by Didana et al. (2015) and Rizzello et al. (2021) at Tendaho and Alalobeda Ethiopia, respectively, where they have been interpreted as possible upflow zones.

A deep conductor **C3** has been detected south of the Ngozi volcano at a depth of 6 km below the Ndaga ring structure (Fig. 8, slice 6000 m b.s.l; TL2 and TL6 in Fig. 9) and may be related to a magmatic heat source. A second deep conductor **C4** occurs along the Mbaka fault south of Rungwe volcano between Tukuyu and Kiejo volcanoes (Fig. 8, slice 6000 m b.s.l; TL5 in Fig. 9).

To qualitatively investigate the reliability of our model, we have also used a different 3D MT inversion software (ModEM, Egbert and Kelbert, 2012; Kelbert et al., 2014) with a simplified model discretization (minimum horizontal cell size 400 m) and a reduced data set obtained by excluding the on-diagonal components of the impedance tensor that sometimes may give artifacts (see e.g. Newman et al., 2008; Cumming and Mackie, 2010) due to their inherent lower signal to noise ratio. We also applied a static shift correction using TEM data where it was available (see e.g. Sternberg et al., 1988; Pellerin and Hohmann, 1990; Árnason, 2015) and a topographic correlation approach consistent with Jiracek (1990).

In Fig. 10 we compare the resistivity cross-section PL1 from the ModEM 3D resistivity model (uppermost panel) with a final nRMS of 1.5, CGG GeoTools model (middle panel) against 1D MT inversion (lowermost panel, modified from Didas and Hersir, 2021). The three sections appear very similar down to the base of the shallow **RNCA** conductor. Both the 1D and 3D models indicate a strong up doming of the **RNCA** conductive clay cap beneath the Rungwe volcano and its absence beneath the Ngozi caldera. Below **RNCA**, 1D model shows larger differences compared to the 3D models. However, the 3D models also show some differences with respect to the upper parts of resistive anomaly **R2**. At depth, the conductive anomaly **C3** is clearly visible only in CGG model. We have concluded, however, that the CGG model including **C3** should be preferred since forward tests have shown that its removal results in a considerable increase of the RMS error (3 as compared to 1.7), especially for the tipper data.

## 6. Geological and structural interpretations

### 6.1. Lithology

Based on geological observations over the area, we interpret the shallow resistive anomaly **R1** as being due to unaltered volcanic ash, pumice and lava flows on the volcanoes and, in the basins, sandstones and shallow metamorphic rocks. This interpretation is supported by the stratigraphy from a 118 m deep borehole (labelled SGB01 in Fig. 4) recently drilled for $CO_2$ gas exploration studies south of the Rungwe volcano, 100 m from the $CO_2$ gas emitting vents (Fig. 8). The borehole encountered 17 m of volcanic ash pumice followed by fresh basalts to a depth of 45 m, thermally altered red sandstone with carbonate-rich fluids to a depth of 89 m, followed by an epidote/chlorite-altered white sandstone to a depth of 95 m, below which fresh obsidian was encountered (O. Mwijage, personal communication, September 21, 2022).

The high resistivity domains **R2** (reaching values of some thousands of Ωm) are found below the **RNCA** and **UCA** conductive layers and on their SW and the NE margins (Fig. 8, slices 1000 m a.s.l down to 6000 m b.s.l). To the SW of **RNCA**, this resistive domain (**R2-Mbaka**) is associated with the Precambrian metamorphic basement on the uplifted block of the Mbaka fault (TL3-6 in Fig. 9). To the NW of the Ngozi caldera, **R2-Mbeya** is associated with the Precambrian basement horst of the Mbeya front fault (400 m a.s.l in Fig. 8 and TL1 in Fig. 9). To the east of the Ngozi caldera, **R2-Ngozi** and **R2-Usangu** (TL2 and TL6 in Fig. 9, and 1600 m a.s.l to 400 m a.s.l in Fig. 8) mark the outcropping phonolite domes from the north to the southeast of the Ngozi caldera and in the vicinity of the Rungwe volcano. **R2-Ngozi** corresponds to an ENE topographic ridge interpreted by Ebinger et al. (1989) as a buried accommodation zone comprised of eroded polyphase volcanic centres separating the Rukwa rift and Malawi rift. To the SE of the Rungwe volcano and in the vicinity of the Kiejo volcano, **R2-Kiejo** is interpreted as shallow concealed Precambrian basement (PL1 in Fig. 10).

### 6.2. RNCA and UCA correlations with fault zones

Structural mapping (Ebinger et al., 1989&, 1993b; Delvaux and Hanon, 1993; Delvaux et al., 2010; Fontijn et al., 2010a; Alexander et al., 2016; Rizzello et al., 2022) show an extensive NW-SE (Rukwa rift fault system) trending fault zone which cuts through the Rungwe and Ngozi volcanoes, which we identify as the Ngozi-Rungwe fault zone (**NRFZ**). The location of the shallow low-resistivity layer **RNCA** is strongly correlated with **NRFZ** as shown in the horizontal map slice at elevation 1000 m a.s.l in Fig. 8. We therefore, interpret the **RNCA** as a result of enhanced alteration due to hydrothermal circulation along the **NRFZ** that formed an extensive clay cap over the investigated area. The same interpretation applies to **UCA**, that is correlated with the Usangu fault zone, a NE-trending feature (Usangu rift trend) north of the Ngozi caldera. that is correlated with the low-resistivity cap **UCA**.

**C2a** anomaly likely represents a possible continuation of the NRFZ to the northwest. The margin of the **C2b** anomaly correlates with the Mbeya front range fault. $NaHCO_3$ warm springs are located over anomalies **C2a** and **C2b** (8 km and 7-12 km NW and west of the Ngozi caldera, respectively). They have been interpreted as conductively heated meteoric water at ~120–130°C (Josephat, 2016; Alexander et al., 2016).

### 6.3. The Ndaga ring structure

The analysis of the digital elevation model suggests the existence of a cauldron-like feature of about 15 km in diameter located north of the Rungwe volcano and encompassing the Ngozi caldera (Figs. 8 and 11). We name it the 'Ndaga ring structure' after the nearby town of Ndaga. The Ndaga ring structure is surrounded by phonolite domes (Fig. 11) that can be identified in the resistivity slices as thick resistive anomalies that reach the surface. To the east and southeast, phonolites extend from the Usangu basin and are covered by young ash pumice in the vicinity of the Ngozi volcanic dome (Alexander et al., 2016). The phonolite dome in the west near the Shiwaga $CO_2$ gas vents is a part of the western rim of the Ndaga ring structure while the northern rim is identified by the

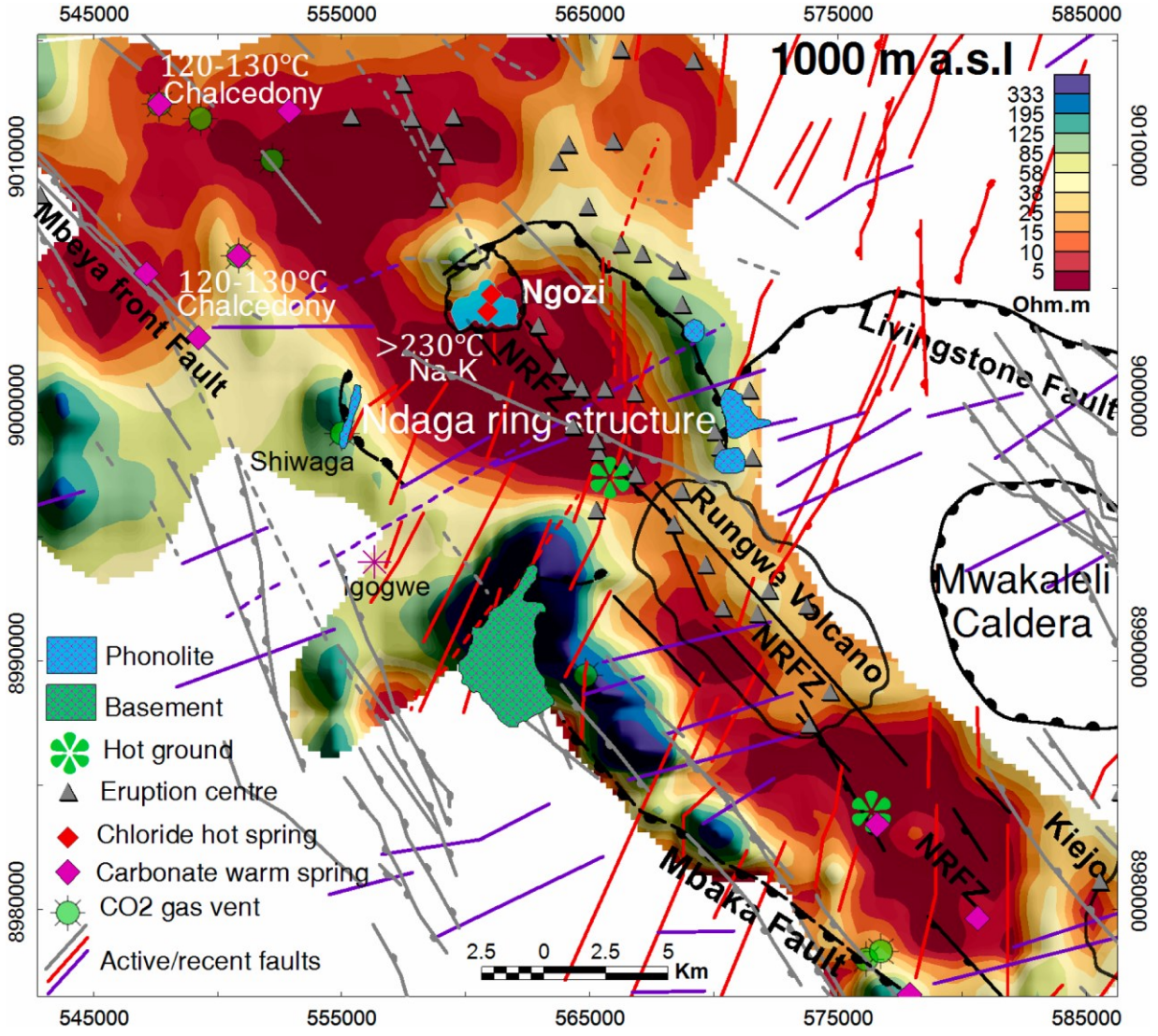


**Fig. 11.** Horizontal resistivity depth slice at 1000 m a.s.l with the possible concealed Ndaga ring structure (new inferred caldera) superimposed. The outline of the caldera is defined by the curvilinear resistive anomaly and the presence of the phonolite domes.

resistive anomaly of the Ngozi dome (PL1 in Fig. 10).

Permeability may be enhanced within the Ndaga ring structure by the intersection of at least three sets of fault systems including the NE-SW Usangu trend fault system, the N-S Nyasa rift trend fault system and the extensive NW-SE Rukwa rift fault system trending fault zone that cut through the Ngozi and Rungwe volcanoes (Fig. 11). From a volcanological perspective, the Ndaga ring structure was likely reactivated between ca. 4 ka and 1 ka by at least 10 small volcanic eruption centres identified by Ebinger et al. (1989) and Fontijn et al. (2012). Within the Ndaga ring structure, the thickness of the **RNCA** clay cap is greatest to the south (see TL6 in Fig. 9 and PL1 in Fig. 10) where hot ground >53°C at 70 cm below surface has been mapped recently (TGDC, 2022), west and northwest near the Ngozi caldera (see TL2, TL6 in Fig. 9), while thinning to the east and southeast near the Rungwe volcano (see PL1 in Fig. 10).

### 6.4. Possible magmatic chambers

A deep conductor **C3** occurs at a depth of about 6 km below the Ndaga ring structure (slice 6000 m b.s.l in Fig. 8, TL2 and TL6 in Fig. 9). This conductive anomaly has been interpreted as a partial melt related to a magmatic chamber. The conductor depth is coherent with the estimated depth of a possible magma chamber inferred by Alexander et al. (2016) based on the co-existence of biotite and hauyne in the trachytic pumice from Rungwe volcano (Fontijn et al., 2013). A second low resistivity zone **C4** occurs below the Tukuyu volcano to the SE of the Rungwe volcano (slice 6000 m b.s.l in Fig. 8, TL5 in Fig. 9), in the vicinity of the Kiejo volcano. However, being located at the edge of the survey area with limited MT station coverage, it is not discussed further here.

Similar conductive features have been interpreted as magma bodies at other volcanoes, for instance below the Kirishima volcano on Kyushu Island, Japan (Aizawa et al., 2014), below the Tengchong volcano on the south-eastern Tibetan Plateau (Ye et al., 2018) and in the Ethiopian rift segment of the EARS (Didana et al., 2015; Samrock et al., 2021; Samrock et al., 2023).

It must also be stressed that undetected smaller magmatic sources are possible, given the decreasing resolution capability of MT investigations with depth (e.g. Piña-Varas et al., 2018; Lee et al., 2020) and therefore, cannot be completely excluded. For instance, where magma has actually been demonstrated by drilling at developed geothermal fields, such as Menengai in the EARS in Kenya (Mbia et al., 2015; Mutonga and Mungai, 2017), MT resistivity models were not interpreted to image any relatively shallow magma body.

### 6.5. New geothermal conceptual model for the Ngozi-Rungwe system

Because of its unusual geochemistry and hydrology, investigators have proposed a variety of geothermal conceptual models for the Ngozi geothermal system (see subchapter 3) but, because of a lack of relevant data, no model has yet been proposed for Rungwe.

In our proposed geothermal conceptual model shown in Fig. 13, based on the new extended 3D resistivity model, we have integrated all the available geological, structural, geochemical and geophysical results. Two separate geothermal upflows and >230˚C reservoirs are proposed below the Ngozi and Rungwe volcanoes, respectively.

### 6.6. Clay cap

The conductive layer **RNCA** with resistivity 1-15 Ωm is interpreted as a typical low-temperature smectite alteration zone with high cation exchange capacity (CEC) values (Ussher et al., 2000; Lévy et al., 2018; Rizzello et al., 2021, 2022; Hersir et al., 2022), sealing possible underlying geothermal reservoirs (Cumming, 2016a; Cumming and Mackie, 2010; Muñoz, 2014). In profile PL1 in Fig. 10, the base of the clay cap **RNCA** shows a large up doming below the Rungwe volcano. Below the Ngozi caldera, clay cap **RNCA** is interpreted as being truncated by the high resistivity impermeable metamorphic basement **R2-Ngozi** (Fig. 10), consistent with the shallow models by Alexander et al. (2016) and Didas and Hersir (2021). Recent geological mapping by TGDC in the study area identified intense hydrothermal alteration of a sedimentary formation exposed on the southern flank of the Rungwe volcano (Fig. 12) which corresponds to the identified conductive clay cap (TGDC, 2022). Additionally, the clay cap might also be formed by the altered old basalts overlaying the Cretaceous and Karoo sedimentary formations.

It is important to note that the location of the largest thickness of clay cap layer **RNCA** at the flanks of the Rungwe volcano corresponds to the hot grounds and fault intersections (Fig. 13), likely indicating enhanced permeability for geothermal fluid circulation on the edge of the reservoir. North of the Ngozi caldera, the conductive layer **UCA** might be locally capping an additional secondary low-temperature geothermal system suggested by Alexander et al. (2016). However, although parts of the **UCA** very likely act as a clay cap to the deep circulation geothermal system at Songwe, most of the **UCA** probably correlates with lake sediments and weathered volcanoclastics, as confirmed by erosion that has exposed these formations near Songwe (Hinz et al., 2018).

### 6.7. Geothermal reservoirs

#### 6.7.1. Ngozi reservoir

The existence of the proposed reservoir >230˚C below Ngozi, consistent with the model by Alexander et al. (2016), is based on available evidence including the chloride hot springs in the caldera area (Fig. 13b).

The outflow from the Ngozi reservoir is limited by the impermeable Proterozoic basement surrounding the Ngozi volcanic edifice. Nevertheless, a significant amount of NaCl was measured in Igogwe River in the SW of the Ngozi caldera (Fig. 13a) and has been associated with the outflow of the Ngozi reservoir (UNEP/ARGeo, 2016), likely controlled by secondary permeability induced by some mapped Usangu rift trend faults (Fig. 13a).

The heat source for the small prospective reservoir below the Ngozi caldera is proposed to be a magma chamber (imaged by **C3** anomaly on slice 6000 m b.s.l in Fig. 8 and sections TL2, TL6 in Fig. 9) at a depth of 5 to 8 km.

The Ngozi geothermal system is likely recharged locally by the meteoric water infiltrating the Ngozi highlands as suggested by the study of stable isotopes of oxygen, $\delta^{18}O$, and hydrogen, δD of the hot springs at the bottom of the Ngozi caldera Lake (Alexander et al., 2016).

#### 6.7.2. Rungwe reservoir

The main evidence of the existence of the Rungwe reservoir is the typical (e.g. Hersir et al., 2022) imaged up-dome at the base of the clay cap below the Rungwe volcano, associated with the presence of (i) areas of hot ground to the northwest and southeast flanks related to either conductively heated groundwater or condensed steam, (ii) hot springs to the south, and (iii) $CO_2$ seeps where the clay cap terminates to the west (Fig. 13a and b). Although the $CO_2$ in the seeps has been interpreted to be of mantle origin (Delalande et al., 2011), it is possible that the $CO_2$ of deep origin is a component of the leakage from the prospective geothermal reservoir.

The reservoir volume is constrained by the updome at the base of the low resistivity smectite zone below the Rungwe volcanic edifice, capping a >1000 m thick relatively high resistivity zone which we interpret as made by permeable volcanic and sedimentary formations (Fig. 13b) affected by high-temperature low-conductivity alteration (e.g. Muñoz, 2014). The bottom of the reservoir is likely marked by the impermeable Proterozoic metamorphic basement at unknown depth. The sparse bicarbonate thermal manifestations, the lack of a chloride

**Fig. 12.** Outcropped altered clay-rich sandstone at the footwall of the Mbaka fault south of the Rungwe volcano imaged as the very conductive formation in the MT soundings. Photo by Ariph Kimani, October 25, 2022.

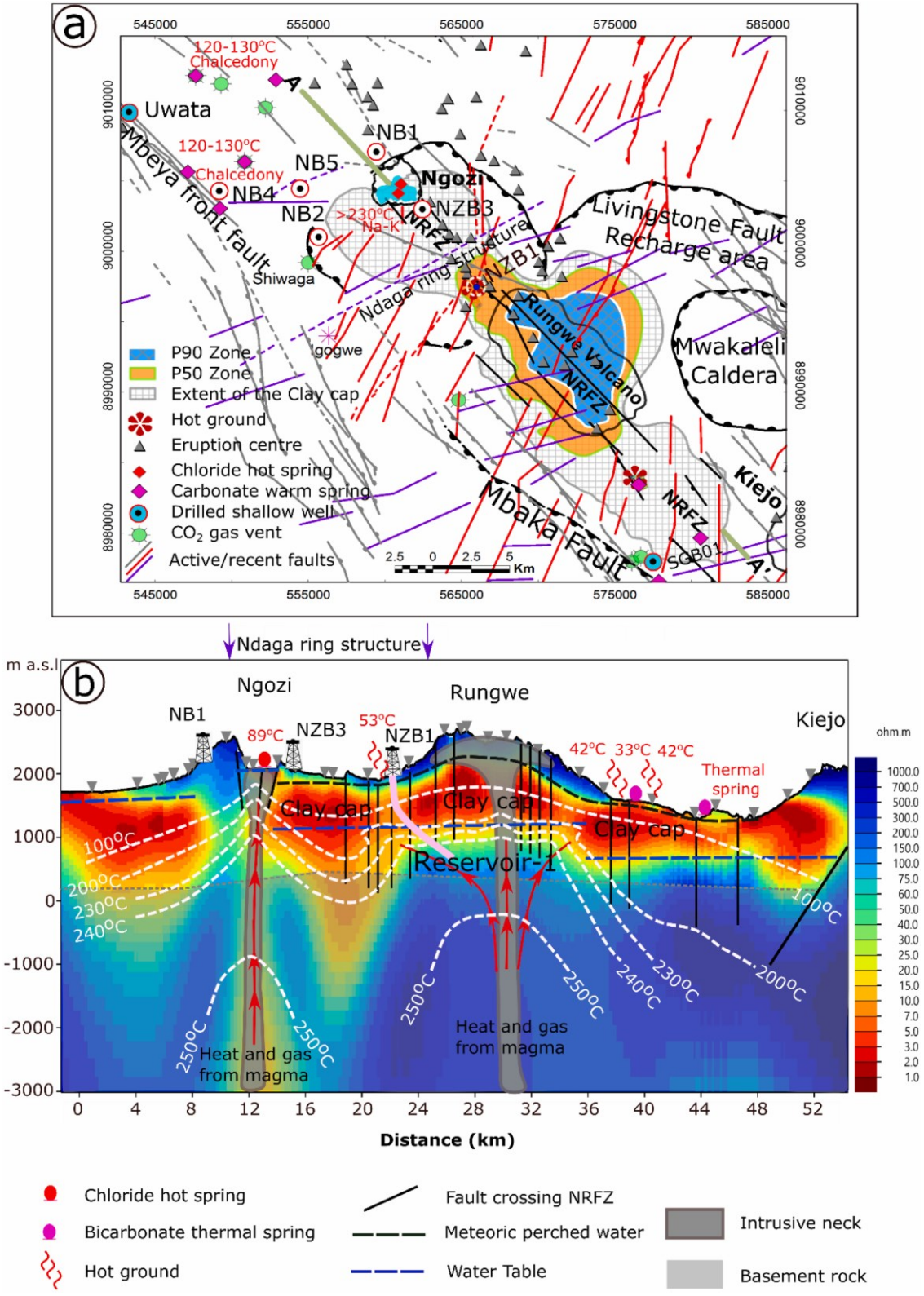


**Fig. 13.** Our proposed updated geothermal conceptual model based on the integrated geoscientific results. **(a)** Prospective resource minimum (P90 zone), medium (P50 zone) and maximum (P10 zone represented by the extent of the clay cap) boundaries with a confidence level 90%, 50% and 10%, respectively, estimated on the base of the geometry of the clay cap, surface manifestation and mapped faults. **(b)** A model consisting of two separate reservoirs, beneath Rungwe and Ngozi volcanoes, respectively. The 100°C to 250°C white dotted lines indicate tentative isothermal lines qualitatively traced on the base of the resistivity distribution. The arrows indicate the inferred flow direction of the geothermal fluids. The separate 250°C zones define the upflows.

outflow, and the association with the spring south of Rungwe are consistent with an effectively sealed high temperature geothermal reservoir.

Some inferences about the lateral boundaries of the Rungwe reservoir are based on the following observations. Northwest of Rungwe, the reservoir may be limited by the low permeability outcropping Proterozoic metamorphic basement (Fig. 11) or by a low permeability and low resistivity smectite clay rich cap made by low temperature altered volcaniclastics and sediments that directly overlie the basement (Fig. 13b). To the west of Rungwe, Proterozoic rocks outcrop, which are not directly overlain by conductive volcaniclastic with high smectite content. To the southeast, the resistivity pattern suggests again a zone of thick volcaniclastics and sediments containing smectite clay that likely directly overlie low permeability Proterozoic metamorphic rocks. The eastern boundary remains unknown due to a limited number of MT soundings (Fig. 8, slices 1600 m a.s.l down to 1000 m a.s.l, TL3 and TL4 in Fig. 9).

The local water table below Rungwe is expected to be isolated by low permeability smectite-bearing sediments and volcaniclastics that directly overlie low permeability Proterozoic metamorphic rocks (Fig. 13b). At Ngozi, the water table is expected at a much higher elevation given by the Ngozi caldera Lake neutral chloride water level (Fig. 13b). On the other end, the water table level associated with the Kiejo deep circulation geothermal system to the southeast (Fig. 13b) is expected to be at a lower level than the Rungwe one.

The recharge area for the Rungwe system may be located to the NE of the volcano, in the highlands that represent the west extension of the Elton plateau. This interpretation is supported by the observed several sets of NE-SW faults in this area. The Livingstone fault escarpments bounding the eastern side of the Malawi rift basin, that rise 1 km or more above the mean regional topography (Ebinger et al., 1993b) forming the curvilinear geometry east of the Rungwe volcano (Fig. 13a), likely represent the possible main recharge features through which the meteoric water infiltrates into the reservoir below the Rungwe volcano. Since the Livingstone fault is supposed to reach down to ~20 km (Ebinger et al., 2019), it is likely that the waters that recharge the geothermal system through this fault percolate deep enough to be heated by deep heat sources below the Rungwe volcano. Alternatively, the Rungwe system may be recharged locally by the meteoric water infiltrating the Rungwe highlands over an area of 20 km where the water table is higher (Fig. 13b).

### 6.8. Risk assessment of the proposed drilling locations

The proposed locations of slim wells NB1, NB2, NB4, NB5 (Alexander et al., 2016), and NZB3 (Didas and Hersir, 2021), shown in Figs. 4 and 13 may be assessed on the base of our new resistivity model. Our results indicate that NB1, which is located about 3 km north of the Ngozi caldera, will penetrate through a resistive body interpreted here as an impermeable Precambrian metamorphic basement/phonolite dome. NB5 and NB2, which are located about 4 km west of the Ngozi caldera, are located over an outflow zone far from the Ngozi prospective geothermal system. NB4, located 7.5 km west of the Ngozi caldera near Swaya warm spring, would intersect the low-temperature reservoir corresponding to the **C2b** conductive anomaly in the Mbeya front fault. NZB3 is located 1.5 km south of the Ngozi caldera and 6.5 km northwest of the main upflow zone of the prospective geothermal reservoir beneath the Rungwe volcano. It is located above the deep conductor **C3** interpreted as a magmatic heat source located between the Ngozi and Rungwe volcanoes below the Ndaga ring structure. The Ndaga ring structure is intersected by the NW, NS and NE trending fault systems (see Fig. 13) and is characterised by hot ground >53 °C, a widespread thick clay cap and many small young volcanic eruption centres which could enhance fluid temperature if the associated dikes are cooling intrusives. High-density intersections of faults within the caldera suggest an enhanced permeability that might facilitate the hydrothermal convective process. It is expected that NZB3 will intersect the closest outflow zone of the Ngozi prospective geothermal system at a depth of about 1500 m which discharges the chloride hot springs at the bottom of the Ngozi caldera. Based on our results we suggest, therefore, a new directional exploratory well NZB1 located at the northern flank of the Rungwe volcano (Fig. 13) directed towards the resistivity up-dome.

Because no geothermal wells have been drilled so far in the area, direct information on the subsurface temperature and permeability is lacking. Uncertainties in the presented conceptual model include the possibility that (i) part of the **RNCA** conductive layer may be generated by highly conductive sediments not necessarily representing a hydrothermal low temperature cap or that (ii) cold water might downflow through volcanic vents that breach the clay cap and cool the underlying reservoir as it has been shown to occur at some geothermal reservoirs throughout the EARS (Kandie et al., 2016; Mibei et al., 2016; Lichoro, 2019). In such a case, the resistivity pattern might reflect an earlier period of higher temperature that has now cooled down. The benefits of a conceptual model approach to target geothermal wells include the integration of all relevant data and the identification of data gaps that might reduce uncertainty and risk.

Therefore, we recommend that further research should include seismic monitoring to evaluate the presence of a magma chamber below Ngozi and Rungwe and detailed structural mapping to define the permeability of the geothermal system below Rungwe volcano. The detailed geothermal-focused structural and reservoir rock property assessment of Ngozi and Rungwe would follow up on the regional work of Delvaux et al. (2010). A dense gravity survey might improve assessments of the resource boundaries and capacity. Geochemical assessment (still lacking) of the newly identified warm spring at the SE flank of Rungwe volcano could help to establish the correlations with the Rungwe prospective reservoir and the areas of hot ground. Additional MT data to the east of Rungwe could better constrain the edge of the prospective reservoir.

## 7. Conclusions

Our interpretation of the new 3D electrical resistivity model integrated with the geological and geochemical evidence supports the hypothesis that the Ngozi and Rungwe geothermal systems are likely to have larger prospective capacity than the previous studies suggested. In our new geothermal conceptual model, we have considered two separate magmatically heated reservoirs below Rungwe and Ngozi volcanoes. The main reservoir zone with geochemically estimated maximum temperature >230 °C, has been imaged below the Rungwe volcano, indicated by a 20 km x 5 km up doming of the clay cap. This interpretation is based on evidence of heat loss (hot ground) and the transition from low resistivity smectite clay to higher resistivity that is characteristic of geothermal fields. Because no outflow has been detected and the reservoir margins seem to be sealed, it is possible that the geothermal reservoir below Rungwe might be vapour-dominated.

The accumulation of the geothermal water inside the Ngozi caldera is likely caused by the presence of the impermeable Precambrian basement/phonolite dome that prevents the flow of the high-temperature geothermal reservoir water further to the north. The surficial outflow from above the geothermal system below the Ngozi volcano is directed to SE into the Igogwe river, where relatively high concentrations of chloride and sodium ions have been measured. The warm springs NW and W of the Ngozi caldera are associated with conductively heated meteoric water flowing along parallel fracture zones affecting the impermeable Precambrian basement.

The Ngozi-Rungwe geothermal system may, therefore, generally be considered as a semi-blind system. This system is assumed to have a very effective clay cap with bounding structures sealing the geothermal reservoirs except at the outflow terminations at the Ngozi caldera Lake, where the reservoir(s) discharges the chloride hot springs. The Ngozi geothermal reservoir is recharged by local meteoric water while the reservoir below Rungwe volcano is likely recharged from either NE of

Rungwe in the west extension of Elton highlands through the Livingstone faults or recharged locally by meteoric water infiltrating the Rungwe highlands.

Because no geothermal wells have been drilled in the area to test the proposed conceptual models and significant uncertainty remains, before drilling we recommend conducting follow-up geochemistry analyses of recently sampled springs, additional MT to constrain the east margin of Rungwe, detailed structural geology and stratigraphic mapping to better predict permeable zones and reservoir margins, and seismic monitoring to characterize magmatic heat source(s). The focus of these studies will be to improve the Rungwe geothermal conceptual model because it has more upside potential than Ngozi.

## CRediT authorship contribution statement

**Makoye Mabula Didas:** Conceptualization, Methodology, Software, Formal analysis, Writing – original draft, Writing – review & editing. **Egidio Armadillo:** Conceptualization, Methodology, Data curation, Resources, Writing – review & editing. **Gylfi Páll Hersir:** Funding acquisition, Project administration, Writing – review & editing, Supervision, Resources. **William Cumming:** Resources, Writing – review & editing, Supervision. **Daniele Rizzello:** Supervision, Writing – review & editing. **Ásdís Benediktsdóttir:** Software, Supervision, Writing – review & editing. **Halldór Geirsson:** Supervision.

## Declaration of Competing Interest

The authors declare that they have no known competing financial interests or personal relationships that could have appeared to influence the work reported in this paper.

## Data availability

The authors do not have permission to share data.

## Acknowledgments

This research is financially supported by the GRÓ Geothermal Training Programme in Iceland (GRÓ GTP) under the auspices of UNESCO (formerly UNU-GTP). It is a part of the PhD programme of the first author carried out at the University of Iceland. The geophysical database was provided by the Tanzania Geothermal Development Company (TGDC). The authors would like to express their gratitude to TGDC for the permission to use their GeoTools licence using CGG server computing facilities. We greatly acknowledge the support from CGG including Alice Pavesi and Wolfgang Soyer on the use of GeoTools software. Furthermore, we thank ModEM Geophysics for providing an academic license to the ModEM software for the 3D MT inversion. We are thankful to Naser Meqbel for useful discussions, and insights on the use of the ModEM software. Iceland GeoSurvey (ÍSOR) is thanked for helping with running the 3D MT inversion. We acknowledge the extensive reviews from the anonymous reviewers that have greatly improved the manuscript.

## References

Aizawa, K., Koyama, T., Hase, H., Uyeshima, M., Kanda, W., Utsugi, M., et al., 2014. Three-dimensional resistivity structure and magma plumbing system of the Kirishima Volcanoes as inferred from broadband magnetotelluric data. J. Geophys. Res. Solid Earth 119, 198–215. https://doi.org/10.1002/2013JB010682.

Alexander, K., Cumming, W.B., Malini, L., 2016. Technical review of the geothermal potential of Ngozi and Songwe geothermal prospects. In: Proceedings of the 6th African Rift Geothermal Conference. Addis Ababa, Ethiopia.

Anderson, E., Crosby, D., Ussher, G., 2000. Bulls-eye! - Simple resistivity imaging to reliably locate the geothermal reservoir. In: Proceedings of the World Geothermal Congress. Kyushu - Tohoku, Japan.

Ardid, A., Archer, R., Bertrand, E., Sepulveda, F., Tarits, P., Dempsey, D., 2021. Heat transfer through the Wairakei-Tauhara geothermal system quantified by multi-channel data modeling. Geophys. Res. Lett. 48, e2020GL092056 https://doi.org/10.1029/2020GL092056.

Armadillo, E., Rizzello, D., Pasqua, C., Pisani, P., Ghirotto, A., Didas, M., et al., 2020. Geophysical constraints on the Luhoi (Tanzania) geothermal conceptual model. Geothermics 87, 101875. https://doi.org/10.1016/j.geothermics.2020.101875.

Asnin, S.N., Nnko, M., Josephat, S., Mahecha, A., Mshiu, E., Bertotti, G., Brehme, M., 2022. Identification of water–rock interaction of surface thermal water in Songwe medium temperature geothermal area, Tanzania. Environ. Earth Sci. 81, 513. https://doi.org/10.1007/s12665-022-10594-4.

Árnason, K., 2015. The static shift problem in MT soundings. In: Proceedings of the World Geothermal Congress 2015, Melbourne, Australia.

Bendat, J.S., Piersol, A.G., 1971. Random Data: Analysis and Measurement Procedures. John Wiley, New York. ISBN: 978-0-470-24877-5.

Boniface, N., 2019. An overview of the Ediacaran-Cambrian orogenic events at the southern margins of the Tanzania craton: implication for the final assembly of Gondwana. J. Afr. Earth Sci. 150, 123–130. https://doi.org/10.1016/j.jafrearsci.2018.10.015.

Catuneanu, O., Wopfner, H., Eriksson, P.G., Cairncross, B., Rubidge, B.S., Smith, R.M.H., Hancox, P.J., 2005. The Karoo basins of south-central Africa. J. Afr. Earth Sci. 43, 211–253. https://doi.org/10.1016/j.jafrearsci.2005.07.007.

Chave, A., Jones, A., 2012. The Magnetotelluric Method: Theory and Practice. Cambridge University Press. https://doi.org/10.1017/CBO9781139020138. A. Chave and A. Jones (eds.).

Chave, A.D., Thomson, D.J., 1989. Some comments on magnetotelluric response function estimation. JGR 94, 14215–14225. https://doi.org/10.1029/JB094iB10p14421.

Cumming, W., Mackie, R., 2010. Resistivity imaging of geothermal resources using 1D, 2D and 3D MT inversion and TDEM static shift correction illustrated by a glass mountain case history. In: Proceedings of the World Geothermal Congress, Bali, Indonesia.

Cumming, W., 2016a. Geophysics and resource conceptual models in geothermal exploration anddevelopment. Geotherm. Power Gener. 33–75. https://doi.org/10.1016/B978-0-08-100337-4.00003-6 (Chapter 3).

Cumming, W., 2016b. Resource conceptual models of volcano-hosted geothermal reservoirs for exploration well targeting and resource capacity assessment: construction, pitfalls and challenges. GRC Trans. 40, 2016.

Cumming, W., 2016c. Resource capacity estimation using lognormal power density from producing fields and area from resource conceptual models; advantages, pitfalls and remedies. In: Proceedings of the 41 st Workshop on Geothermal Reservoir Engineering. Stanford University, Stanford, California.

Delvaux, D., Kraml, M., Sierralta, M., Wittenberg, A., Mayalla, J.W., Kabaka, K., Makene, C., GEOTHERM working group, 2010. Surface exploration of a viable geothermal resource in Mbeya Area, Sw Tanzania. Part I: geology of the Ngozi - Songwe Geothermal System. In: Proceedings of the World Geothermal Congress, Bali, Indonesia.

Delvaux, D., Kervyn, F., Vittori, E., Kajara, R.S.A., Kilembe, E., 1998. Late Quaternary tectonic activity and lake level change in the Rukwa Rift Basin. J. Afr. Earth Sci. 26, 397–421. https://doi.org/10.1016/S0899-5362(98)00023-2.

Delvaux, D., Hanon, M., 1993. Neotectonics of the Mbeya Area, SW Tanzania. Royal Museum for Central Africa, Tervuren, Belgium, pp. 87–97. Annual reports 1991–1992.

Delvaux, D., Levi, K., Kajara, R., Sarota, J., 1992. Cenozoic palaeostress and kinematic evolution of the Rukwa–North Malawi rift valley (East African Rift System). Bull. Cent. Rech. Explor. Prod. Elf Aquitaine 16, 383–406.

Delalande-Le, M.M., Gherardi, F., Williamson, D., Kajula, S., Kraml, M., Noret, A., Abdallah, I., Mwandapile, E., Massault, M., Majule, A., Bergonzini, L., 2015. Hydrogeochemical features of Lake Ngozi (SW Tanzania). J. Afr. Earth Sc. https://doi.org/10.1016/j.jafrearsci.2014.11.004.

DECON, SWECO and Inter-Consult, 2005. Tanzanian Rural Electrification Study – Technical Report on Geothermal Power – Activity 1.4.1, Dar es Salaam, Tanzania, 22 pp. plus 24 appendices. Unpublished report.

Delalande, M., Bergonzini, L., Gherardi, F., Guidi, M., Andre, L., Abdallah, I., Williamson, D., 2011. Fluid geochemistry of natural manifestations from the southern Poroto-Rungwe hydrothermal system (Tanzania): preliminary conceptual model. J. Volcano Geotherm. Res. 199, 127–141. https://doi.org/10.1016/j.jvolgeores.2010.11.002.

Didas, M.M., Hersir, G.P., 2021. 1D joint inversion of MT and TEM data from Ngozi geothermal prospect, southwest Tanzania. An integrated interpretation of geoscientific results. In: Proceedings of the World Geothermal Congress 2020+1, Reykjavik, Iceland.

Didas, M.M., 2018. 1D Joint Inversion of MT and TEMData from Ngozi Geothermal Prospect, Southwest Tanzania: an Integrated Interpretation of Geoscientific Results. United Nations University, Geothermal Training Programme, Reykjavik, Iceland. https://rafhladan.is/bitstream/handle/10802/18944/UNU-GTP-2018-13.pdf?sequence=1.

Didas, M.M., Armadillo, E., Hersir, G.P., Cumming, W., Rizzello, D., 2022. Regional thermal anomalies derived from magnetic spectral analysis and 3D gravity inversion: Implications for potential geothermal sites in Tanzania. Geothermics 103 (2022), 10243. https://doi.org/10.1016/j.geothermics.2022.102431.

Didana, Y.L., Thiel, S., Heinson, G., 2015. Three-dimensional conductivity model of the Tendaho high enthalpy geothermal field, NE Ethiopia. J. Volcanol. Geotherm. Res. 290, 53–62. https://doi.org/10.1016/j.jvolgeores.2014.11.013.

Dypvik, H., Nesteby, H., Ruden, F., Aagard, P., Johansson, T., Msindai, J., Massay, C., 1990. Upper paleozoic and mesozoic sedimentation in the Rukwa-Tukuyu Region,

Tanzania. J. Afr. Earth Sci. 11, 437–456. https://doi.org/10.1016/0899-5362(90)90022-7.

Ebinger, C.J., Deino, A.L., Drake, R.E., Tesha, A.L., 1989. Chronology of volcanism and rift basin propagation – Rungwe Volcanic Province, East Africa. J. Geophys. Res. 94, 15785–15803. https://doi.org/10.1029/JB094iB11p15785.

Ye, T., Huang, Q., Chen, X., Zhang, H., Chen, Y.J., Zhao, L., Zhang, Y., 2018. Magma chamber and crustal channel flow structures in the Tengchong volcano area from 3-D MT inversion at the intracontinental block boundary southeast of the Tibetan Plateau. J. Geophys. Res. Solid Earth 123. https://doi.org/10.1029/2018JB015936, 11,112–11,126.

Ebinger C., Klerkx J., Delvaux D., Wüest A., 1993a. Evaluation of natural hazards in the northern part of the Malawi rift (Tanzania). Mus Roy Afr Centr Tervuren (Belg.). Dépt. Géol. Min., Rapp. Ann. 1991–1992, 83–86.

Ebinger, C.J., Deino, A.L., Tesha, A.L., Becker, T., Ring, U., 1993b. Tectonic controls on rift basin morphology – Evolution of the Northern Malawi (Nyasa) Rift. J. Geophys. Res. Solid Earth 98, 17821–17836. https://doi.org/10.1029/93JB01392.

Ebinger, C.J., Oliva, S.J., Pham, T.Q., Peterson, K., Chindandali, P., Illsley-Kemp, F., et al., 2019. Kinematics of active deformation in the Malawi rift and Rungwe Volcanic Province, Africa. Geochem. Geophys. Geosyst. 20, 3928–3951. https://doi.org/10.1029/2019GC008354.

Egbert, G.D., Kelbert, A., 2012. Computational recipes for electromagnetic inverse problems. Geophys. J. Int. 189 (1), 251–267. https://doi.org/10.1111/j.1365-246X.2011.05347.x.

EAGER, 2018. Enhanced resource modelling at Songwe. TGDC Unpublished internal report number T74 – D05, p. 30.

ELC, TGDC, 2017. Surface Exploration and Training in Kiejo-Mbaka Geothermal Area, Tanzania. TGDC internal unpublished technical report, p. 98.

Fontijn, K., Elburg, M.A., Nikogosian, I.K., van Bergen, M.J., Ernst, G.G.J., 2013. Petrology and geochemistry of Late Holocene felsic magmas from Rungwe volcano (Tanzania), with implications for trachytic Rungwe Pumice eruption dynamics. Lithos 177, 34–53. https://doi.org/10.1016/j.lithos.2013.05.012.

Fontijn, K., Williamson, D., Mbede, E., Ernst, G.G.J., 2012. The Rungwe volcanic province, Tanzania-a review. J. Afr. Earth Sci. 63, 12–31. https://doi.org/10.1016/j.jafrearsci.2011.11.005.

Fontijn, K., Ernst, G.G.J., Bonadonna, C., Elburg, M.A., Mbede, E., Jacobs, P., 2011. The 4 ka Rungwe Pumice (SW Tanzania): a wind-still Plinian eruption. Bull. Volcanol. 73, 1353–1368. https://doi.org/10.1007/s00445-011-0486-8.

Fontijn, K., Delvaux, D., Ernst, G.G.J., Kervyn, M., Mbede, E., Jacobs, P., 2010a. Tectonic control overactive volcanism at a range of scales: case of the Rungwe Volcanic Province, SW Tanzania; and hazard implications. J. Afr. Earth Sci. 58, 764–777. https://doi.org/10.1016/j.jafrearsci.2009.11.011.

Fontijn, K., Ernst, G.G.J., Elburg, M.A., Williamson, D., Abdallah, E., Kwelwa, S., Mbede, E., Jacobs, P., 2010b. Holocene explosive eruptions in the Rungwe Volcanic Province, Tanzania. J. Volcanol. Geotherm. Res. 196, 91–110. https://doi.org/10.1016/j.jvolgeores.2010.07.021.

Fritz, H., Abdelsalam, M., Ali, K., Bingen, B., Collins, A., Fowler, A., et al., 2013. Orogen styles in the East African Orogen: a review of the Neoproterozoic to Cambrian tectonic evolution. J. Afr. Earth Sci. 86, 65–106. https://doi.org/10.1016/j.jafrearsci.2013.06.004.

Gamble, T.D., Goubau, W.M., Clarke, J., 1979. Magnetotellurics with a remote magnetic reference. Geophysics 44, 53–68. https://doi.org/10.1190/1.1440923.

Gibert, E., Bergonzini, L., Massault, M., Williamson, D., 2002. AMS-14C chronology of 40.0 cal ka BP continuous deposits from a crater lake (Lake Massoko, Tanzania): Modern water balance and environmental implications. Palaeogeogr. Palaeoclimatol. Palaeoecol. 187 (3–4), 307–322. https://doi.org/10.1016/S0031-0182(02)00483-2.

Harkin, D.A., 1960. The Rungwe Volcanics at the northern end of Lake Nyasa. Geological Survey of Tanganyika, Dodoma, 172pp.

Hersir, G.P., Kristinsson, S.G., Mnjokava, T., 2015. Tanzania visit in January 2015. Assessment of areas for surface exploration studies and training needs. Internal Report Prepared for TGDC with Funding from ICEIDA. Iceland GeoSurvey. Report number ÍSOR-2015/025. 48pp.

Hersir, G.P., Weisenberger, T.B., 2015. Rungwe Volcanic Region, SW-Tanzania - A proposal for surface exploration studies prepared for TGDC, Supported by ICEIDA/NDF. Iceland GeoSurvey, short report ÍSOR-15048,, 11p.

Hersir, G.P., Guðnason, E.Á., Flóvenz, Ó.G., 2022. Geophysical exploration techniques. Compr. Renew. Energy 7, 26–79. https://doi.org/10.1016/B978-0-12-819727-1.00128-X.

Hinz, N., Cumming, W.B., Sussman, D., 2018. Exploration of fault-related deep circulation geothermal resources in the western branch of the East African rift system: examples from Uganda and Tanzania. In: Proceedings of the 7th African Rift Geothermal Conference. Kigali, Rwanda.

Hochstein, M.P., Temu, E.P., Moshy, C.M.A., 2000. Geothermal resources of Tanzania. In: Proceedings of the World Geothermal Congress, Kyushu-Tohoku, Japan, May 28 - June 10, 2000, pp. 1233–1238.

Iliceto, V., Santarato, G., 1999. On the interference of man-made EM fields in the magnetotelluric "dead band. Geophys. Prosp. 47, 707–719. https://doi.org/10.1046/j.1365-2478.1999.00153.x.

Ivanov, A.V., Rasskazov, S.V., Boven, A., Punzalan, L., Brandt, I.S., Brandt, S.B., Fernandez Alonso, M., 1999. Timing and Late Cenozoic volcanic activity and rift basin formations in the Rungwe province of Tanzania substantiated by K–Ar and 40Ar/39Ar dating. In: Proceedings of the Rifting in Intracontinental Setting: Baikal Rift System and Other Continental Rifts, 22–30 August 1999, Irkutsk and Lake Baikal, Russia.

Jiracek, G., 1990. Near-surface and topographic distortions in electromagnetic induction. Surv. Geophys. 11, 163–203. https://doi.org/10.1007/BF01901659 v.

Jolie, E., 2019. Detecting gas-rich hydrothermal vents in Ngozi crater Lake using integrated exploration tools. Nat. Sci. Rep. 9 (2019), 12164. https://doi.org/10.1038/s41598-019-48576-5.

Josephat, S., 2016. Geothermometry and Quantifying of Mixing and Water-Rock Interactions in the Ngozi Geothermal Field, SW-Tanzania. UNU-GTP, Iceland, pp. 289–310. Report 26pp.

Kajugus, S.I., Kabaka, K.T., Mnjokava, T.T., 2021. Tanzania geothermal resources development – Current status. In: Proceedings of the World Geothermal Congress 2020+1. Reykjavik, Iceland.

Kalberkamp, U., Schaumann, G., Ndonde, P.B., Chiragwile, S.A., Mwano, J.M, GEOTHERM Working Group, 2010. Surface exploration of a viable geothermal resource in Mbeya area, SW Tanzania. Part III: geophysics. In: Proceedings of the World Geothermal Congress. Bali, Indonesia, p. 6.

Karingithi, C.W., Arnórsson, S., Grönvold, K., 2010. Processes controlling aquifer fluid compositions in the Olkaria geothermal system, Kenya. J. Volcanol. Geoth. Res. 196, 57–76. https://doi.org/10.1016/j.jvolgeores.2010.07.008.

Kelbert, A., Meqbel, N., Egbert, G.D., Tandon, K., 2014. ModEM: a modular system for inversion of electromagnetic geophysical data. Comput. Geosci. 66, 40–53. https://doi.org/10.1016/j.cageo.2014.01.010.

Kandie, R., Mbuthia, P., Stimac, J., 2016. Use of leapfrog geothermal software in data integration and 3D visualization case study of Olkaria. In: Proceedings of the 6th ARGeo Conf. Addis Ababa, Ethiopia.

Kraml, M., Schaumann, G., Kalberkamp, U., Stadtler, C., Delvaux, D., Ndonde, P.B., Mnjokava, T.T., Chiragwile, S.A., Mayalla, J.W., Kabaka, K., Mwano, J.M., Makene, C., 2008. Geothermal energy as an alternative source of energy for Tanzania. In: Proceedings of the GEOTHERM project Technical Cooperation with the Republic of Tanzania, final technical report BGR, Germany, p. 235.

Kraml, M., Schaumann, G., Kalberkamp, U., Stadtler, C., Delvaux, D., Ndonde, P.B., Mnjokava, T.T., Chiragwile, S.A., Mayalla, J.W., Kabaka, K., Mwano, J.M., Makene, C., 2010. Surface exploration of a viable geothermal resource in Mbeya Area, SW Tanzania Part II: geochemistry. In: Proceedings of the World Geothermal Congress, Bali, Indonesia.

Lee, B., Unsworth, J.M., Árnason, K., Cordell, D., 2020. Imaging the magmatic system beneath the Krafla geothermal field, Iceland: A new 3-D electrical resistivity model from inversion of magnetotelluric data. Geophys. J. Int. https://doi.org/10.1093/gji/ggz427.

Lenoir, J.L., Lǐ Egois, J.P., Theunissen, K., Klerkx, J., 1994. The Palaeoproterozoic Ubendian shear belt in Tanzania: geochronology and structure. J. Afr. Earth Sci. 19 (3), 169–184. https://doi.org/10.1016/0899-5362(94)90059-0.

Lévy, L., Gibert, B., Sigmundsson, F., Flóvenz, Ó.G., Hersir, G.P., Briole, P., Pezard, P.A., 2018. The role of smectites in the electrical conductivity of active hydrothermal systems: electrical properties of core samples from Krafla volcano, Iceland. Geophys. J. Int. 215 (3), 1558–1582. https://doi.org/10.1093/gji/ggy342.

Lichoro, M.C., 2019. Regional Geothermal Characterization of Northern Kenya Rift from Resistivity and Gravity, PhD Dissertation. Faculty of Earth Sciences, University of Iceland, p. 169.

Mibei, G., Mutua, J., Njue, L., Ndongoli, C., 2016. Conceptual model of Menengai geothermal field. In: Proceedings of the ARGeo Conf. Addis Ababa, Ethiopia.

Mbia, P.K., Mortensen, A.K, Oskarsson, N., Hardarson, B.S., 2015. In: Sub-Surface Geology, Petrology and Hydrothermal Alteration of the Menengai Geothermal Field, Kenya: Case Study of Wells MW-02, MW-04, MW-06 and MW-07 Proceedings World Geothermal Congress 2015 Melbourne, Australia.

Mnzava, L.J., Mayo, A.W., Katima, J.H.Y., 2004. In search of geothermal energy power potential in Tanzania: the role of geophysics. Geo Environ. 25–36.

Mruma, A.H., 1995. Stratigraphy and palaeodepositional environment of the Palaeoproterozoic volcano-sedimentary Konse Group in Tanzania. J. Afr. Earth Sci. 21 (2), 281–290. https://doi.org/10.1016/0899-5362(95)00065-2.

Muñoz, G., 2014. Exploring for geothermal resources with electromagnetic methods. Surv. Geophys. 35, 101–122. https://doi.org/10.1007/s10712-013-9236-0.

Mutonga, M., Mungai, K., 2017. Case study of geothermal directional drilling: The Menengai geothermal field. GRC Trans. 41.

Newman, A.G., Gasperikova, E., Hoversten, M.G., Wannamaker, E.P., 2008. Three-dimensional magnetotelluric characterization of the Coso geothermal field. Geothermics 37 (2008), 369–399.

Mackie, R., Watts, M.D., 2012. Detectability of 3-D sulphide targets with AFMAG. SEG 2012 Expanded Abstracts 1–4. https://doi.org/10.1190/segam2012-1248.1.

Norton Rose Fulbright in Consortium with Omenda, P., 2017: Consultancy services for preparation of geothermal energy development projects proposal document and M&E system manual for the project. Project proposal document for geothermal resource development. TGDC-September 2017 technical internal report, Unpublished, 139 pp.

Ochmann N., and Garofalo K., 2013. Geothermal energy as an alternative source of energy for Tanzania, final technical report of phase II (2010-2013), Technical Cooperation with United Republic of Tanzania, GEOTHERM-Project 2002.2061.6, Unpublished Report, 156 pp.

Pellerin, L., Alumbaugh, D., Cueva, N., 2003. Characterization of cultural noise in the AMT band. In: Proceedings of the ASEG 16th Geophysics Conference and Exhibition, Extended Abstracts, Brisbane, Australia.

Pellerin, L., Hohmann, G., 1990. Transient electromagnetic inversion: a remedy for magnetotelluric static shifts. Geophysics 55, 1242–1250. https://doi.org/10.1190/1.1442940.

Piña-Varas, P., Ledo, J., Queralt, P., Marcuello, A., Perez, N., 2018. On the detectability of Teide volcano magma chambers (Tenerife, Canary Islands) with magnetotelluric data. Earth Planets Space 70 (2018), 14. https://doi.org/10.1186/s40623-018-0783-y.

Rasskazov, S.V., Logachev, N.A., Ivanov, A.V., Boven, A.A., Maslovskaya, M.N., Saranina, E.V., Brandt, I.S., Brandt, S.B., 2003. A magmatic episode in the western rift of East Africa (19–17 Ma). Geol. Geofiz. 44, 317–324.

Ring, U., Betzler, C., Delvaux, D., 1992. Normal vs. strike-slip faulting during rift development in East Africa: the Malawi rift. Geology 20, 1015–1018. https://doi.org/10.1130/0091-7613(1992)020<1015:NVSSFD>2.3.CO;2.

Rizzello, D., Armadillo, E., 2023. Smooth magnetotelluric impedance estimation by optimization. J. Appl. Geophys. https://doi.org/10.1016/j.jappgeo.2023.104952.

Rizzello, D., Armadillo, E., Pasqua, C., Pisani, P., Principe, C., Lelli, M., Didas, M., Giordan, V., Mnjokava, T., Kabaka, K., Tumbu, L., Marini, L., 2022. Assessment of the Kiejo-Mbaka geothermal field by three-dimensional geophysical modelling. Geomech. Geophys. Geo Energ. Geo Resour. 8, 143. https://doi.org/10.1007/s40948-022-00456-5.

Rizzello, D., Armadillo, E., Pasqua, C., Pisani, P., Balsotti, R., Kebede, S., Mengiste, A., Kebede, Y., Hailegiorgis, G., Mengesha, K., 2021. The geophysical recognition of a vapor-cored geothermal system in divergent plate tectonics: the Alalobeda (Alalobad) field, Ethiopia. Tectonophysics 813 (2021), 228933. https://doi.org/10.1016/j.tecto.2021.228933.

Roberts, E.M., O'Connor, P.M., Gottfried, M.D., Stevens, N., Kapalima, S., Ngasala, S., 2004. Revised stratigraphy and age of the Red Sandstone Group in the Rukwa Rift basin, Tanzania. Cretaceous Res. 25 (5), 749–759. https://doi.org/10.1016/j.cretres.2004.06.007.

Samrock, F., Grayver, A., Dambly, M.L.T., Müller, M.R., Saar, M.O., 2023. Geophysically guided well siting at the Aluto-Langano geothermal reservoir. Geophysics 88, 5.

Samrock, F., Grayver, A.V., Bachmann, O., Karakas, Ö., Saar, O.M., 2021. Integrated magnetotelluric and petrological analysis of felsic magma reservoirs: Insights from Ethiopian rift volcanoes. Earth Planet Sci. Lett. 559 (2021), 116765 https://doi.org/10.1016/j.epsl.2021.116765.

Soyer, W., Mackie, L.R, Hallinan, S., Miorelli, F., Pavesi, A., Garanzini, S., Sagala, B., Siagian, H., 2021. Geophysics over high enthalpy fields: lessons from RLM-3D magnetotelluric and joint inversions. In: Proceedings of the World Geothermal Congress 2020+1 Reykjavik, Iceland.

Sternberg, B.K., Washburne, J.C., Pellerin, L., 1988. Correlation for the static shift in magnetotellurics using transient electromagnetic soundings. Geophysics 53, 1459–1468. https://doi.org/10.1190/1.1442426.

Sutarno, D., 2008. Constrained robust estimation of magnetotelluric impedance functions based on a bounded-influence regression M-estimator and the Hilbert transform. Geophysics 15, 287–293. https://doi.org/10.5194/npg-15-287-2008.

SWECO, 1978. Reconnaissance of geothermal resources. Report for the Ministry of Water, Energy and Minerals of Tanzania. SWECO, Stockholm, Sweden, p. 51.

TGDC, 2022. Geophysical assessment of potential $CO_2$ natural gas reservoirs using Magnetotelluric (MT) method in Tukuyu, Mbeya Region. TGDC-UDSM consultancy services, Unpublished internal report, p. 27.

Ussher, G., Harvey, C., Johnstone, R., Anderson, E., 2000. Understanding resistivities observed in geothermal systems. In: Proceedings of the World Geothermal Congress 2000, Kyushu-Tohoku, Japan.

UNEP/ARGeo, 2016. Geothermal resource assessment report Ngozi and Songwe Geothermal Prospects, Tanzania. TGDC unpublished internal technical report, p. 695.

Walker, B.G., 1969. Springs of deep-seated origin in Tanzania. In: Proceedings of the 23rd Intern. Geological Congress, p. 19.

# Paper III

**Imaging and modelling the subsurface structure of the Rungwe Volcanic Province in SW Tanzania with aeromagnetic data: An improved structural map to support geothermal exploration.**

**Makoye M. Didas,** Egidio Armadillo, Gylfi Páll Hersir, William Cumming, Daniele Rizzello, Halldór Geirsson.

Manuscript submitted to Journal of African Earth Sciences

# Imaging and modelling the subsurface structure of the Rungwe Volcanic Province in SW Tanzania with aeromagnetic data: An improved structural map to support geothermal exploration

**Makoye M. Didas [a, f, g, *], Egidio Armadillo [b], Gylfi Páll Hersir [c], William Cumming [d], Daniele Rizzello [e], Halldór Geirsson [f]**

[a] *Tanzania Geothermal Development Company Ltd (TGDC), P. O. Box: 14801, Ursino House No. 25, Dar es Salaam, Tanzania*
[b] *Applied Geophysics Laboratory, DISTAV, University of Genoa, Italy*
[c] *Independent Researcher, Reykjavik, Iceland, formerly at Iceland GeoSurvey (ÍSOR), Urdarhvarf 8, IS-203 Kópavogur, Iceland*
[d] *Cumming Geoscience, Santa Rosa, California, USA*
[e] *Tellus-Explora S.a.s, Italy*
[f] *Faculty of Earth Sciences, University of Iceland, Sturlugata 7, 101 Reykjavík, Iceland*
[g] *GRÓ GTP, Urdarhvarf 8, IS-203 Kópavogur, Iceland*

***Keywords***
*Rungwe Volcanic Province, East African Rift System, aeromagnetic data, magnetic bodies, magnetic lineaments, neotectonic structural map*

## Abstract

The Rungwe Volcanic Province (RVP) in the East African Rift System, SW Tanzania, provides a unique opportunity to investigate geothermal resources in the context of particularly complex continental rifting processes. To support geothermal resource targeting in the RVP, we present a revised neotectonic structural map based on an interpretation of aeromagnetic data constrained by 2D-forward modelling of magnetic anomalies integrated with the distribution of previously reported faults, seismic epicentre locations, 3D magnetotelluric resistivity models and surface geothermal manifestations. Magnetic anomalies in the RVP, including the nationally prominent Mbeya anomaly, are related to the high magnetic susceptibility or remanent magnetism of Precambrian rocks and Cretaceous carbonatite intrusions buried in the rift under a varying thickness of non-magnetic sediments and volcanic rocks. Magnetic lineaments are related to structures controlling the geometry of the Precambrian rocks and concealed dikes and the thickness of the sediments and volcanics. The recent Ngozi and Rungwe trachyte volcanics have relatively low magnetic susceptibility comparable to the low susceptibility of the sediments in the rift basins. The revised neotectonic structural map shows prominent NW, NE and NS-trending magnetic lineaments that correlate with previously reported faults and alignments of seismic epicentres in the study area and with the regional trend of the rift segments. The NE-trending magnetic lineaments are consistent with interpretations of the current stress field in the RVP. The main volcanoes in the RVP, Ngozi, Rungwe and Kiejo (also known as Kyejo and Kieyo), are aligned with the NW-trending linear magnetic feature joining the Lupa and Livingstone rift border faults. This lineament is intersected and frequently displaced by the NE and NS-trending lineaments, suggesting that the NE to NS-striking structures are younger. The Rungwe and Ngozi volcanoes as well as numerous ‘’monogenetic’’ eruption centres and the Mwakaleli caldera, which originated ca. 2 Ma ago (Ebinger et al., 1989) following a large explosive eruption emplacing widespread ignimbrite deposits, are located within a zone of low-intermediate magnitude magnetic features forming a basin-like structure surrounded by magnetic high anomalies of the Precambrian basement structures. We interpret the intersections between the NW-trending intra-rift faults and the NS and NE-trending faults as favourable locations for wells to target high permeability within the geothermal resource conceptual models previously constructed using 3D MT resistivity imaging integrated with supporting geoscientific data. The intersections provide a focus area for follow-up ground mapping of subtle features that may be associated with very recent fault movement

## 1 Introduction

The interaction of faults and fractures with lithological properties controls the deep permeability that supports fluid circulation in geothermal fields (e.g., Ikhwan et al., 2020).

Structures are important both for enhancing permeability and for limiting permeability at field boundaries, as observed in geothermal fields such as Krafla in Iceland (Árnason, 2020) and Olkaria, Paka, and Menengai in Kenya (Mibei, 2021). As a result, to help locate sites for wells that may have higher output, structural studies have been conducted at geothermal prospects in East Africa like Alalobeda in Ethiopia (Rizzello et al., 2021) and Songwe, Luhoi and Kiejo-Mbaka geothermal prospects in Tanzania (Hinz et al., 2018; Armadillo et al., 2020; Rizzello et al., 2022) among others.

In geothermal areas where the geological structures are hidden by thick superficial sedimentary formations or tephra deposits, surface geological mapping, including Lidar supported ground mapping of structures, may detect only the most recently active faults and, in some cases, no structures can be reliably mapped. In such cases and depending on the physical properties of the rocks and structures, a geophysical survey or a combination of surveys such as magnetic, gravity, magnetotelluric (MT) or seismic surveys might be suitable for mapping concealed structures. The magnetic method is particularly useful in mapping or assessing the existence of faults, dikes, or subvolcanic intrusions that create lateral contrasts in magnetic properties buried below rocks with relatively uniform magnetic properties. This method is effective where mafic and ultramafic crystalline rocks contrast sharply with rocks that typically have much lower magnetite content, such as felsic igneous rocks, volcaniclastics and sediments. It is also widely used to estimate depths to concealed crystalline basement rocks and depths to the Curie temperature at crustal scales (e.g., Didas et al., 2022).

The Rungwe Volcanic Province (RVP) is situated in the Mbeya Region of SW Tanzania, at the triple junction of the East African Rift System (EARS). The South-Rukwa and the seismically inactive Usangu basin rifts, which are the southern ends of the west and east branches of the EARS, respectively, meet the North-Malawi rift at this junction (Fig. 1). The RVP includes five prominent volcanoes, namely Rungwe, Ngozi, Kiejo (also known as Kyejo or Kieyo), Tukuyu, and Katete (also known as Mwakaleli; ELC and TGDC, 2017; Didas et al., 2023), as well as over 100 smaller volcanic eruptive centres (Figs. 2 & 3). Rungwe, Ngozi and Kiejo are considered active (dormant, Fontijn et al., 2012). The region is largely covered by volcanic rocks of trachytic composition that originated from effusive and explosive volcanic eruptions of the prominent volcanoes (Harkin, 1960). The volcaniclastic rocks have largely obscured the faults that localized the fossil and active hydrothermal systems that have formed during the ongoing development of the triple junction (Fontijn et al., 2012).

Two types of geothermal systems are likely to exist in the RVP: high-temperature magmatically heated systems and low-medium temperature fault-controlled deep circulation systems. The Ngozi and Rungwe prospects have been interpreted as hosting two separate high-temperature geothermal systems that are heated by magma and have an estimated reservoir fluid temperature greater than 230℃ according to cation geothermometry from the Ngozi caldera lake (Delalande et al., 2015; UNEP/ARGeo, 2016) and based on alteration patterns typical of boiling detected by MT at Rungwe (Didas et al., 2023). Rungwe has been interpreted as hosting a >250℃ geothermal reservoir based on its resistivity pattern

characteristic of volcano-hosted geothermal systems where low resistivity, low temperature smectite clay updomed above the water table over high resistivity, high temperature alteration of a boiling reservoir zone (Didas et al., 2023). The Kiejo-Mbaka and Songwe prospects likely host geothermal systems with reservoir fluid temperature estimates ranging from 112 to 140°C, supported by deep fluid circulation through faults (Alexander et al., 2016; Asnin et al., 2022; Rizzello et al., 2022). The estimated power capacity, at a 10% confidence level, is 140 MWe for Ngozi (UNEP/ARGeo, 2016; Didas and Hersir, 2021), 10 MWe for Kiejo-Mbaka (ELC and TGDC, 2017), and 38 MWe for Songwe (EAGER, 2018) as shown in Fig. 2. However, many uncertainties remain about the conceptual models of these systems (e.g., Rizzello et al., 2022; Didas et al., 2023) and other systems may exist.

In order to extend the knowledge of fault distribution over the RVP to predict the likely location of highly permeable zones and impermeable boundaries for potential geothermal resource targeting, in this paper we have analysed aeromagnetic data collected by Geosurvey International between 1976 and 1980 (Marobhe, 1989; Stendal et al., 2004). Our primary goals are to map the extent of faults where they are concealed below sediments and volcanics and to investigate their relationships with the hot springs with >44°C discharge temperature (UNEP/ARGeo, 2016) and the previously interpreted geothermal systems within the RVP. The aeromagnetic interpretations and models have been constrained by the regional geological structure, the existing structural maps (e.g., Ebinger et al., 1989; Delvaux et al., 2010; Fontijn et al., 2012), the available petrophysical information (Marobhe, 1989), the location of seismic epicentres (Ebinger et al., 2019), and the MT resistivity patterns detected over the RVP geothermal systems (Hinz et al., 2018; Rizzello et al., 2022; Didas et al., 2023).

## 2 Geological and geophysical setting of the Rungwe Volcanic Province

The RVP covers approximately 1500 $km^2$ at the intersection between the eastern (Usangu Rift Basin), western (Rukwa Rift Basin), and southern (Malawi Rift Basin) branches of the Cenozoic EARS (Figs. 1 & 2). It is located to the south of the Archean Tanzanian craton, within the Paleoproterozoic Ubendian orogenic belt (Fig. 1) that resulted from the collision of the Archean Tanzanian Craton and the Paleoproterozoic Bangweulu block during the Gondwanaland amalgamation process from 1950 to 1850 Ma (Fritz et al., 2013; Boniface and Appel, 2018; Boniface, 2019). These collision events produced igneous intrusion complexes and Paleoproterozoic sedimentary formations in depocentres. The collision events were followed by the first rifting phases that created the basins of the RVP during Permo-Triassic time. The Mesozoic era brought a rejuvenation of the rifting, with the Karoo and Red Sandstone sedimentary groups deposited in Permo-Triassic and Jurassic-Cretaceous times, respectively (Delvaux and Hanon, 1993), along the western sides of the Rukwa and Malawi rift basins (Fig. 3). Fault reactivation during Cretaceous time brought also some carbonatite magmatic intrusions within the RVP particularly along the Mbeya fault and in the Mbozi Precambrian basement block (Fig. 3; McFarlane, 1966; Boniface, 2017; Sun et al., 2021). The Cenozoic continental extension led to the initiation of the EARS and volcanic activity in the RVP (Ebinger et al., 1989). During that time, the Usangu basin was developed, the Rukwa and Malawi rifts were reactivated, and volcanism began in the RVP (Ebinger et al., 1989).

Magnetic anomalies in the RVP are created by lateral changes in lithology with contrasting magnetic properties and so the location of structures that offset such contrasting types of lithology can be inferred from magnetic data. Precambrian crystalline rocks and Cretaceous Carbonatite are expected to have higher magnetic susceptibility relative to recent trachytic volcanic rocks and sedimentary rocks. The exposure of the Precambrian and carbonatite rocks outside the rift and their depth of burial below the sediments and more recent volcanic and volcaniclastic rocks within the rift has a prominent effect on the magnetic anomaly pattern.

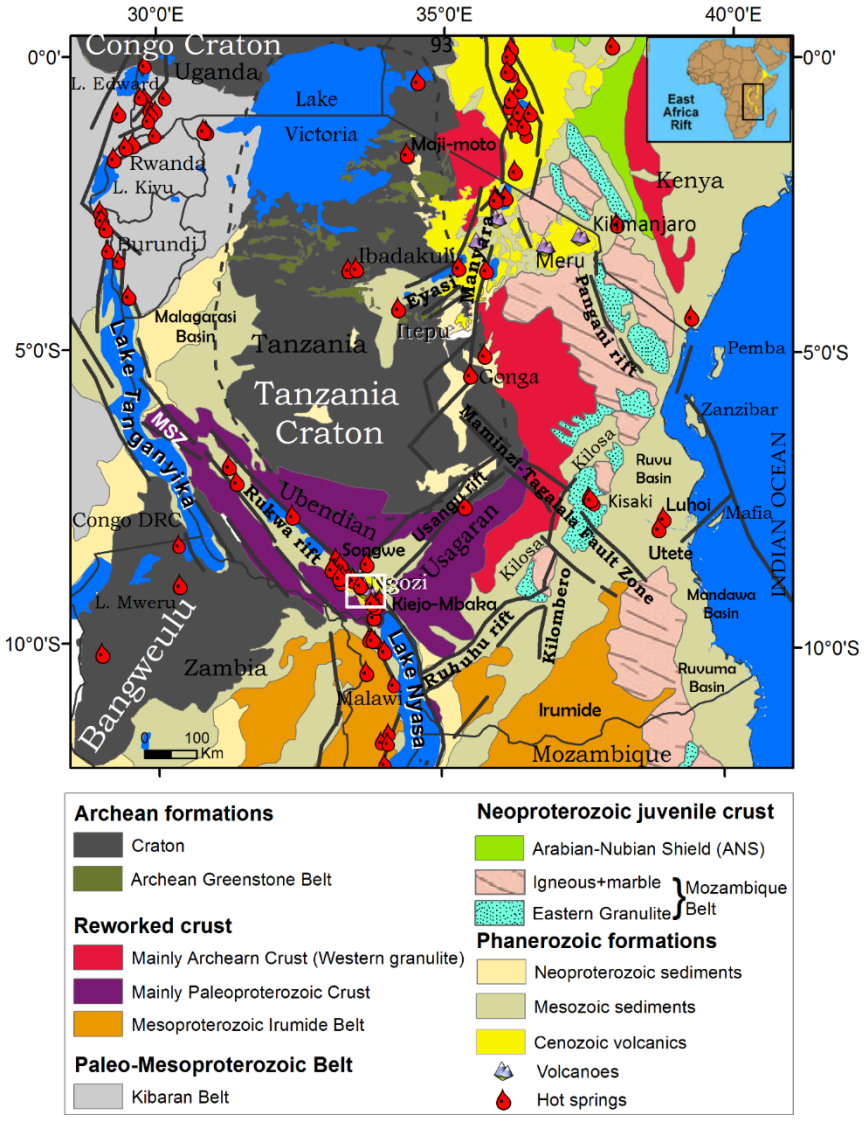


***Fig. 1.*** *Geological map of Tanzania modified from Fritz et al. (2013) and Didas et al. (2022) showing the main geological domains and hot springs distribution. The EARS margins are shown as thick black segment lines. The continuous thin gray lines define the political boundaries. MSZ: Mungese shear zone. The study area is indicated by a white square located at the triple junction of the east (Usangu rift), the west (Rukwa rift) branches of the EARS and its extension to the south along the Nyasa (Malawi) rift. The inset figure shows the location of the geological map of Tanzania on the African continent.*

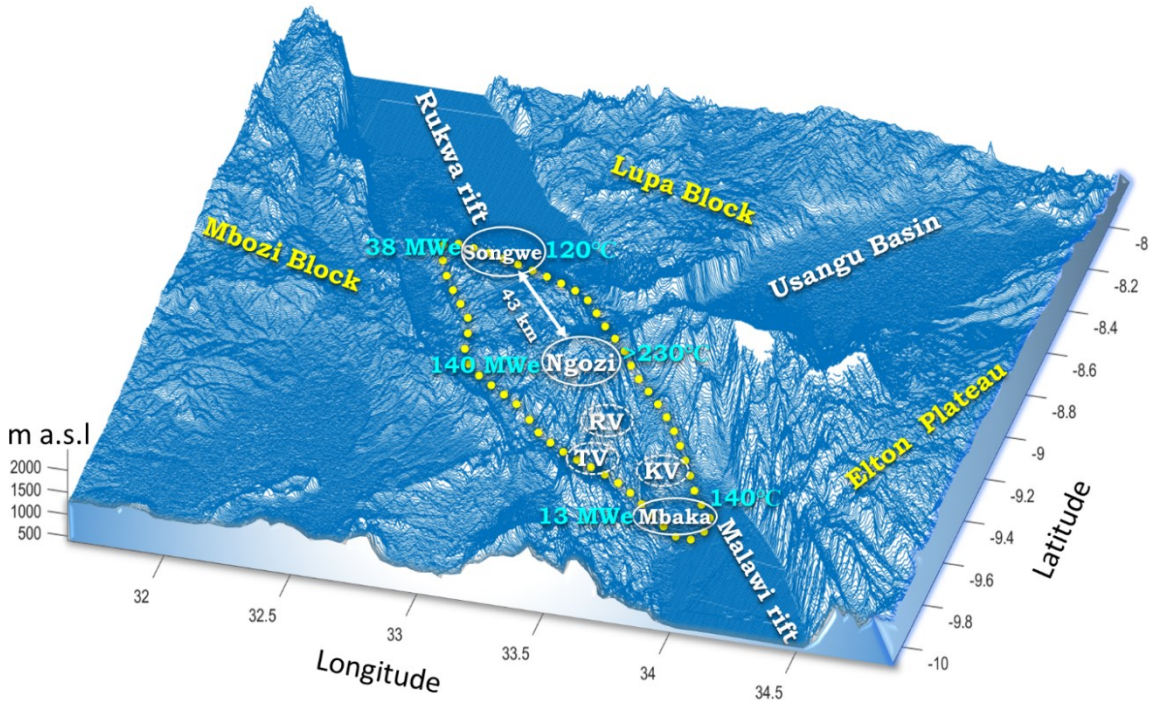


*Fig. 2. Location of the RVP (area enclosed by yellow dotted polygon) at the triple junction of the EARS in southwest Tanzania. Songwe, Ngozi, and Kiejo-Mbaka are geothermal prospects (Hinz et al., 2018; Rizzello et al., 2022; Didas et al., 2023). Estimated temperature based on geothermometry (Delalande et al., 2015; UNEP/ARGeo, 2016; Asnin et al., 2022; Rizzello et al., 2022; Didas et al., 2023) and evaluated electric potential (UNEP/ARGeo, 2016; ELC and TGDC, 2017; EAGER, 2018; Didas and Hersir, 2021) are indicated for each prospect in red and green, respectively. Three large volcanoes dominate the landscape: Ngozi volcano, Rungwe volcano (RV), and Kiejo volcano (KV). TV: highly eroded Tukuyu volcano.*

In the RVP area as elsewhere in the EARS, the recent faults associated with geothermal systems are often reactivated along Precambrian faults with their motion changing to accommodate changes in regional tectonics (Delvaux et al., 2006; Hinz et al., 2018). In the RVP, older structures are currently reactivated as strike-slip faults. A step-over in a reactivated strike-slip fault likely accounts for the permeability of the deep circulation geothermal system that supports the Songwe hot springs (Hinz et al., 2018). Similar structures likely provide conduits for deep-seated magma movement to shallow depths, as dikes and intrusions (Ebinger et al., 1989) that may support the development of high enthalpy geothermal systems.

### 2.1 Paleoproterozoic Ubendian belt

The Ubendian belt is a geological feature that spans approximately 500 km in length and 150 km in width, trending in a northwest-southeast direction. It borders the southern and southwestern margins of the Archean Tanzanian Craton and the Bangweulu block and is sutured with the NE-trending Paleoproterozoic Usagaran belt (Fig. 1). The Ubendian belt serves as the underlying basement in the rift segments (Figs. 1 & 3). Lithologies comprise metamorphic rocks including biotite gneisses, schists, amphibolites, and metagabbroid

bodies with granodiorite and diorite intrusions that were primarily formed due to igneous activity during Gondwanaland suturing in the Paleoproterozoic period, followed by regional metamorphism (Fritz et al., 2013; Boniface and Schenk, 2012; Boniface and Appel, 2017). The Ubendian belt in the RVP is partly covered by Paleoproterozoic to recent aged sedimentary formations and Neogene-Quaternary volcanic rocks associated with the development of the EARS (Fig. 3). The three basement blocks of the Ubendian belt namely, the Mbozi, Lupa, and Elton blocks are separated by the rift branches, the Rukwa, Usangu and Malawi rift basins (Fig. 3).

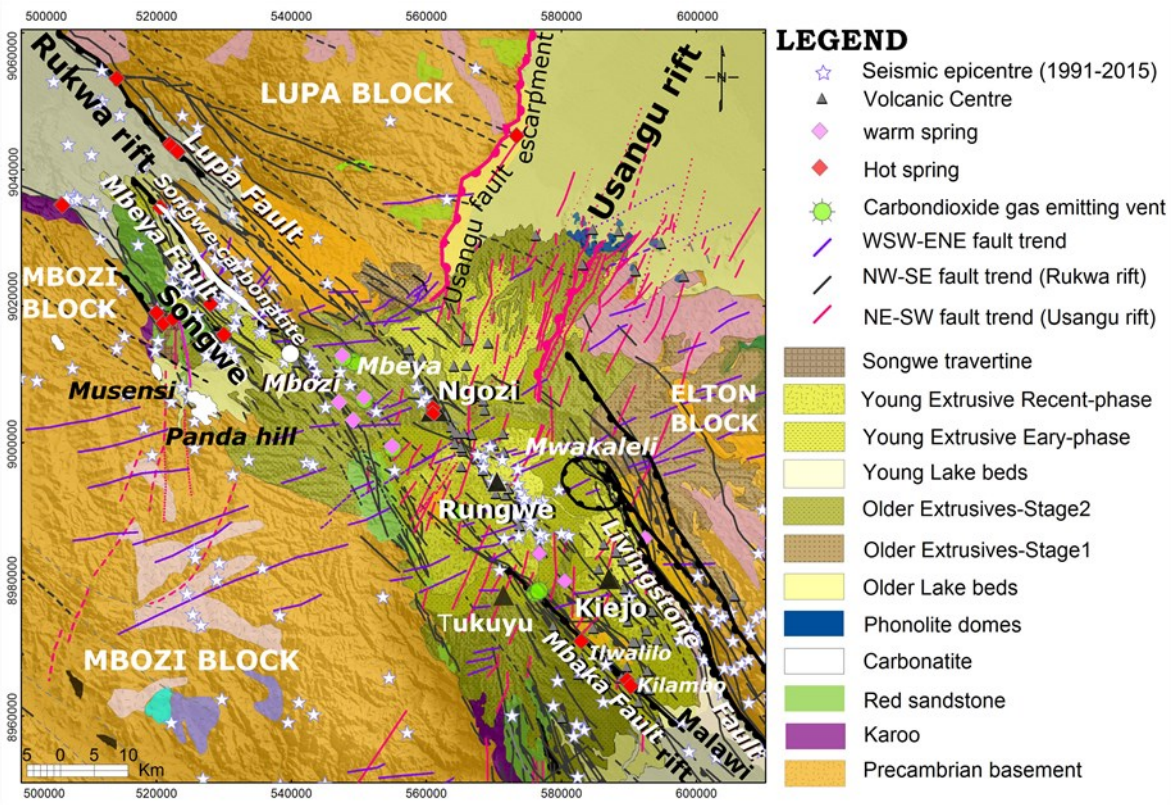


*Fig. 3.Geological map of the RVP showing the hot springs associated with three geothermal prospects, Songwe, Ngozi-Rungwe and Kiejo-Mbaka. Map modified after Fontijn et al. (2012). The faults are drawn from Ebinger et al. (1989) and Delvaux et al. (2010). The epicentres of local earthquakes are obtained from Delvaux and Hanon (1993) and Ebinger et al. (2019). The thick lines (red and black) indicate the main rift border faults. The thick black circular shape indicates the Mwakaleli caldera.*

## 2.2 Cenozoic East African Rift System and volcanic activity

The RVP includes the active (dormant) volcanoes, Rungwe, Ngozi and Kiejo, and non-active volcanoes Mwakaleli, and Tukuyu, as well as over 100 monogenetic eruption centres that appear as small cones and domes (Ebinger et al., 1989; Fontijn et al., 2010b, 2012). In contrast, the rift segments that meet at the Mbeya triple junction have sparse magmatic activity elsewhere (Ebinger et al., 1989) and generally contain Karoo to recent sedimentary

formations, partially covered by widespread Holocene tephra deposits from Rungwe and Ngozi (Delvaux, 2001; Mbede, 2002).

The RVP likely became active during the Early Miocene, between 19 and 17 Ma (Ivanov et al., 1999). During this period of volcanic activity, phonolite domes were formed in the Usangu Basin. The Late Cenozoic volcanic activity of the RVP can be divided into three stages (Fontijn et al., 2012) based on field relationships (Harkin, 1960) and radiometric ages of volcanic rocks, primarily lava flows and some ignimbrite deposits (Ebinger et al., 1989, 1993; Ivanov et al., 1999).

The first stage of activity occurred during the Late Miocene, between approximately 9.2 and 5.4 Ma. This stage was characterized by effusive eruptions of basaltic and phonolitic magma. Widespread phonolitic ignimbrites were also erupted from an unidentified vent (Fontijn et al., 2012). The volcanic rocks of the first stage mainly occur at the uplifted basement of Elton plateau and south of the Lupa block (Fig. 3).

The second stage of activity occurred during the Late Pliocene-Early Pleistocene, ca. 3-1.6 Ma. This stage produced extrusives similar to those of stage 1 but was dominated by effusive activity from the largely eroded Tukuyu volcano (Ivanov et al., 1999). Several eruptive centres were spread around the RVP, with old basalts and phonolites emplaced in the Poroto mountains, where the Ngozi volcano is located (Harkin, 1960). Volcaniclastic deposits of the second stage occur all over the RVP in the accommodation zone between the rift basins (Fig. 3).

The third stage of activity occurred during the mid-Pleistocene to Recent, since ca. 0.6 Ma (Harkin, 1960; Fontijn et al., 2012). This stage includes at least eight explosive eruptions in the RVP, including Plinian-style eruptions, from the Latest Pleistocene to Holocene (Fontijn et al., 2010b). Volcaniclastic deposits of stage 3 are more focused on zones near the three largest volcanoes, Ngozi, Rungwe, and Kiejo. This distribution aligns with a tectonic regime that exhibits increased volcanic activity compared to the first two stages of volcanism (Fontijn et al., 2012).

The Rungwe and Ngozi volcanoes experienced several Plinian and sub-Plinian eruptions. Ngozi had a major Plinian eruption ca. 10 ka and an ignimbrite-forming eruption within the last 1 ka, while Rungwe had at least five moderately explosive to Plinian-style eruptions within the Late Holocene (Fontijn et al., 2010a). The Kiejo activity started in the mid-Pleistocene with the oldest basaltic flow dated at 0.42 Ma (Ebinger et al., 1989). The most recent eruption of the Kiejo volcano is a tephrite basaltic lava flow dated to approximately 200 years ago (Harkin, 1960; Fontijn et al., 2012). The onset of the young extrusives corresponds to the inferred stress inversion associated with the evolution from the triple junction and a transform fault zone, as constrained by the dating of lava flows between 0.55 and 0.42 Ma (Delvaux et al., 1992)

### 2.3 Structures

The available structural data, constrained by aerial photograph and remote sensing interpretations and confirmed by ground mapping to characterize fault motion and history (e.g., Delvaux et al., 2010), suggest that the RVP is characterized by three sets of fault systems with different trends: NW-SE (Rukwa rift fault system), NE-SW (Usangu rift fault system), and NS (Malawi rift fault system). The Mbaka fault developed at approximately 2.5 Ma (Ebinger et al., 1993) during the second stage of the volcanic activity of the RVP and has undergone significant stress regime changes from extension to strike-slip compression since about 0.6 Ma (Ring et al., 1992; Delvaux, 2001; Delvaux and Barth, 2010). These changes have led to the development of transtensional pull-apart basins that have been interpreted as potential areas for the geothermal reservoir in the Songwe prospect (Hinz et al., 2018) and the formation of major volcanoes and numerous monogenetic volcanic centres and associated dike intrusions in the RVP (Ebinger et al., 1989; Fontijn et al., 2010a, 2012). According to Fontijn et al. (2010a), the Ngozi and Rungwe volcanoes are aligned with an obscured NW-trending fault and active NE-SW strike-slip faults linked to the Usangu basin that have induced significant transtensional movements at these volcanoes, enhancing volcanic activity over time.

The RVP area is extensively covered by sedimentary formations and tephra deposits that present a significant challenge in mapping faults within the rift basins (e.g., UNEP/ARGeo, 2016). However, where this cover is thin or absent, it has been possible to map major Proterozoic deformational structures on the rift basement horsts in the Lupa (e.g., Lawley et al., 2013), Mbozi (e.g., Marobhe, 1989), Elton, and Mbaka areas (e.g., ELC and TGDC, 2017). Remote sensing and geophysical data analysis (e.g., Fontijn et al., 2010a; ELC and TGDC, 2017; Mshiu, 2020) have been used to interpret the rift border faults and the NW-trending intra-rift Mbaka fault, which extends over 35 km from Lake Malawi to the south of the Rungwe volcano (Fontijn et al., 2010a). The Livingstone border fault has dips of 60-70° west (Ebinger et al., 1989), and the vertical displacement has been about 6 km in the north and 9 km in the south, respectively, over 24 My (Shillington et al., 2020). The Lupa border fault is steeply dipping towards the SW and has a vertical displacement ranging from about 2 to 5 km to the north and south of Lake Rukwa since Mesozoic time, respectively (Mulaya et al., 2021). The Usangu Basin border fault has a vertical displacement of more than 3 km since Karoo time but recent faulting mechanisms based on the interpretation of earthquake and reflection seismic data suggest that deformation on the Usangu border fault is predominantly strike-slip (Mbede, 2002). Based on sparse geodetic data (e.g., Stamps et al., 2018) and focal mechanisms (e.g., Ebinger et al., 2019) the current regional extension in the rift is ENE-WSW or E-W, resulting in a shift of the rift border faults to strike-slip deformation. The structures within the rift basins and at the triple junction in the RVP have remained unlevelled and so their motion is poorly constrained by geophysical data.

The kinematics of the rift in the RVP have been debated for over three decades, and several models have been proposed (e.g., Ebinger et al., 1989; Delvaux et al., 1992 & 2006; Ring et al., 1992; Delvaux and Hanon, 1993; Delvaux, 2001; Mortimer et al., 2007; Delvaux and Barth, 2010; Stamps et al., 2018; Heilman et al., 2019) with the most recent studies (e.g.,

Ebinger et al., 2019; Shillington et al., 2020) suggesting a ENE-WSW rift extension model. Several studies (e.g., Ring et al., 1992; Delvaux et al., 1992; Delvaux and Hanon, 1993; Brazier et al., 2005; Delvaux et al., 2010; Delvaux and Barth, 2010; Stamps et al., 2018; Ebinger et al., 2019; Shillington et al., 2020) suggest that the extensional direction in the RVP has remained roughly ENE-WSW over the past approximately 8 My (Ebinger et al., 1993), affecting the rift border and intrabasinal faults with sinistral/dextral shear movements. Normal faulting still occurs along the major long-lived faults which separate the basins from the uplifted Precambrian basements (Brazier et al., 2005; Delvaux and Barth, 2010; Fontijn et al., 2010a). Additionally, regional tectonics likely control the relationship between the large volcanoes, Rungwe, Ngozi, and Kiejo, and the spatial distribution of their associated eruptive vents (Ebinger et al., 1989 & 1993; Fontijn et al., 2010a).

Understanding the currently active kinematic model of the rift in the RVP is important to predicting permeability in the geothermal resource conceptual models based on the structures and formation pattern. For example, faults that are currently active as strike-slip are more likely to act as barriers to fluid flow that were hypothesised by Didas et al. (2023) and extensional areas between them would presumably be more favourable for enhanced permeability as observed by Hinz et al. (2016) in Songwe geothermal prospect. Except where fractured or intruded, the Precambrian basement would likely have low permeability and so would be a less favourable geothermal resource target. According to Shillington et al. (2020), the intrabasinal faults are still undergoing extension, contributing to the opening of the basin. The cumulative displacement on the intrabasinal faults increases from the Malawi rift in the south towards the north in the RVP, significantly offsetting late Quaternary syn-rift sediments implying that the faults are likely active and so are more likely to enhance permeability. The current study is directed at locating concealed structures favourable to enhanced permeability of the geothermal systems and the structures and formations likely to act as boundaries to geothermal systems in the RVP.

### 2.4 Earthquake activity

Geothermal areas are often associated with microearthquake activity which have been frequently used for geothermal exploration and reservoir monitoring of geothermal systems (Amoroso et al., 2022). The most commonly used microearthquake techniques are (i) time-dependent tomography using velocities of P-wave (Vp), S-wave (Vs) and Vp/Vs, (ii) accurate microearthquake hypocentral and epicentral locations to delineate faults that represent valuable zones of permeability and favourable targets for production wells, and (iii) microearthquake moment tensors to obtain the detailed information about the locations and modes of failure of geological structures. Unfortunately, the RVP area lacks permanent seismic networks. However, several temporary seismic monitoring networks have been installed to monitor the seismic activity in the area. Delvaux and Hanon (1993) and Ebinger et al. (2019) recorded earthquakes using networks of five and nineteen three-component digital seismic stations installed from 1991 to 1992 and from 2013 to 2015, respectively (Fig. 4). The epicentres shown in Fig. 3 and 4 indicate that the earthquakes are concentrated along the Rukwa and north Malawi rift segments, while the Usangu rift is seismically inactive (Ebinger et al., 2019).

The Songwe basin in the RVP had been very seismically active during the surveys, with events of magnitude ranging from 1.8 to 5.2 associated with several active faults that penetrate the lower crust at depths of 6 to 30 km, occurring along steeply dipping rift border faults and intrabasinal faults (Ebinger et al., 2019). The earthquake activity is caused by oblique strike-slip reactivation of the NW-SE trending rift border faults and the intrabasinal faults (Delvaux and Hanon, 1993; Ebinger et al., 2019).

The Rungwe and Kiejo volcanoes are also seismically active areas, while the Ngozi volcano and its surrounding area are less seismically active and the Usangu basin is seismically inactive (Fig. 4). Additionally, the RVP is known for lower P and S-wave velocities beneath the crust than the surrounding Tanzania and Bangweulu cratonic blocks and the Usagaran orogenic belt (e.g., Mulibo and Nyblade, 2013; Grijalva et al., 2018).

The published seismological data of the RVP from the temporary seismic monitoring networks have been combined with a larger set of seismic events from 1900 to 2019 with magnitudes above 5 $M_L$ from the International Seismological Centre (2023) catalogue to interpret faults in magnetic data.

## 3 Geothermal exploration

The RVP has been studied as a potential source of geothermal energy since 1949 (e.g., Walker, 1969; SWECO, 1978; McNitt, 1982; Hochstein et al., 2000; DECON et al., 2005; Kraml et al., 2010; JICA, 2014; UNEP/ARGeo, 2016; Alexander et al., 2016; Hinz et al., 2018; Didas and Hersir, 2021; Rizzello et al., 2022; Didas et al., 2022 and 2023). The heat flux distribution in the RVP has been investigated by Didas et al. (2022) using spectral analysis of aeromagnetic data and 3D gravity inversion. The establishment of the Tanzania Geothermal Development Company Limited (TGDC) in 2013 accelerated exploration for power production. Research thereafter has focused on the geothermal exploration of individual prospects in the RVP where high- and low-medium temperature geothermal systems have been inferred from geothermometry of hot springs, including Songwe (Kraml et al., 2008; UNEP/ARGeo, 2016; EAGER, 2018; Hinz et al., 2018; Asnin et al., 2022), Ngozi (Kraml et al., 2010; UNEP/ARGeo, 2016; Didas and Hersir, 2021; Didas et al., 2023), and Kiejo-Mbaka (Kraml et al., 2012; Kraml et al., 2013; Hersir and Weisenberger, 2015; ELC and TGDC, 2017; Rizzello et al., 2022). The likely extent of the geothermal systems has been inferred from 1D and 3D resistivity modelling using magnetotelluric (MT) data. In the case of the Rungwe prospect, the potential existence of a resource has been inferred from the indicative MT resistivity pattern (Didas et al., 2023). Integrated assessments of these prospects have concluded that the Kiejo-Mbaka (Rizzello et al., 2022) and Songwe (Hinz et al., 2018) prospects are likely to be associated with deep circulation fault-focused geothermal systems whereas the Ngozi and Rungwe prospects are more likely to be associated with high-temperature magmatically-heated geothermal systems (Didas et al., 2023).

Although geothermal exploration of RVP has increasingly focused on the Ngozi and Rungwe prospects, this study covers all of the RVP prospects. The Ngozi and Rungwe geothermal prospects are located at the triple rift junction in the RVP (Fig. 2 & 3). The

reservoir fluid temperature at the Ngozi prospect has been estimated to be over 230°C, with a resource capacity of 140 MWe at a 10% level of confidence (Alexander et al., 2016; Didas and Hersir, 2021). A deep electrically conductive body located at a depth of 6 km between the Ngozi and Rungwe volcanoes has been interpreted as a magma reservoir that is heating the adjacent geothermal systems (Didas et al., 2023). The prospective geothermal reservoir fluid temperature in the Songwe prospect is estimated to be between 112℃ to 120℃ (Alexander et al., 2016; Asnin et al., 2022), with a resource capacity of 38 MWe at a 10% confidence (EAGER, 2018). The Kiejo-Mbaka geothermal prospect is in the northern Malawi rift in the southernmost RVP. Its reservoir temperature is 140℃ and the potential is 10 MWe with a 10% level confidence limit (ELC and TGDC, 2017). The geothermal resources in the RVP will be tested by drilling planned in 2024, with the first priority being the Ngozi prospect where a 1200 to 1500 m deep slim well will be drilled to test the presence of a viable geothermal system by directly measuring temperature, fluid chemistry, permeability, and rock properties (Cumming et al., 2024).

## 4 Data and methods

The main data in this study are aeromagnetic data collected in 1976 and 1980 (Marobhe, 1989; Stendal et al., 2004). We have used aeromagnetic data to map structural highs and lows in the Precambrian basement rocks, Cenozoic volcanics, concealed igneous bodies in the near-surface as well as contacts of basement rocks with different magnetic susceptibilities. We have also applied the magnetic method to map zones of weaknesses within the basement rocks, including faults, shear zones, and contacts produced by igneous intrusive and extrusive rocks in the study area. In gridded magnetic anomaly maps, zones of weaknesses in the basement rocks appear as linear features terminating two blocks of different magnetic properties. Several other phenomena might cause magnetic lineaments aside from faults such as aligned geological variations unrelated to structures. For example, magnetic lineaments can also be caused by deposition of a lava flow that is magnetized differently from adjacent rocks or by erosion that varies the thickness of non-magnetic sediments overlying magnetic volcanic or basement rocks. Therefore, to avoid wrong interpretations, it is essential to establish the correlations with the geology and known faults of the area (Fig. 3), paleomagnetism of the rocks, and seismic history of the area (Fig. 4) before interpreting the magnetic lineaments.

### 4.1 Aeromagnetic data

The present study is based on the airborne total magnetic intensity (TMI) dataset that was acquired by Geosurvey International between 1976 and 1980 (Marobhe, 1989; Stendal et al., 2004). The flight lines were oriented in an East-West direction, spaced 1 km apart, and sampled every 50 m at a nominal altitude of 120 m above the surface over the entire study area (Fig. 4). The Tanzania Geothermal Development Company Limited (TGDC) provided the dataset. We used the International Geomagnetic Reference Field version 3 (IGRF-3) model for the year 1980 (Alken et al., 2021) to subtract the Geomagnetic field from the total magnetic field data corrected for diurnal variations. To remove the linear trend anomalies caused by initially incorrect levelling of the flight lines, we applied microlevelling filtering (Ferraccioli et al., 1998). This produced the Residual Total Magnetic-field Intensity (RTMI)

data set (Dentith, 2011), that was gridded with 250 m grid spacing, one-fourth of the survey line spacing, to create the RTMI map in Fig. 5. We then shifted magnetic anomalies to positions directly above their sources using the Reduction to the Magnetic North Pole (RTP) technique (Baranov and Naudy, 1964) for the medium magnetic inclination of this study area near -42°, as compared to the Reduction to the Equator (RTE) approach (Rusman et al., 2023). To downweight the effects of the shallow high-frequency magnetic anomalies and noise, we applied a 5 km low pass filter to the RTP map shown in Fig. 6.

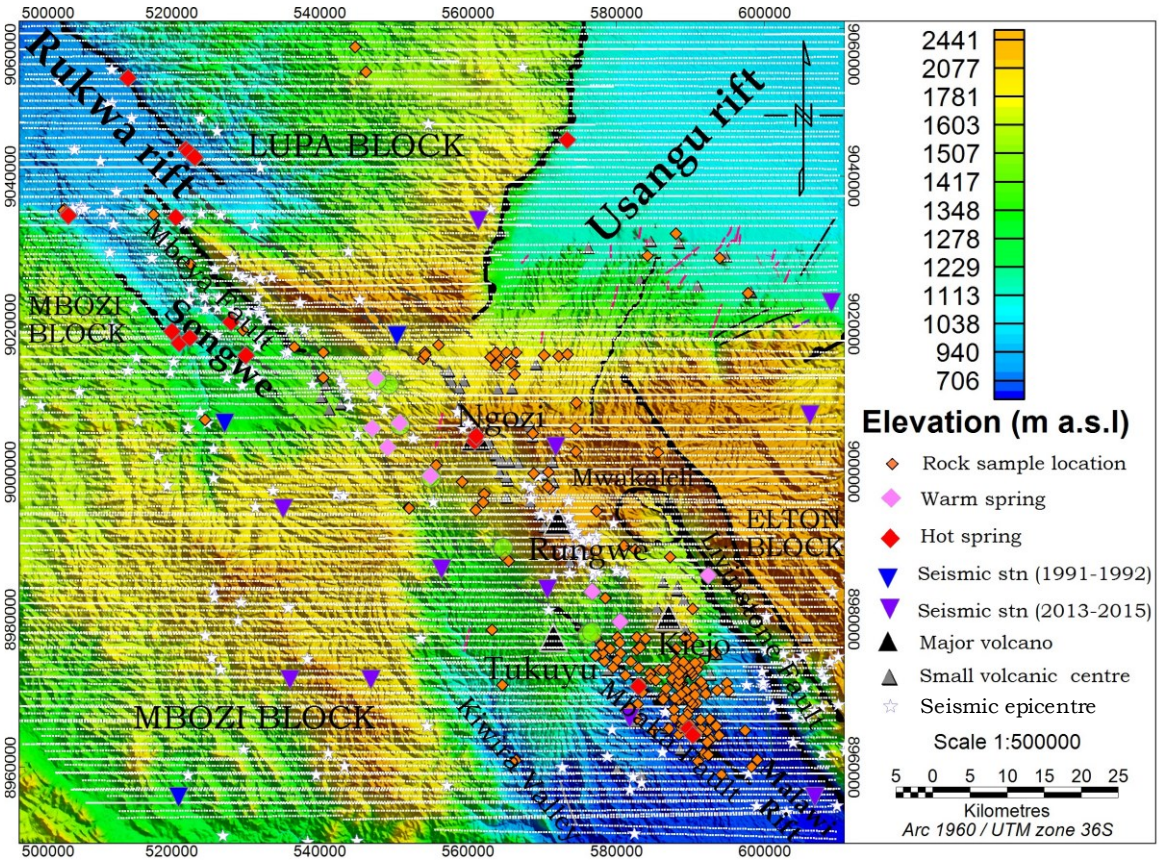


*Fig. 4. Aeromagnetic survey lines (white dotted lines) superimposed on the SRTM30 digital elevation model of the RVP. White stars are the locations of seismic epicentres. Orange diamonds are locations of the rock samples with petrophysical information shown in the supplementary material in Table 1.*

### 4.2 Petrophysical data

The petrophysical data used in this study were obtained from laboratory measurements of various rock units compiled from several research studies, including Miller and Brown (1963), Van Straaten (1989), Marobhe (1989), Fontijn et al. (2010b), Boniface and Schenk (2012), and Sun et al. (2021). The data, shown in Table 1 of the supplementary material, include density, geochronology, volume susceptibility, induced magnetization, remanent magnetization, and Koenigsberger ratio (Q-value) of different rock types in the study area. Fig. 4 shows the sample locations. These petrophysical data complement the interpretation of the magnetic anomalies of rocks emplaced in different magnetic-polarity epochs.

Precambrian basement rocks in Lupa, Mbozi and Elton blocks and the Cretaceous Carbonites intrusions rich in iron oxide minerals have Q-values greater than 1 and also the remanent component dominates the induced magnetization. Most rock samples in the RVP, except for basalts in Mbeya city and Tukuyu town, have a Q-value less than 1, so the induced magnetization dominates the remanent magnetization (Marobhe, 1989).

## 4.3 Aeromagnetic data processing and modelling

### 4.3.1 Depth estimation of magnetic sources

Estimating the depth of magnetic sources is a common step used to guide interpretations of magnetic data. To accomplish this, we utilized the Source Parameter Imaging (SPI) technique (Thurston and Smith, 1997), which is a fast and generally effective method (Kamba and Ahmed, 2017) that can be applied to grids or profiles. Since the magnetic data in the study area show abundant evidence of near-surface contrasts in magnetic susceptibility, more representative depth estimations were computed directly from the aeromagnetic profile data. In this case, artifacts related to poor draping were avoided. This approach also avoids the aliasing and misleveling artifacts caused by interpolating a grid across profiles and most importantly, it exploits all of the survey's realistic resolution of shallow features.

### 4.3.2 Lineament analysis

To highlight trends in the aeromagnetic data, we adopted both a semi-automatic approach and a more subjective manual approach. First, we calculated the Tilt Derivative (TDR) of the gridded TMA, in order to enhance the signature of magnetic sources with geological significance (e.g., Salem et al., 2007), such as fault-related lateral contrasts in lithology, volcanic cone alignments, lava flows, and so on. Then, we applied the phase congruency operator (Kovesi, 1999, 2003) to the TDR, tracing the local positive picks. Then, we transformed the phase into a black-and-white image and applied a skeleton algorithm (Lee et al., 1994) to reduce the binary image to 1-pixel wide curved lines without changing the essential structure. Finally, we applied the Hough Transform to automatically detect and statistically analyse the lineaments in the image (Ghirotto et al., 2023). In the manual approach, we digitized the linear patterns of the peaks in the magnitude of the colour-shaded RTP map. First, magnetic lineaments that matched known faults were digitized, followed by lineaments that extended over a length greater than 3 km, while magnetic lineaments shorter than 3 km that did not correlate with known faults were excluded. The distribution trend of the lineaments was visualized in Rose Diagrams, depicting the relationship between cumulative length and the number of lineaments. In order to highlight the edges of the geological sources in the total magnetic field data, we applied normalized derivatives methods developed by Ferreira et al. (2013) to the RTP map which involves the calculation of the Tilt Angle of the Total Horizontal Gradient (TAHG). The normalized derivatives methods equalize signals from sources at different depths and enhance edge detection of magnetic bodies by placing the maxima values over the source edges (Ferreira et al., 2013). Although a variety of enhancements were tested, including the Analytic signal (Nabighian, 1972), Tilt Derivative (Miller and Singh, 1994), total horizontal derivative (Cordell and

Grauch, 1985), first vertical derivative (Cordell and Grauch, 1985) and other edge enhancement filtering (Nasuti et al. 2018), the RTP and TAHG maps were used in the interpretation.

### 4.3.3 The 2-Dimensional forward modelling of selected magnetic anomalies

We used 2-dimensional (2D) forward modelling techniques to estimate the geometry and depth of subsurface sources responsible for the main magnetic anomalies. Magnetic modelling has been constrained by the magnetization values and petrophysical data collected from the literature (Table 1 in the supplementary material). The geometries of the models were constrained by a previously developed 3D MT resistivity model (Didas et al., 2023). The 2D modelling software is based on the techniques described by Talwani and Heirtzler (1964) and Rasmussen and Pedersen (1979), as well as algorithms proposed by Won and Bevis (1987).

We selected three profiles (Fig. 6) for the magnetic modelling, with a focus on the magnetic anomalies across the prominent Mbeya Anomaly (profile AA'), another across the Rungwe volcano (profile BB'), and the third across the Mbaka and Livingstone faults at the Kiejo volcano (profile CC'). In each profile, the starting model was obtained from MT resistivity cross-sections from Didas et al. (2023). The obtained models are presented in Figs. 7-9 and are discussed in subsection 6.2.

Despite the significant ambiguity in the magnetic properties and body geometries of the 2D models, the models provide useful constraints on the geothermal interpretation of the Rungwe prospect.

## 5 Results

The results obtained from the aeromagnetic data are presented as gridded maps integrated with the geology (Figs. 5-6 and 10-12) and with the 3D MT resistivity as cross-sections (Figs. 7-9).

### 5.1 Magnetic anomalies

The RTMI and RTP maps illustrating the magnetic anomalies within the RVP are presented in Figs. 5 and 6, respectively. The main magnetic anomalies are shown in the low-frequency RTP map (Fig. 6) obtained by applying a low pass filter. The low-frequency RTP map is used here to describe the anomalies because they have been simplified and are positioned directly above their sources (Rusman et al., 2023). The map displays magnetic anomalies that possess characteristic geometrical and physical features reflective of the diverse geology of the RVP.

Predominantly long-wavelength magnetic anomalies are located in areas where Precambrian basement rocks are covered by extensive, thick lake beds and volcaniclastics, such as the Rukwa-Songwe trough and Usangu basin, and, similarly, in areas where the basement is covered by Paleoproterozoic continental sedimentary formations, such as the northern part of the Elton block and the southwest part of the Lupa basement block. Conversely,

intermediate to high-magnitude magnetic anomalies with short wavelength components can be found in regions where volcanic rocks cover old lake beds, such as the southern extents of the Rukwa and Usangu rift basins. In addition, areas with exposed Precambrian basement rocks, such as large parts of Lupa, Elton and Mbozi basement blocks and along the footwall of the Mbaka fault (Fig. 3), exhibit magnetic anomalies of varying intensities with shorter wavelengths.

The Lupa basement block is an area where low-magnitude magnetic anomalies with an irregular, shorter wavelength pattern, are prevalent, implying the area has undergone high deformation with shallow geology changing over short distances on the order of a few centimetres to a few kilometres as reported by Lawley (2013). These anomalies differ from the magnetic anomalies found in the Mbozi and Elton basement blocks that form the western and eastern margins of the Rukwa and Malawi rift segments, respectively. The Mbozi basement block is generally characterized by high-magnitude magnetic anomalies, strongly contrasting with magnetic anomalies in the Lupa and Elton blocks. The central portion of the Mbozi block experienced a Precambrian meteorite impact and possesses the lowest magnetic field anomaly in the study area at approximately 400 nT. The lowest magnetic field anomaly in the Mbozi block is flanked by high-magnitude magnetic anomalies, peaking at 3800 nT. Remarkably, the Panda Hill and Musensi carbonatite intrusions in the Mbozi block are aligned with the NW-trending high magnetic anomaly of the exposed Paleoproterozoic rocks separated by a low magnetic anomaly in the Songwe basin to the north. This observation suggests that the carbonatite intrusions may contain a significant amount of ferromagnetic minerals, which align with magnetite layers on the carbonatite outcrops at Panda Hill as reported by Boniface (2017).

The Mbalizi carbonatite shown in Fig. 6 (Sun et al., 2021) exhibits a high-magnitude magnetic anomaly as well, while the southeastern part of Songwe scarp carbonatite shown in Fig. 6 (McFarlane, 1966; Boniface, 2017), exhibits magnetic anomalies with reduced intensity and its northwestern part has a predominantly low magnetic anomaly.

The outcropping Precambrian basement along the footwall of the Mbaka fault coincides with a linear high-magnetic anomaly (Fig. 6), whereas the hanging wall, where the basement is covered by thick sediments and overlaying volcanics, is correlated with moderate to low magnetic anomalies.

Volcanic eruption centres at the triple junction, near Kiejo volcano and in the Mbaka graben are commonly linked with linear high magnetic anomalies, while the Miocene phonolite domes (including the Kongolo hill quarry) in the Usangu basin exhibit very low magnetic anomalies. The surrounding areas are mainly covered by volcanic rocks with magnetic susceptibility values ranging from 0.002 to 0.2 SI (Marobhe, 1989). These areas exhibit magnetic anomalies of varying intensities that do not correlate with the geology or other geophysical data, presumably caused by different weathering intensities of permeable volcanics. For instance, the areas surrounding the Ngozi, Rungwe, and Tukuyu volcanoes and the western part of Mwakaleli caldera (ELC and TGDC, 2017; Didas et al., 2023) display intermediate-weak magnetic anomalies, whereas areas surrounding the Kiejo volcano and the eastern part of Mwakaleli caldera exhibit high magnetic values probably associated with the Precambrian basement features with magnetic susceptibility ranging from 0.1 to 0.3 SI (Marobhe, 1989).

The northwestern region of the study area, comprising the Rukwa-Songwe trough, is primarily characterized by low-intermediate magnetic anomalies with relatively long wavelengths demarcating the rift boundaries and deep-seated (see Fig. 10) magnetic sources. Another low-intermediate magnetic zone is outlined in Fig. 6 by a blue-dotted polygon. It is situated southeast of the Songwe trough, separated by the NE-trending Mbeya magnetic high anomaly. This zone is correlated with outcrops of Cretaceous Red Sandstone (Fig. 3) to the west of the triple junction and volcanic tuffs from Ngozi and Rungwe volcanoes. It extends to the east through the Ngozi and Rungwe volcanoes and disappears in the Mwakaleli caldera. The zone is limited to the east by the Livingstone escarpment, to the north by Mbeya high magnetic anomaly and the Lupa basement block. To the south, the zone is limited by the Mbaka basement horst and to the west it is demarcated by the Mbozi basement block. Between the Ngozi and Rungwe volcanoes, this low-intermediate magnetic zone is intercalated by high magnetic anomalies at a cluster of monogenetic volcanic eruption centres. Additionally, the area of the warm springs with discharge temperatures ranging from 32°C to 44°C (UNEP/ARGeo, 2016) to the west of the triple junction and southeast of the Rungwe volcano are a part of this low-intermediate magnetic zone. This zone extends to the southeast following the Mbaka graben into Lake Nyasa (also known as Lake Malawi).

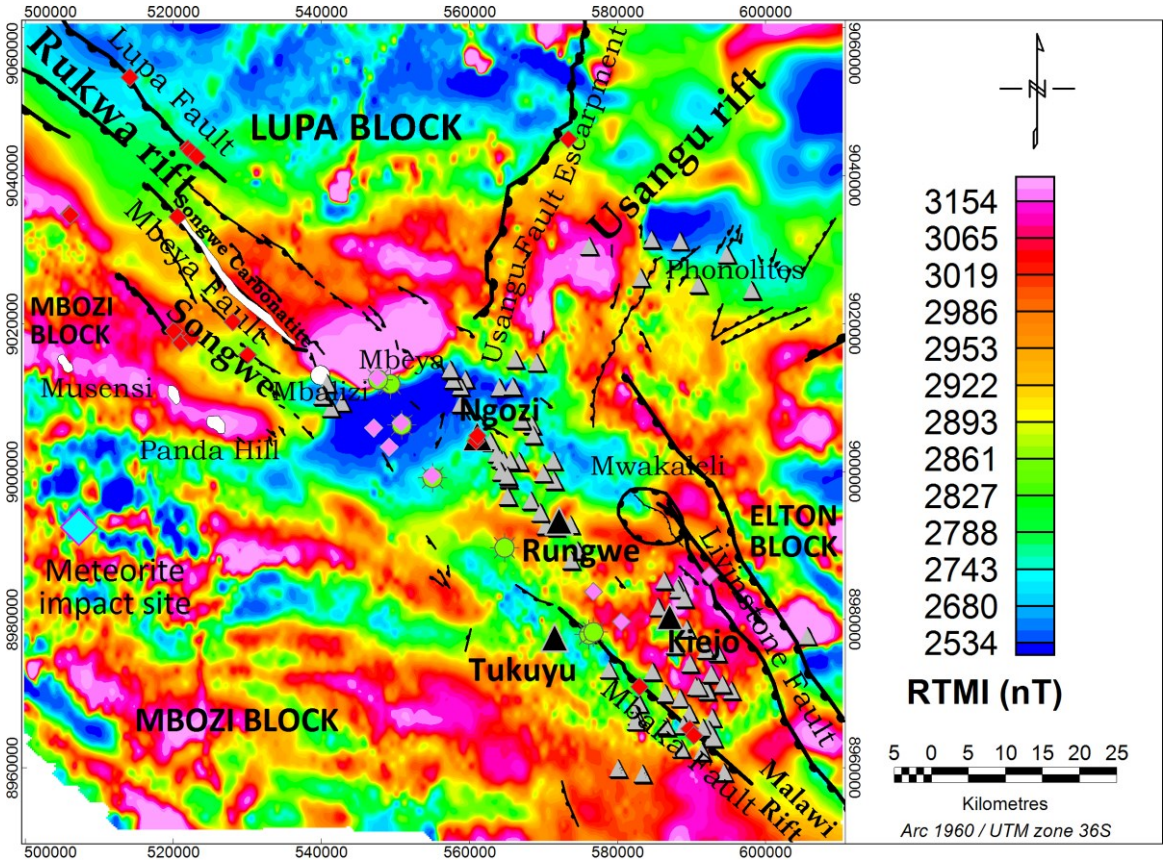


*Fig. 5. RTMI map of the RVP. The grey triangles are small volcanic eruption centres, black triangles represent major volcanoes. White patches indicate the Carbonatite intrusions. Black lines are known faults.*

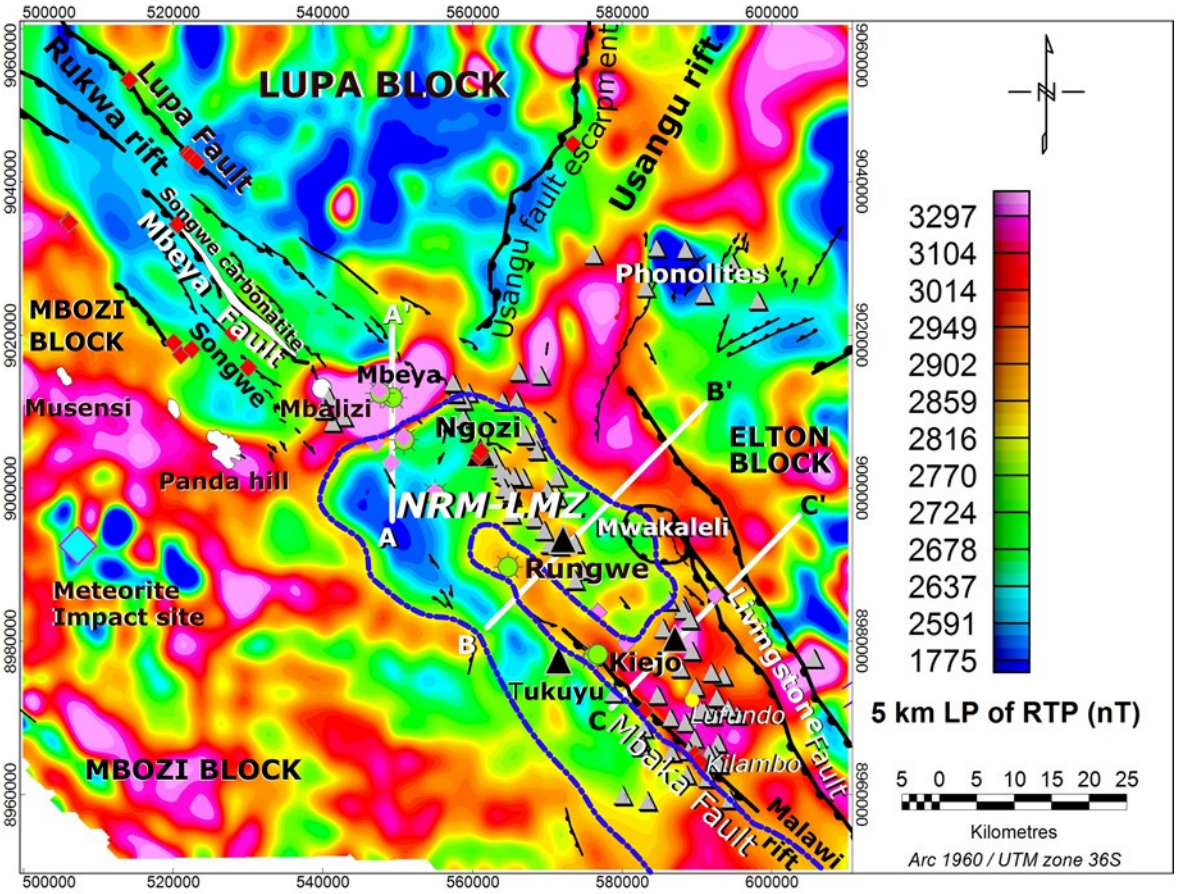


*Fig. 6. The 5 km low pass filtered RTP map of the RVP visualizing major magnetic anomalies. Thick yellow lines represent the 2D magnetic profiles along with resistivity cross-sections based on 3D inversion of MT data used to constrain the magnetic models shown in Figs. 7-9. The dotted blue outline is a low-intermediate magnitude zone of the magnetic anomaly within the RVP. White patches indicate the Carbonatite intrusions. For figure legend, see Fig. 3.*

The Mbeya magnetic high anomaly is the most prominent magnetic anomaly in the RVP region and among the most prominent anomalies in Tanzania. It is located south of Lupa basement block at the junction of the Mbeya fault and the Usangu border fault (Fig. 6). This anomaly was initially identified and modelled by Marobhe (1989) and the anomaly has been suggested by several authors to be a concealed carbonatite intrusion within the Precambrian basement (e.g., Marobhe, 1989; UNEP/ARGeo, 2016; Hinz et al., 2018). The Mbalizi carbonatite mapped by Sun et al. (2021) outcrops at the western end of this magnetic anomaly. The Mbalizi exposure of a carbonatite intrusion may be a northwest extension of a larger carbonatite intrusion below the Mbeya anomaly to the northeast (Fig. 6).

The 5 km low pass filtered RTP map of the RVP visualizing major magnetic anomalies. Thick yellow lines represent the 2D magnetic profiles along with resistivity cross-sections based on 3D inversion of MT data used to constrain the magnetic models shown in Figs. 7-9. The dotted blue outline is a low-intermediate magnitude zone of the magnetic anomaly within the RVP. White patches indicate the Carbonatite intrusions. For figure legend, see Fig. 3.

Other prominent variations in the magnetic field in the RVP rift basins occur in the Malawi and Usangu basins. The Usangu basin has a NE striking magnetic high anomaly suggesting the presence of ferromagnetic-rich mafic intrusions extending into the basin, similar to those observed cross-cutting the Usangu fault escarpment (see Fig. 6). However, the Usangu anomaly is disrupted by the low magnetic anomaly associated with phonolite domes (Fig. 6).

In the Malawi rift, a NW-trending magnetic high zone extends from the east on the Livingstone fault, tracing the intrabasinal basement horst of the Mbaka fault region punctuated by numerous Quaternary monogenetic volcanic eruption centres. Interestingly, the high magnetic anomaly in this region is smooth in its southern reach (see Fig. 6) and decreases further towards Lake Malawi, as the horst is buried below younger lake beds (see Fig. 3).

### 5.2 2D forward modelling of the magnetic anomalies

The 2D modelling results of selected magnetic profiles are shown as cross-sections in Fig. 7 to 9. Their quantitative information about the sources of the magnetic anomalies is interpreted in light of the geological knowledge of the area. In all profiles, the outcropping structures were constrained by the available geological data (Fig. 3 and Table 1), MT resistivity anomalies (Didas et al., 2023) and seismic interpretations (Mbede and Marobhe, 1989). The magnetization values used in the modelling are from the study of Marobhe (1989). The estimated thicknesses of the sediments are discussed in detail in paragraph 5.3.

#### 5.2.1 2D modelling of profile AA'

Profile AA' (Fig. 7) lies NS across the Mbeya positive magnetic anomaly in the low pass filtered RTP map (for location, see Fig. 6). The resulting model shows an excellent fit between the observed and calculated data with a misfit error of 1.2. The magnetic susceptibility values used for the model were 0.02 SI for the volcanics and dikes and 0.1 SI for the Proterozoic basement. This model is affected by the east Rukwa rift border fault (Lupa fault) and probably the Mbeya fault and Usangu basin border fault, shown on the geological map (Fig. 3). According to this model, the Mbeya anomaly is caused by a volcanic plug, that has been interpreted by several authors (e.g., Marobhe, 1989; UNEP/ARGeo, 2016; Hinz et al., 2018) as a Cretaceous carbonatite intrusion along the Mbeya fault within the Precambrian basement. The Mbeya fault was reactivated by the EARS in the Late Miocene and possibly acted as a conduit for basaltic lava to reach the surface. The area occupied by the Mbeya fault and the carbonatite intrusion is visible in the 3D MT resistivity cross-section (Fig. 7, lowest panel) as an intermediate resistivity zone that was interpreted by Didas et al. (2023) as a fault zone hosting a low-temperature geothermal system which is conductively heated by the Ngozi high-temperature geothermal system located 10 km to the southeast. In contrast, the Lupa fault does not have a high magnetic signature implying less magmatic activity. The carbonatite intrusion is concealed by both a generally thin shallow moderately resistive layer, consistent with less altered Pliocene-Early Pleistocene (~3-1.6 Ma) basaltic lava (Ivanov et al., 1999) overlying a thick conductive layer with a thickness of

about 1000 m consistent with altered basalts and/or clay-rich sediments and the Paleoproterozoic sediments, in turn overlying the resistive Precambrian basement.

### 5.2.2 2D modelling of profile BB'

Profile BB' (Fig. 8) has a NE-SW direction, traversing the Proterozoic basement exposed adjacent to the Mbaka fault, the Rungwe volcano, and the Livingstone border fault (for location see Fig. 6). The resulting model displays a good match between the observed and calculated data, with a misfit error of 2.3. The magnetic susceptibility values used for the model were 0 for the Cretaceous Red Sandstone in the Mbaka graben and a comparable formation or altered volcanics below the Rungwe volcano. The susceptibility values used were 0.01 SI for the Precambrian sediments, 0.03 for the Rungwe edifice, and 0.1 SI for the Proterozoic basement. The model shows that the magnetic anomalies are influenced primarily by the Precambrian basement, where shallow basement rocks exhibit high amplitude magnetic anomalies that decrease as the depth to the basement rocks increases. High magnetic anomalies over the Rungwe volcano and the footwall of the Livingstone fault are interpreted as dikes and volcanic rocks. The low magnetic anomalies (S=0) below the Rungwe volcano and Mbaka graben correspond to low resistivity zones that are interpreted as older volcanic rocks that have been hydrothermally altered to smectite clay. Smectite clay zones detected by 3D MT resistivity models have been interpreted as the hydrologic seals that isolate both a medium-temperature geothermal system associated with the Mbaka Fault in the conceptual model proposed by Rizzelo et al. (2022) and the high-temperature geothermal system interpreted below the Rungwe volcano by Didas et al. (2023). In addition, low magnetic anomalies that correspond with low resistivity zones could be associated with clay-rich formations in Cretaceous Red Sandstone and/or Karoo sediments. The low magnetic anomalies (S=0.01) over the Elton plateau are caused by Paleoproterozoic sediments overlying the Precambrian basement.

### 5.2.3 2D modelling of profile CC'

Profile CC' (Fig. 9) runs in a NE-SW direction from the Mbaka graben, across the Kiejo volcano and the Livingstone border fault (for location, see Fig. 6). The resulting model exhibits an excellent fit between the observed and calculated anomalies, with a misfit error of 1.3. The magnetic susceptibility values were assigned as follows: 0.4 SI for the volcanics covering Kiejo volcano, 0.005 SI for the Tukuyu lava, 0.01 SI for the Precambrian sediments, and 0.1 SI and 0.3 SI for the Proterozoic basement. The Cretaceous Red Sandstone was assumed to be non-magnetic. The model is affected by the Livingstone border fault, which is visible on the geological map (Fig. 3). The high magnetic amplitude over Kiejo volcano fits quite well with a dike system. The low magnetic susceptibilities in the Mbaka graben correspond to the low resistivity layer which is consistent with the hydrothermally altered Tukuyu lava and/or clay-rich Cretaceous Red Sandstone and Karoo sediments overlaying the Paleoproterozoic basement. Although the low resistivity layer below Kiejo volcano does not have much influence on the magnetic anomalies, it could be linked to hot saline fluids and low-temperature hydrothermally altered zone of basaltic rock and probably the top section of the Paleoproterozoic basement consistent with the model of Didas et al. (2023), while the magnetic anomaly is linked to lithology (i.e., basalt and dike system). On the other hand, the Mbaka fault associated with the hot springs is consistent

with intermediate resistivity values implying a fault zone hosting a fault controlled deep circulation geothermal system with a reservoir fluid temperature estimated to be 140℃ (Rizzello et al., 2022).

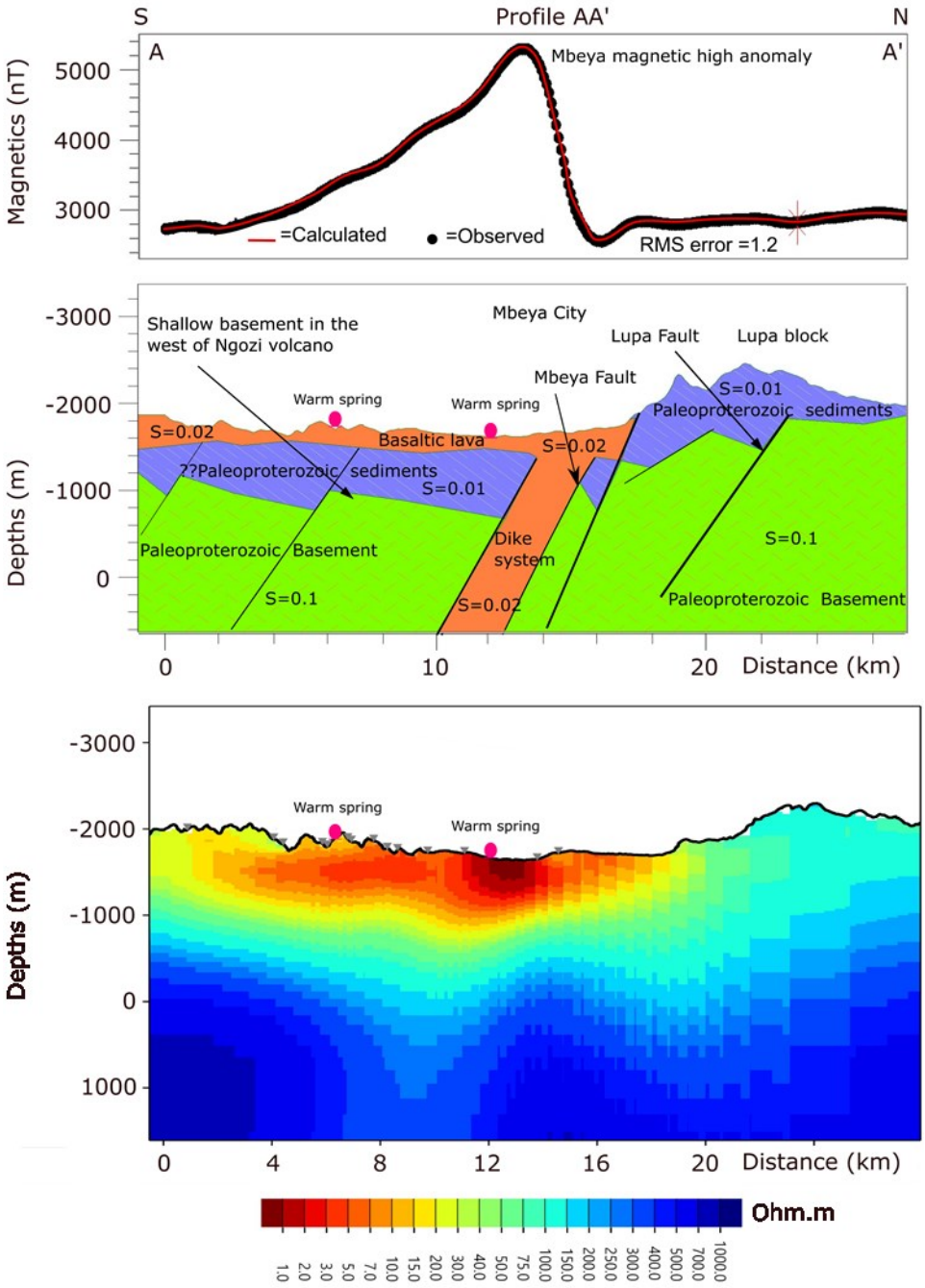


*Fig. 7. A 2D model of magnetization of low pass filtered RTP for profile AA' and resistivity cross-section based on 3D inversion of MT data across the Mbeya positive magnetic anomaly. Areas in the resistivity cross-section without MT data coverage should not be emphasized. The location of the profile is shown on Fig. 6. Geological features on the figure are from Fig. 3 and the 3D MT resistivity model is from Didas et al. (2023). The vertical exaggeration on the figures is 3.*

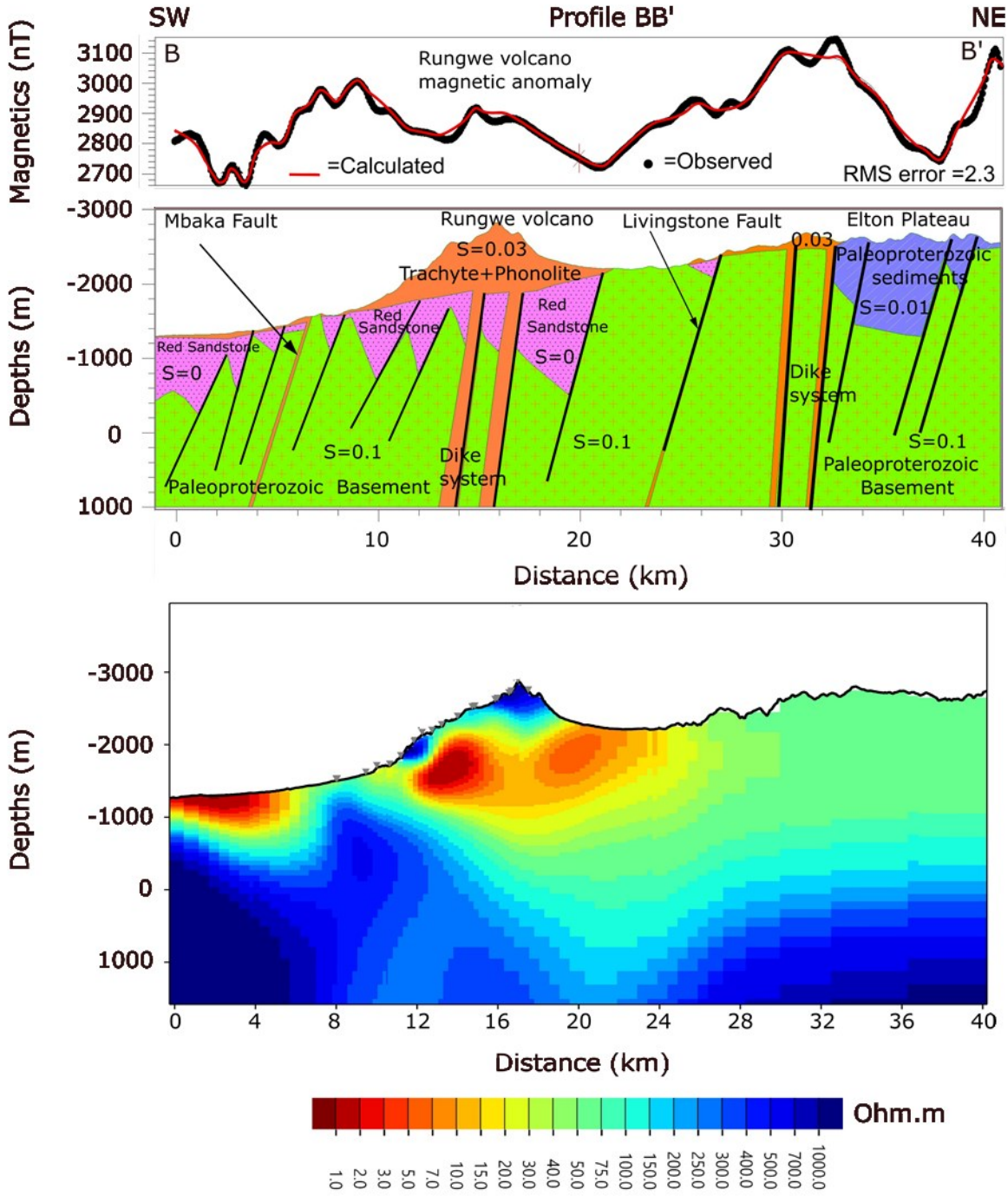


*Fig. 8. A 2D model of magnetization of low pass filtered RTP for profile BB' and resistivity cross-section based on 3D inversion of MT data across the Rungwe volcano magnetic anomaly. Areas in the resistivity cross-section without MT data coverage should not be emphasized. The location of the profile is shown in Fig. 6. Geological features on the figure are from Fig. 3 and the 3D MT resistivity model is from Didas et al. (2023). The vertical exaggeration on the figures is 3.*

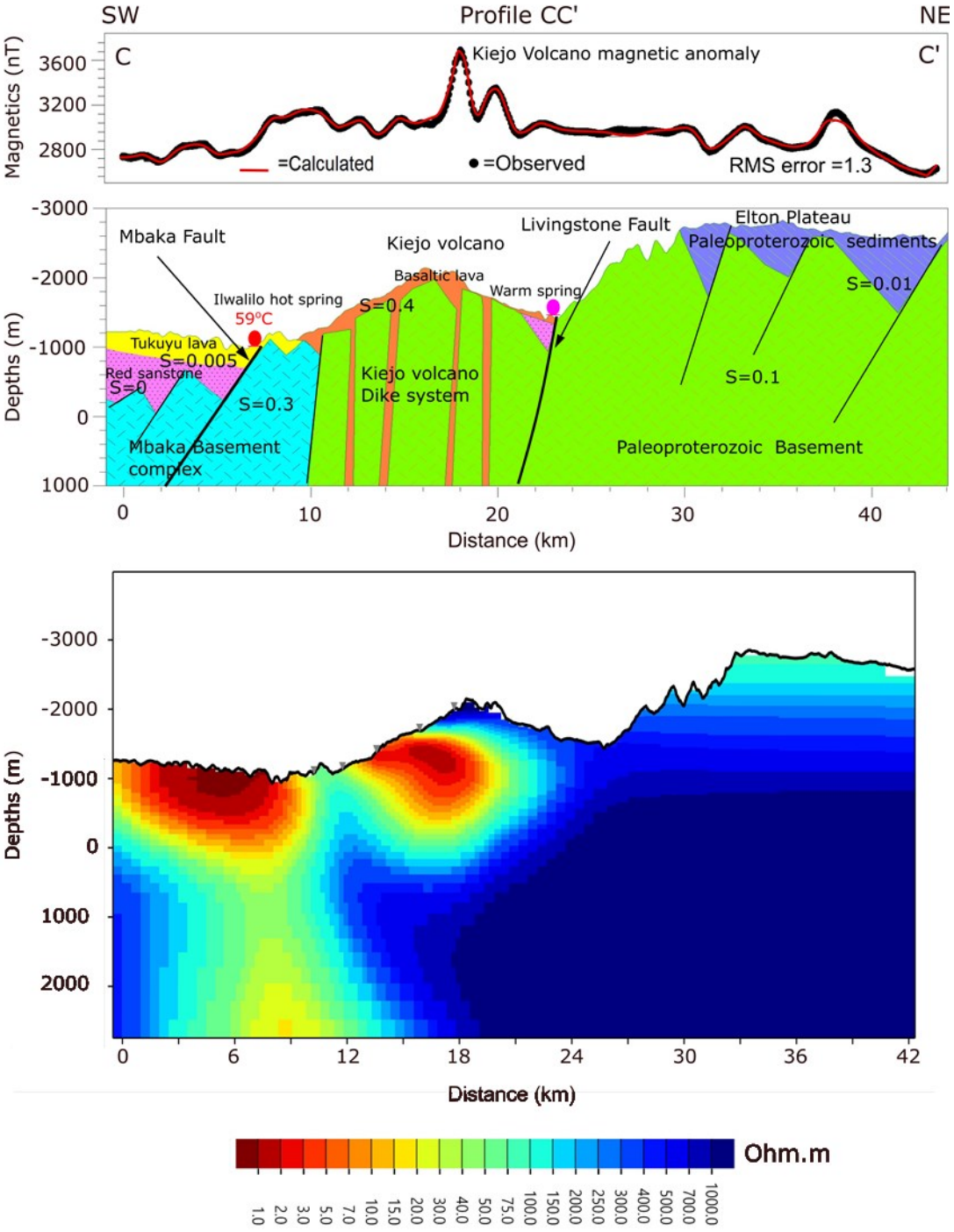


*Fig. 9. A 2D model of magnetization of low pass filtered RTP for profile CC' and resistivity cross-section based on 3D inversion of MT data across Mbaka fault and Kiejo volcano magnetic anomaly. Areas in the resistivity cross-section without MT data coverage should not be emphasized. The location of the profile is shown in Fig. 6. Geological features in the figure are from Fig. 3 and the 3D MT resistivity model is from Didas et al. (2023). The vertical exaggeration on the figures is 3.*

140

### 5.3 Estimated depths to the magnetic sources

Fig. 10 shows estimates of depth to magnetic bodies associated with magnetic volcanics, igneous intrusions and Precambrian basement covered by volcanics and sedimentary formations. These estimates give insight into the thickness of the sedimentary cover, especially in rift basins. Depths to magnetic basement may be over-estimated if the upper layer of the basement is non-magnetic due to weathering, hydrothermal alteration, or initial lack of ferromagnetic minerals.

There are two clusters in these depth estimates: shallow magnetic bodies ranging from 0 m to <450 m and deep magnetic bodies ranging from >450 m to ~7250 m. Shallow magnetic bodies are found in the outcropping basement rocks in the Lupa, Mbozi, and Elton blocks, as well as within the rift (see Fig. 3). In contrast, deeper magnetic bodies, which might be linked to the Ruangwa rift (see Fig. 2), are present in the southern part of the Mbozi block.

The deep-seated magnetic bodies correspond with magnetic anomalies with a smooth texture, while shallow bodies are associated with a rough texture (Fig. 6). Generally speaking, the parts of rift segments covered by lake sediments have deeper magnetic bodies. The areas covered by volcanic rocks exhibit shallow magnetic sources except for the area north of the Rungwe and Mwakaleli volcanoes. The Mbeya high magnetic anomaly is detected as a magnetic body located at a depth ranging from 600 m to 2100 m (Fig. 10).

Based on the 1D and 3D MT resistivity cross-sections of UNEP/ARGeo (2016) and Didas et al. (2023), respectively, the Mbeya magnetic anomaly area is largely covered by generally thin volcanics that overlie a ~1 km thick low resistivity zone interpreted as hydrothermal smectite alteration of basaltic volcanics and sediments that, in turn, overlie resistive Red Sandstone sediments and Precambrian basement (see Fig. 7 lower panel).

The shallow magnetic bodies at 200 m to 400 m depth within the rift segments extend from the south of the Usangu basin to the triple junction near Ngozi volcano and the northern part of the Rungwe volcano. This finding aligns with the shallow basement in the southern part of the Usangu basin according to the interpretation of seismic data (Mbede, 2002). Near the triple junction, the 600 m to 1600 m deeper magnetic bodies occur west and northwest of Ngozi volcano below the Mbeya magnetic high anomaly and the warm springs (<40 °C), respectively, and in the Rungwe volcano area and extend east towards the Mwakaleli caldera. This narrow zone of east-trending deep magnetic bodies that connects the Rungwe and Mwakaleli volcanoes separates two wide zones with shallow magnetic bodies. One wide zone extends northeast from Ngozi volcano to the Usangu basin. In contrast, the other wider zone covers the Kiejo and Tukuyu volcanoes and the Mbaka fault in the northern part of the Malawi rift.

Deep-lying magnetic bodies at a depth range from 800 m to 1500 m have been identified in the central Malawi rift basin, which is covered by sedimentary formations. Along the west side of the basin, Fig. 10 shows magnetic bodies located at a relatively great depth ranging from 500 m to 1000 m below the outcropping Karoo and Cretaceous Red Sandstone formations. Furthermore, the results show deep-lying magnetic bodies along the Livingstone border fault, reaching a depth of 1600 m, which corresponds to the thickness of the lake

sediments estimated from reflection seismic data by Shillington et al. (2020). Another study by Rizzello et al. (2022) using 3D MT inversion has revealed a similar increase in the depth of the Precambrian basement from ~800 m in the northwest to 2000 m in the southeast in the Mbaka graben.

In the Rukwa rift, deep-lying magnetic bodies with a depth range from 800 m to 3000 m are found in areas covered by sedimentary formations to the northwest towards the Songwe trough. These depths reach a maximum of 3000 m, which is similar to the thickness of the lake beds according to drilling and interpretation of reflection seismic data in the northwest Songwe basin (Mulaya et al., 2021). Shallow magnetic bodies have been observed along the Mbeya fault, partly covered by the Songwe scarp carbonatite and recent volcanic rocks, indicating that magnetic sources are mainly found within the carbonatite and volcanic rocks.

In the Usangu basin, magnetic bodies are found at a depth of 250 m in the south near the triple junction, reaching 5000 m in the northeast. These depths to the basement are close to a maximum depth of 3500 m estimated from the limited coverage of reflection seismic data published by Mbede (2002) and Marobhe and Mbede (1996) using gravity data.

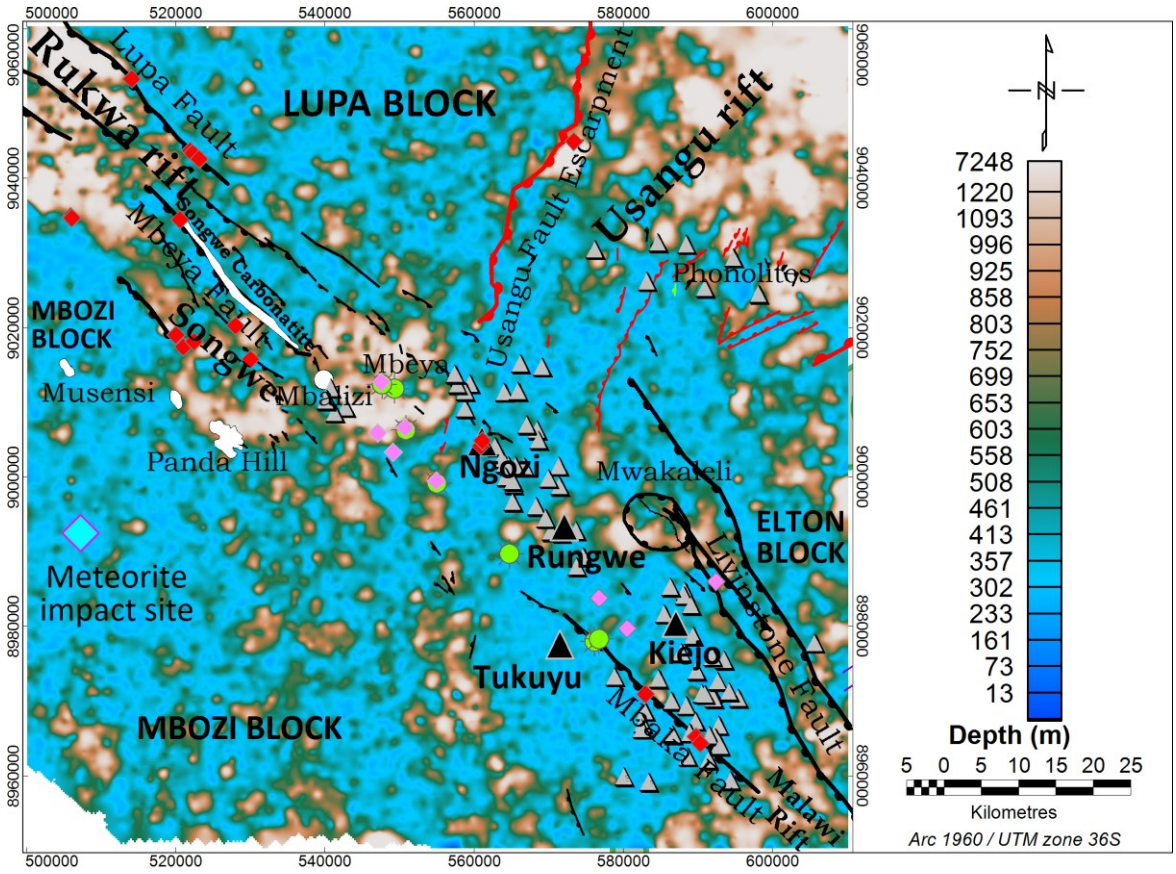


*Fig. 10. Estimated depths to the magnetic sources using the SPI method. For figure legend, see Fig. 3.*

## 5.4 Magnetic lineaments

The spatial extent of the magnetic lineaments obtained by applying the RTP and normalized derivatives methods described in subsections 4.1 and 4.4.2, respectively, are shown as linear features in enhanced RTP and TAHG maps (Figs. 11 & 12). The TAHG map is superimposed with the seismic epicentres to show the correlation between active faults and magnetic lineaments. Although the RTP map shows some high frequency artifacts, it provides some important information about the structural trends in the RVP. Magnetic lineaments extracted from the maps have been plotted as coloured dotted lines together with known faults on the map shown in Fig. 13. The known intrusions are presented as semi-circular and circular dotted features. In order to separate the lineaments caused by active and inactive known faults and lithological contacts, the lineaments have been displayed together with known faults and earthquake epicentres.

The magnetic expressions of known faults seem to extend beyond their surface exposure, therefore, we have extended them, as shown in Fig. 13. For example, the magnetic signature of the NW-trending Livingstone border fault extends further NW for about 26 km beyond its surface limits until it intersects the NW-trending Lupa and NE-SW trending Usangu border faults. This intersection area is also the NW end of the 'Ngozi-Rungwe-Mwakaleli low magnetic zone'(NRM-LMZ) shown in Fig. 11. The magnetic expression of the Mbaka fault extends further in the NW direction, more than 15 km.

The maps reveal four distinct groups of magnetic lineaments: one with a dominant NW-trending set, a less dominant NE-trending set, and a few NS-trending and minor ENE-trending lineaments. The NW, NE and N-S lineaments trends correspond to the regional strikes of the rift system, while ENE-trending lineaments coincide with the current stress field in the study area as discussed in subsection 2.3 above.

### 5.4.1 Magnetic lineaments in Precambrian basement blocks

Magnetic lineaments that primarily trend NW-SE, with a few E-W and N-S lineaments in the southern part, have been identified in the Mbozi block (Figs. 11 & 12). The Elton plateau features a few ENE and NS-trending magnetic lineaments and circular anomalies that intersect with NW-trending magnetic lineaments, which appear to cross-cut the Usangu basin and continue into the Lupa basement block. In contrast, the Lupa basement block is characterized by magnetic lineaments that trend in the NE, NS, and NW directions (Figs.11 & 12).

### 5.4.2 Magnetic lineaments in the RVP

The RVP (i.e., Songwe, Ngozi, Rungwe, Mbaka, Kiejo and Mwakaleli regions) is characterized by a statistical dominance of NW-SE magnetic lineaments, with some NNE-SSW, NNW-SSE, N-S, NE and ENE to ESE lineaments, as shown in the rose diagrams (Fig. 13) corresponding to the known main sets of fault system discussed in subchapter 2.3. The NW-SE magnetic lineaments correspond with the trend of the Rukwa rift basin, the NNE-SSW, NNW-SSE and N-S trending lineaments align with the general trend of the Malawi rift basin, and NE lineaments correspond with the main trend of the Usangu rift basin. In addition, the ENE to ESE trending lineaments are consistent with interpretations of the

current stress field in the study area (Ebinger et al., 2019). The four most prominent magnetic lineaments are the NW-trending lineament aligned with the Livingstone fault, a lineament associated with Mbaka fault, a lineament aligned parallel to the Mbaka fault and the extended lineament which connects the Ngozi, Rungwe and Kiejo volcanoes (Figs. 11 & 12). Several other NW-trending magnetic lineaments which are sub-parallel to the Livingstone fault are prominent in the Mbaka graben (Figs. 11 & 12). Many of these NW-trending magnetic lineaments seem to converge with the Mbaka fault in the vicinity of the eroded Tukuyu volcano. There are a few magnetic lineaments parallel to the Mbaka fault, the most prominent being the ''Mbaka parallel lineament'' (MP-lineament).

The NW-trending magnetic lineament that connects the Ngozi, Rungwe and Kiejo volcanoes consists of a set of small second-order lineaments that is more apparent in the RTP map (Fig. 11) and less visible in the TAHG map (Fig. 12). For this reason, we consider this feature to represent a regional first order lineament. The ''Ngozi-Rungwe-Kiejo-lineament'' (NRK-lineament) is named after the three volcanoes aligned with this lineament. The NRK and MP lineaments are located within the seismically active block separated by the Mbaka fault and the Livingstone border fault (Figs. 11 & 12). The NRK lineament extends northwest to the Lupa block and in the southeast, it joins with the Livingstone fault (Fig. 11). The Ngozi-Rungwe fault zone, which appears between the Ngozi and Rungwe volcanoes, is a part of this long-standing lineament (Fig. 13). In this same area, a 3D MT resistivity model has been interpreted by Didas et al. (2023) as resolving a low resistivity clay cap above an active high-temperature geothermal system. Researchers (e.g., Marobhe, 1989; Fontijn et al., 2012; Mulaya et al., 2021) propose this magnetic lineament to be the southeast extension of the Lupa border fault, which vanishes in the triple rift junction.

The prominent magnetic lineament of the Mbaka fault extends from Lake Malawi and terminates south of Ngozi volcano (Fig. 11). The MP-lineament seems to have a limited extension and is only visible from south of Kiejo volcano to the south of Rungwe volcano (Fig. 12). This lineament is associated with the warm springs (Fig. 12) and hot ground area mapped on the southeast flank of Rungwe volcano (Didas et al., 2023). The Mbaka fault and the sub-parallel magnetic lineaments in the graben, NRK and MP lineaments are cross-cut obliquely by the other two sets of magnetic lineaments, the NW-trending magnetic lineaments which are parallel to the Livingstone fault and the NS-trending magnetic lineaments which cut through the hot spring area at the Mbaka fault and Kiejo volcano and associated volcanic centres (Fig. 11 & 12). From Kiejo volcano, the NS-trending magnetic lineaments extend through the Elton basement block until they disappear further in the Usangu basin near the Phonolite domes. The intersection of these NS-trending magnetic lineaments with NW-trending magnetic lineaments along the Mbaka fault is likely to be the locus of surface hydrothermal manifestations.

The NE and ENE to ESE trending lineaments are predominant in the Usangu basin and in the area between the Ngozi and Rungwe volcanoes which displays the NE-trending magnetic lineaments and are less common in other parts of the RVP. These NE to ESE-trending magnetic lineaments extend from the NW-end of the Mbaka graben towards NE by crossing the Precambrian basement into the NRM-LMZ (Figs. 11, 12 & 13). Many NE-trending magnetic lineaments, which are seismically active, correlate with the known faults that cross-cut the volcanoes (e.g., Delvaux et al., 2010), suggesting that they might be due to

concealed young dikes that formed contemporaneously with the volcanoes and current stress field which changed from the ENE extension to ESE compressional strike-slip orthogonal to the Mbaka fault (Ebinger et al., 2019). However, to support this interpretation, further investigation is needed, including a detailed analysis of the spatial distribution of the volcanic vents, geomorphological analysis, and InSAR studies.

In general, the Usangu, Rukwa-Songwe trough and the central part of the Malawi rift have a few magnetic lineaments. Magnetic lineaments are rare to the east of the Usangu basin, while a few of them are visible in the south near the triple rift intersection (Figs. 11 & 12). In the northern part of the Malawi Rift, the Mbaka graben has more magnetic lineaments than Usangu and Rukwa rift basins. It can be inferred that the intrabasinal NW-trending magnetic lineaments correspond to clusters of dike intrusions within the Mbaka graben. The intra-rift magnetic lineaments are not observed in the Usangu and Rukwa rift basins possibly due to the presence of a non-magnetic thick sedimentary cover overlaying the magnetic basement and the absence of dikes along the faults.

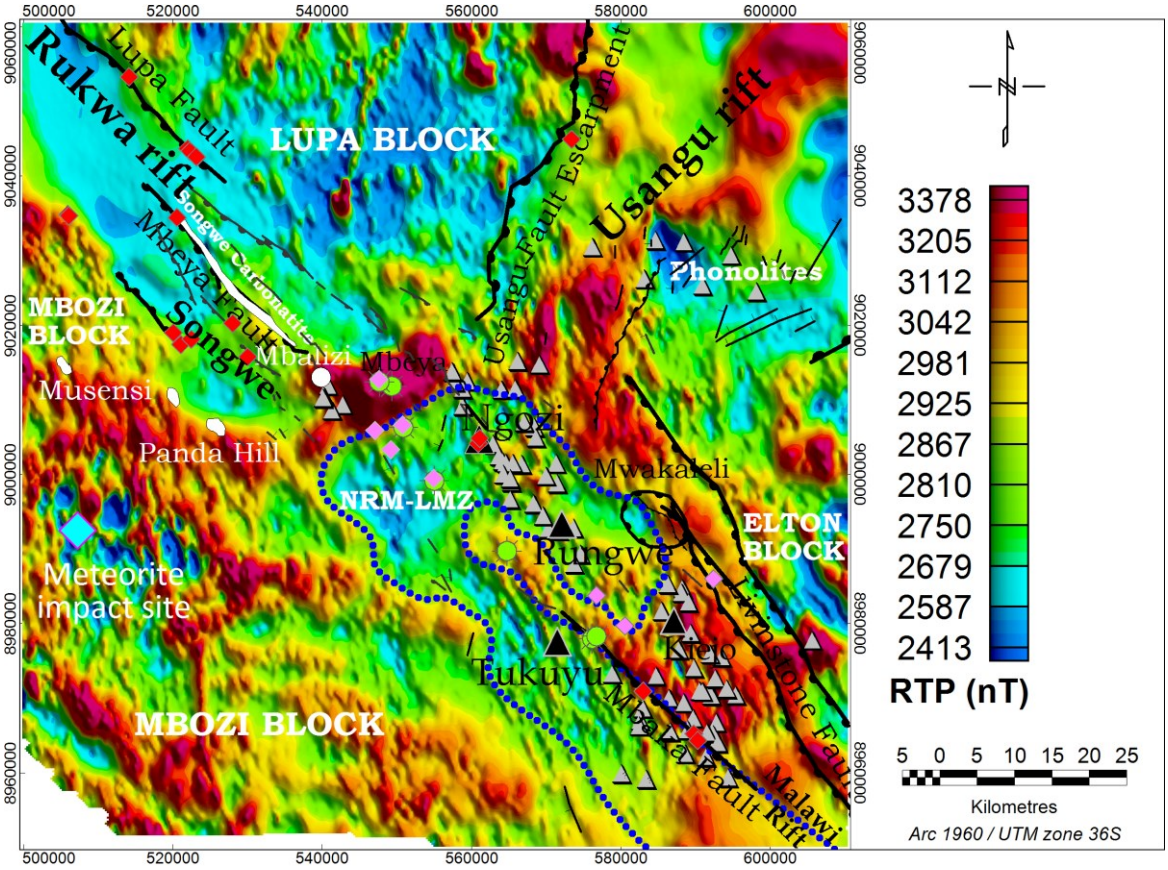


*Fig. 11. RTP colour-shaded map of the RVP visualizing magnetic lineaments. The dotted blue outline is a low-intermediate magnitude zone of the magnetic anomaly within the RVP. White patches indicate the Carbonatite intrusions. For figure legend, see Fig. 3.*

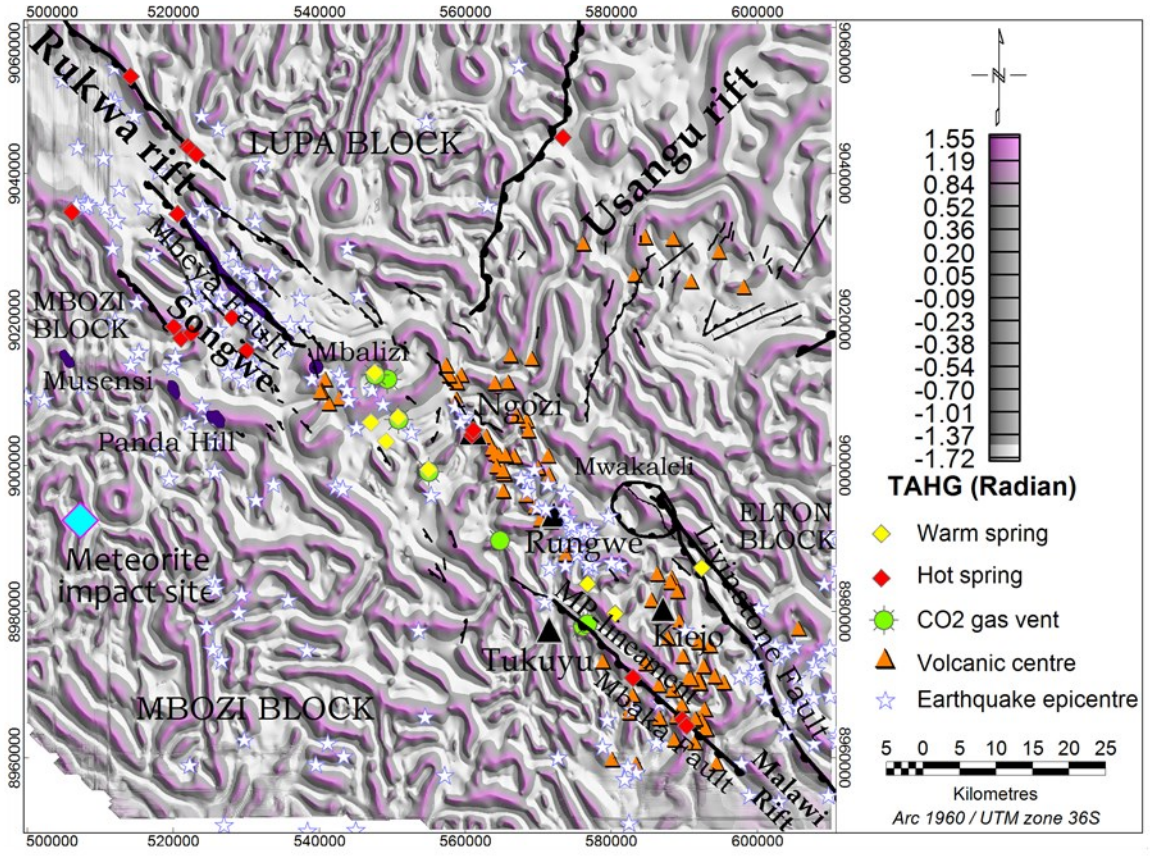


*Fig. 12. TAHG colour-shaded map of the RVP highlighting magnetic lineaments displayed in pink colour. For figure legend, see Fig. 3. Note the correlations between magnetic lineaments and seismic epicentres.*

In the Rukwa rift, magnetic lineaments are generally absent except for a few in the Songwe basin and the Lupa and Mbeya border faults which display prominent magnetic lineaments consistent with the locations of the earthquake epicentres. The Mbeya front fault, a prominent feature in the enhanced magnetic maps (Figs. 11 & 12), becomes fainter and eventually dissipates as it approaches the rift triple junction and does not appear to join the Mbaka fault. It is possible that the southeast extension of the fault together with the northwest extension of the Mbaka fault are accommodated in the NRM-LMZ in the rift triple junction (Fig. 11). A few NW-trending magnetic lineaments present in the Songwe basin are cross-cut by the NNE and NNW lineaments running from the Mbozi basement block through the Panda Hill, Songwe hot springs area, and Lupa basement block. Mulaya et al. (2021) reported that the NNE and NNW faults are the predominant faults extending into the Mbozi block, based on 2D reflection seismic data in the Rukwa basin.

The Lupa border fault which separates the Rukwa rift and the Lupa Precambrian basement block to the north is clearly visible in the topographical (Fig. 4) and magnetic data (Fig. 11). However, the southeast extension of the Lupa fault disappears in the rift triple junction (Figs. 4, 11 & 13). Despite claims made by several authors that the Lupa fault may extend through the RVP (e.g., Marobhe 1989; Delvaux and Bath, 2010; Delvaux et al., 2010; Fontijn et al., 2012; Mulaya et al., 2021), our findings do not support this notion. It is possible that the

Lupa fault is not associated with rocks with contrasting magnetic properties or is obscured by the Mbeya magnetic high anomaly (Fig. 11)

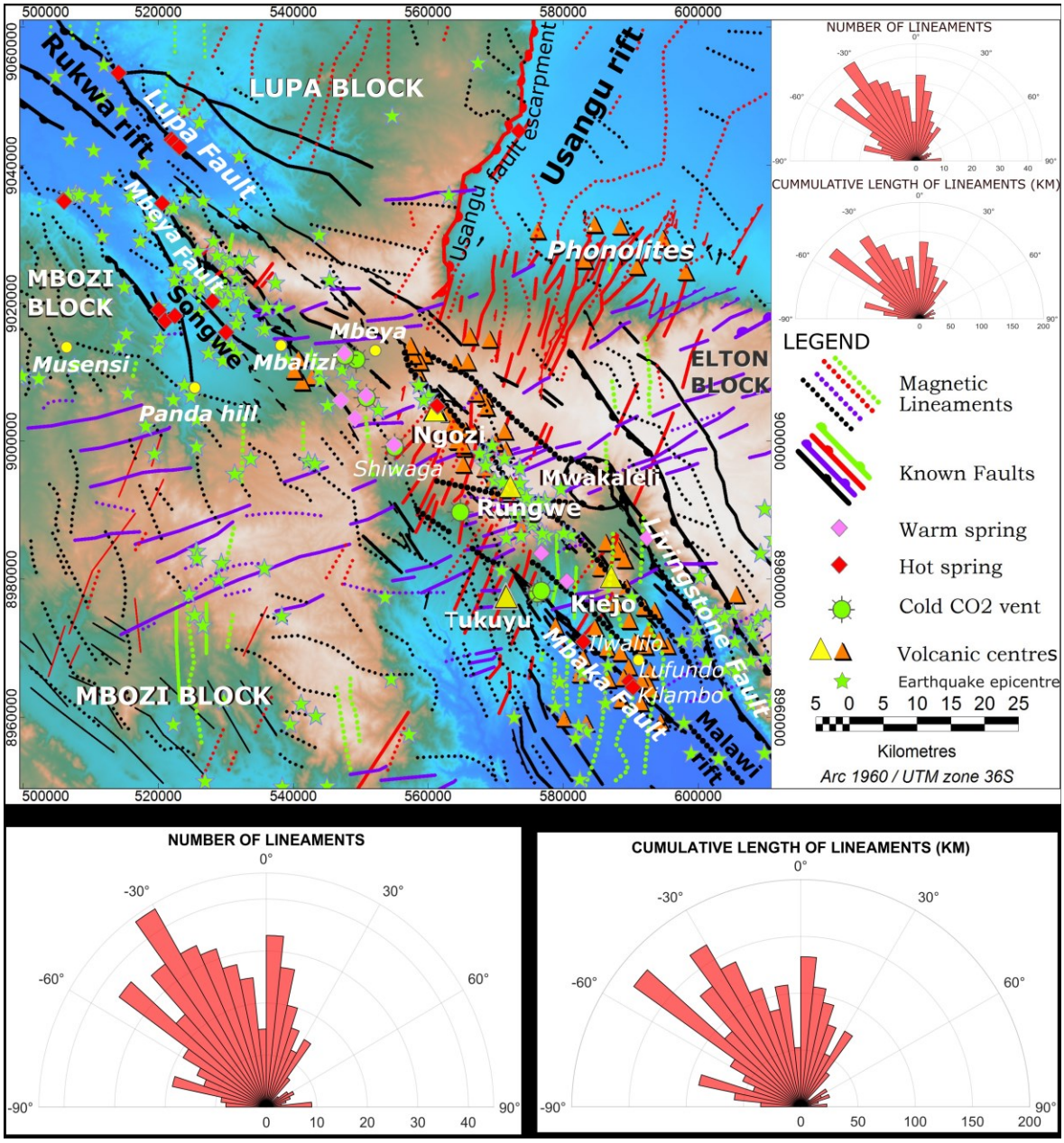


*Fig. 13. Improved lineament and structural map of the RVP, combining known faults (confirmed by surface mapping and seismic data) and magnetic lineaments superimposed on the SRTM-30 m resolution topographic map.*

## 6 Geological interpretations of the magnetic anomalies

### 6.1 Possible sources of the magnetic anomalies

Within this study, we explore the main magnetic anomalies of the RVP by comparing them with known geology, faults, intrusions, age and petrophysical measurements of the rocks reported by several authors (e.g., Marobhe 1989; Fontijn et al., 2012; Delvaux et al., 2010; Hinz et al., 2018). We also interpret the anomalies and compare them with the depths estimated from this study and previous studies based on MT resistivity data (Rizzello et al., 2022; Didas et al., 2023) and reflection seismic data (Mbede, 2002; Shillington et al., 2020; Mulaya et al., 2021).

Based on the geology of the RVP (see Fig. 3), the magnetic anomalies displayed in Fig. 6 are primarily caused by Precambrian basement rocks that are either exposed at the surface or buried by lake sediments in the rift segments. The Precambrian basement rocks exposed include the Lupa, Mbozi and Elton blocks. These blocks border the rift segments, and display magnetic anomalies with mixed patterns. In areas covered by volcanic rocks, the magnetic anomalies are greatly influenced by the volcanics and dikes possibly feeding eruptions (Figs. 7-9).

In the Lupa basement block, low magnetic anomalies (see Fig. 6) covering large areas are mainly associated with granitoids rich in magnetite of high remanent reverse magnetization compared to the induced magnetization hence causing reversal magnetization (Marobhe, 1989). The high magnetic anomalies are due to mafic and ultramafic intrusives which include the metaperidotites and metagabbros which extend into the Usangu basin where they are covered by lake sediments. The prominent elongated magnetic linear feature trending NS was interpreted by Marobhe (1989) as dolerite dikes along possible NS trending faults that do not outcrop on the surface.

In the Elton basement block, the NW trending high magnetic anomalies at the escarpment of the Livingstone fault are caused by mafic-ultramafic intrusion bodies including meta-anorthosites, gabbros and norites reported by Marobhe (1989) that have filled the extension shear zones or faults which likely formed pull-apart basins. These intrusions extend to the west forming the intrusive Precambrian basement complex along the horst of the Mbaka fault reported by Rizzello et al. (2022).

The Mbozi block has many magnetic high anomalies compared to the Elton and Lupa blocks. These anomalies are attributed to the presence of carbonatite intrusions that are rich in pyrrhotite (Boniface, 2017), as well as gabbroid and pyroxenite bodies that contain primarily pyrrhotite, magnetite, chalcopyrite, and pyrite, all of which have high magnetic susceptibility (Marobhe, 1989). It is assumed that the intrusive rocks in the Mbozi block were formed due to the collision between the Ufipa block (located east of the Mbozi block but not shown on the map) and Mbozi block during the Proterozoic period (Nanyaro, 1984). The north-trending high magnetic lineament was interpreted by Marobhe (1989) as the pigeonite dolerite dike intruded along the fault trend. A zone of low magnetic anomaly is likely caused by the demagnetization of the rocks due to a meteorite impact.

Within the RVP, magnetic anomalies are significantly influenced by volcanic rocks and intrusions that are concealed by volcanics. The interpreted carbonatite intrusion (Fig. 6 and 7), modelled at around 800 m depth below the Mbeya high magnetic anomaly, is consistent with the model reported by Marobhe (1989). This dike system may be an extension of the Mbalizi carbonatite (Sun et al., 2021) exposed to the west within the same anomaly (Fig. 6). Low magnetic anomalies at the triple junction may also be caused by the chemical weathering of volcanic tuffs. This weathering occurs due to the interaction with meteoric water, which converts magnetite into non-magnetic limonite and hematite. Yellow-brown and reddish-black weathered volcanic tuffs have been mapped at the triple junction at a depth greater than 3 m (Fontijn et al., 2010b). In the Usangu basin, a NW-SE trending high magnetic anomaly covered by lake sediments (Fig. 6) corresponds to the ultramafic intrusion outcropping on the northeast part of the Lupa block (Fig. 3). The source of the NE-trending high magnetic anomaly within the basin is still unknown, however, it has variability (Fig. 6), estimated depth (Fig. 10) and properties similar to the the ultramafic intrusion in the Lupa block. The NE-trending high magnetic anomaly is truncated by the very low magnetic anomaly of Miocene-aged phonolite domes. The truncation of the NE-trending high magnetic anomaly at the phonolite domes shows that the phonolite volcanism that occurred in the Miocene post-dates the rocks that create the high magnetic anomalies in the Usangu basin. This high magnetic anomaly is also associated with a positive regional Bouguer gravity anomaly (Marobhe and Mbede, 1996), indicating an uplift in the basement. Therefore, based on the stratigraphic sequence of the basin (Mbede, 2002), we propose that the NE-trending high magnetic anomaly is likely associated with the old intrusions that preceded the development of the EARS in the Upper Miocene to Pliocene.

A similar high magnetic anomaly in the southern part of the Usangu basin, near the triple junction, seems to be the NW extension of the ultramafic bodies with high magnetic values that have filled the extensional shear zones along the Livingstone fault escarpment. Based on the geology of the area (Fig. 3), the intrusion bodies are covered by old lake beds (Upper Miocene-Pliocene).

The low magnetic values within the rift segments are associated with basement rocks that are buried deep beneath the Karoo, Cretaceous Red Sandstone, lake sediments and overlaying volcaniclastic formations. The interpretation of deep basement rocks is consistent with low gravity values of the sedimentary formation and Cenozoic volcanics (Ebinger et al., 1989; Marobhe and Mbede, 1996; Rizzello et al., 2022; Hinz et al., 2018) and thick sedimentary formations overlaying the Precambrian basement interpreted using reflection seismic data (Mbede, 2002; Mulaya et al., 2021; Shillington et al., 2020). Such areas include (i) Rukwa-Songwe trough, where the basement is covered by the Karoo formation, Cretaceous Red Sandstone, and lake sediments, (ii) the NE-trending low magnetic zone covering the Ngozi-Rungwe-Mwakaleli volcanoes, where the basement is covered by Cretaceous Red Sandstone, which is largely covered by Neogene volcanics and (iii) the Mbaka graben, where the basement rocks are covered by Karoo sediments and Cretaceous Red Sandstone, which is largely overlain by Neogene volcanic products. We, therefore, refer to the low magnetic zone covering the Ngozi-Rungwe-Mwakaleli volcanoes as the NRM-LMZ after the enclosed volcanoes therein (see Fig. 6).

The basement depth estimates from magnetic data using the SPI method (Fig. 10) are consistent with the thicknesses of the sedimentary formations derived from the interpretations of reflection seismic data in the rift basins that have detected the Precambrian basement concealed by thick sedimentary formations. In the Usangu basin, the thickness of the sedimentary formation is about 3 km in the northeast and decreases south towards the triple junction (Mbede, 2002), and in the Songwe basin, a maximum thickness of 3 km was interpreted by Mulaya et al. (2021) while in the Malawi rift basin, the thickness is about 5 km to the north near the RVP and decreases to the south (Shillington et al., 2020).

In particular, the triple junction area, comprising the Ngozi, Rungwe, Kiejo, Mwakaleli, and Tukuyu volcanoes and their surrounding areas, are associated with shallow magnetic anomalies. These shallow magnetic anomalies arise from the presence of volcanic rocks overlying the Cretaceous Red Sandstone and Karoo sandstone. At the western and southeastern borders of the NRM-LMZ, the area is largely covered by Karoo sandstone and Cretaceous Red Sandstone with fewer volcanic rocks. Magnetic anomalies in these areas are largely influenced by deep Precambrian basement rocks which are overlain by the Karoo sandstone and Cretaceous Red Sandstone rocks (Fig. 10).

### 6.2 Improved structural map of the RVP and its geothermal implications

In this subsection, we present a comprehensive analysis of the magnetic anomalies, surface geothermal manifestations, and geothermal systems in the RVP as illustrated in Fig. 14.

In the Rungwe geothermal prospect, the results have revealed that the high-temperature prospective reservoir interpreted below the Rungwe volcano by Didas et al. (2023) is located at the intersection between the NW, NS, and ESE-trending magnetic lineaments including the NW-SE trending fault zone, which connects the Ngozi, Rungwe and Kiejo volcanoes (Figs. 11 & 12).

The NRM-LMZ includes prospective high-temperature reservoirs situated underneath the Ngozi and Rungwe volcanoes. This interpretation is based on the combined geothermometry data obtained from chloride hot springs beneath the Ngozi caldera lake, an updomed base of the clay cap beneath Rungwe volcano, hot ground areas with temperature exceeding 53°C on the northeastern flank of Rungwe volcano, an inferred shallow magma body from a deep conductor at a depth of 6 km between the Ngozi and Rungwe volcanoes, and the presence of several monogenetic volcanic eruption centres that provide strong evidence for the presence of prospective high-temperature reservoirs in the region. The NRM-LMZ is also home to several Na-$HCO_3$ warm springs (<40°C) west and northwest of the Ngozi caldera, on the southern flank of the Rungwe volcano and along the Mbaka fault which further supports the potential for a low-temperature conductively heated geothermal system west and northwest of the Ngozi caldera (UNEP/ARGeo, 2016) and a medium temperature deep circulation fault-controlled geothermal system in the Kiejo-Mbaka prospect (ELC and TGDC, 2017; Rizzello et al., 2022).

The area of the updoming of the clay cap beneath the Rungwe volcano (Didas et al., 2023) is cross-cut by the NE-trending magnetic linements and ESE magnetic lineament that connects the Rungwe and Mwakaleli volcanoes. This doming resistivity structure is likely to be correlated with a transition from the low resistivity smectite clay cap to the more

resistive chlorite and illite clay characteristic of geothermal reservoirs, consistent with fracture permeability interpreted based on these lineament analyses. In addition, the 2D forward modelling of the magnetic anomalies over the Rungwe volcano requires a magnetic layer with zero susceptibility overlying the Precambrian basement which could indicate propylitically altered Cretaceous Red Sandstone, Karoo sandstone and /or old volcanics (Fig. 8). Moreover, seismically active areas in the NRM-LMZ particularly below Rungwe volcano (Delvaux and Hanon, 1993; Ebinger et al., 2019; see Figs. 3 & 4), suggest a highly faulted area that has likely increased the permeability of the geothermal reservoir.

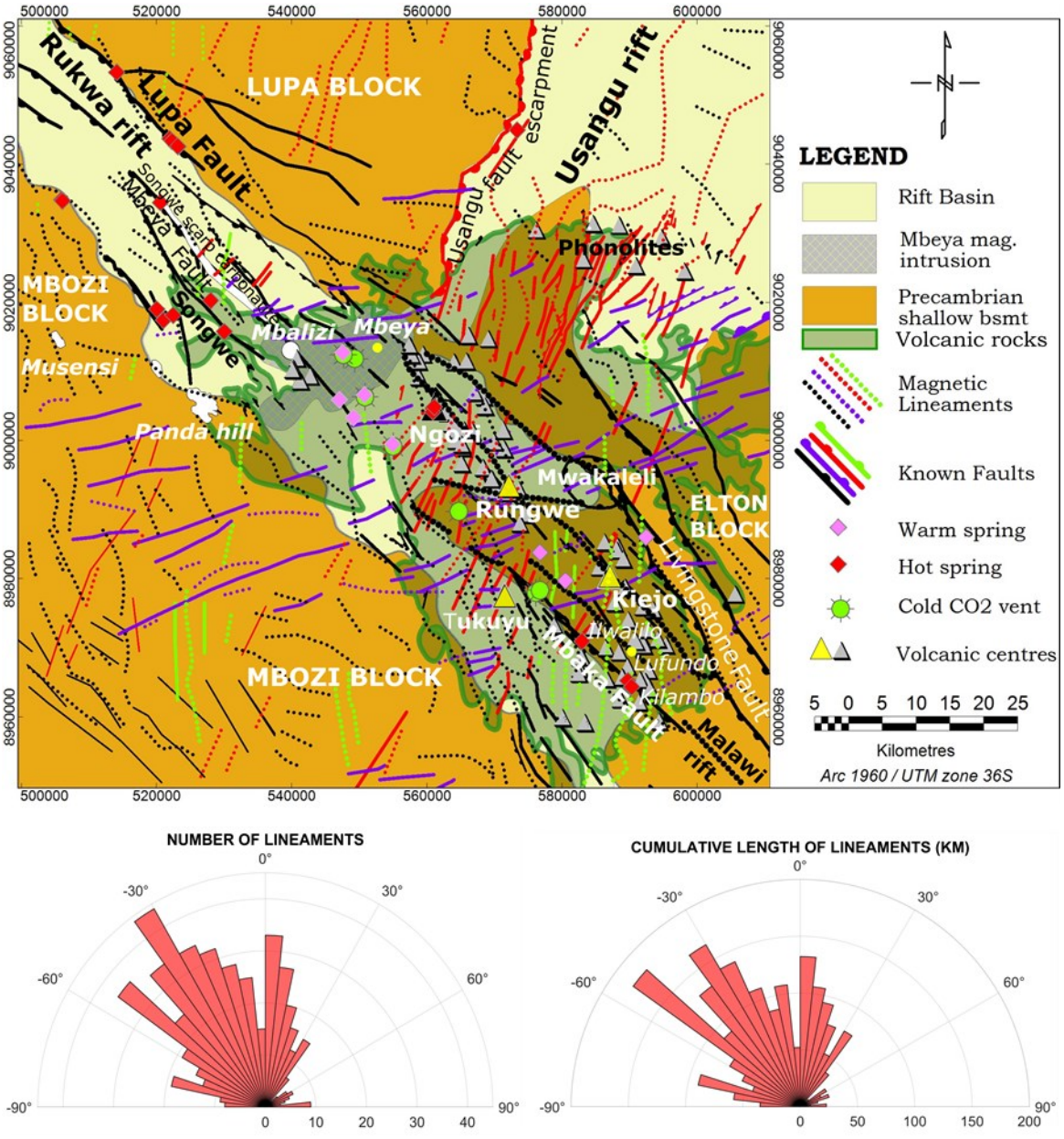


*Fig. 14: Improved structural map of the RVP. Rift segments are plotted by combining known faults and magnetic lineaments from this study. The green outline feature indicates the area covered by volcanic rocks.*

In the Kiejo-Mbaka prospect to the south of Rungwe, the geothermal manifestations including Kilambo-Kajala and Ilwalilo hot springs are present at the intersection between the Mbaka fault and the NS trending magnetic lineaments. A closer examination of the Mbaka fault shows several NE trending magnetic lineaments that extend from the hanging wall into the NRM-LMZ through the Rungwe and Ngozi volcanoes and across the monogenetic volcanic eruption centres. Additionally, NS trending magnetic lineaments also cross-cut the Mbaka fault and they are consistent with the observation from surface geological mapping in the Mbaka prospect (ELC and TGDC, 2017).

The fault which connects the Ngozi, Rungwe and Kiejo volcanoes is also partially revealed in gravity data from the Kiejo-Mbaka prospect and passes through the Lufundo fossil manifestation (Rizzello et al., 2022). This fault is associated with a moderately conductive anomaly within a highly resistive basement (ELC and TGDC, 2017; Rizzello et al., 2022).

The extensive magnetic lineament of the Livingstone fault to the east of Rungwe and Ngozi volcanoes, defines the boundary of NE-trending magnetic lineaments and NE-trending known faults from the triple junction and Usangu basin, respectively (Fig. 13). This boundary aligns with the eastern limit of the Ndaga ring structure, which Didas et al. (2023) using 3D MT resistivity model have interpreted as containing the magmatic heat source heating the Ngozi and Rungwe high-temperature geothermal systems. Therefore, it is likely that SE of the triple junction, the extent of the high-temperature geothermal system below Rungwe volcano is limited to the east by the Livingstone fault which might be causing cold meteoric water inflow to the system while to the west, the system is limited by the less permeable Mbaka uplifted basement created by the Mbaka fault.

At Songwe geothermal prospect, the findings demonstrate that the surface geothermal manifestations are found at the intersection between the NS and NW trending magnetic lineaments likely forming the strike-slip stepover geometry as reported by Hinz et al. (2018). Furthermore, between Ngozi and Songwe, the Mbeya front range fault appears to penetrate through the low-temperature reservoir interpreted as a conductive heated geothermal system to the northwest of the Ngozi volcano based on geochemistry and resistivity pattern (UNEP/ARGeo, 2016). This fault could potentially serve as a significant conduit for meteoric water recharge for the low-medium temperature geothermal system in Songwe and northwest of Ngozi volcano.

## 7 Conclusions

In this study, subsurface structures concealed by sedimentary formations and recent volcanics have been investigated using aeromagnetic data and correlated with known faults and seismic epicentres to evaluate structural permeability and impermeable boundaries for the geothermal prospects in the Rungwe Volcanic Province (RVP). Our detailed analysis of the magnetic anomalies has revealed the possible existence of significantly locally enhanced permeability in the region with deep water circulation limited by generally low permeability Precambrian rocks, which is important for the geothermal development of the RVP. The analysis of the magnetic lineaments and known faults revealed a good correlation. However,

the magnetic lineaments of the known faults extend far beyond the mapped surface expression of the known faults.

Our research has further clarified the structural alignment between the known geothermal prospects and geological features, including faulting, young intrusions, and surface geothermal manifestations. The primary outcome is an updated neotectonic structural map of the RVP, which has significant implications for geothermal resource targeting in the Ngozi, Rungwe, Songwe, and Kiejo-Mbaka prospects. We believe that this enhanced map will serve as a valuable tool for understanding the geological fracture system controlling hydrologic fluid circulation and impermeable boundaries of geothermal resources in the RVP.
The distinctive magnetic anomalies in the RVP emanate primarily from the Precambrian basement rocks and Cretaceous carbonatite intrusions. Our analysis has proposed intrusions that can account for magnetic anomalies. Areas where the surface rock exposures consist of Paleoproterozoic basement rocks of mafic-ultramafic and banded iron composition exhibit the highest magnetic intensity, while areas covered by felsic rocks or Miocene phonolites show intermediate-low magnetic intensities.

Neogene volcanic eruption centres such as Rungwe, Tukuyu and Kiejo volcanoes and several monogenetic eruption centres exhibit magnetic high anomalies, but these intensities diminish away from the volcanic centres, resulting in intermediate-low magnetic anomalies. Longer wavelength magnetic anomalies are observed in sedimentary-filled rift basins that lack shallow volcanic rocks. At the triple junction and in some parts of the rift basins where volcanic rocks dominate over sedimentary rocks, generally short wavelength magnetic anomalies are seen. Shallow magnetic bodies coincide with the outcropping basement rocks and Neogene volcanics.

Our analysis also revealed that a NW trending magnetic lineament connects the Ngozi, Rungwe, and Kiejo volcanoes and it is parallel to the Mbaka fault. The Rungwe volcano is intersected by at least four sets of magnetic lineaments trending in ESE, NE, NS, and NW directions, respectively. By contrast, the Ngozi volcano is mainly intersected by the NW trending magnetic lineament, while the Kiejo volcano and Mwakaleli caldera are intersected by NW and NS trending magnetic lineaments. This suggests that fracture permeability might be enhanced below the Rungwe, Kiejo, and Mwakaleli volcanoes but to a lesser extend below the Ngozi volcano.

Furthermore, the magnetic data do not support the extension of the Mbaka fault NW to the Songwe basin, but it appears to extend further SE into Lake Nyasa. It disappears in a broad low magnetic zone likely to be a basin enclosing the Ngozi, Rungwe, and Mwakaleli volcanoes.

A large number of magnetic lineaments are observed within the Mbaka graben, but very few magnetic lineaments are found in the Rukwa-Songwe trough and the Usangu basin. This suggests that the Mbaka fault is affected by dike intrusions, while the Rukwa-Songwe and Usangu basins are less affected.

Finally, we have identified a magnetic low enclosing the Ngozi, Rungwe, and Mwakaleli volcanoes, monogenetic volcanic eruption centres, and hot springs as an area with the relatively impermeable Paleoproterozoic crystalline basement at a depth ranging from 600 m to 1600 m. Profiles across these zones were modelled using 2D magnetic and 3D MT resistivity methods. They were interpreted as zones with rock properties and structures favourable to the enhanced fracture permeability of a geothermal reservoir. Consequently, we propose the present results be followed by gravity, seismic surveys and Lidar-supported ground mapping of the currently active faults that would support our interpretation of the areas with enhanced permeability as potential targets for a high-temperature geothermal system imaged by magnetotelluric (MT) data in the RVP.

## Acknowledgements

This research is financially supported by the GRÓ Geothermal Training Programme in Iceland (GRÓ GTP) under the auspices of UNESCO (formerly UNU-GTP). It is a part of the PhD programme of the first author carried out at the University of Iceland. We thank Tanzania Geothermal Development Company (TGDC) for providing the aeromagnetic data. Sincere appreciation is extended to the PhD committee member, Ásdís Benediktsdóttir for useful discussions, insights and reviews during this study. Egidio Armadillo has been supported by the University of Genoa (FRA 2023). We acknowledge the extensive reviews from Professor Karen Fontijn and an anonymous reviewer that have greatly improved the manuscript.

## Supplementary materials

Supplementary material associated with this article is attached as a separate document.

## References

Alexander, K., Cumming, W.B., Malini, L., 2016. Technical review of the geothermal potential of Ngozi and Songwe geothermal prospects. In: Proceedings of the 6th African Rift Geothermal Conference. Addis Ababa, Ethiopia.

Amoroso, O., Napolitano, F., Hersir, G.P., Agustsdottir, T., Convertito, V., De Matteis, R., Gunnarsdóttir, S.H., Hjörleifsdóttir, V., Capuano, P., 2022. 3D seismic imaging of the Nesjavellir geothermal field, SW-Iceland. Front. Earth Sci. 10:994280. https://doi.org/10.3389/feart.2022.994280.

Armadillo, E., Rizzello, D., Pasqua, C., Pisani, P., Ghirotto, A., Didas, M., et al., 2020. Geophysical constraints on the Luhoi (Tanzania) geothermal conceptual model. Geothermics 87, 101875. https://doi.org/10.1016/j.geothermics.2020.101875.

Árnason, K., 2020. New Conceptual Model for the Magma-Hydrothermal-Tectonic System of Krafla, NE Iceland. Geosciences 10, 34. https://doi.org/10.3390/geosciences10010034.

Asnin, S.N., Nnko M., Josephat, S., Mahecha A., Mshiu, E., Bertotti, G., Brehme M., 2022. Identification of water–rock interaction of surface thermal water in Songwe medium temperature geothermal area, Tanzania. Environmental Earth Sciences 81:513. https://doi.org/10.1007/s12665-022-10594-4.

Baranov, V., Naudy, H., 1964. Numerical calculation of the formula of reduction to the magnetic pole. Geophysics, 29, 67-79. https://doi.org/10.1190/1.1439334.
Boniface, N., Schenk, V., 2012. Neoproterozoic eclogites in the Paleoproterozoic Ubendian belt of Tanzania: evidence for a pan-African suture between the Bangweulu block and the Tanzania Craton. Precambrian Res. 208, 72–89. https://doi.org/10.1016/j.precamres.2012.03.014.
Boniface, N., Appel, P., 2017. Stenian - Tonian and Ediacaran metamorphic imprints in the southern Paleoproterozoic Ubendian Belt, Tanzania: constraints from in-situ monazite ages. J. Afr. Earth Sci., 133, 25–35. https://doi.org/10.1016/j.jafrearsci.2017.05.005.
Boniface, N., 2017. Crystal chemistry of pyrochlore from the Mesozoic Panda Hill carbonatite deposit, western Tanzania. J. Afr. Earth Sci. 126, 33–44. https://doi.org/10.1016/j.jafrearsci.2016.11.026.
Boniface, N., Appel, P., 2018. Neoproterozoic reworking of the Ubendian belt crust: implication for an orogenic cycle between the Tanzania Craton and Bangweulu block during the assembly of Gondwana. Prec. Research., 305, 358–385. https://doi.org/10.1016/j.precamres.2017.12.011.
Boniface, N., 2019. An overview of the Ediacaran-Cambrian orogenic events at the southern margins of the Tanzania craton: implication for the final assembly of Gondwana. J. Afr. Earth Sci. 150, 123–130. https://doi.org/10.1016/j.jafrearsci.2018.10.015.
Brazier, R.A., Nyblade, A.A., Florentin, J., 2005. Focal mechanisms and the stress regime in NE and SW Tanzania, East Africa. Geophysical Research Letters 32, L14315. https://doi.org/10.1029/2005GL023156.
Butler, R.F., 1992. Paleomagnetism Magnetic domains to geologic terranes: Boston, Blackwell, 319 p.
Campbell, W.C., 1997. Introduction to geomagnetic fields. Cambridge University Press.
Cooper, G.R.J., Cowan, D.R., 2004. The detection of circular features in irregularly spaced data. Computers and Geosciences, 30(1), 101–105.
Cordell, L., Grauch, V.J.S., 1985. Mapping basement magnetization zones from aeromagnetic data in the San Juan Basin, New Mexico. The Utility of Regional Gravity and Magnetic Anomaly Maps, pp. 181–197
Cumming, W., Colvin, A., Haizlip, J., 2024. USEA-USAID Team Report: Ngozi Geothermal Prospect Technical Review Meeting, March 20th -22nd Mbeya, Tanzania. TGDC internal report (not published), 89 pp.
DECON, SWECO and Inter-Consult, 2005. Tanzania rural electrification study and technical report on geothermal power – Activity 1.4.1, Dar es Salaam, Tanzania, 22 pp.
Delvaux, D., Levi, K., Kajara, R., Sarota, J., 1992. Cenozoic palaeostress and kinematic evolution of the Rukwa–North Malawi rift valley (East African Rift System). Bulletin des Centres de Recherches Exploration-Production Elf Aquitaine 16, 383–406.
Delvaux, D., Hanon, M., 1993. Neotectonics of the Mbeya area, SW Tanzania. Royal Museum for Central Africa, Tervuren, Belgium, Annual reports 1991–1992, 87–97.
Delvaux, D., 2001. Tectonic and palaeostress evolution of the Tanganyika-Rukwa-Malawi rift segment, East African rift System. Peri-Tethys Memoir, 6, 545–567.
Delvaux, D., Kervyn, F., Macheyeki, A.S., Temu, E.B., 2006. Dynamics of the Tanganyika–Rukwa–Malawi Rift transfer zone in the Rungwe–Mbozi area. 21st Colloquium of

African Geology, Maputo, Mozambique, 3–5 July 2006. Geosciences for Poverty Relief, Abs. Vol., pp. 44–45.
Delvaux, D., Kraml, M., Sierralta, M., Wittenberg, A., Mayalla, J.W., Kabaka, K., Makene, C., GEOTHERM working group, 2010. Surface Exploration of a Viable Geothermal Resource in Mbeya Area, Sw Tanzania. Part I: Geology of the Ngozi - Songwe Geothermal System. Proceedings World Geothermal Congress, Bali, Indonesia.
Delvaux, D., Barth, A., 2010. African stress pattern from formal inversion of focal mechanism data. Tectonophysics, 482(1–4), 105–128. https://doi.org/10.1016/J.TECTO.2009.05.009.
Delvaux, D., Kervyn, F., Macheyeki, A.S., Temu, E.B., 2012. Geodynamic significance of the TRM segment in the East African Rift (W-Tanzania): Active tectonics and paleostress in the Ufipa plateau and Rukwa basin. J. of Structural Geology, 37, 161-180. https://doi.org/10.1016/j.jsg.2012.01.008.
Delalande-Le, M.M., Gherardi, F., Williamson, D., Kajula, S., Kraml, M., Noret, A., Abdallah, I., Mwandapile, E., Massault, M., Majule, A., Bergonzini, L., 2015. Hydrogeochemical features of Lake Ngozi (SW Tanzania). J. Afr. Earth Sc. http://dx.doi.org/10.1016/j.jafrearsci.2014.11.004.
Dentith, M.C., 2011. Magnetic methods, airborne. In: Gupta, H.K. (Ed.), Encyclopedia of Solid Earth Geophysics SE-119, Encyclopedia of Earth Sciences Series. Springer, Netherlands, pp. 761–766. https://doi.org/10.1007/978-90-481-8702-7_119.
Didas, M.M., Hersir, G.P., 2021. 1D joint inversion of MT and TEM data from Ngozi geothermal prospect, southwest Tanzania. An integrated interpretation of geoscientific results. Proceedings of the World Geothermal Congress 2020+1, Reykjavik, Iceland.
Didas, M. M., Armadillo, E., Hersir, G. P., Cumming, W., Rizzello, D., 2022. Regional thermal anomalies derived from magnetic spectral analysis and 3D gravity inversion: Implications for potential geothermal sites in Tanzania. Geothermics, 103, 10243. https://doi.org/10.1016/j.geothermics.2022.102431.
Didas, M. M., Armadillo, E., Hersir, G. P., Cumming, W., Rizzello, D., Benediktsdóttir, Á., Geirsson, H., 2023. New MT surveys and 3D resistivity imaging beneath the Ngozi-Rungwe volcanoes at the triple rift junction of the East African Rift System in SW Tanzania: Support for integrated interpretations of geothermal conceptual models. Geothermics, 118, 102893 https://doi.org/10.1016/j.geothermics.2023.102893.
EAGER (East Africa Geothermal Energy facility), 2018. Enhanced resource modelling at Songwe. Unpublished report number T74 – D05, 30 pp.
Ebinger, C.J., Deino, A.L., Drake, R.E., Tesha, A.L., 1989. Chronology of volcanism and rift basin propagation – Rungwe Volcanic Province, East Africa. J. Geophys., Research 94, 15785–15803. https://doi.org/10.1029/JB094iB11p15785.
Ebinger, C.J., Deino, A.L., Tesha, A.L., Becker, T., Ring, U., 1993. Tectonic Controls on Rift Basin Morphology – Evolution of the Northern Malawi (Nyasa) Rift. J. Geophys. Res.-Solid Earth 98, 17821–17836. https://doi.org/10.1029/93JB01392.
Ebinger, C.J., Oliva, S.J., Pham, T.Q., Peterson, K., Chindandali, P., Illsley-Kemp, F., et al., 2019. Kinematics of active deformation in the Malawi rift and Rungwe Volcanic Province, Africa. Geochem., Geophy., Geosys., 20, 3928–3951. https://doi.org/10.1029/2019GC008354.

ELC and TGDC, 2017. Surface Exploration and Training in Kiejo-Mbaka Geothermal Area, Tanzania. TGDC internal unpublished technical report, p. 98.

Ferdinand R., Arvidsson, R., 2013. The influence of local topographic relief on regional stress: an example from the Rukwa rift. TJES, 2, 91-107. https://www.researchgate.net/publication/352992803.

Ferraccioli, F., Gambetta, M., Bozzo, E., 1998. Microlevelling procedures applied to regional aeromagnetic data: an example from the Transantarctic Mountains (Antarctica). Geophysical Prospecting, 46, 177-196. https://doi.org/10.1046/j.1365-2478.1998.00080.x.

Ferreira, F.J., de Souza, J., de Bongiolo, B.E.S.A., de Castro, L.G., 2013. Enhancement of the total horizontal gradient of magnetic anomalies using the tilt angle. Geophysics, 78(3), 33–41. https://doi.org/10.1190/geo2011-0441.1.

Finn, C.A., Morgan, L.A., 2002. High-resolution aeromagnetic mapping of volcanic terrain, Yellowstone National Park. JVG. Res. 115, 207–231. https://doi.org/10.1016/S0377-0273(01)00317-1.

Fontijn, K., Delvaux, D., Ernst, G.G.J., Kervyn, M., Mbede, E., Jacobs, P., 2010a. Tectonic control overactive volcanism at a range of scales: case of the Rungwe Volcanic Province, SW Tanzania; and hazard implications. J. Afr. Earth Sci., 58, 764–777. https://doi.org/10.1016/j.jafrearsci.2009.11.011.

Fontijn, K., Ernst, G.G.J., Elburg, M.A., Williamson, D., Abdallah, E., Kwelwa, S., Mbede, E., Jacobs, P., 2010b. Holocene explosive eruptions in the Rungwe Volcanic Province, Tanzania. JVG Research 196, 91–110. https://doi.org/10.1016/j.jvolgeores.2010.07.021.

Fontijn, K., Williamson, D., Mbede, E., Ernst, G.G.J., 2012. The Rungwe volcanic province, Tanzania-a review. J. Afr. Earth Sci. 63, 12–31. https://doi.org/10.1016/j.jafrearsci.2011.11.005.

Fritz, H., Abdelsalam, M., Ali, K., Bingen, B., Collins, A., Fowler, A., et al., 2013. Orogen styles in the East African orogen: a review of the Neoproterozoic to Cambrian tectonic evolution. J. Afr. Earth Sci. 86, 65–106. https://doi.org/10.1016/j.jafrearsci.2013.06.004.

Ghirotto, A., Armadillo, E., Crispini, L., Zunino, A., Caratori Tontini, F., & Ferraccioli, F. (2023). The sub-ice structure of Mt. Melbourne Volcanic Field (Northern Victoria Land, Antarctica) uncovered by high-resolution aeromagnetic data. Journal of Geophysical Research: Solid Earth, 128, e2022JB025687. https://doi.org/10.1029/2022JB025687.

Grauch, V.J.S., Sawyer, D.A., Friedrich, C.J., Hudson, M.R., 1997. Geophysical Interpretations West of and Within the Northwestern Part of the Nevada Test Site. U.S. Geological Survey Open-File Report 97-476, p. 45.

Grijalva, A., Nyblade, A.A., Homman, K., Accard, N.J., Gaherty, J.B., Ebinger, C.J., Mulibo, G., 2018. Seismic evidence for plume-and craton-influenced upper mantle structure beneath the Northern Malawi rift and the Rungwe Volcanic Province, East Africa. Geochem. Geophys. Geosyst. 19 (10), 3980–3994. https://doi.org/10.1029/2018GC007730.

Harkin, D.A., 1960. The Rungwe volcanics at the northern end of Lake Nyasa. Geological Survey of Tanganyika, Dodoma, p. 172.

Heilman, E., Kolawole, F., Atekwana, E. A., Mayle, M., 2019. Controls of basement fabric on the linkage of rift segments. Tectonics, 38, 1337–1366. https://doi.org/10.1029/2018TC005362.

Hersir, G.P., Weisenberger, T.B., 2015. Rungwe Volcanic Region, SW-Tanzania - A Proposal for Surface Exploration Studies, Supported by ICEIDA/NDF. Iceland GeoSurvey, short report ÍSOR-15048, 11p.

Hinz, N., Cumming, W.B., Sussman, D., 2018. Exploration of fault-related deep circulation geothermal resources in the western branch of the East African rift system: examples from Uganda and Tanzania. In: Proceedings of the 7th African Rift Geothermal Conference. Kigali, Rwanda.

Hochstein, M.P., Temu, E.P., Moshy, C.M.A., 2000. Geothermal Resources of Tanzania. Proceedings World Geothermal Congress, Kyushu-Tohoku, Japan, May 28 - June 10, 2000, pp. 1233–1238.

Alken, P., Thébault, E., Beggan, C.D. et al. 2021. International Geomagnetic Reference Field: the thirteenth generation. Earth Planets Space 73, 49. https://doi.org/10.1186/s40623-020-01288-x.

Ikhwan, M., Wallis, C.I., Rowland, V.J., 2020. Integrated Analysis of Surface and Borehole Data to Construct the Stratigraphy Model of Bukit Daun Field, Indonesia. Proceedings World Geothermal Congress 2020 Reykjavik, Iceland, April 26 – May 2, 2020.

International Seismological Centre, 2023. Online Event Bibliography. https://doi.org/10.31905/EJ3B5LV6.

Ivanov, A.V., Rasskazov, S.V., Boven, A., Punzalan, L., Brandt, I.S., Brandt, S.B., Fernandez Alonso, M., 1999. Timing and Late Cenozoic volcanic activity and rift basin formations in the Rungwe province of Tanzania substantiated by K–Ar and $^{40}Ar/^{39}Ar$ dating. Proc. Rifting in intracontinental setting: Baikal Rift System and other continental Rifts, 22–30 August 1999, Irkutsk and Lake Baikal, Russia.

JICA, 2014. Data collection Survey on Geothermal Energy Development in East Africa. Final report (Tanzania), 109 pp.

Kamba, A.H, Ahmed, S.K., 2017. Depth to Basement Determination Using Source Parameter Imaging (SPI) of Aeromagnetic Data: An Application to Lower Sokoto Basin, Northwest, Nigeria. International J. of Modern Applied Physics 7(1), 1-10.

Kovesi, P., 1999. Image features from phase congruency. Videre: A Journal of Computer Vision Research, 1(3), 1-26.

Kovesi, P., 2003. Phase congruency detects corners and edges. In the Australian pattern recognition society conference: Digital image computing: Techniques and applications pp. 309-318.

Kraml, M., Schaumann, G., Kalberkamp, U., Stadtler, C., Delvaux, D., Ndonde, P.B., Mnjokava, T.T., Chiragwile, S.A., Mayalla, J.W., Kabaka, K., Mwano, J.M., and Makene, C., 2008. Geothermal Energy as an alternative source of energy for Tanzania. BGR, Germany, GEOTHERM project Technical Cooperation with the Republic of Tanzania, final technical report, 235 pp.

Kraml, M., Schaumann, G., Kalberkamp, U., Stadtler, C., Delvaux, D., Ndonde, P.B., Mnjokava, T.T., Chiragwile, S.A., Mayalla, J.W., Kabaka, K., Mwano, J.M., and Makene, C., 2010. Surface Exploration of a Viable Geothermal Resource in Mbeya

Area, SW Tanzania Part II: Geochemistry. Proceedings World Geothermal Congress, Bali, Indonesia.
Kraml, M., Kreuter, H., Robertson, G. and Mbaka exploration team members, 2012. Small-scale rural electrification and direct use of low-temperature geothermal resources at Mbaka Fault in SW Tanzania. Proceedings: 4th African Rift Geothermal Conference, Nairobi, Kenya, 11 pp.
Kraml, M., H. Kreuter, and Project team, 2013. Project Development in Tanzania: Geothermal resources, surface Exploration, conceptual Models and Potential—status report. GRC Transactions, 37, 957-962.
Lawley, C., Imber, J., Selby, D., 2013. Structural Controls on Orogenic Au Mineralization During Transpression: Lupa Goldfield, Southwestern Tanzania. Economic Geology, 108(7), 1615–1640. https://doi.org/10.2113/econgeo.108.7.1615.
Lee, T.C., Kashyap, R.L., Chu, C.N., 1994. Building skeleton models via 3-D medial surface axis thinning algorithms. CVGIP: Graphical Models and Image Processing, 56(6), 462–478. https://doi.org/10.1006/cgip.1994.1042.
Marobhe, I.M., 1989. Interpretation of aerogeophysical anomalies of southwestern Tanzania, Geol. Surv. Fin. Bull. 350, 72.
Marobhe, I.M., Mbede, E.I., 1996. Gravity data interpretation of the Usangu Basin, Tanzania. Tanz. J. Sc. 21: 56-66. https://doi.org/10.3997/2214-4609-pdb.221.026.
Mbede, E.I., 2002. Interpretation of reflection seismic data from the Usangu Basin, East African Rift System. Tanzania Journal of Science, 28, 83–97. https://doi.org/10.4314/tjs.v28i1.18321.
McFarlane, A., Brock, P.W.G., 1966. Brief explanation of the geology of Tunduma, QDS257. Mineral Resources Division Tanzania. 1 p.
McNitt, J.R., 1982. The Geothermal Potential of East Africa. UNESCO/USAID Geothermal Seminar, Nairobi, Kenya, June 15–21, 1–9.
Mibei, G., 2021. The magmatic evolution, eruptive history and geothermal reservoir assessment of the Paka volcanic complex, Northern Kenya rift. PhD thesis, University of Iceland. https://hdl.handle.net/20.500.11815/2706.
Miller, H.G, Singh, V.J.,1994. Potential Field tilt - A new concept for location of potential field sources. Applied Geophysics, 32, 213-217.
Miller, J.A., Brown, P.E., 1963. The age of some carbonatite igneous activity in southwest Tanganyika. Geol. Mag. 100, 276–279. https://doi.org/10.1017/S0016756800055229.
Mulibo, G.D., Nyblade, A.A., 2013. The P and S wave velocity structure of the mantle beneath eastern Africa and the African superplume anomaly. Geochemistry, Geophysics, Geosystems, 14, 2696–2715. https://doi.org/10.1002/ggge.20150.
Mshiu E.E, 2020. Mapping of the Geological Structures Using Digital Elevation Model (DEM)-Derived Flow Direction: A Case Study of Rungwe Volcanic Province, Southwest Tanzania. Tanz. J. Sci. 46, 1.
Mortimer, E., Paton, D. A., Scholz, C. A., Strecker, M. R., Blisniuk, P., 2007. Orthogonal to oblique rifting: effect of rift basin orientation in the evolution of the North basin, Malawi Rift, East Africa. Basin Research, 19(3), 393–407. https://doi.org/10.1111/j.1365-2117.2007.00332.x.

Mulaya, E., Gluyas, J., McCaffrey, K., Phillips, T., Ballentine, C., 2021. Structural geometry and evolution of the Rukwa Rift Basin, Tanzania: Implications for helium potential. Basin Research. 34, 938–960. https://doi.org/10.1111/bre.12646.

Nanyaro, J.T., 1984. Technical report on the Geotraverse across the Ukingan and Ubendian fold belts in SW Tanzania. unpublished report, University of Dar-es-Salaam, 20 p.

Nasuti, Y., Nasuti, A., Moghadas, D., 2018. STDR: A Novel Approach for Enhancing and Edge Detection of Potential Field Data. Pure and Applied Geophysics. https://doi.org/10.1007/s00024-018-2016-5.

Rasmussen, R., Pedersen L.B., 1979. End corrections in potential field modelling. Geophys Prospect 27, 749–760. https://doi.org/10.1111/j.1365-2478.1979.tb00994.x.

Ring, U., Betzler, C., Delvaux, D., 1992. Normal vs. strike-slip faulting during rift development in East Africa: the Malawi rift. Geology, 20, 1015–1018. https://doi.org/10.1130/0091-7613(1992)020<1015:NVSSFD>2.3.CO;2.

Rizzello, D., Armadillo E., Pasqua, C., Pisani, P., Principe C., Lelli M., Didas, M., Giordan, V., Mnjokava, T., Kabaka, K., Tumbu, L., Marini L., 2022. Assessment of the Kiejo-Mbaka geothermal field by three-dimensional geophysical modelling. Geomech. Geophys. Geo-energ. Geo-resour. 8, 143. https://doi.org/10.1007/s40948-022-00456-5.

Rizzello, D., Armadillo, E., Pasqua, C., Pisani, P., Balsotti, R., Kebede, S., Mengiste, A., Kebede, Y., Hailegiorgis, G., Mengesha, K., 2021. The geophysical recognition of a vapor-cored geothermal system in divergent plate tectonics: the Alalobeda (Alalobad) field, Ethiopia. Tectonophysics 813 (2021), 228933. https://doi.org/10.1016/j.tecto.2021.228933.

Roberts, E.M., O'Connor, P.M., Gottfried, M.D., Stevens, N., Kapalima, S., Ngasala, S., 2004. Revised stratigraphy and age of the Red Sandstone Group in the Rukwa Rift basin, Tanzania. Cretaceous Res., 25(5), 749-759. https://doi.org/10.1016/j.cretres.2004.06.007.

Rusman, M.N., Alawiyah, S., Gunawan, I., 2023. Study on the Significance of Reduction to the Equator (RTE), Reduction to the Pole (RTP), and Pseudogravity in Magnetic Data Interpretation. Jurnal Penelitian Pendidikan IPA, 9(8), 6197–6205. https://doi.org/10.29303/jppipa.v9i8.4705.

Salem, A., Williams, S., Fairhead, J.D., Ravat, D., Smith, R., 2007. Tilt-depth method: A simple depth estimation method using first-order magnetic derivatives. The Leading Edge, 26(12), 1502–1505. https://doi.org/10.1190/1.2821934.

Shillington, D. J., Scholz, C. A., Chindandali, P. R. N., Gaherty, J. B., Accardo, N. J., Onyango, E., et al., 2020. Controls on rift faulting in the North Basin of the Malawi (Nyasa) Rift, East Africa. Tectonics, 39, e2019TC005633. https://doi.org/10.1029/2019TC005633.

Stamps, D. S., Saria, E., Kreemer, C., 2018. A geodetic strain rate model for the East African Rift System. Scientific Reports 8(1), 732. https://doi.org/10.1038/s41598-017-19097-w.

Stendal, H., Frei, R., Muhongo, S., Rasmussen, T.M., Mnali, S., Petro, F., Temu, E.B., 2004. Gold potential of the Mpanda mineral field, SW Tanzania: evaluation based on geological, lead isotopic and aeromagnetic data. J. Afr. Earth Sci., 38, 437–447. https://doi.org/10.1016/j.jafrearsci.2004.04.005.

Sun, K., Zhang, L., Zhao, Z., He, F., He, S., Wu, X., Qiu, L., Ren, X., 2021. Geochronology, petrography and Sr-Nd-Hf isotopes of Mbalizi carbonatite, southwestern Tanzania. J. Afr. Earth Sci. 184, 104308. https://doi.org/10.1016/j.jafrearsci.2021.104308.

SWECO, 1978. Reconnaissance of geothermal resources. Report for the Ministry of Water, Energy and Minerals of Tanzania, SWECO, Stockholm, Sweden, 51 pp.

Talwani, M, Heirtzler, J.R, 1964. Computation of magnetic anomalies caused by two-dimensional bodies of arbitrary shape. In: Parks GA (ed) Computers in the mineral industries, Part 1. Stanford Univ Publ Geological Sciences 9:464–480.

Thurston, J.B, Smith R.S., 1997. Automatic conversion of magnetic data to depth, dip, and susceptibility contrast using the SPITM method. Geophysics 62(3), 807-813. https://doi.org/10.1190/1.1444190.

UNEP/ARGeo, 2016. Geothermal resource assessment report Ngozi and Songwe Geothermal Prospects, Tanzania. Unpublished report, 695 pp.

van Straaten, P., 1989. Nature and structural relationships of carbonatites from Southwest and West Tanzania. In: Bell, K. (Ed.), Carbonatites: Genesis and Evolution. Unwin Hyman, London, pp. 177–199.

Walker, B.G., 1969. Springs of deep-seated origin in Tanzania. Proceedings of the 23rd Intern. Geological Congress, 19.

Won, I.J., Bevis, M., 1987. Computing the gravitational and magnetic anomalies due to polygon: Algorithms and Fortran subroutines. Geophysics, 52, 232-238. https://doi.org/10.1190/1.1442298.

## Supplementary material

**TABLE 1:** Geochronology and petrophysical data compiled from several authors

Earth's field inclination = 42°, declination = 2.2°, and magnetic field intensity of 33807 nT were used in the calculation of the total magnetization vector; Q = Koenigsberger ratio.

| Rock type | UTMX | UTMY | Area | Age | Density ($Kgm^{-3}$) | Susceptibility | JR ($Am^{-1}$) | JI ($Am^{-1}$) | Q-ratio | Authors |
|---|---|---|---|---|---|---|---|---|---|---|
| *Carbonatite* | 524503 | 9007054 | Panda hill | 113.0 ± 6 Ma | 3120 | 0.0007 | 0.8 | 2.3 | 0.35 | a, b & h |
| *Carbonatite* | 524503 | 9007054 | Panda hill | 113.0 ± 6 Ma | 3770 | 0.0057 | 100 | 19 | 5.21 | a, b & h |
| *Carbonatite* | 524503 | 9007054 | Panda hill | 113.0 ± 6 Ma | 2890 | 0.0005 | nil | 1.8 | nil | a, b & h |
| *Carbonatite* | 524503 | 9007054 | Panda hill | 113.0 ± 6 Ma | 3430 | 0.0024 | 176 | 8 | 22.08 | a, b & h |
| *Carbonatite* | 524503 | 9007054 | Panda hill | 113.0 ± 6 Ma | 2880 | 0.0024 | 6.1 | 8 | 0.77 | a, b & h |
| *Carbonatite* | 524503 | 9007054 | Panda hill | 113.0 ± 6 Ma | 3140 | 0.0048 | 665 | 16 | 41.56 | a, b & h |
| *Carbonatite* | 524503 | 9007054 | Panda hill | 113.0 ± 6 Ma | 2890 | 0.0003 | 0 | 0.9 | 0.04 | a, b & h |
| *Carbonatite* | 524503 | 9007054 | Panda hill | 113.0 ± 6 Ma | 2690 | 0.0005 | 0.6 | 1.6 | 0.38 | a, b & h |
| *Carbonatite* | 524503 | 9007054 | Panda hill | 113.0 ± 6 Ma | 2800 | 0.0027 | 10 | 9.2 | 1.13 | a, b & h |
| *Carbonatite* | 524503 | 9007054 | Panda hill | 113.0 ± 6 Ma | 2930 | 0.0107 | 102 | 36 | 2.85 | a, b & h |
| *Carbonatite* | 524503 | 9007054 | Panda hill | 113.0 ± 6 Ma | 2760 | 0.0015 | 1.3 | 5.1 | 0.26 | a, b & h |
| *Carbonatite* | 524503 | 9007054 | Panda hill | 113.0 ± 6 Ma | 2810 | 0.0006 | 0.3 | 2 | 0.15 | a, b & h |
| *Carbonatite* | 524503 | 9007054 | Panda hill | 113.0 ± 6 Ma | 2770 | 0.0082 | 0.4 | 27 | 0.01 | a, b & h |
| *Carbonatite* | 524503 | 9007054 | Panda hill | 113.0 ± 6 Ma | 3740 | 0.0845 | ### | 283 | 3.71 | a, b & h |
| *Carbonatite* | 524503 | 9007054 | Panda hill | 113.0 ± 6 Ma | 2690 | 0.0034 | 100 | ### | 0.01 | a, b & h |
| *Carbonatite* | 524503 | 9007054 | Panda hill | 113.0 ± 6 Ma | 3150 | 0.0445 | ### | 149 | 8.72 | a, b & h |
| *Carbonatite* | 524503 | 9007054 | Panda hill | 113.0 ± 6 Ma | 2520 | 0.0009 | 0.3 | 3.2 | 0.08 | a, b & h |
| *Carbonatite* | | | Mbalizi | 113.0 ± 6 Ma | | | | | | c |
| *Carbonatite* | | | Sengeri hill | 113.0 ± 6 Ma | | | | | | b |
| *Carbonatite* | | | Nachendezwaya | 685.0±62 Ma | | | | | | b |
| *Carbonatite* | | | Songwe scarp | 100.0± 10 Ma | | | | | | b & d |
| *Carbonatite* | | | Musensi | 101.0±12;96±9 Ma | | | | | | b |
| *basalt* | 581205 | 8967731 | Rungwe | | 3070 | 0.0681 | 101 | 228 | 0.44 | h |
| *basalt* | 581205 | 8967731 | Rungwe | | 2900 | 0.0149 | 631 | 50 | 12.65 | h |
| *basalt* | 581205 | 8967731 | Rungwe | | 3020 | 0.0425 | 84 | 142 | 0.59 | h |
| *basalt* | 581205 | 8967731 | Rungwe | | 2970 | 0.0466 | 48 | 156 | 0.31 | h |
| *trachyte* | 564997 | 8988433 | Rungwe | 0.00029-0.00054 Ma | 2360 | 0.0094 | 27 | 31 | 0.87 | e & h |
| *basalt* | 564997 | 8988433 | Rungwe | 0.00029-0.00054 Ma | 2870 | 0.0161 | 12 | 54 | 0.22 | e & h |
| *basalt* | 564997 | 8988433 | Rungwe | 0.00029-0.00054 Ma | 2870 | 0.0152 | 31 | 51 | 0.61 | e & h |
| *basalt* | 564997 | 8988433 | Rungwe | 0.00029-0.00054 Ma | 2880 | 0.0681 | 22 | 228 | 0.09 | e & h |
| *trachyte* | 564997 | 8988433 | Rungwe | 0.00029-0.00054 Ma | 2600 | 0.0094 | 0.5 | 32 | 0.02 | e & h |

| | | | | | | | | | | |
|---|---|---|---|---|---|---|---|---|---|---|
| *trachyte* | 564997 | 8988433 | Rungwe | 0.00029-0.00054 Ma | 2750 | 0.0673 | 32 | 225 | 0.14 | e & h |
| *trachyte* | 564997 | 8988433 | Rungwe | 0.00029-0.00054 Ma | 2630 | 0.0176 | 3.4 | 59 | 0.06 | e & h |
| *basalt* | 564997 | 8988433 | Rungwe | 0.00029-0.00054 Ma | 2870 | 0.0587 | 7.9 | 197 | 0.04 | e & h |
| *basalt* | 590277 | 8981451 | Kiejo | 0.42±0.03 Ma | 2950 | 0.0102 | 17 | 342 | 0.05 | e & h |
| *trachyte* | 590277 | 8981451 | Rungwe | | 2440 | 0.0287 | 5 | 96 | 0.05 | h |
| *trachyte* | 590277 | 8981451 | Rungwe | | 2420 | 0.0225 | 245 | 75 | 3.25 | h |
| *basalt* | 590277 | 8981451 | Rungwe | | 2610 | 0.0877 | 64 | 294 | 0.22 | h |
| *basalt* | 590277 | 8981451 | Rungwe | | 2770 | 0.0045 | 65 | 15 | 4.28 | h |
| *basalt* | 590277 | 8981451 | Rungwe | | 2800 | 0.0094 | 27 | 31 | 0.87 | h |
| *scoria* | 590277 | 8981451 | Rungwe | | 2630 | 0.0058 | 20 | 19 | 1.06 | h |
| *scoria* | 590277 | 8981451 | Rungwe | | 2720 | 0.0051 | 5 | 17 | 0.30 | h |
| *basalt* | 540439 | 9012750 | Rungwe | | 2810 | 0.0102 | 20 | 342 | 0.06 | h |
| *basalt* | 540439 | 9012750 | Rungwe | | 2640 | 0.0466 | 84 | 156 | 0.54 | h |
| *basalt* | 540439 | 9012750 | Rungwe | | 2790 | 0.073 | 160 | 245 | 0.65 | h |
| *basalt* | 540439 | 9012750 | Rungwe | | 2630 | 0.0033 | 14 | 11 | 1.29 | h |
| *basalt* | 540439 | 9012750 | Rungwe | | 2600 | 0.0022 | 3.1 | 7.2 | 0.42 | h |
| *basalt* | 540439 | 9012750 | Rungwe | | 2640 | 0.0236 | 42 | 79 | 0.53 | h |
| *basalt* | 540439 | 9012750 | Rungwe | | 2690 | 0.0221 | 172 | 74 | 2.32 | h |
| gabbro | 481452 | 8989396 | Mbozi | 2050-1800 Ma | 2920 | 0.0007 | 121 | 2.2 | 55.00 | f, g & h |
| gneiss | 481452 | 8989396 | Mbozi | 2050-1800 Ma | 2770 | 0.0026 | 41 | 8.7 | 4.69 | f, g & h |
| dolerite | 481452 | 8989396 | Mbozi | 2050-1800 Ma | 3040 | 0.0321 | 231 | 108 | 2.14 | f, g & h |
| gneiss | 481452 | 8989396 | Mbozi | 2050-1800 Ma | 2690 | 0.0040 | 65 | 14 | 4.84 | f, g & h |
| dolerite | 481452 | 8989396 | Mbozi | 2050-1800 Ma | 2720 | 0.0076 | 83 | 25 | 3.26 | f, g & h |
| breccia | 481452 | 8989396 | Mbozi | 2050-1800 Ma | 3120 | 0.0071 | 267 | 24 | 11.27 | f, g & h |
| breccia | 481452 | 8989396 | Mbozi | 2050-1800 Ma | 2750 | 0.0428 | 69 | 143 | 0.48 | f, g & h |
| breccia | 481452 | 8989396 | Mbozi | 2050-1800 Ma | 3110 | 0.0099 | 220 | 33 | 6.61 | f, g & h |
| dolerite | 481452 | 8989396 | Mbozi | 2050-1800 Ma | 2910 | 0.0074 | 422 | 25 | 17.09 | f, g & h |
| gabbro | 481452 | 8989396 | Mbozi | 2050-1800 Ma | 3190 | 0.0117 | ### | 39 | 56.89 | f, g & h |
| pyroxenite | 481452 | 8989396 | Mbozi | 2050-1800 Ma | 3260 | 0.034 | 801 | 114 | 7.03 | f, g & h |
| pyroxenite | 481452 | 8989396 | Mbozi | 2050-1800 Ma | 3290 | 0.0266 | 156 | 89 | 1.75 | f, g & h |
| dolerite | 481452 | 8989396 | Mbozi | 2050-1800 Ma | 3160 | 0.0058 | ### | 20 | ##### | f, g & h |
| pyroxenite | 481452 | 8989396 | Mbozi | 2050-1800 Ma | 3300 | 0.0845 | ### | 283 | 4.13 | f, g & h |
| pyroxenite | 481452 | 8989396 | Mbozi | 2050-1800 Ma | 3370 | 0.0132 | ### | 44 | 90.50 | f, g & h |
| pyroxenite | 481452 | 8989396 | Mbozi | 2050-1800 Ma | 3480 | 0.0197 | ### | 878 | 8.44 | f, g & h |
| gabbro | 481452 | 8989396 | Mbozi | 2050-1800 Ma | 2940 | 0.05 | 65 | 167 | 0.39 | f, g & h |
| gabbro | 481452 | 8989396 | Mbozi | 2050-1800 Ma | 3140 | 0.0019 | 388 | 6.5 | 59.42 | f, g & h |
| syenite | 481452 | 8989396 | Mbozi | 2050-1800 Ma | 2610 | 0.0031 | 75 | 10 | 7.23 | f, g & h |
| syenite | 481452 | 8989396 | Mbozi | 2050-1800 Ma | 2650 | 0.0544 | 242 | 182 | 1.33 | f, g & h |
| syenite | 481452 | 8989396 | Mbozi | 2050-1800 Ma | 2640 | 0.0526 | ### | 176 | 11.36 | f, g & h |
| syenite | 481452 | 8989396 | Mbozi | 2050-1800 Ma | 2620 | 0.0414 | 83 | 139 | 0.59 | f, g & h |
| syenite | 481452 | 8989396 | Mbozi | 2050-1800 Ma | 2690 | 0.0467 | ### | 156 | 6.47 | f, g & h |

| | | | | | | | | | | |
|---|---|---|---|---|---|---|---|---|---|---|
| dolerite | 481452 | 8989396 | Mbozi | 2050-1800 Ma | 3010 | 0.0703 | ### | 236 | 32.92 | f, g & h |
| gabbro | 481452 | 8989396 | Mbozi | 2050-1800 Ma | 2790 | 0.0793 | 645 | 266 | 2.42 | f, g & h |
| gabbro | 481452 | 8989396 | Mbozi | 2050-1800 Ma | 2910 | 0.0058 | 254 | 20 | 13.03 | f, g & h |
| gabbro | 481452 | 8989396 | Mbozi | 2050-1800 Ma | 3300 | 0.0264 | ### | 88 | 34.16 | f, g & h |
| gabbro | 481452 | 8989396 | Mbozi | 2050-1800 Ma | 3210 | 0.0341 | ### | 114 | 49.65 | f, g & h |
| gabbro | 481452 | 8989396 | Mbozi | 2050-1800 Ma | 3300 | 0.0228 | ### | 76 | 88.22 | f, g & h |
| syenite | 481452 | 8989396 | Mbozi | 2050-1800 Ma | 2590 | 0.0059 | 95 | 20 | 4.79 | f, g & h |
| gabbro | 481452 | 8989396 | Mbozi | 2050-1800 Ma | 3220 | 0.0161 | 786 | 54 | 14.58 | f, g & h |
| gabbro | 481452 | 8989396 | Mbozi | 2050-1800 Ma | 3100 | 0.0202 | ### | 68 | 38.70 | f, g & h |
| gabbro | 481452 | 8989396 | Mbozi | 2050-1800 Ma | 3210 | 0.0169 | 624 | 57 | 11.02 | f, g & h |
| syenite | 481452 | 8989396 | Mbozi | 2050-1800 Ma | 2770 | 0.0016 | 3.6 | 5.3 | 0.68 | f, g & h |
| syenite | 481452 | 8989396 | Mbozi | 2050-1800 Ma | 2740 | 0.0006 | 127 | 2.1 | 60.48 | f, g & h |
| dolerite | 481452 | 8989396 | Mbozi | 2050-1800 Ma | 3120 | 0.0049 | 854 | 16 | 52.07 | f, g & h |
| quartzite | 546218 | 9054162 | Chunya | 2050-1800 Ma | 3300 | 0.0986 | ### | 330 | 46.36 | f, g & h |
| quartzite | 546218 | 9054162 | Chunya | 2050-1800 Ma | 3360 | 0.0146 | ### | 49 | 71.43 | f, g & h |
| quartzite | 546218 | 9054162 | Chunya | 2050-1800 Ma | 3420 | 0.011 | ### | 37 | ##### | f, g & h |
| quartzite | 546218 | 9054162 | Chunya | 2050-1800 Ma | 3360 | 0.0455 | ### | 152 | 58.95 | f, g & h |
| quartzite | 546218 | 9054162 | Chunya | 2050-1800 Ma | 3320 | 0.0074 | ### | 25 | 91.16 | f, g & h |
| gneiss | 546218 | 9054162 | Chunya | 2050-1800 Ma | 2600 | 0.0009 | 0.4 | 3.1 | 0.13 | f, g & h |
| gneiss | 546218 | 9054162 | Chunya | 2050-1800 Ma | 2590 | 0.0009 | 0.1 | 2.9 | 0.04 | f, g & h |
| quartzite | 546218 | 9054162 | Chunya | 2050-1800 Ma | 3360 | 0.0206 | ### | 69 | ##### | f, g & h |
| quartzite | 546218 | 9054162 | Chunya | 2050-1800 Ma | 3150 | 0.0122 | ### | 41 | ##### | f, g & h |
| quartzite | 546218 | 9054162 | Chunya | 2050-1800 Ma | 3220 | 0.068 | ### | 228 | ##### | f, g & h |
| gneiss | 546218 | 9054162 | Chunya | 2050-1800 Ma | 2630 | 0.0012 | 44 | 3.9 | 11.31 | f, g & h |
| diorite | 544773 | 9057532 | Chunya | 2050-1800 Ma | 3050 | 0.0005 | 0.4 | 1.8 | 0.24 | f, g & h |
| gneiss | 544773 | 9057532 | Chunya | 2050-1800 Ma | 2690 | 0.0005 | 44 | 1.9 | 23.62 | f, g & h |
| diorite | 544773 | 9057532 | Chunya | 2050-1800 Ma | 3100 | 0.0009 | 1.6 | 3.2 | 0.50 | f, g & h |
| diorite | 544773 | 9057532 | Chunya | 2050-1800 Ma | 3050 | 0.0023 | 602 | 7.6 | 79.21 | f, g & h |
| granite | 544773 | 9057532 | Chunya | 2050-1800 Ma | 2590 | 0.0004 | 2.5 | 1.5 | 1.66 | f, g & h |
| diorite | 544773 | 9057532 | Chunya | 2050-1800 Ma | 3070 | 0.0013 | 2.4 | 4.2 | 0.57 | f, g & h |
| diorite | 544773 | 9057532 | Chunya | 2050-1800 Ma | 3020 | 0.0008 | 1.2 | 2.7 | 0.45 | f, g & h |
| granite | 507695 | 9072700 | Lupa | 2050-1800 Ma | 2730 | 0.0021 | 33 | 6.9 | 4.78 | f, g & h |
| granite | 507695 | 9072700 | Lupa | 2050-1800 Ma | 2660 | 0.0008 | 0.4 | 2.7 | 0.15 | f, g & h |
| contaminated granite | 507695 | 9072700 | Lupa | 2050-1800 Ma | 2760 | 0.0033 | 261 | 11 | 23.73 | f, g & h |
| contaminated granite | 507695 | 9072700 | Lupa | 2050-1800 Ma | 2710 | 0.0019 | 10 | 6.5 | 1.59 | f, g & h |
| dolerite | 507695 | 9072700 | Lupa | 2050-1800 Ma | 2880 | 0.0010 | 0.9 | 3.4 | 0.26 | f, g & h |
| contaminated granite | 507695 | 9072700 | Lupa | 2050-1800 Ma | 2720 | 0.0021 | 17 | 6.9 | 2.43 | f, g & h |
| sheared granite | 507695 | 9072700 | Lupa | 2050-1800 Ma | 2670 | 0.0032 | 14 | 11 | 1.32 | f, g & h |
| aplite | 507695 | 9072700 | Lupa | 2050-1800 Ma | 3080 | 0.0027 | 4.6 | 9.2 | 0.50 | f, g & h |
| diorite | 507695 | 9072700 | Lupa | 2050-1800 Ma | 2850 | 0.0019 | 2.3 | 6.6 | 0.35 | f, g & h |
| mafic | 507695 | 9072700 | Lupa | 2050-1800 Ma | 2780 | 0.0203 | ### | 68 | 34.41 | f, g & h |

| | | | | | | | | | | |
|---|---|---|---|---|---|---|---|---|---|---|
| mafic | 507695 | 9072700 | Lupa | 2050-1800 Ma | 2780 | 0.0152 | ### | 51 | 45.19 | f, g & h |
| mafic | 507695 | 9072700 | Lupa | 2050-1800 Ma | 2800 | 0.0165 | ### | 55 | 50.09 | f, g & h |
| norite | 527920 | 9073423 | Lupa | 2050-1800 Ma | 2950 | 0.0012 | 19 | 3.9 | 4.78 | f, g & h |
| norite | 527920 | 9073423 | Lupa | 2050-1800 Ma | 2970 | 0.0012 | 74 | 4 | 18.36 | f, g & h |
| norite | 527920 | 9073423 | Lupa | 2050-1800 Ma | 2980 | 0.0049 | 267 | 17 | 16.18 | f, g & h |
| diorite | 503602 | 9068126 | Lupa | 2050-1800 Ma | 2720 | 0.0013 | 34 | 4.4 | 7.72 | f, g & h |
| dolerite | 503602 | 9068126 | Lupa | 2050-1800 Ma | 2970 | 0.0089 | ### | 30 | 96.66 | f, g & h |
| granite | 503602 | 9068126 | Lupa | 2050-1800 Ma | 2640 | 0.0009 | 9.9 | 3.3 | 3.04 | f, g & h |
| aplite | 503602 | 9068126 | Lupa | 2050-1800 Ma | 2870 | 0.0009 | 0.6 | 3.1 | 0.19 | f, g & h |
| diorite | 503602 | 9068126 | Lupa | 2050-1800 Ma | 2650 | 0.0049 | 36 | 16 | 2.23 | f, g & h |
| granite | 503602 | 9068126 | Lupa | 2050-1800 Ma | 2720 | 0.0090 | 3.6 | 30 | 0.12 | f, g & h |
| granodiorite | 503602 | 9068126 | Lupa | 2050-1800 Ma | 3030 | 0.0010 | 0.7 | 3.5 | 0.21 | f, g & h |
| gneiss | 503602 | 9068126 | Lupa | 2050-1800 Ma | 2870 | 0.0009 | 0.1 | 3.1 | 0.03 | f, g & h |
| granite | 492046 | 9075830 | Lupa | 2050-1800 Ma | 2610 | 0.0002 | 0 | 0.6 | 0.02 | f, g & h |
| granite | 492046 | 9075830 | Lupa | 2050-1800 Ma | 2590 | 0.0003 | 0 | 1 | 0.01 | f, g & h |
| gneiss | 492046 | 9075830 | Lupa | 2050-1800 Ma | 2640 | 0.0004 | 0 | 1.4 | 0.03 | f, g & h |
| gneiss | 492046 | 9075830 | Lupa | 2050-1800 Ma | 2640 | 0.0004 | 0 | 1.4 | 0.01 | f, g & h |
| sheared gneiss | 492046 | 9075830 | Lupa | 2050-1800 Ma | 2660 | 0.0004 | 0 | 1.4 | 0.03 | f, g & h |
| granite | 492046 | 9075830 | Lupa | 2050-1800 Ma | 2660 | 0.0003 | 0 | 0.9 | 0.03 | f, g & h |
| diorite | 492046 | 9075830 | Lupa | 2050-1800 Ma | 2900 | 0.0003 | 0 | 1.1 | 0.02 | f, g & h |
| banded quartzite | 477600 | 9096536 | Lupa | 2050-1800 Ma | 2710 | 0.0003 | 0.1 | 1.1 | 0.06 | f, g & h |
| Biotite granite | 477600 | 9096536 | Lupa | 2050-1800 Ma | 2630 | 0.0005 | 0 | 1.6 | 0.02 | f, g & h |
| porphyry granite | 477600 | 9096536 | Lupa | 2050-1800 Ma | 2570 | 0.0003 | 0.1 | 0.9 | 0.06 | f, g & h |
| sandstone | 477600 | 9096536 | Lupa | 2050-1800 Ma | 2600 | 0.0002 | 0 | 0.6 | 0.02 | f, g & h |
| Biotite granite | 477600 | 9096536 | Lupa | 2050-1800 Ma | 2590 | 0.0004 | 0 | 1.4 | 0.01 | f, g & h |
| gabbro | 614113 | 9018288 | Chimala | 2050-1800 Ma | 2750 | 0.0074 | ### | 25 | 43.55 | f, g & h |
| dolerite | 614113 | 9018288 | Chimala | 2050-1800 Ma | 2850 | 0.0051 | 171 | 17 | 10.06 | f, g & h |
| gabbro | 614113 | 9018288 | Chimala | 2050-1800 Ma | 2580 | 0.0028 | 24 | 9.3 | 2.53 | f, g & h |
| dolerite | 614113 | 9018288 | Chimala | 2050-1800 Ma | 2830 | 0.0017 | 34 | 5.6 | 6.06 | f, g & h |
| granite | 614113 | 9018288 | Chimala-Msusule | 2050-1800 Ma | 2550 | 0.0007 | 7.5 | 2.4 | 3.14 | f, g & h |
| quartzite | 637708 | 9027919 | Msusule | 2050-1800 Ma | 2550 | 0.0005 | 5.9 | 1.8 | 3.37 | f, g & h |
| granodiorite | 637708 | 9027919 | Msusule | 2050-1800 Ma | 2800 | 0.0039 | 9.8 | 13 | 0.73 | f, g & h |
| granodiorite | 637708 | 9027919 | Msusule | 2050-1800 Ma | 2630 | 0.0041 | 14 | 14 | 1.01 | f, g & h |
| granodiorite | 637708 | 9027919 | Msusule | 2050-1800 Ma | 2740 | 0.0032 | 976 | 11 | 89.54 | f, g & h |
| granodiorite | 637708 | 9027919 | Msusule | 2050-1800 Ma | 2690 | 0.0011 | ### | 3.8 | ##### | f, g & h |
| dolerite | 637708 | 9027919 | Msusule | 2050-1800 Ma | 2900 | 0.0049 | ### | 17 | 81.33 | f, g & h |
| dolerite | 637708 | 9027919 | Msusule | 2050-1800 Ma | 2790 | 0.0015 | 485 | 5.2 | 92.73 | f, g & h |
| granodiorite | 637708 | 9027919 | Msusule | 2050-1800 Ma | 2760 | 0.0018 | 518 | 6.1 | 84.50 | f, g & h |
| granodiorite | 637708 | 9027919 | Msusule | 2050-1800 Ma | 2750 | 0.0015 | 36 | 5.1 | 7.03 | f, g & h |

**Authors:**
**a**: Snelling (1965);
**b**: Van Straaten (1989);
**c**: Sun et al. (2021);
**d**: Miller and Brown (1963);
**e**: Fontijn et al. (2010);
**f**: Boniface and Schenk (2012);
**g**: Hansen (2003);
**h**: Marobhe (1989)

## References


Boniface, N., Schenk, V., 2012. Neoproterozoic eclogites in the Paleoproterozoic Ubendian belt of Tanzania: evidence for a pan-African suture between the Bangweulu block and the Tanzania Craton. Precambrian Res. 208, 72–89. https://doi.org/10.1016/j.precamres.2012.03.014.

Fontijn, K., Ernst, G.G.J., Elburg, M.A., Williamson, D., Abdallah, E., Kwelwa, S., Mbede, E., Jacobs, P., 2010b. Holocene explosive eruptions in the Rungwe Volcanic Province, Tanzania. JVG Research 196, 91–110. https://doi.org/10.1016/j.jvolgeores.2010.07.021.

Marobhe, I.M., 1989. Interpretation of aerogeophysical anomalies of southwestern Tanzania, Geol. Surv. Fin. Bull. 350, 72

Miller, J.A., Brown, P.E., 1963. The age of some carbonatite igneous activity in southwest Tanganyika. Geol. Mag. 100, 276–279.

Snelling, N.J., 1965. Age determinations on three African carbonatites. Nature 205, 491.

Sun, K., Zhang, L., Zhao, Z., He, F., He, S., Wu, X., Qiu, L., Ren, X., 2021. Geochronology, petrography and Sr-Nd-Hf isotopes of Mbalizi carbonatite, southwestern Tanzania. J. Afr. Earth Sci. 184, 104308. https://doi.org/10.1016/j.jafrearsci.2021.104308.

van Straaten, P., 1989. Nature and structural relationships of carbonatites from Southwest and West Tanzania. In: Bell, K. (Ed.), Carbonatites: Genesis and Evolution. Unwin Hyman, London, pp. 177–199.

# Appendix A: MT data

| Station | Easting | Northing | Elevation(m) | Station | Easting | Northing | Elevation(m) |
|---|---|---|---|---|---|---|---|
| 15-ng00 | 558296 | 8999722 | 1792 | 15-ng40 | 557039 | 9013129 | 1809 |
| 15-ng01 | 557642 | 9000887 | 1907 | 15-ng49 | 567812 | 9010370 | 2119 |
| 15-ng01a | 542665 | 9013697 | 1601 | 15-ng50a | 543691 | 8996565 | 2093 |
| 15-ng03a | 549413 | 9013056 | 1724 | 15-ng51a | 546892 | 8995812 | 2027 |
| 15-ng04 | 565005 | 9000780 | 1983 | 15-ng6a | 550266 | 9011188 | 1659 |
| 15-NG04 | 543480 | 9010649 | 1609 | 16-1 | 551958 | 9006727 | 1888 |
| 15-ng05 | 564078 | 9003408 | 2087 | 16-2 | 561376 | 9001327 | 1988 |
| 15-ng07 | 552167 | 9012257 | 1723 | 16-3 | 551920 | 9005403 | 1907 |
| 15-ng08 | 558649 | 9011373 | 1919 | 16-4 | 555328 | 9005426 | 2108 |
| 15-ng09 | 559741 | 9008764 | 2185 | 16-5 | 561212 | 9007690 | 2301 |
| 15-ng10 | 560489 | 9008217 | 2286 | 16-6 | 562727 | 9000231 | 1946 |
| 15-ng13 | 561011 | 9012454 | 1889 | 16-7 | 557429 | 9001732 | 1896 |
| 15-ng14a | 553253 | 9009191 | 1813 | 16-8 | 558977 | 9007783 | 2316 |
| 15-ng15 | 563150 | 8999650 | 1936 | 16-9 | 556812 | 9005937 | 2270 |
| 15-ng16 | 568361 | 9001346 | 2094 | 16-nz2 | 560080 | 9008248 | 2233 |
| 15-ng17 | 567774 | 9004301 | 2246 | 16-nz219 | 556445 | 9009405 | 1864 |
| 15-ng18 | 565268 | 9006769 | 2245 | 16-nz220 | 556905 | 9008861 | 1937 |
| 15-ng18a | 568249 | 9007212 | 2240 | 16-nz221 | 556124 | 9009620 | 1848 |
| 15-ng19 | 567346 | 9009127 | 2158 | 16-nz222 | 559071 | 9009785 | 2049 |
| 15-ng20 | 565137 | 9008784 | 2193 | 16-NZ223 | 556391 | 9008345 | 1905 |
| 15-ng21 | 565130 | 9011652 | 2047 | 16-nz224 | 559616 | 9010724 | 2002 |
| 15-ng21a | 545262 | 9006572 | 1592 | 16-nz225 | 557734 | 9010229 | 1909 |
| 15-ng21b | 547795 | 9008246 | 1726 | 16-nz226 | 554498 | 9008360 | 1857 |
| 15-ng22a | 547812 | 9004542 | 1779 | 16-nz229 | 552818 | 9005718 | 1986 |
| 15-ng23 | 564347 | 9011202 | 2081 | 16-nz230 | 553648 | 9007179 | 1909 |
| 15-ng24 | 563175 | 9009693 | 2120 | 16-nz233 | 553084 | 9003749 | 2044 |
| 15-ng24a | 543076 | 9004210 | 1706 | 16-nz234 | 553808 | 9001743 | 2052 |
| 15-ng25a | 545001 | 9002485 | 1717 | 16-nz235r | 554841 | 9002736 | 2060 |
| 15-ng27a | 543720 | 9000425 | 1959 | 16-nz236 | 558010 | 9008546 | 2144 |
| 15-ng29a | 550595 | 9005282 | 1972 | 16-nz237 | 557769 | 9008998 | 2100 |
| 15-ng30 | 564665 | 9005421 | 2081 | 16-nz239 | 560767 | 9010154 | 2037 |
| 15-ng31 | 569103 | 9003000 | 2309 | 16-NZ240 | 561931 | 9008927 | 2164 |
| 15-ng31a | 551253 | 9004338 | 2061 | 16-nz241 | 561704 | 9008307 | 2227 |
| 15-ng32 | 567438 | 8998510 | 1954 | 16-nz242 | 563310 | 9008320 | 2196 |
| 15-ng32a | 551523 | 9002888 | 1867 | 16-nz243 | 564115 | 9007210 | 2352 |
| 15-ng33 | 564979 | 8997949 | 1923 | 16-nz244 | 557332 | 9002165 | 1966 |
| 15-NG34 | 562152 | 8997778 | 1874 | 16-nz246 | 555000 | 9000709 | 1806 |
| 15-NG35 | 559683 | 8998058 | 1800 | 16-nz247 | 566181 | 9003048 | 2058 |
| 15-ng36 | 556847 | 8997860 | 1723 | 16-nz248 | 563898 | 9001636 | 1991 |

| Station | Easting | Northing | Elevation(m) | Station | Easting | Northing | Elevation(m) |
|---|---|---|---|---|---|---|---|
| 15-ng37 | 554389 | 8998155 | 1748 | 16-nz249 | 558329 | 9001368 | 1952 |
| 16-nz250r | 560050 | 9000969 | 1906 | 20-nz340 | 561093 | 9005878 | 2271 |
| 16-nz252 | 561685 | 8999787 | 1906 | 20-nz342 | 565256 | 9014339 | 1933 |
| 16-nz253 | 564298 | 9005029 | 2112 | 20-nz343 | 566692 | 9012850 | 1961 |
| 16-nz254 | 562124 | 9007198 | 2421 | 20-NZ344 | 568767 | 9012055 | 1983 |
| 16-nz255 | 563872 | 9004293 | 2111 | 20-nz346 | 566511 | 9004930 | 2159 |
| 16-nz302 | 559624 | 9007468 | 2337 | 20-nz347 | 566124 | 8999885 | 1949 |
| 16-nz304 | 557566 | 9007527 | 2198 | 20-KABAL | 571514 | 8983678 | 1732 |
| 16-nz309 | 557045 | 9004315 | 2206 | 22-nz348 | 570432 | 8999920 | 2095 |
| 16-nz310 | 561912 | 9006605 | 2427 | 22-nz349 | 568959 | 8999091 | 2047 |
| 16-nz311 | 563507 | 9005469 | 2191 | 22-nz350 | 570600 | 8998249 | 2079 |
| 16-nz312 | 562977 | 9004272 | 2174 | 22-nz351 | 570858 | 8995712 | 2326 |
| 16-nz315 | 559839 | 9006593 | 2540 | 22-nz352 | 569025 | 8996821 | 2316 |
| 19-REM | 569441 | 9002523 | 2284 | 22-nz353a | 567425 | 8996351 | 2076 |
| 20-A | 569282 | 9009118 | 2189 | 22-nz354 | 566041 | 8996037 | 2059 |
| 20-ng02 | 560188 | 8999320 | 1847 | 22-NZ355 | 564484 | 8995763 | 1912 |
| 20-ng11 | 563411 | 9008114 | 2296 | 22-NZ356 | 562791 | 8996223 | 1868 |
| 20-ng30A | 555425 | 9007382 | 1949 | 22-NZ357 | 561831 | 8995156 | 1788 |
| 20-nz227 | 550029 | 9007116 | 1738 | 22-NZ358 | 559686 | 8996302 | 1710 |
| 20-nz231 | 556147 | 9006165 | 2203 | 22-NZ359 | 558627 | 8994494 | 1666 |
| 20-nz317 | 559997 | 9001912 | 1998 | 22-NZ360 | 570949 | 8993820 | 2603 |
| 20-nz318 | 559968 | 9003082 | 2171 | 22-NZ361 | 569652 | 8993718 | 2665 |
| 20-nz319 | 559252 | 9003734 | 2296 | 22-NZ362 | 567485 | 8994158 | 2187 |
| 20-nz320 | 558240 | 9003349 | 2059 | 22-NZ363 | 566101 | 8993466 | 1933 |
| 20-nz321 | 559165 | 9005083 | 2528 | 22-NZ364 | 563827 | 8993614 | 1784 |
| 20-nz322 | 562105 | 9004691 | 2268 | 22-NZ365 | 562728 | 8993345 | 1749 |
| 20-nz323 | 561712 | 9003457 | 2233 | 22-NZ366 | 560440 | 8992265 | 1604 |
| 20-nz324 | 556374 | 9004761 | 2180 | 22-NZ367 | 571243 | 8992311 | 2534 |
| 20-nz325 | 556301 | 9003038 | 2021 | 22-NZ368 | 570219 | 8991945 | 2419 |
| 20-nz326 | 557067 | 9005003 | 2171 | 22-NZ369 | 567786 | 8993313 | 2139 |
| 20-nz327 | 559257 | 9005632 | 2533 | 22-NZ371 | 564023 | 8992093 | 1710 |
| 20-nz328 | 562315 | 9002329 | 2016 | 22-NZ372 | 563247 | 8991619 | 1640 |
| 20-nz331 | 548554 | 8999376 | 1888 | 22-NZ374 | 572451 | 8992002 | 2746 |
| 20-nz332 | 546757 | 8997753 | 1993 | 22-nz375 | 569376 | 8994738 | 2623 |
| 20-nz333 | 545356 | 9000126 | 1869 | 22-NZ376 | 569332 | 8989044 | 2004 |
| 20-nz334 | 548958 | 9002554 | 1869 | 22-NZ379 | 565746 | 8988850 | 1669 |
| 20-nz335 | 548065 | 9006249 | 1825 | 22-NZ380 | 563608 | 8989969 | 1604 |
| 20-nz336 | 546107 | 9008380 | 1705 | 22-NZ381 | 571899 | 8988815 | 2324 |
| 20-nz337a | 551324 | 9009581 | 1744 | 22-NZ382 | 569608 | 8988122 | 1894 |
| 20-nz338 | 555289 | 9010927 | 1773 | 22-NZ383 | 567141 | 8989069 | 1767 |
| 20-nz339 | 561144 | 9005190 | 2074 | 22-NZ384 | 573330 | 8990173 | 2942 |

| Station | Easting | Northing | Elevation(m) |
|---|---|---|---|
| 22-NZ385 | 564177 | 8988592 | 1505 |
| 22-NZ386 | 573546 | 8991447 | 2630 |
| 22-NZ390 | 557495 | 8990528 | 1462 |
| 22-nz391 | 573383 | 8984399 | 1702 |
| 22-nz392 | 575386 | 8985086 | 1756 |
| 22-nz393 | 577510 | 8986216 | 1636 |
| 22-nz394 | 578923 | 8986615 | 1592 |
| 22-nz394N | 571739 | 8984869 | 1811 |
| 22-nz395 | 573878 | 8981275 | 1518 |
| 22-nz396 | 575746 | 8981953 | 1532 |
| 22-nz397 | 577454 | 8982810 | 1408 |
| 22-NZ397H | 576558 | 8983444 | 1481 |
| 22-nz398 | 579421 | 8983663 | 1471 |
| 22-nz399 | 581467 | 8984313 | 1750 |
| 22-nz399N | 568553 | 8986561 | 1670 |
| 22-nz400R | 576336 | 8979037 | 1332 |
| 22-nz401 | 577915 | 8979685 | 1329 |
| 22-nz402 | 579711 | 8980446 | 1400 |
| 22-nz403 | 581568 | 8981373 | 1514 |
| 22-nz404N | 566163 | 8986276 | 1497 |
| 22-nz405 | 578815 | 8976624 | 1239 |
| 22-nz406 | 580195 | 8977331 | 1367 |
| 22-nz407R | 581881 | 8978135 | 1375 |
| 22-nz408 | 584099 | 8979040 | 1665 |
| 22-nz408N | 568060 | 8984108 | 1596 |
| 22-nz409 | 585429 | 8980324 | 1817 |
| 22-nz410 | 574537 | 8989385 | 2412 |
| 22-nz411 | 576107 | 8988734 | 2133 |
| 22-nz413 | 574566 | 8987302 | 2140 |
| 22-NZ414 | 571280 | 8987619 | 2088 |
| 22-NZ415 | 572562 | 8985942 | 1940 |
| 22-NZ416 | 570146 | 8986564 | 1904 |
| 22-REKAB | 571459 | 8983724 | 1727 |
| 22-RRISAK | 554702 | 8988115 | 1464 |
| 22-RRNKU | 558272 | 8979163 | 1239 |
| 23-nz412 | 572362 | 8993526 | 2464 |
| 23-nz417 | 571057 | 8990831 | 2491 |
| 23-nz418 | 568433 | 8991466 | 2101 |
| 23-nz419 | 567435 | 8991332 | 1990 |
| 23-nz422 | 566421 | 8991297 | 1860 |

# Appendix B: MT Phase tensor

Phase tensor maps of MT data for the Ngozi and Rungwe geothermal prospects in the Rungwe Volcanic Province.

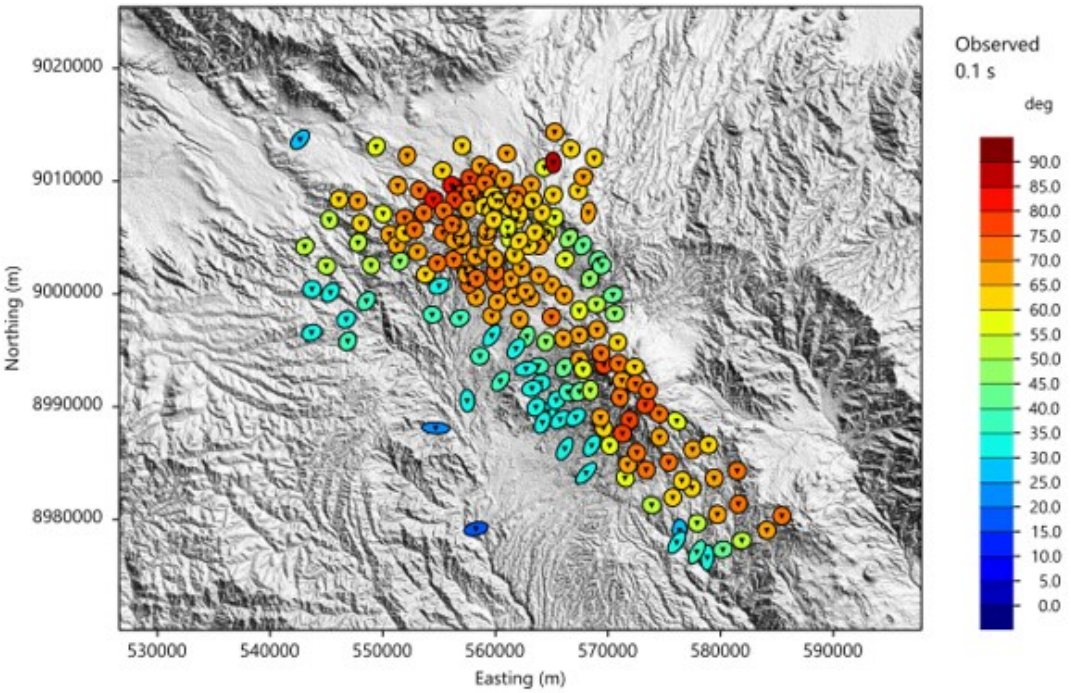


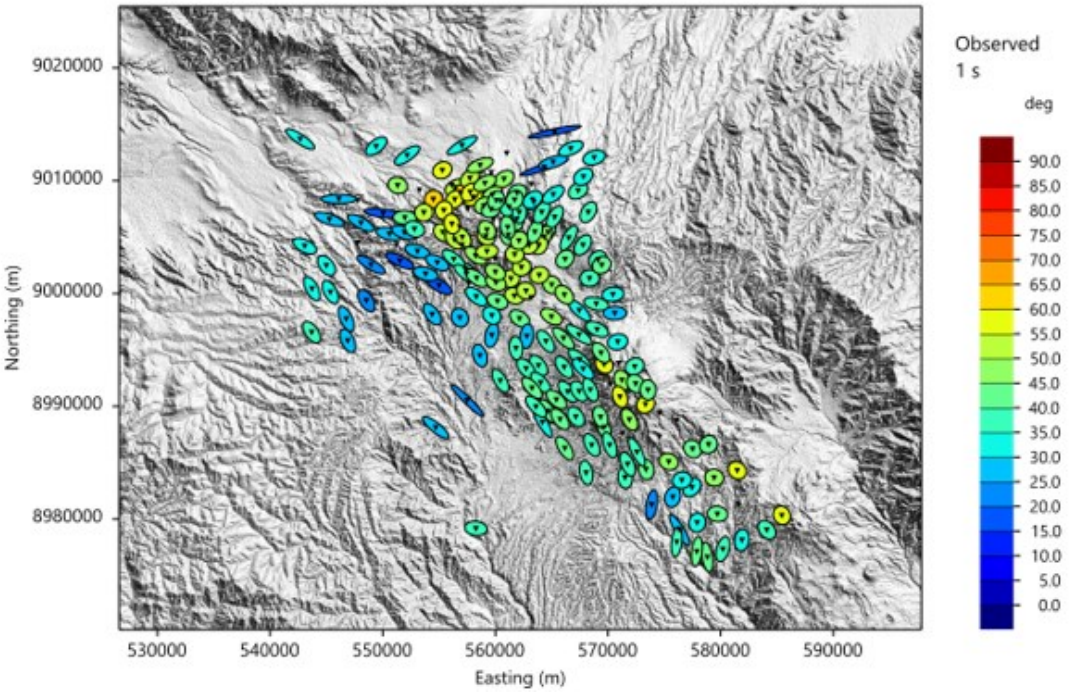

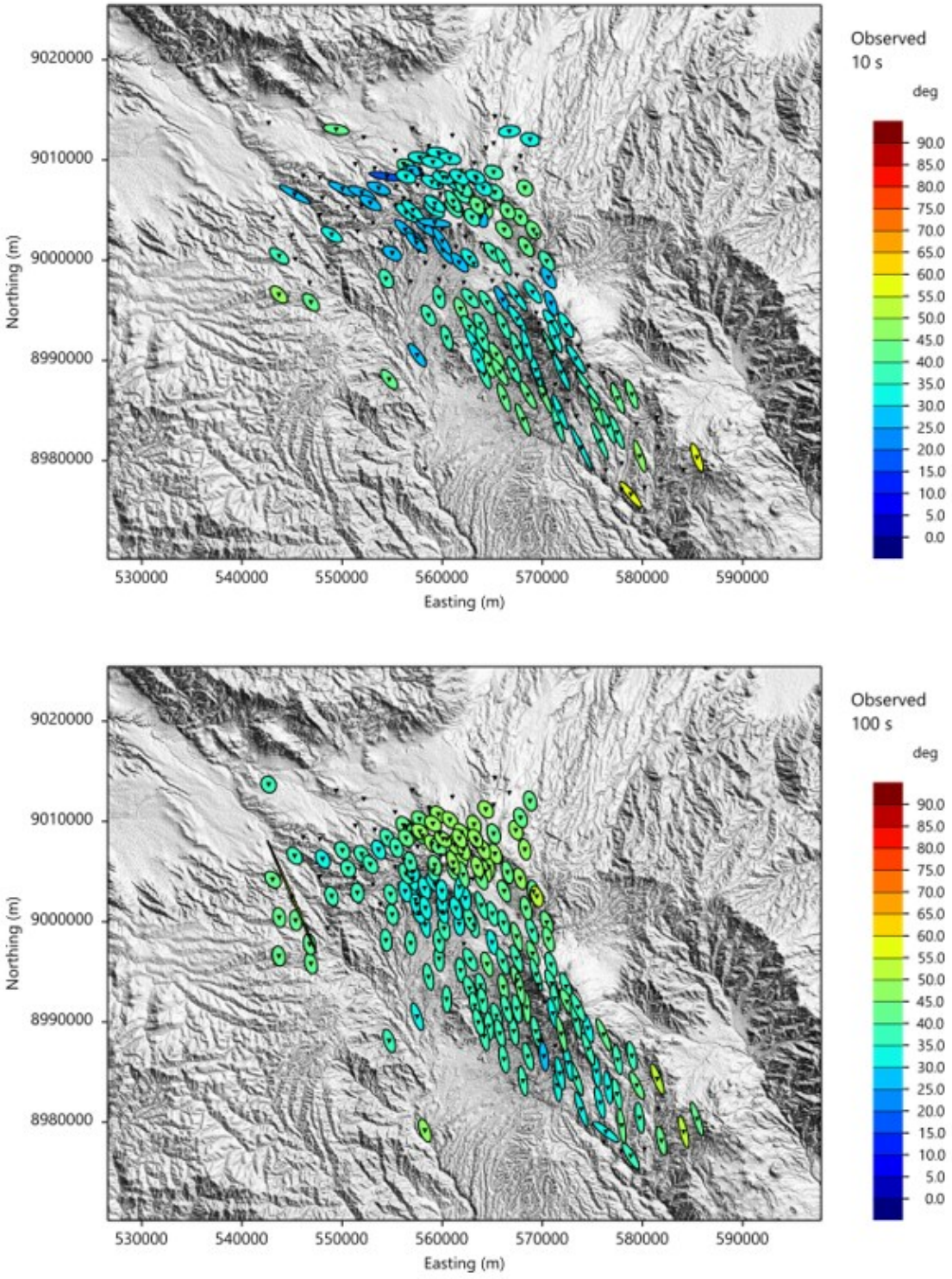
Observed
10 s
deg
90.0
85.0
80.0
75.0
70.0
65.0
60.0
55.0
50.0
45.0
40.0
35.0
30.0
25.0
20.0
15.0
10.0
5.0
0.0
Northing (m)
9020000
9010000
9000000
8990000
8980000
530000
540000
550000
560000
570000
580000
590000
Easting (m)
Observed
100 s
deg
90.0
85.0
80.0
75.0
70.0
65.0
60.0
55.0
50.0
45.0
40.0
35.0
30.0
25.0
20.0
15.0
10.0
5.0
0.0
Northing (m)
9020000
9010000
9000000
8990000
8980000
530000
540000
550000
560000
570000
580000
590000
Easting (m)

# Appendix C: MT Induction arrows

Induction arrow maps of MT data for the Ngozi and Rungwe geothermal prospects in the Rungwe Volcanic Province. Arrows point towards the conductor.

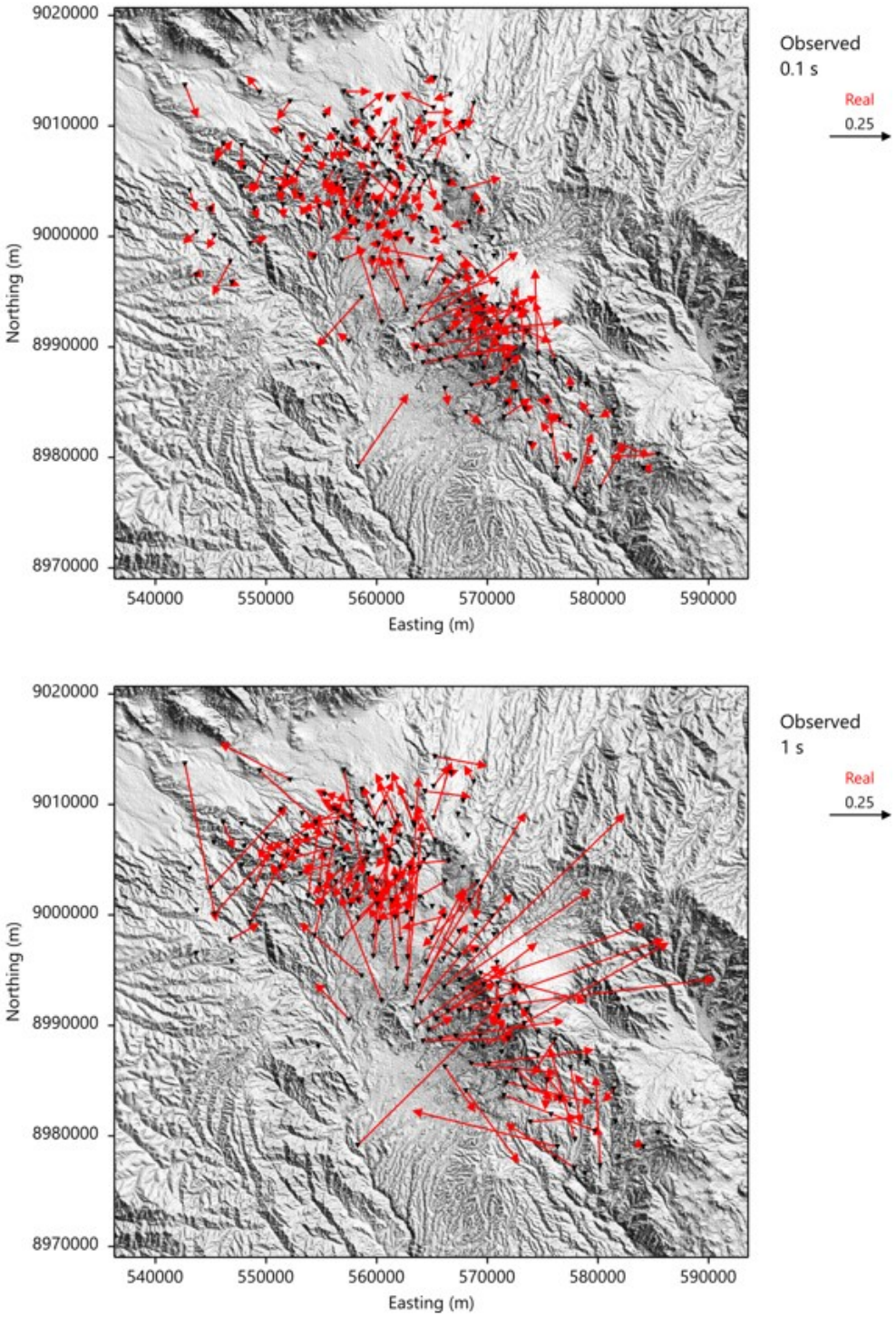

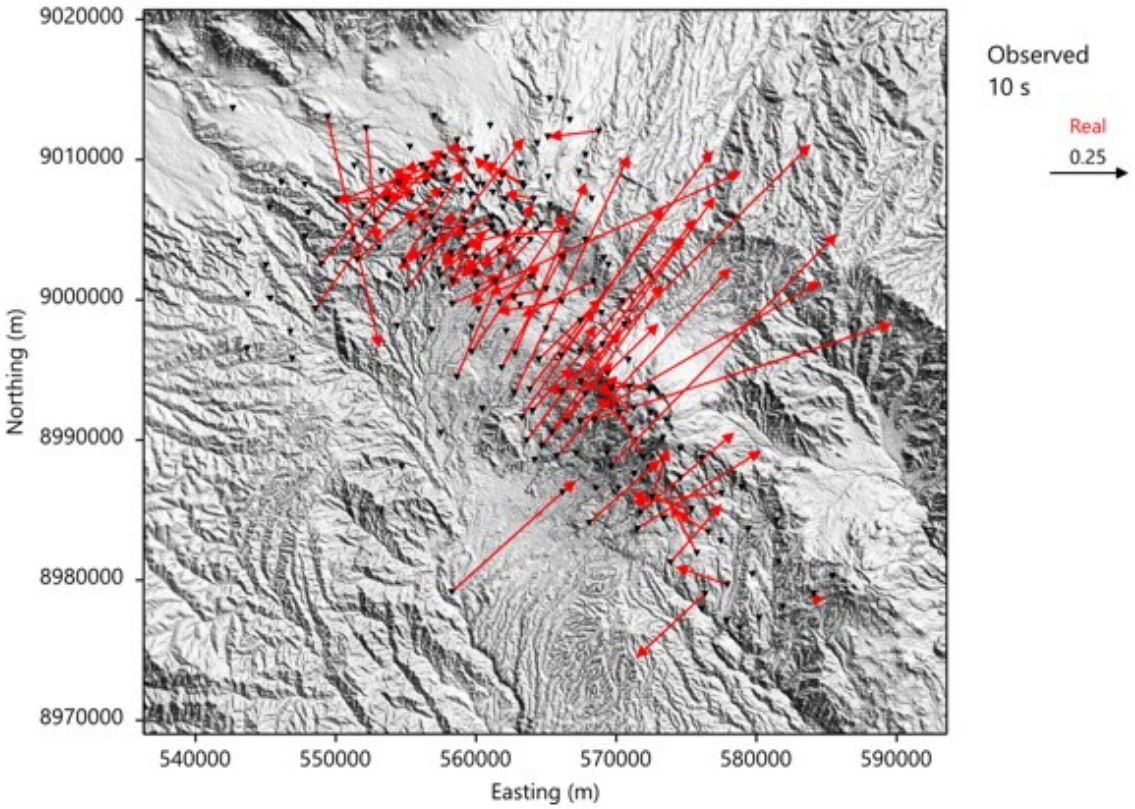
9020000
9010000
9000000
8990000
8980000
8970000
Northing (m)
540000
550000
560000
570000
580000
590000
Easting (m)
Observed
10 s
Real
0.25

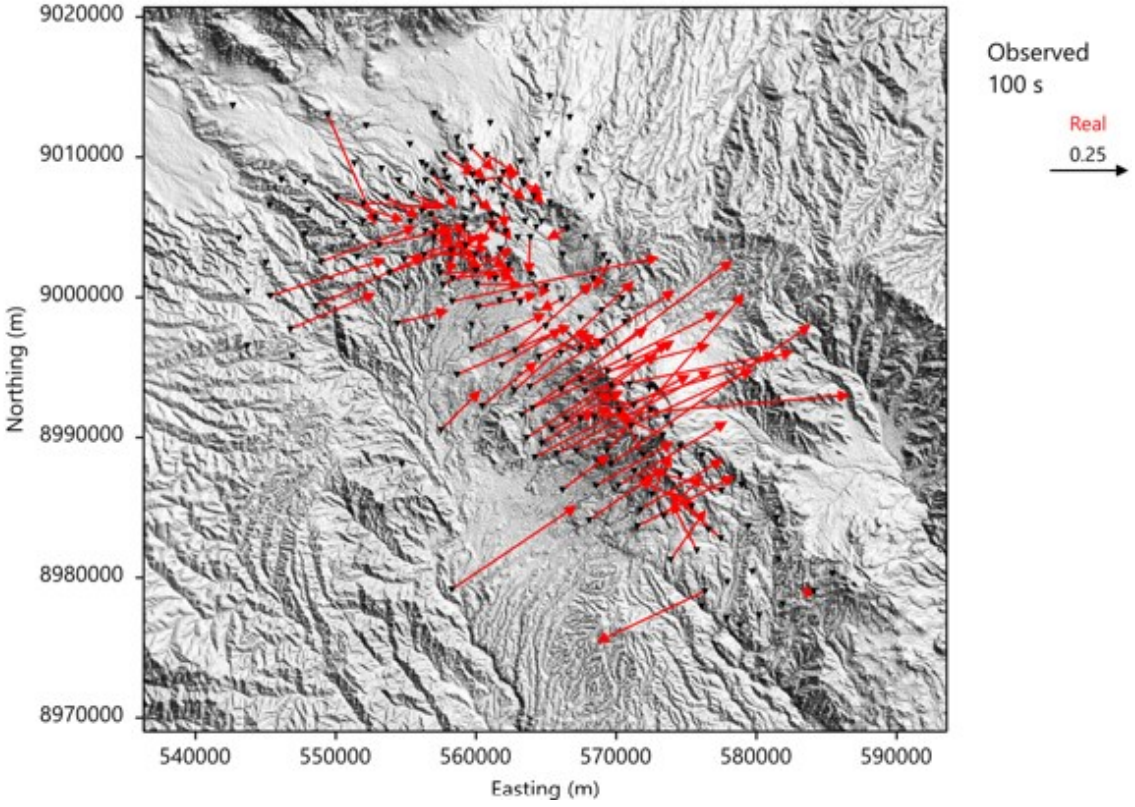
9020000
9010000
9000000
8990000
8980000
8970000
Northing (m)
540000
550000
560000
570000
580000
590000
Easting (m)
Observed
100 s
Real
0.25

# Appendix D: Gravity data

**PROFILE 1: BA Before and After Sediments correction Compared with Topography and Geological domains**

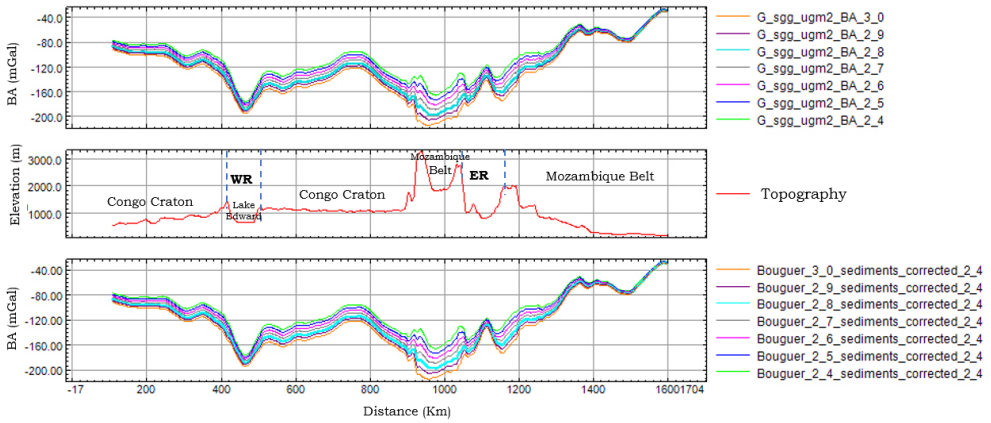


**PROFILE 2: BA Before and After Sediments correction Compared with Topography and Geological domains**

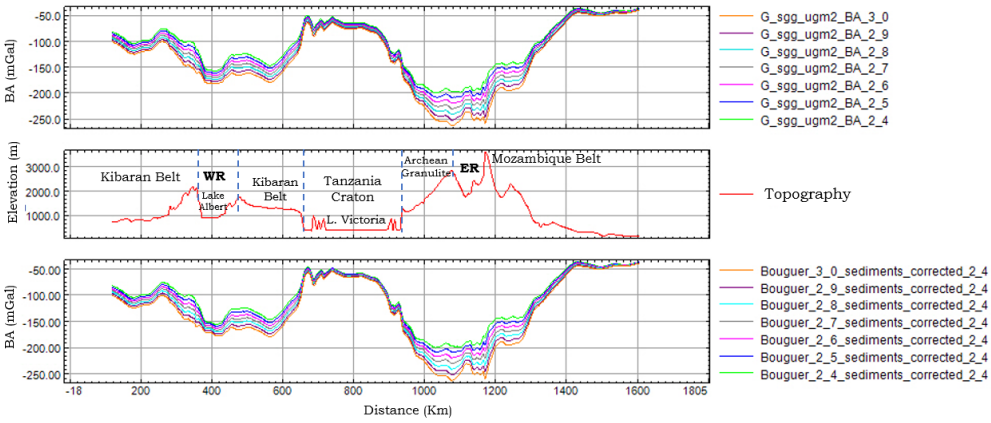


**PROFILE 5: BA Before and After Sediments correction Compared with Topography and Geological domains**

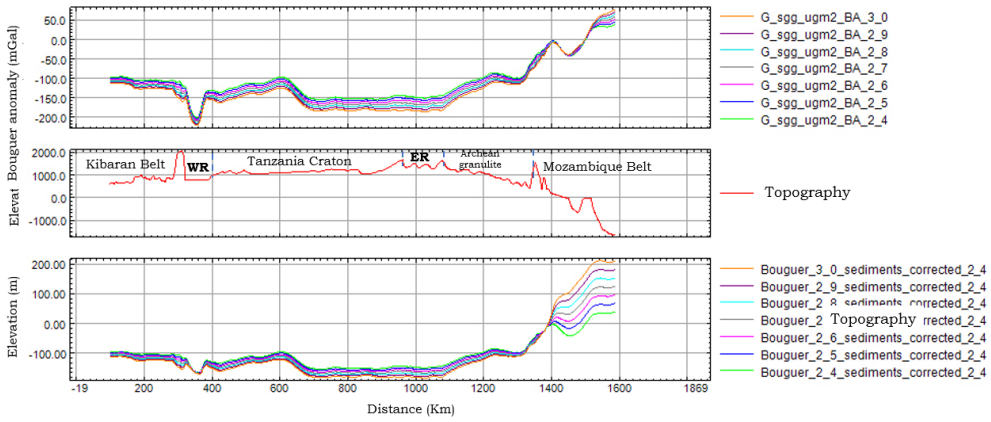

**PROFILE 6: BA Before and After Sediments correction Compared with Topography and Geological domains**

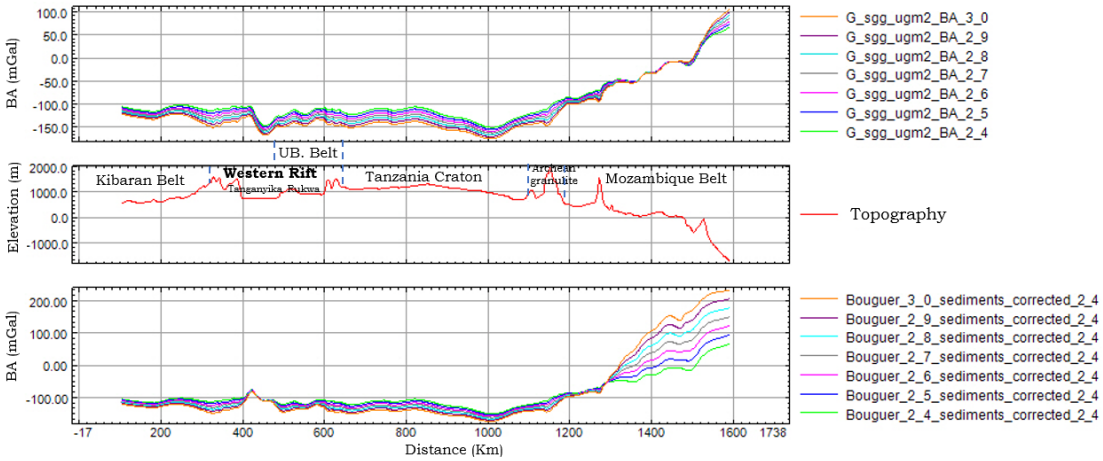


**PROFILE 7: BA Before and After Sediments correction Compared with Topography and Geological domains**

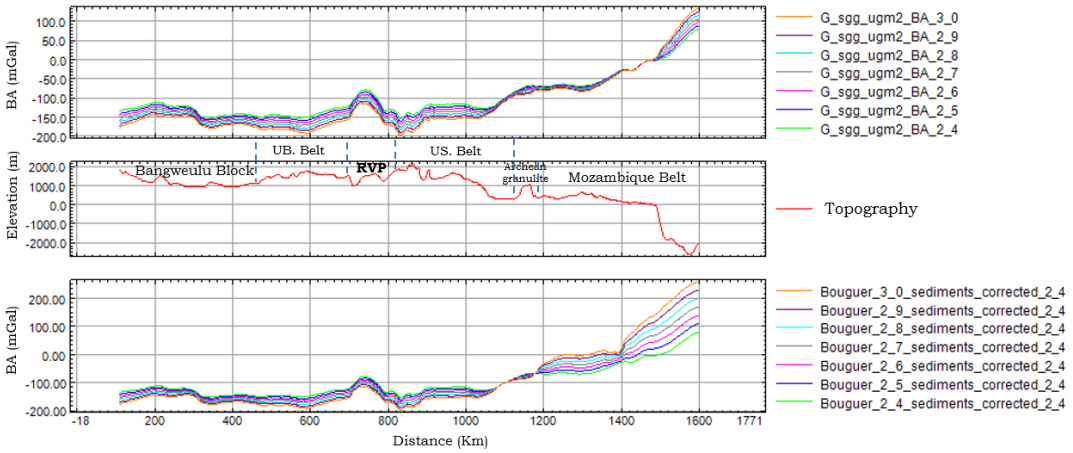


**PROFILE 8: BA Before and After Sediments correction Compared with Topography and Geological domains**